Fused Filament Fabrication of Metal-Ceramic High-Density Polyethylene Composites

by

Nancy Bhardwaj

A thesis submitted in partial fulfillment of the requirements for the degree of

Master of Science

in

MATERIALS ENGINEERING

Department of Chemical and Materials Engineering

University of Alberta

ABSTRACT

This thesis focuses on the manufacturing of high carbide content wear-resistant parts by extrusion-based Additive Manufacturing (AM) based on the principles of Powder Metallurgy (PM). A new manufacturing technique, termed Fused Filament Fabrication of Cermets (FFFC) is presented. First, particle packing theory is applied to develop a methodology for maximizing packing density and carbide content in non-ideal binary powder mixtures. Based on this optimization, sinterable metal-ceramic polymer filaments suitable for Fused Filament Fabrication (FFF) are prepared and printed. It is shown that a traditional polymer 3D printer can be used to successfully deposit high-density polyethylene (HDPE) composite filaments containing up to 46 vol% Ni-TiC and Ni-WC fillers, to produce dense green parts for sintering. A characterization of the composite filaments and resultant printed parts is provided. An analysis of the random loose void fractions in dry fillers and the fraction of polymer in the composite after polymer is injected into the dry filler is presented. It is concluded that, the maximum void contraction ($\Delta\Theta_{max}$) is a function of the ratio of mean particles sizes (δ) in binary dry powder mixtures. As δ decreases and the particle sizes become more dissimilar, an increasing deviation from the ideal rule-of-mixtures law is observed. The critical δ is revealed to be 0.65. Furthermore, when dry filler is mixed with HDPE to form composite filaments for FFF, the particles are rearranged, and the polymer content of the filled composite is greater than the void fraction observed in dry filler packing. Fillers having lower dry void fractions, reported higher polymer contents in their composites. The important role of non-ideal particle packing in binary filler mixtures is emphasized, where the goal is to produce high carbide content cermet parts. Some remarks about process parameters that influence part quality and suggestions for future work are included.

DEDICATION

To Jameel, Mariah, and Aly. The realest ones I’ve ever known. Your unwavering faith in me and my work throughout all the difficult times in my life means more than you can ever know. I couldn’t have done it without your unconditional love and support. Thank you. I am so grateful.

ACKNOWLEDGEMENTS

First and foremost, a heartfelt thank you to both my advisors Hani and Tonya. I appreciate the time, effort, opportunities, and mentorship you both have provided for me since my undergraduate years. Without your encouragement and guidance, I would not have had the courage to enroll in this program or the perseverance to complete it. Thank you for believing in me.

To my AMPL and AM2G research colleagues, past and present, thank you for your support and more importantly your friendship. I am so lucky to have worked alongside each and every one of you - Aziz, Jonas, Sandy, Daniela, Akankshya, Dylan, Bilal, Vanda, Tailin, Lu, Anne, Baltej, Thomas, Pepe, Marcelino, Remy, Steffen, Billy, Kartik, and Lily.

Thank you to Syncrude Canada for funding this project and for supplying all metal and ceramic powders. A sincere thanks to Stefano Chiovelli for his time and effort in reviewing all documents and presentations.

Thank you to InnoTech Alberta for financial support and providing facilities for extrusion. A special thanks to TriDung Ngo and Juan Segura for training on the extruder system, as well as patience and support during filament making. Thank you for sharing your knowledge, expertise, and for generously providing countless hours of your time and dedication to my thesis work. Additional thanks to Gary Fisher, Nina Laderoute, Johanna Meier, Ron Rau, and Mike Danysh.

To NSERC, Hi-AM, and Saturn Machine Works for financial support and invaluable contributions to this project. Thank you.

Table of Contents

LIST OF TABLES

TABLE OF FIGURES

LIST OF ABBREVIATIONS AND SYMBOLS

Abbreviations

PM	Powder Metallurgy
AM	Additive Manufacturing
FFFC	Fused Filament Fabrication of Cermets
MMC	Metal-Matrix Composites
LPS	Liquid Phase Sintering
MIM	Metal Injection Molding
IM	Injection Molding
3DP	Three-dimensional Printing
CAD	Computer Aided Design
STL	Standard Tessellation Language
SLA	Stereolithography
SLS	Selective Laser Sintering
FDM	Fused Deposition Modelling
FFF	Fused Filament Fabrication
EBM	Electron Beam Melting
PMC	Polymer Matrix Composites
PF	Volumetric Packing Fraction
ROM	Rule-of-mixtures
TRS	Transverse Rupture Strength
MW	Molecular Weight
TGA	Thermogravimetric Analysis
TPE	Thermoplastic Elastomer
ASTM	American Society for Testing and Materials
SEM	Scanning Electron Microscopy
EDX	Energy Dispersive X-ray
PSD	Particle Size Distribution
MPIF	Metal Powder Industries Federation
HDPE	High-density Polyethylene

Symbols

A_F	Cross-sectional area of filament (mm^2)
D	Average filament diameter (mm)
$d50_{Ni}$	Mean particle size of Ni Powder
$d50_C$	Mean particle size of carbide powder (TiC or WC)
FF	Filament feed rate (mm/s)
FR_{air}	Volumetric filament flow rate in air (mm^3/s)
FR_P	Volumetric filament flow rate during printing (mm^3/s)
$f_{f,cal}$	Average calibrated filler feed rate (kg/min)
m	Mass (kg) or Material Feed Rate (kg/min)
ρ	Density (kg/m^3)
ρ_c	Composite Density (kg/m^3)

V	Volume (m^3)
V_T	Total Volume (m^3)
$V_{pyc,T(°C)}$	Calibrated volume of pycnometer (m^3) at a specific temperature
V_C	Calibrated Container Volume (m^3)
v	Volume Fraction
w	Mass Fraction
X_{max}	Mixture composition at maximum void fraction (vol%)
X_{min}	Mixture composition at minimum void fraction (vol%)
δ	Mean size ratio of particles in a binary mixture
Φ	Dimension – length, width, or height (mm)
Θ	Volumetric Void Fraction
$\mathbf{\Theta}_{filament}$	Volume fraction of polymer in filament
$\mathbf{\Theta}_{printed}$	Volume fraction of polymer in printed part
Θ_{min}	Minimum void fraction
Θ_{max}	Max void fraction (equal to 0.5)
Θ_S	Void fraction in a mixture of purely mono-sized small particles
Θ_L	Void fraction in a mixture of purely mono-sized large particles
$\Delta\mathbf{\Theta}_{dry}$	Difference in experimental and ROM void fractions of a dry filler powder mixture
$\Delta\mathbf{\Theta}_{polymer}$	Difference in volume fraction of polymer in composite and ROM void fraction in a dry filler powder mixture
$\Delta\mathbf{\Theta}_{max}$	Maximum void depression

Subscript

f	filler
p	polymer
v	void
E	excess polymer and voids
S	sample
dry	random loose dry packed state
T	true
B	bulk
ROM	rule-of-mixtures
exp	experimental average
1	powder 1
2	powder 2
EA	ethanol solution
T	temperature (°C)
fit	best fit line
O	original CAD model
AP	nominal actual printed
S	sample
m	average measured

1. INTRODUCTION

The first chapter begins by introducing the industrial need for wear-resistant metal-ceramic parts, followed by a description of metal manufacturing processes based on Powder Metallurgy (PM), and innovative methods such as Additive Manufacturing (AM). A relatively new method of producing metal-ceramic parts, termed Fused Filament Fabrication of Cermets (FFFC) is described. The framework of the proposed process is followed by the objectives, technical contributions, and general outline of thesis work.

1.1 The Need for Wear Resistant Materials

The increasing demand for economical production of complex parts from high-performance materials such as metal-ceramic composites, presents a constant challenge in the gas and mining industries in Canada. Minimizing the loss of production time due to regular maintenance of equipment subjected to wear-related issues is a critical issue. A loss of 2% in production at Syncrude can result in a revenue loss of approximately $40M *(Canadian Oil Sands, 2013).* In surface mining applications the major mode of wear is abrasive wear, which is heavily dependent on hardness of a material usually around 1200 HV *(Duncan, 2016).* Four common classes of metallic materials exist to combat wear: iron-based alloys, nickel-based alloys, cobalt-based alloys, and carbide-containing composites *(McKee and Wu, 1997).* For purposes of oil sands equipment protection, where high wear resistant critical components are required, carbide-containing composites are most commonly used *(Duncan, 2016).* Such composites are named Metal-Matrix Composites (MMC) and are usually composed of a soft Ni-alloy matrix, reinforced by tungsten carbide hard phase *(Yarmuch et. al, 2009)*. A MMC composed of a metal and ceramic material are called cermets. This material is made by "cementing" very hard ceramic such as tungsten monocarbide (WC) or titanium carbide (TiC) grains in a binder matrix of a softer metal, usually cobalt (Co) or nickel (Ni) metal by Liquid Phase Sintering (LPS) *(Rodea, 2012)*. Figure 1.1 shows the microstructure of a NiCrBSi-WC cermet material, the hard phase is clearly identified by the dark-colored WC ceramic particles of angular shape, dispersed within a light-colored NiCrBSi metallic matrix *(Oerlikon Metco, 2016)*. Components made from cermets are those subjected to severe impact and wear conditions, such as drill bits and mining tips, milling products (end mills and mill inserts), crushers, picks for road maintenance, and saw blade inserts *(Antonov et al., 2017).*

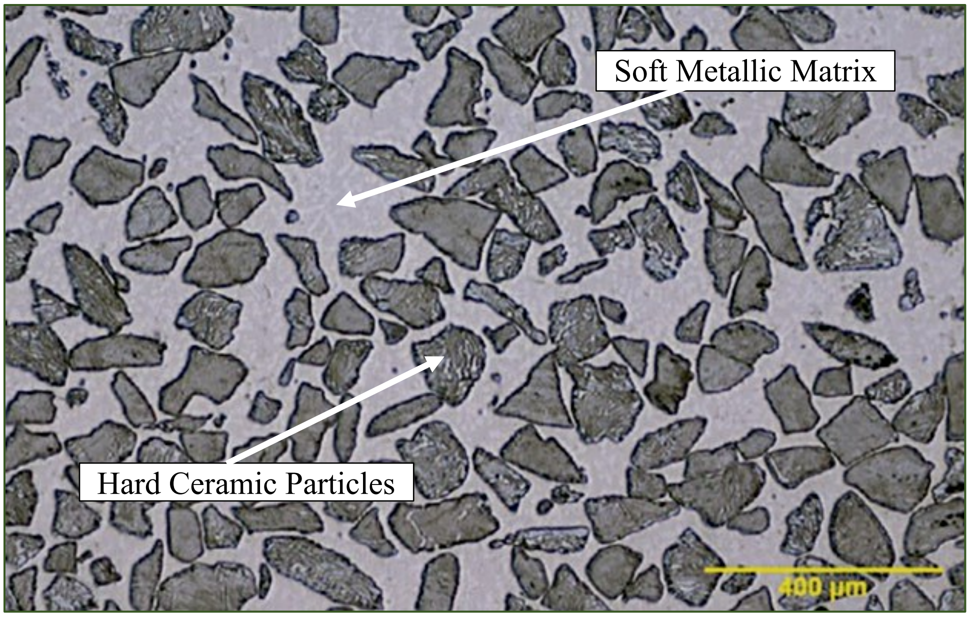

Figure 1.1 Microstructure of Cermet Material

1.2 Powder Metallurgy Manufacturing Processes

Powder metallurgy (PM) approaches to metal manufacturing are widely recognized for the ability to produce high-quality parts. PM is a process where metal powder is compacted to form a part of desired shape, followed by heating of the compacted part to metallurgically bond the particles (referred to as “sintering”) and produce a fully dense metal part. The popularity is due to three main advantages in manufacturing ability: 1) create parts with sophisticated and complex geometries, 2) create parts from difficult-to-shape materials, and 3) potential to manufacture alloys that would otherwise be impossible to create *(German and Bose, 1997).* An example of this is the forming of refractory materials such as WC, or carbide-containing cermet parts. The high hardness and melting temperatures of refractory materials present great difficulty in processability using traditional methods of shaping such as machining or casting *(Beddoes and Bibby, 1999).* The process of machining requires the use of a variety of cutting tools to precisely cut a specific geometry out of a bulk material. Casting is a process whereby molten material is poured into a mold of desired shape. Both practices are unsuitable for cermet processing due to high costs from waste removed material, blade replacement, high energy requirements for heating, and mold fabrication. The general steps involved in most PM manufacturing processes are shown by the flow diagram in Figure 1.2 *(Powder Metallurgy Review, 2020)*. The process consists of raw material (or alloying elements) mixing to form a composite feedstock, compaction of feedstock into a desired shape, heating to metallurgically bond particles or “sintering”, followed by optional secondary post-processing of the sintered part. Secondary processing steps may include further machining or finishing of the post-sintered part to achieve a desired surface finish or to meet the requirements of geometric tolerance. Softer powders can be shaped by compaction or pressing; however, hard powders are resistant to deformation and must be mixed with polymers to aid in shaping of the powders into a desired form (*German, 2005).* Thus, the raw materials are comprised of polymer and metal and/or ceramic powders, which are mixed and used as feedstock for molding. The polymeric material acts as a binder to improve the flow properties of the powder, holding the powder particles in place until they are bonded by sintering, and provides strength to the part after shaping. PM processes can be tailored to achieve desired microstructures, resulting in consistent mechanical properties in final parts *(Beddoes and Bibby, 1999)*.

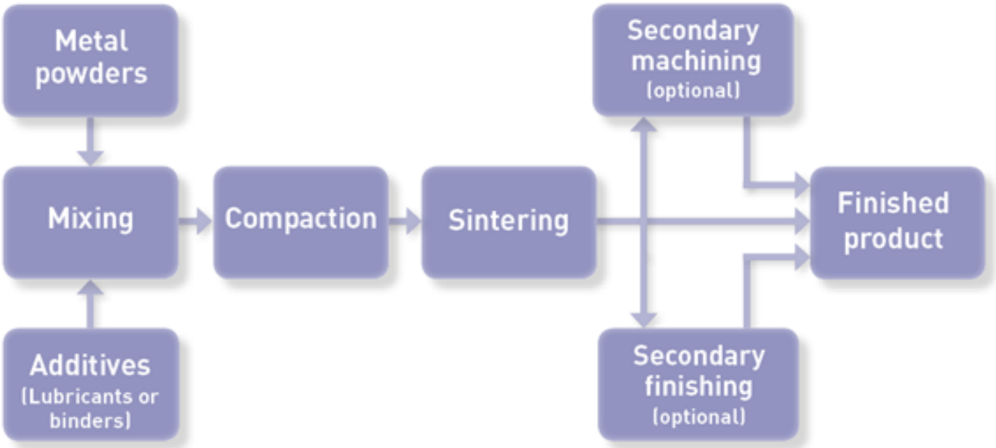

Figure 1.2 General PM Manufacturing Processes

The capability of fabricating parts to final size, shape, and within tight dimensional tolerances can be seen as an economic benefit, as the need for post-processing resulting in material wastage is reduced or entirely removed *(German, 2005)*.

1.2.1 Metal Injection Molding (MIM)

The most common PM method for producing metal-ceramic parts is Metal Injection Molding (MIM). The process begins by heated mixing of polymeric binder and metal-ceramic powder materials to produce a flowable composite which is then extruded and granulated to form feedstock pellets. The feedstock pellets are then reheated and injected into a mold cavity of desired shape. The mixture is pressurized by a piston to melt and consolidate the pellets and mold the material. After molding, the part is ejected and referred to as a “green-body” part. Next, the polymeric binder component of the green-body part must be removed using either a solvent or thermally burningout the polymer, forming a “brown-body” part after debinding. Following this, the powder particles are densified by fusing the metal-ceramic particles together at high temperatures by sintering to form the final product. The MIM process *(MPIF, 2020)* is illustrated in Figure 1.3.

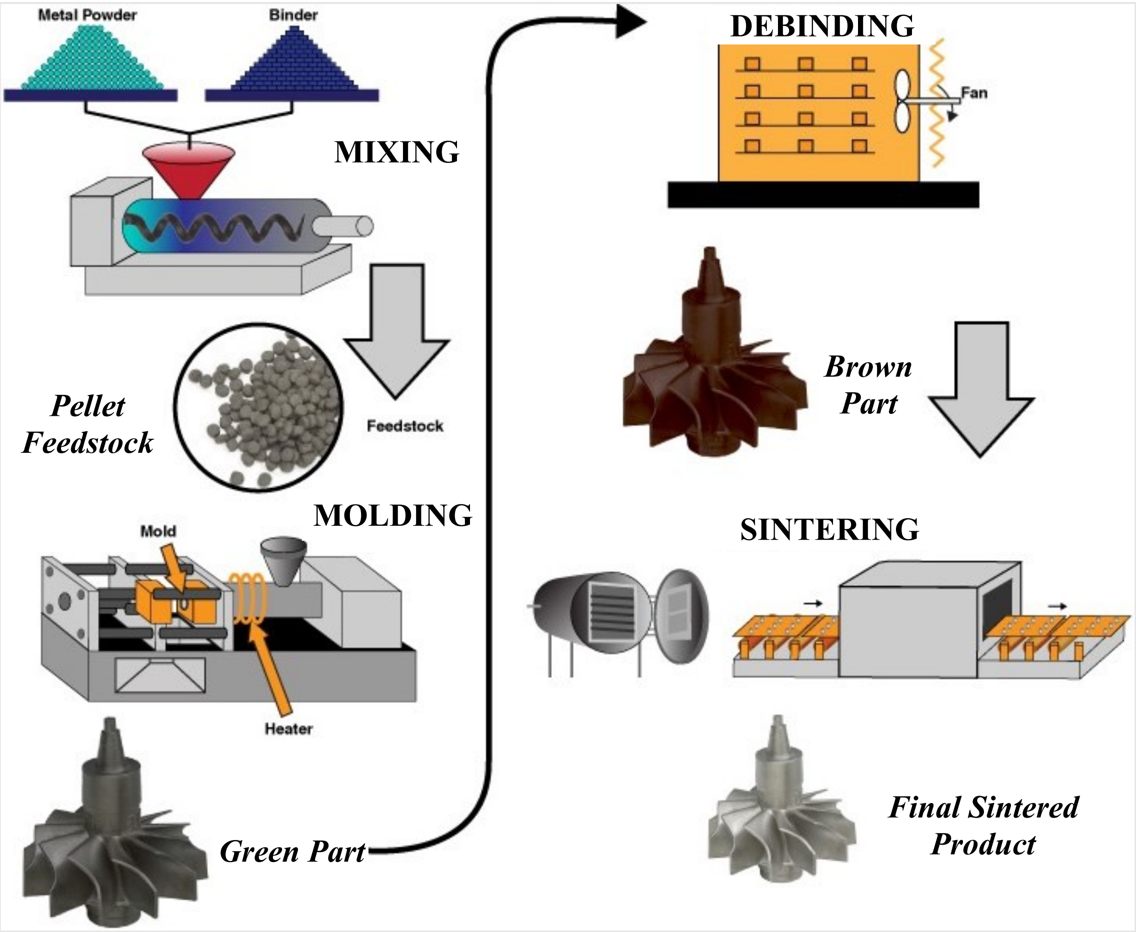

Figure 1.3 Detailed Schematic of the MIM Process

Many manufacturing processes are limited by their ability to produce parts with complex geometries and low shape tolerances. The general tolerance for parts produced by MIM *(German and Bose, 1997)* are presented in Table 1.1. It is clear based on the data in Table 1.1 that one of the greatest constraints is part size. Essentially, MIM is suitable for manufacturing of small parts, less than 1000 mm (or 1 m) in length and 25 mm in thickness. Also, part thickness is understood to be directly proportional to the time required for debinding, which contributes to increases in both production time and part manufacturing cost. Additional limitations include edge radius (min = 0.05 mm) and corner radius or hole diameter (min = 0.1 mm).

Table 1.1 Limitations of MIM Produced Parts

Attribute	Minimum	Maximum	Typical
Mass (g)	0.2	20,000	40
Thickness (mm)	0.2	25	10
Variation in Thickness	none	100:1	2:1
Longest Dimension (mm)	2	1000	100
Dimensional Tolerance (%)	0.05	2.0	0.3
Material	Simple element	composites	alloys

Three major disadvantages exist for IM processes. The first, and presumably most critical factor is the high cost associated with mold requirements, a new design requires a new mold. Molds may be re-used, however, the cost of manufacturing a new mold can range between \$1,000 – \$100,000 *(German, 2005)*. Consequently, this creates a huge limitation to IM processes as the requirement of a new mold for each new part, additionally making the modification of designs a difficult and costly task. Similarly, the second disadvantage is the high cost of feedstock powders used in IM, specifically, small average particle sizes of about 10 microns or less. Such powders are very costly due to the mechanical processing required to achieve such small sizes. The third disadvantage is operational, as a great deal of attention to detail is required for the shaping (molding) step in this process. This includes, the proper feedstock formulation, design factors such as shape and specific geometric part features, mold material, and properties of the molding equipment must all be taken into account to achieve a quality green-part part with precise dimensions and desired properties. This requires a highly qualified person to design and control this process to achieve optimal final results. MIM is ideal for producing high volumes of identical objects, with the capability to produce complex 3D geometries parts with low tolerances. The values presented in Table 1.1 serve as an important benchmark for evaluating the range of shape capability achievable by manufacturing parts using MIM and comparing against additive manufactured parts in future chapters. However, a simpler method of part shaping is required for efficient and reliable manufacturing of difficult to shape hard cermet powders.

1.3 Additive Manufacturing Process

Additive manufacturing, known more commonly as three-dimensional printing (3DP) is a fast-growing and innovative technology used to manufacture 3D structures using a layer-by-layer additive approach. The steps involved in 3DP *(Campbell et al, 2011)* are illustrated in Figure 1.4, where the process begins by using Computer aided design (CAD) software such as Solidworks, to generate a 3D-model of a physical part to be printed. The CAD model is then converted into a printable file type, most commonly called Standard Tessellation Language (.STL) file format. The STL files describe the surface geometry of a 3D object by a triangulated 3D Cartesian coordination system. The STL file is uploaded to a slicing software; some common slicing software include slic3r, Cura and Simplify3D, where the model is converted into “slices” of horizontal layers and the software generates toolpaths for the printer to follow in order to efficiently print each layer to the design specifications controlled by the user. At this stage, various printing parameters such as layer height, printing speed, border thickness, infill density and raster angle may be modified. The slicing software can also provide printing statistics, which provide the user with valuable information regarding the printing time, length of filament needed and the layer count for any specific model to be printed. The sliced model is then exported as a g-code, which is a generated code outlining a set of instructions in the form of movements for the printer to follow to build the part. This g-code is then used to print the 3D model, usually using a printing host or interface software, such as Repetier Host. This interface connects the printer with the 3D model and printing controls.

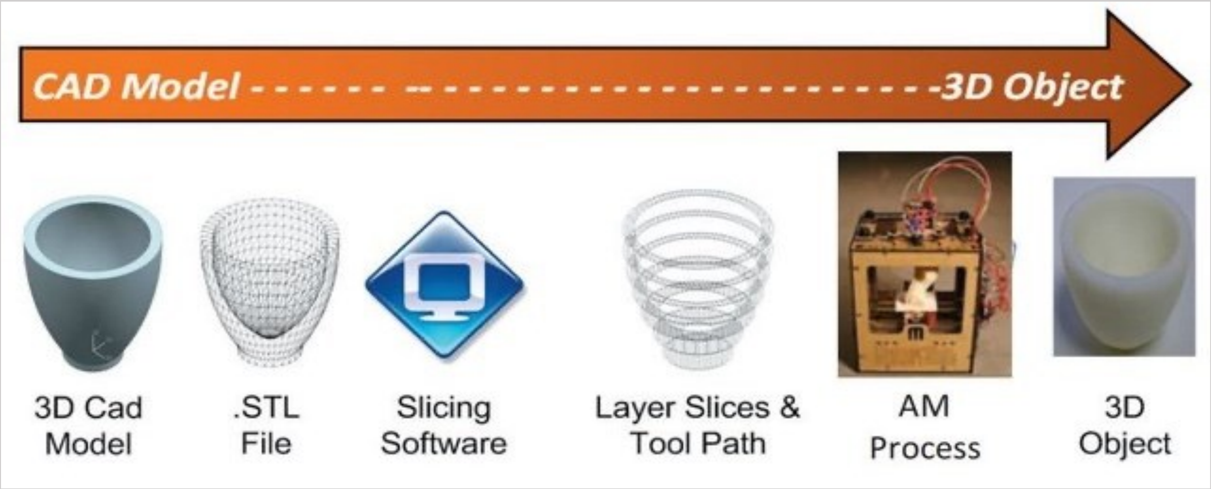

Figure 1.4 Schematic of 3DP process step-by-step ***(Campbell et al, 2011)***

The technology, which today encompasses 5 commercially available distinct process variations, began first emerging in the 1980's with the first successful patent for Stereolithography (SLA) filed in 1984 *(Hull, 1984)*. 3D printing technologies in the early years were mainly used to produce non-functional prototypes. In 1986, another 3DP technology was developed and patented, Selective Laser Sintering (SLS) *(Deckard, 1986)*. The most popularly used extrusion-based 3DP technology, Fused Deposition Modeling (FDM), was invented and patented in 1989 *(Crump,* 1989). The term FDM was trademarked in 1991 by Stratasys, henceforth the technology was commonly referred to as Fused Filament Fabrication (FFF). Lastly, Electron Beam Melting (EBM) was devised in 1995 at MIT *(Dave, 1995)*. Figure 1.5 describes principles of operation for the five main 3DP techniques and applicable material types *(Geissbauer et al, 2017).* This marked the start of an intense gain in momentum for 3DP related research, which has gained strong foot hold in the last decade. According to the 2016 Wohlers report, the AM sector worldwide grew by 25.6% to $5.17 billion in 2015 *(Wohlers, 2016)* and is projected to reach $17.7 billion by 2020 (*Garter, 2016)*.

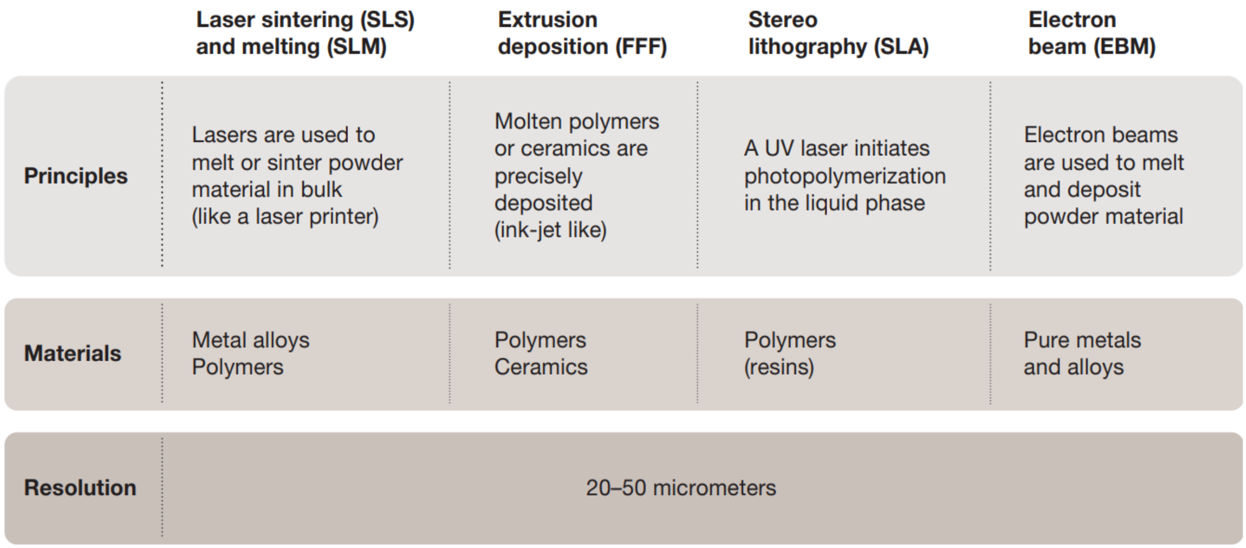

	Laser sintering (SLS) and melting (SLM)	Extrusion deposition (FFF)	Stereo lithography (SLA)	Electron beam (EBM)
Principles	Lasers are used to melt or sinter powder material in bulk (like a laser printer)	Molten polymers or ceramics are precisely deposited (ink-jet like)	A UV laser initiates photopolymerization in the liquid phase	Electron beams are used to melt and deposit powder material
Materials	Metal alloys Polymers	Polymers Ceramics	Polymers (resins)	Pure metals and alloys
Resolution	20–50 micrometers			

Figure 1.5 Main 3D-Printing Techniques *(Geissbauer et al, 2017)*

A 2020 worldwide survey conducted with 1600 3DP users from 71 countries revealed that FFF, SLS and SLA are the top three 3DP technologies used. FFF accounted for 61% of in-house operations *(Alsop, 2020).* The main benefit of 3DP technology is the ability to fabricate parts of intricate geometries and fine details by fast and cost-effective means, which may be costly, extremely difficult or impossible using traditional methods of manufacturing. 3DP has applications in aerospace, defense, healthcare, automotive and consumer retail markets. Therefore, the materials used for 3DP must also be wide-ranging as many applications require the use of polymeric, metallic or ceramic type materials.

1.4 Material Extrusion Deposition Process

Fused Filament Fabrication (FFF) is considered as the most common, versatile, and user-friendly method of AM available globally. The FFF technique is demonstrated by the schematic in Figure 1.6 *(Montero et al, 2019)*.

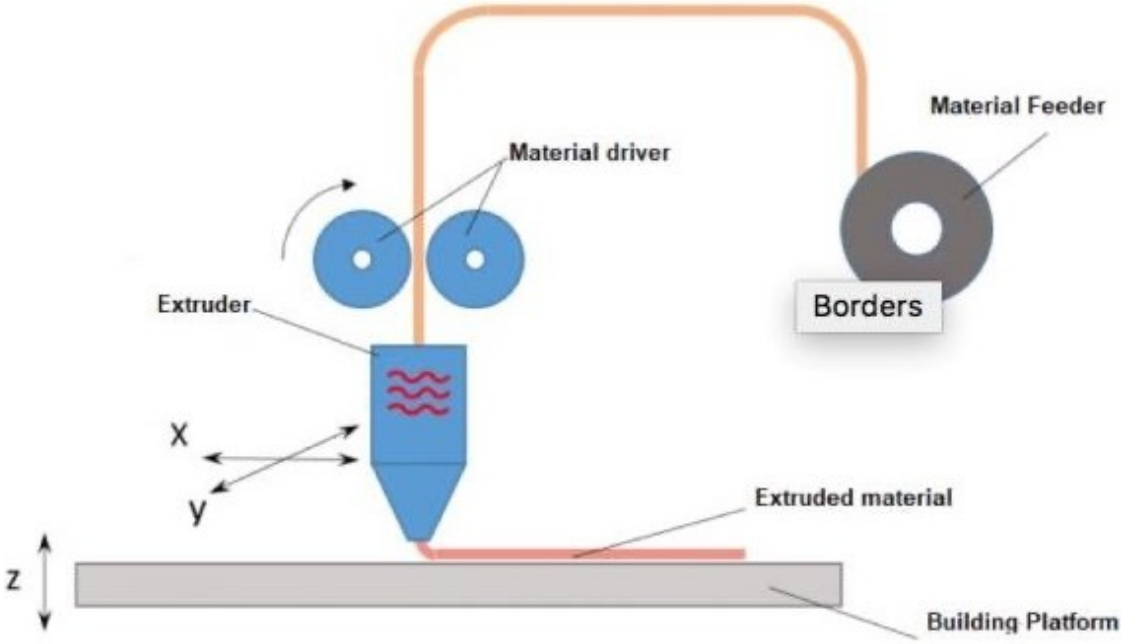

Figure 1.6 The FFF Process

This method requires a "rod-like" filament feedstock, most commonly 1.75 mm (or 2.85 mm) in diameter, made of thermoplastic polymer material. The filament is stored coiled onto a spool where it is guided into the top of the extruder by two material driving gears. Inside the extruder, the filament is heated, causing molten extruded material to flow out of the nozzle. Nozzle sizes typically range between 0.4 to 1.0 mm in diameter and affect the print resolution, as larger nozzle sizes limit the printing of fine geometric features. The material is uniformly deposited onto the surface of the printing platform, referred to as the building platform or print bed. The bed surface may require heating, depending on the material characteristics of the deposited material. Figure 1.6 shows that the extruder is capable of moving in x and y directions, while the bed moves in the z direction. The direction of printing, however, is referred to as the raster angle, a parameter that can be set by the user. The raster angle is described as the orientation or direction in which the extruder will move to fill-in or print the part. Four common raster angle configurations are seen in Figure 1.7. Many researchers have studied the effect of printing parameters on mechanical properties of the final 3D-printed part, as each parameter affects the properties of the final print in a unique way. In the case of raster angle, it is generally agreed upon that parts printed using a 45/-45° configuration show the greatest mechanical tensile strength.

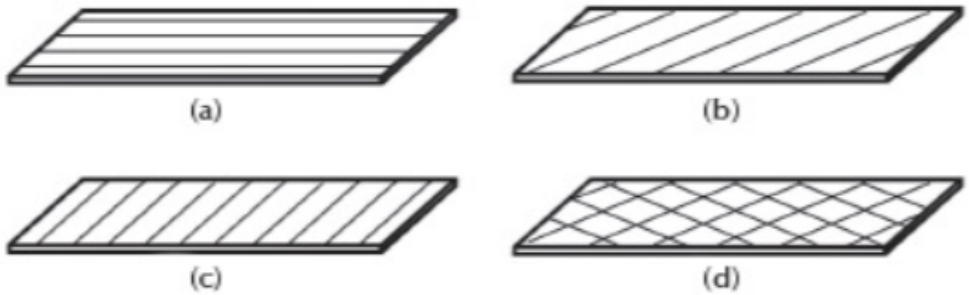

Figure 1.7 Raster Angle Configurations: a) 0°, b) 45°, c) 90°, and d) 45/-45°

The FFF machine begins operation by heating the extrusion nozzle and the build platform up to the temperatures specified by the g-code. Once the temperatures have been reached, the gears will activate to feed the solid filament into the heated nozzle. Molten material then flows out of the nozzle and the extruder head moves following a toolpath in the raster configuration controlled by the g-code, uniformly depositing material one line at a time to form a single layer. Once a single layer has been deposited to the print bed, the extruder head moves up in the Z-direction a distance equal to the layer height and begins once again to deposit molten material on the surface of the previously deposited first layer. As each layer is printed, the previous layers bond to each other by solidifying upon cooling. The initial layer of deposited material is crucial in achieving a high-quality finished print such that there is good adhesion to the heat bed. FFF technology is able to successfully print designs with a limited range of overhangs, meaning that some structures become unstable due to lack of support from lower layers and are subject to slumping print failures. Warping can also be a result of shrinkage of the polymer, causing subsequent layers that are printed further away from the heated bed plate to separate from the initial layers. Modifications in printing parameters can be made to promote adhesion between the heated bad and the first layer of print. For example, a single layer of packing tape can be applied to the glass bed to improve bed adhesion for some types of materials. These practices are not yet standard but are shared between users as best practices. The most commonly used materials for FFF feedstock are thermoplastic polymer filaments. Polylactic acid (PLA), polyethylene terephthalate (PET), and Acrylonitrile Butadiene Styrene (ABS) are among these common types of 3DP polymers. It is very simple to achieve good flowability and results when printing with polymer materials, the applications of these materials, however, is fairly limited. Certain disadvantages exist for 3D printed parts made of polymeric materials, including low strength and easy distortion by heat. These disadvantages strongly restrict the application of FFF printed parts in functional & load-bearing engineering applications. Therefore, the increasing demand for engineered materials with low weight and high strength has led to a major interest in the development of polymer matrix composites (PMC). Due to the low cost of tooling or in some cases no cost of tooling associated with FFF processing, it is the most attractive method for 3D-part shaping. The traditional process of FFF used in polymeric printing will be adapted for printing of cermet-polymer green-parts.

1.5 Technical Contribution

3D-printing technology has advanced considerably in the last decade with focus on adapting new materials for existing AM technologies such as SLS or SLA. These approaches are both expensive, inaccessible, and less user-friendly than FFF. A relatively new and adapted method of FFF, termed Fused Filament Fabrication of Cermets (FFFC), is a unique approach for producing wear-resistant cermet parts using a layer-by-layer AM approach. Figure 1.8 outlines the major steps involved in the FFFC process.

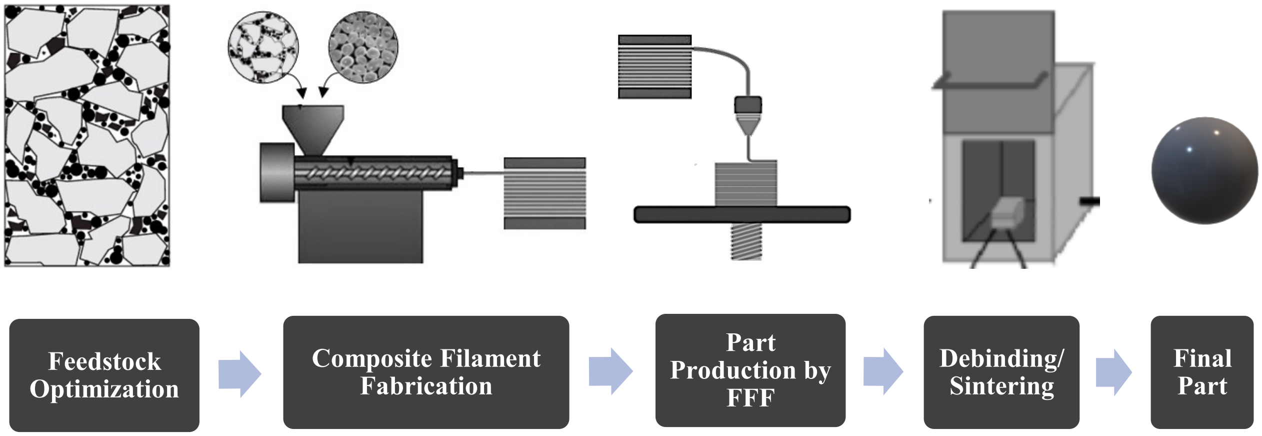

Figure 1.8 The proposed FFFC manufacturing method

The process begins with the development of novel PMC filaments with high filler contents tailored for sintering, thus an optimization of the filler powder is initially required. Unfortunately, a lack of published literature on this topic fails to provide a reasonable methodology for the development of composite filaments containing fillers of all materials and particle types. The research gap extends to a lack of knowledge in particle packing of powder mixtures, specifically particles having non-ideal characteristics. Since particle packing is essential to achieving successful sintering, this is a crucial element for filament development. Sinterable 3D-printing filaments present a major opportunity in the market for simple and cost-effective production of wear-resistant metal-ceramic parts. This innovative approach aims at reducing costs associated with production shutdown for routine equipment maintenance in the oil, gas, and mining industries. In addition to the opportunity for cost-effective manufacturing, FFF potentially allows for on-site part production, repair capabilities, control of design parameters, and overall operational efficiency. This thesis presents the novel findings for producing wear-resistant metal-ceramic parts using the FFFMC technique. The data and conclusions established by this work will serve as the fundamental basis necessary to continue future work in this field.

1.6 Objectives

The main research goals of this thesis are to:

1. Develop a methodology for producing sinterable polymer-metal-ceramic filaments for FFF
2. Determine the key properties of powder mixtures that influence particle packing
3. Characterize the properties of the composite filaments and printed green parts
4. Determine the validity of the ideal particle packing model

To achieve these goals, the particle packing behaviour of binary particles mixtures is investigated and powder mixtures are optimized for mixing with polymer to form composite filament for FFF. A characterization of the composite filaments and green-body parts defines the limits of production as well as assesses the quality of parts that can be manufactured using this method.

1.7 Thesis Outline

The thesis is organized in the following manner: Chapter 2 is a literature review, Chapter 3 describes the experimental apparatus and analysis methods used, Chapter 4 are the results and analysis of particle packing in binary mixtures, Chapter 5 discusses the results of the filament manufacturing and FFF processes as well as provides a characterization of the produced filaments, Chapter 6 is a brief conclusion of the overall results found in this study. Future work is also addressed in Chapter 6.

2. LITERATURE REVIEW

This chapter begins with an introduction to principles of particle packing theory. Following this, a review of relevant literature regarding the selection of feedstock material, powder and binder systems is presented. Finally, current developments in composite filaments for 3DP are reviewed.

2.1 Particle Packing Theory

One of the most important aspects of powder-based manufacturing is particle packing. Particle packing is crucial in determining the solids loading, binder content and the shrinkage during future densification processes *(German, 2005).* The degree of packing in a bed of particles, such as a powder, is referred to as "solids loading" or packing fraction. The packing fraction (PF) is described as the volume fraction of particles occupying a defined volume of space. The remaining fraction of volume is occupied by air or inter-particle "voids" formed between adjacent particles, simply called void fraction (Θ). The void fraction is a function of the bulk density (ρ_B) and true density (ρ_T) of a powder, expressed in Equation 2.1. Where the densities are measured in kg/m^3.

Hence, the PF can be expressed using Equation 2.2, where the sum of the void and packing fractions equal unity.

$$\Theta = 1 - \left(\frac{\rho_B}{\rho_T}\right) \tag{2.1}$$

$$\mathrm{PF} = 1 - \Theta \tag{2.2}$$

As seen in Eqn 2.2, particle packing is then also a function of powder density. The density of is typically reported as either a bulk or true density. Figure 2.1 shows, the bulk density (left) of a powder is equal to the ratio of mass of a powder which occupies a known volume of space. The bulk density includes the mass and volume occupied by both the solid particles and the air voids in between particles. The true density of a powder (right) is the density of the solid particles.

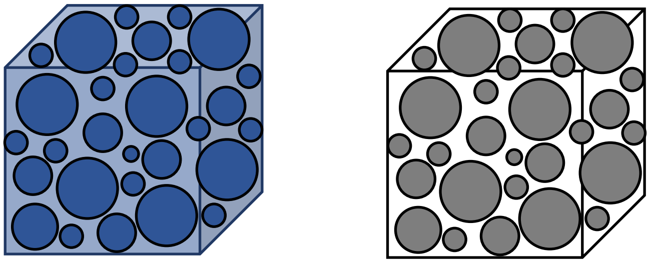

Bulk Density
(particles + voids)

True Density
(particles only)

Figure 2.1 Schematic of Bulk and True Densities of Powders

2.1.1 Ideal Particle Packing using Rule-of-Mixtures (ROM)

The simplest form of particle packing is described as the packing of mono-sized spheres, this is referred to as an ideal packing. In an ideal packing of particles, the fractional packing density of mono-sized spheres is between 0.60 – 0.64 *(German, 2005).* The packing density is often listed as a range of values, as it depends strongly on the conditions under which the packed structure is formed. A packing density of 0.60 (60vol% solids) is reached when the particles are in a state of random or loose packing, this occurs for example when a powder has been poured into a container. The same powder however can reach a maximum packing density of 0.64 (64vol% solids) by mechanically tapping or vibrating the container to settle the particles during filling. In an ideal packing, PF is primarily dependent on the particle size. As shown in Figure 2.2, triangular-shaped voids form between the regions of contact for a densely packed mono-sphere with six contacts.

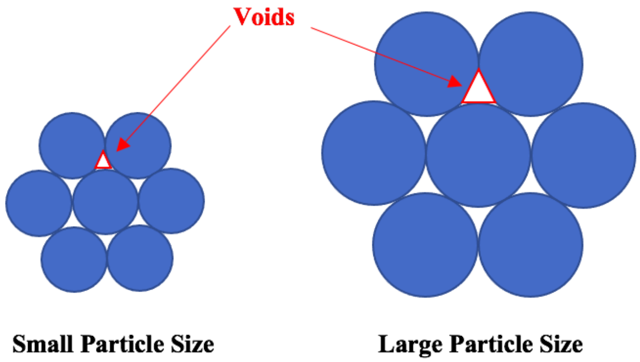

Figure 2.2 Schematic showing the effect of increasing particle size on ideal particle packing

As the size of the particles increase from small to large, the voids created between particles in-contact also increase. By this logic, it can be assumed that the bulk density (ρ_B), which accounts for volume occupied by both the solid particles and the air voids between particles, is also linear with increasing particle size. The true density, which does not consider the volume of voids, is also linear with respect to particle volume. Therefore, the density (true or bulk) of any binary mixture of mono-sized spheres can be calculated using the linear rule-of-mixtures (ROM) model. The ROM density (ρ_{ROM}), at any composition of the two components, is a sum of the products of volume fraction and density of each individual component comprising the mixture, as written in Equation 2.3. Where, the volume fractions of powders 1 and 2 is v_1 and v_2, respectively.

$$\rho_{ROM} = v_1\rho_1 + v_2\rho_2 \tag{2.3}$$

The symbol ρ_{ROM} may be shown with additional subscripts (B or T) to specify bulk or true densities. In order to apply the ROM, the densities of each individual component in the mixture must be known.

2.1.2 Packing of Non-ideal Binary Particle Mixtures

The packing of particles is influenced primarily by the size and shape of the particles. For particles non-spherical or irregular in shape, the packing density is seen to decrease to 30% of the theoretical density of the powder. Non-spherical powders are referred to as non-ideal powders due to the deviation from sphericity. The decrease in packing density due to morphology of the powder is mainly caused by interparticle friction occurring due to the rough surface of non-spherical powders. Depending on the degree of surface roughness, interlocking of irregular shaped powders can occur and cause further reduction of packing densities in powders, especially those having high hardness. Therefore, in order to improve particle packing, a bimodal powder mixture consisting of two different sized particles is commonly used. The advantage of using a bimodal mixture of small and large particles is that the small particles efficiently fill the interstitial voids created between large particles and increase the overall packing density of the powder. Figure 2.3 shows the void fraction as a function of composition for a bimodal mixture of spherical particles. The void fraction of purely mono-sized small particles, Θ_S, occurs for a mixture composition where X (% large) is equal to zero, and labelled "small". Similarly, the void fraction of purely mono-sized large particles, Θ_L , occurs at a mixture composition shown on the x-axis at 100 and labelled "large". Beginning on the left-hand side, mono-sized small spheres are shown in Fig. 2.3 (i). Gradually large particles are added to replace the small particles (ii) and a decrease in void fraction (increase in particle packing density) is observed due to the large dense particles replacing porous regions of small particles. Large particles continue to replace the small particles, effectively depressing voids within the structure until a point of minimum void fraction, $\Theta_{\min}$, is reached at a composition of X_{min} (iii). At this point the maximum particle packing density within the mixture is reached, and all of the interstitial voids between adjacent large particles are filled with small particles as efficiently as possible. Further replacement of small particles with large particles beyond the composition of X_{min} forces small particles to wedge in-between large particles causing void expansions within the mixture and an increase in void fraction. Therefore, the essential factor in achieving particle packing in a bimodal particle system is the particle size ratio or mean size ratio, which is described as the ratio of mean particle sizes of small particles to large particles. Since Θ is shown to be a function of density (Eqn 2.1), the values for Θ (and PF) in dry bimodal powder mixtures as a function of varying volume fractions of large-sized particles (compositions) follows a linear relationship, shown by the blue line labelled "Rule of Mixtures" in Figure 2.3. The clear presence of particle packing is indicated by a negative deviation (below) from the ROM relationship. One form of packing is the particle packing observed in dry powder mixtures, where the volume is occupied by particles and air voids. Another form of packing is observed in a composite material, comprised of polymer (binder) and particles (filler). When dry powder particle mixtures are combined with polymer to form a composite, it is assumed that the volume of voids in the dry powder will be occupied by the polymer.

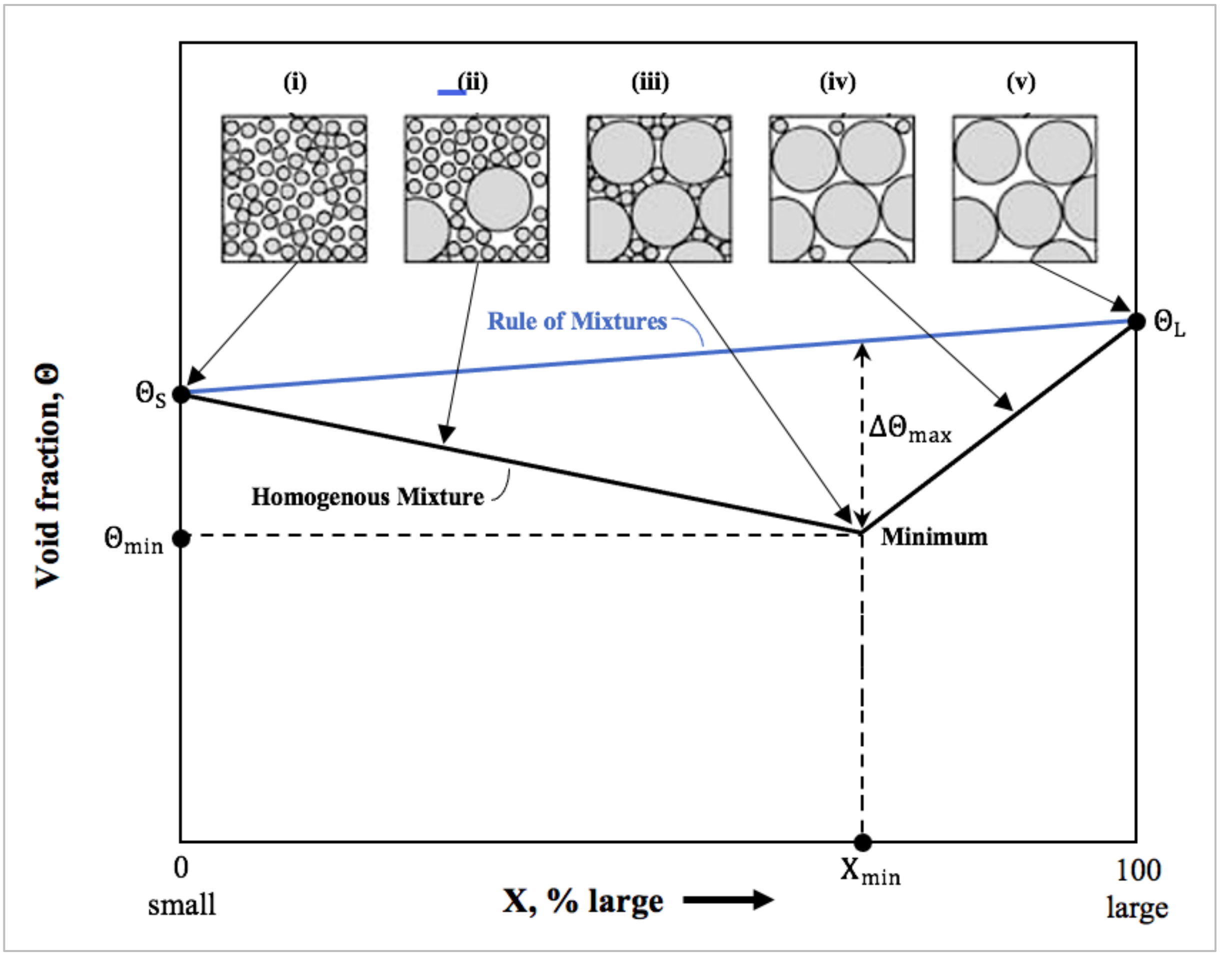

Figure 2.3 Plot of void fraction as a function of composition for bimodal mixtures of large and small spherical particles. Adapted from *(German, 2005)*

In MIM, the proper ratio of filler to polymer is crucial to successful part production. When the filler is in a state of maximum packing and the voids within the filler are fully saturated with polymer, any addition of filler will result in high viscosity and void formation in the composite material due to trapped air pockets within the mixture *(German & Bose, 1997).* In the opposite situation, where there is an excess of polymer, the mixture has a lower viscosity, however the mixture fails to provide sufficient particle-particle contact to ensure shape preservation during debinding, therefore significant shrinkage is seen post-sintering. The optimal polymer concentration is 2-5% lower than the maximum particle packing observed in the dry filler mixture.

2.2 Feedstock

The first step in developing a methodology for creating sinterable filaments for FFFC is the selection of feed stock materials that comprise the composite filament. The main components of the filament include the particle filler and polymeric binder. The requirements for both components, binder and filler, as well as the properties of the composite mixture are reviewed in the following sub-sections. Additionally, a review of the debinding and sintering process in MIM is presented in the final sub-section.

2.2.1 Filler Selection

Most particle-filled polymer composites are created with the intent of the filler particles serving a specific purpose. This purpose may include improved mechanical, optical, electrical, thermal, magnetic, or medical properties. The influencing factors of filler selection are dependent on specific material properties, such as composition, and particle characteristics such as, size, distribution and shape, which ultimately influence the packing conditions. In this work, a focus on wear-resistant cermet materials narrows the search for a filler particle system to cermet materials. The results of an evaluation of a binder for WC based on the hardness and transverse rupture strength (TRS) of various hard metals and cermets is shown in Figure 2.4 *(Viswanadham et al., 1983)*. If the criteria for established for filler hardness is 1200 HV, Figure 2.4 shows Ni-WC and TiC-WC both exceed in the range of hardness <1200 HV, without sacrificing TRS. It has been reported *(Tarrago et al, 2015)* that additions of Cr into Ni increase the hardness and load deflection performance of Ni-WC up to values consistent with Co-WC. Nickel is well-known for corrosion resistance properties. Therefore, Ni-WC and Ni-TiC have been selected as the filler material systems. The main requirement of the filler powder is to achieve a high packing density. This may require adjustments to the particle size distribution or particle morphology. It is well known; smaller particles increase viscosity during mixing and molding due to higher surface area causing interparticle friction *(German and Bose, 1997)*.

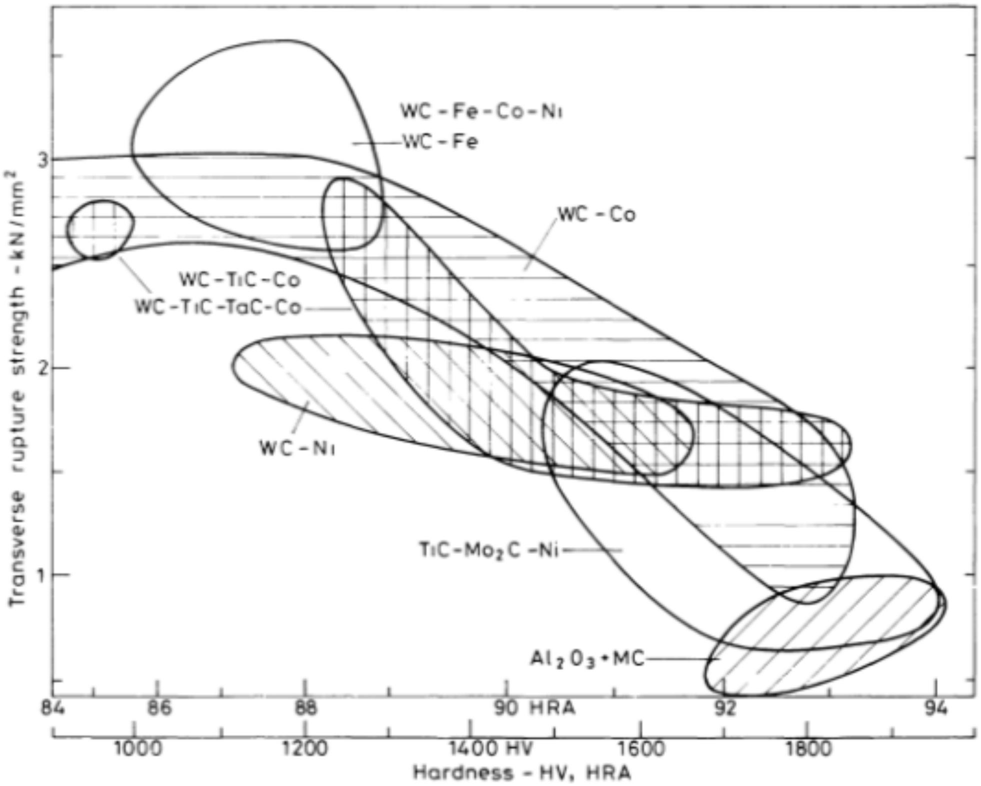

Figure 2.4 Typical range of TRS and hardness for hardmetals *(Viswanadham et al., 1983)*.

Smaller particles tend to agglomerate, increase viscosity and decrease the maximum packing density of the powder *(Torralba et al., 2013) (Fayyaz et al., 2014) (Amin et al., 2014).* Small particles also, however, lead to slower debinding and increased sintering shrinkage *(Torralba et al., 2013).* Advantages of smaller particle sizes are faster sintering and increases maximum packing density. In order to lower sintering shrinkage, a wide particle size distribution is recommended *(German and Bose, 1997) (Amin et al, 2013)*, this will also result in a higher packing density. It is recognized that spherical particles pack to 60-65 vol%, naturally particles with non-spherical morphologies, such as angular or flakey shaped particles, pack less densely *(German and Bose, 1997) (Fayyaz et al., 2014).*

2.2.2 Binder

Binder selection is crucial to the successful molding, debinding and sintering stages that follow. There must be a balance between the ease of molding, geometry, and the need to control the tolerance of the final dimensions. To achieve this balance, the binder is often a mixture of two or more components. First, a low molecular weight polymer wax is used to reduce the viscosity of the mixture at high solids loadings, disperse the particles evenly, improve wettability, and ease the molding process. The second component is a high MW polymer backbone, which is used to provide structure, increase strength of the green part and prevent separation of the powder during flow. In addition to these two main components, several different additives may be added in the form of a dispersant, lubricant, surfactant, or other processing aid. An example of a common additive is stearic acid, which acts as a surfactant used to reduce the contact angle of the powder/binder interface by lowering the surface energy. Its usefulness has been seen to increase as particle size decreases *(Fayyaz et al., 2014)*. Table 2.1 presents a review of various binder systems, fillers, debinding and sintering methods, and critical solids loading reported in literature using MIM processes. Table 2.1 shows that binders are formulated using many different components, which all require complex debinding and sintering processes to remove.

Table 2.1 Binder Systems for MIM

Ref	Binder Composition	Filler	Debinding Method	Ave. Powder Size (μm)	Critical Filler Loading(vol%)
German & Bose, 1997	65PW-30PP-5SA	W		8	56
	55PW-35PE-10SA	-	Thermal	-	-
	50PW-40PP-10CW	-	Thermal	-	-
	65PS-16PE-12SA-7DEP	ceramics	Thermal	-	-
	40EVA-20MAE-30PW-10DBP	ceramics	Thermal	-	-
Fayyaz et al., 2014	65PW-30LDPE-5SA	WC-Co-V	Solvent (heptane) & Thermal (Ar)	WC =<1 Co = <1.6 V = 2.5	as received: 45.8 milled: 53.4 (50)
Amin et al., 2014	60PA-40PE	WC-9Co	--	<10	milled: 65 (61)
Amin et al, 2013	70PA-30PE	WC-9Co	-	4.35	milled: 65 (63)
Yunn et al., 2011	PW-VO-PE-SA	WC-10Co	-	WC = <1 Co = <1.6	46 (44)
Qu et al., 2005	65PW-15VO-15LDPE-5SA	WC-5TiC-10Co	Thermal	0.9	62.5 (57)
Onagoruwa et. al., 2001	44PP-18.7Plasticiser-15.6Wax-13.9Elastomer-7.8Tackifier	Al_2O_3,SiO_2, TiO_2, MgO	-	-	55
Kitzmantel et al., 2018	60TPE-40PP (PP functionalized w/ MAH)	WC-10Co Ti(C,N)-WC-(Ta,Nb)C-Cr_3C_2-Co-Ni	Solvent (cyclohexane) & Thermal	0.8 - 2.5	50
Matula et al., 2008	48HDPE-48PW-4SA	High Speed Steel (HSS)	Thermal	D_{10} = 3.5 D_{50} = 8.2 D_{90} = 16	70

PW = paraffin wax, PP = polypropylene, PE = polyethylene, LDPE = low-density polyethylene, SA = stearic acid, CW = carnauba wax, PS = polystyrene, PA = palm stearin, DEP = diethyl phthalate, DBP = dibutyl phthalate, EVA = ethylene vinyl acetate, MAE = methacrylic acid ester, OA = oleic acid, VO = vegetable oil, MAH = maleic anhydride, TPE = thermoplastic elastomer

It should also be noted that extremely fine average powders sizes are used in these processes, presenting a significant disadvantage in terms of cost of raw materials required. The ideal binder composed of a single component, a polymer having low melting and decomposition temperatures. The polymer binder should reach a critical solid loading greater than 50 vol% and use a thermal method of debinding.

2.2.3 Rheology

Rheological studies dealing with formulations for MIM development mainly focus on the evolution of viscosity of different formulations with the shear rate at a constant temperature. Alternatively, the viscosity versus shear rate may be measured at different temperatures for a single powder loading *(Fayyaz et al., 2014)*. When measuring viscosity, pseudo-plastic flow or shear-thinning is ideal and is achieved when viscosity is seen to decrease as shear rate increases. This is beneficial as this type of flow has been reported to minimize defects in MIM parts and shows improved shape retention of green parts after molding *(Qu et al., 2005)*. Dilatant behaviour, where an increase in viscosity is observed with increasing shear rate, is to be avoid. This type of mixture is reported to have a tendency to segregate between powder and mixture *(Amin et al., 2014)*. Capillary rheometry is especially useful for viscosity and shear rate measurements. For typical MIM mixtures, a mixture viscosity <1000 Pa.s at shear rates between 100-1000 s^{-1} is desired *(Torralba et al., 2013)*

2.2.4 Debinding and Sintering

For the debinding and sintering processes used in MIM, a single method for completing both steps is desired. The debinding of the binder from the solid body of particles in the green part can be extremely inefficient, especially for large parts. The time required for debinding using methods such as solvent debinding, is directly proportional to the size of the part. Therefore, a more direct method is using thermal debinding. Table 2.2 presents a summary of the literature review for debinding and sintering of MIM parts of WC-based materials

Table 2.2 Review of Debinding and Sintering in MIM

Ref.	Filler	Filler Loading (vol%)	Debinding/ Sintering Parameters	Major Findings
(Bigg, 1987)	84WC-9Co-5TiC-2Ta(Nb)C	49.5	**Solvent Debinding:** mineral oil bath at 45C for 8 hr **Thermal Debinding:** H_2 and N_2 atmosphere from 200C-500C for 1 hr **Sintering:** 1400C for 1 hr in vacuum furnace	• Carbon content of sintered WC-Co mainly determined by atmosphere of thermal debinding: • In H_2, residual %C dropped, and decarburization occurred. • In N_2, %C increased, binder removal incomplete and graphite formed • Ideal atmosphere: 20%-50% H_2 + N_2 mixture for complete binder removal w/o decarburization • reached 100% full density & dimensional accuracy within 0.40% • wt% gain or loss of C during PIM causes 1.5%-dimensional change in P30 milling insert.
(Qu et al., 2005)	WC-5TiC-10Co	57	Direct Thermal Debinding Solvent Debinding + Thermal Debinding	• Direct thermal debinding OR solvent + thermal debinding in N2 = residual binder (black phase in sintered compacts) • In H_2 or H_2/N_2 atmosphere = η-phase occurs which means not sintered to full density • Direct vacuum debinding OR solvent (in heptane) + vacuum debinding = perfect microstructure • Dimensional tolerance: 0.2% • %C = 6.2 - 6.35% • Void ratio <0.02% • TRS (2000-2100 MPa), Hardness (90.3-93.5 HRA)
(German & Bose, 1997)	WC-10Co	56	Vacuum (60 mins, 1400C, 10C/min)	• 99 % relative sintered density

Generally, a thermogravimetric analysis (TGA) is conducted to obtain a curve, used to design the thermal debinding cycle. The decomposition temperature ranges can be identified using a TGA curve, and this information is very useful in determining the boundaries of debinding temperatures for the pyrolysis of organic binder material within the green part.

2.3 Review of Particle-filled Polymer Filaments for FFF

This section reviews the commercially available FFF feedstock filaments containing various metal fillers and current experimental works for developing composite filaments for sintering.

2.3.1 Commercial Metal-Polymer Filaments

PMC are comprised of polymers as the base matrix, and reinforced with various fillers, such as metal or ceramic powders *(Mohan et al, 2017).* The addition of filler changes numerous properties of the polymer and the term "functional fillers" is commonly used to describe them *(Rothon, 2003)*. Such materials exhibit remarkable physical and mechanical properties required for specialized use in automotive, aerospace, construction, biomedical, and materials research industries. Due to the development of PMC for IM applications, these composite materials have been adapted for use in FFF. One significant advantage to this method is the ability to retain the fine microstructure of rapidly solidified powders, which are used as fillers in this material to achieve desired mechanical properties in final parts. Currently, there are several metal-filled polymer filaments commercially available for FFF, summarized in Table 2.3 *(Virtual Foundry, 2019) (ColorFabb, 2019) (Formfutura, 2019) (Protopasta, 2019) (Spool3D, 2019) (Filaments, 2019).* In most cases, manufacturers were reluctant to share information regarding such as filler powder density, filler volume content, or type of polymer matrix to retain their competitive advantages. Examples of some commercial composite filaments available are listed in Table 2.3.

Table 2.3 Commercially Available Metal-filled Polymer Filaments

Filler	Manufacturer	Polymer Binder	Filler Content (wt.%)
Bronze	The Virtual Foundry	PLA	87%
	ColorFabb	PLA/PHA	80%
	Formfutura	PLA	80%
	Protopasta	HT-PLA	< 60%
	Spool3D	-	-
Brass	ColorFabb	PLA/PHA	70%
	Formfutura	PLA	70%
	Protopasta	HT-PLA	<60%
	Spool3D	PLA	~10%
Copper	The Virtual Foundry	PLA	90%
	ColorFabb	PLA/PHA	80%
	FormFutura	PLA	80%
	eSun	PLA	>70%
	Protopasta	HT-PLA	<60%
	Filaments.ca	PLA	10-15%
	Spool3D	PLA	~10%
Steel	ColorFabb	PLA/PHA	-
	The Virtual Foundry	PLA	80%
	Protopasta	PLA	<60%
	eSun	PLA	-
Iron	The Virtual Foundry	PLA	80%
	Protopasta	PLA	<45%
	Filaments.ca	PLA	10-15%
	Spool3D	PLA	~10%
Aluminum	The Virtual Foundry	PLA	65%
	Filaments.ca	PLA	10-15%
	Spool3D	PLA	~10%
	eSun	PLA	-
Tungsten	Filaments.ca	PLA	10-15%
	Spool3D	PLA	~10%

Table 2.3 shows that the polymer binder used in all of the composite filaments is Polylactic acid (PLA). PLA is a semi-crystalline biodegradable polyester derived from renewable resources such

as corn starch or sugarcane. PLA is one of the most common thermoplastics used in AM. A reasonable conclusion can be made that due to the good flow properties, ease of printability, and general familiarity of use by buyers of PLA, it was chosen as the base polymer by manufacturers for the development of metal-filled polymer filaments. There appears to be focus on bronze, brass, copper, steel, iron and aluminum- filled filaments in the market, however the filler content of these filaments does not meet the requirements for sintering. Basically, the main purpose of incorporating metal fillers into commercial polymer filaments is for aesthetic, rather than mechanical performance or functionality. The Virtual Foundry is the only manufacturer, listed in Table 2.3 that offers a full system for producing fully dense metal parts. The virtual foundry system consists of an FFF machine using metal-filled polymer filaments as feedstock to produce 3D-printed green-body parts, followed by a sintering furnace complete with instructions on how to sinter printed parts in order to achieve fully dense metal parts. However, it has been shown by researchers *(Ayeni, 2018)* that printed and sintered parts fabricated from the Virtual Foundry filament containing bronze fillers contained significant porosity, and the sintered final parts were reported to be very weak, and brittle compared to the printed green-part.

2.3.2 Current Research in Developing Metal-Polymer Filaments

Similar approaches to fabricating metal parts using FFF technology have been made, mainly through the use of commercially available MIM feedstock in the form of granules or pellets *(Lieberwirth et al., 2017) (Burkhardt et al., 2016) (Lengauer et al., 2019)*. Few attempts have been made to design a process with the preliminary step of developing the feedstock filament using raw materials *(Kukla et al., 2016) (Kitzmantel et al., 2018) (Onagoruwa et. al., 2001).* A summary of the literature review conducted in current work that has been completed in presented in Table 2.4.

Table 2.4 Summary of Literature on Current Methods of Metal Part Production using FFF

Ref.	Feedstock Composition (vol%)		Mixing/ Extrusion	Printing	Debinding/ Sintering	Final Properties
	Binder	Filler				
Onagoruwa et. al., 2001	(45vol%):44PP 18.7Plasticizer 15.6Wax 13.9Elastomer 7.8Tackifier	(55 vol%): $3Al_2O_3$,$2SiO_2$, SiO2, TiO_2, Al_2O_3, MgO	**Mixing** ***Temp:***180°C, ***Speed:***120 rpm ***Time:*** 80 min	**Feed:** 1.78mm rod **Nozzle:** 235°C **Bed:** 48°C **Flow:** 130%	***Debind:*** <200°C ***Sinter:*** 1650°C ***Time:*** 3 hr	***Max Shrinkage:*** 12% ***Geometric tolerance:*** ±1%
Lieberwirth et al., 2017	Commercial MIM feedstock granule (45 vol% binder + 55vol% 1.4542 steel)		Not required	**Feed:** granules **Nozzle**: 0.5 mm **Temp:** 210°C **Speed:** 5-15 mm/s **Layer height:** 0.1-0.25 mm	***Debind:*** <650°C ***Atmosphere:*** H_2 ***Sinter:*** 1365°C ***Time:*** 14 hr (total)	***Shrinkage:*** x-y (14.49%) z (15.8%) ***Density:*** 7.49 ± 0.16 g/cm ***Relative Density:*** 96.03%
Kukla et al., 2016	Proprietary (45 vol%)	316L steel (55 vol%)	**Mixing** ***Temp:*** 200°C ***Time:*** 30 mins **Extrusion** ***Diameter:*** 2 mm ***Temp:*** 185°C ***Speed:*** 0.5 mm/s ***Shear rate:*** 113 s^{-1}	(proprietary)	(proprietary)	***Shrinkage:*** 15% ***Tensile Modulus:*** 415-2700 MPa ***Strain at break:*** 3-50%
Burkhardt et al., 2016	Conventional 316L MIM feedstock granule (45 vol% binder + 55vol% 316L steel)		**Extrusion** 316L MIM feedstock granules	**Feed:** rod **Nozzle:** 0.5mm **Speed:** 50mm/s	***Debind:*** cyclohexane (60°C for 10.5 hr) ***Sinter:*** Standard IM parameters for 316L	***Shrinkage:*** 19.2 ± 0.02% ***Density:*** 7.64 g/cm ***Relative Density:*** 96.03%
Kitzmantel et al., 2018	40 vol% (TPE-PP-maleic anhydride)	***Hardmetal:*** WC-10Co ***Cermet:*** WC, Ti(C, N), (Ta,Nb)C, Co, Ni, Cr_3C_2 (50 vol%)	**Mixing:** ***Temp:*** 200°C ***Speed:*** 60 rpm ***Time:*** 50 min **Extrusion** ***Diameter:*** 1.75mm ***Temp:*** 200°C ***Speed:*** 1mm/s ***Shear rate:*** 215 s^{-1}	**Feed:** 1.75mm rod **Nozzle:** 0.6mm	***Debind:*** cyclohexane (60°C for 48 hr), tube furnace (H_2 atm, 1.3°C/min, 800°C) ***Sinter:*** dwell at 1150 &1430°C or 1175°C & 1300°C & 1480°C for 1 hr	***Filament Ovality:*** ± 0.03 mm ***Shrinkage:*** x-y (~21%) z (~22%)
Lengauer et al., 2019	Commercial Hardmetal MIM feedstock granulate		Not required	**Feed:** granules **Nozzle:** 0.3mm **Temp:** 190°C **Bed:** 100°C **Layer height:** 0.1 mm	***Debind:*** H_2O in 2% inhibitor (60°C for 48 hr) + thermally in tube furnace (H_2 atm, 1.3°C/min, 800°C) ***Sinter:*** dwell at 1150 & 1430°C	***Shrinkage:*** x-y (22.6%) z (23.4%)

TPE = thermoplastic elastomer, PP = polypropylene

This review confirms that the combined MIM and FFF methods have been successful in creating fully dense metal-ceramic parts as presented by other researchers and will serve as a benchmark for the results obtained in this study and future work to be conducted as outlined in this report. It is clear from the literature review presented in Table 2.4, that very little work has been done for developing an extrusion-based AM method for manufacturing difficult to process metal-ceramic material sch as hardmetals or cermets for use in wear resistant applications. Essentially, most researchers have focused on developing stainless steel using this method. This shows a clear research gap in knowledge for this area of study and provides a exclusive opportunity for studying the unique combination of powder metallurgy and metal part manufacturing by AM processes, namely FFF.

2.4 Summary

This chapters includes a detailed review of particle packing theory, MIM process steps and criteria, and current literature on developing sinterable filaments for FFF are presented and reviewed. Based on the review of literature, a general baseline of knowledge gained from this chapter will be used to develop a framework for manufacturing sinterable 1.75 mm nominal diameter metal-ceramic composite filaments suitable for use as feedstock for FFF. Green parts for sintering will be printed using a traditional low-cost polymer 3D printer. The properties of the resultant composites will be characterized and compared to ideal packing theory.

3. EXPERIMENTAL

Chapter 3 details the experimental procedures and apparatus used in this work. Section 3.1 includes all relevant practices for powders, including size and shape characterization, sampling, mixing, and measurement of density. The following Sections 3.2 and 3.3 describe the methods used for developing composite filaments and 3D-printing green parts. The final section of this chapter, Section 3.4, explains the methods used for composite characterization, including filament diameter, filament flowability, and dimensional accuracy of the printed parts.

3.1 Powders

A description of methods and experimental apparatus used to form binary powder mixtures and calculate the void fraction in these mixtures is presented in the following subsections. A characterization of the metallic and ceramic powders, including, particle shape, composition, size distribution, bulk and true densities are included.

3.1.1 Powder Sampling

A 0.5 kg sample of each filler powder is taken from the primary bulk powder stock. Each powder is homogenously mixed (described in Section 3.1.5) and sampled by passing through a Jones Riffle Splitter (Gilson Company Inc. Model: SP-173), as per American Society for Testing and Materials (ASTM) standard B215 for sampling metal powders (*ASTM B215-15, 2015)*. A riffle splitter is a device used for sampling large primary bulk powders. It divides the bulk primary stock into smaller and representative workable sizes for laboratory study. The splitter acts to divide a sample of dry particulate material from a primary bulk quantity (0.5 kg) into two equal sub-samples (0.25 kg/each). The splitter is comprised of a V-shaped hopper, a hopper feed gate located on the bottom of the hopper (called the splitter) which leads the powder through the alternating interior division channels, and into two aluminum sampling pans positioned on either side of the base to collect the divided samples. The process was repeated 15-20 times for each powder, by re-loading the divided samples into the hopper and re-splitting. One of the samples (0.25 kg) is used for powder size analysis and density measurements, whereas the other sample (0.25 kg) is used to prepare mixtures.

3.1.2 Measuring Particle Shape and Composition by Scanning Electron Microscopy

Scanning Electron Microscopy (SEM) is used for characterization of surface topography and determining chemical composition of individual filler powders and cross sections of the composite filaments produced in this study. The Tescan Vega-3 SEM located in the Chemical and Materials Engineering (CME) building at the University of Alberta is used for imaging of composite filaments and filler powders. An identical SEM machine located in the Fabrication and Characterization Facility (nanoFAB) at the University of Alberta is utilized to perform Energy dispersive x-ray spectroscopy (EDX) on the filler powders to determine the chemical composition of powder surfaces. A resolution of 133 eV is observed during SEM imaging.

3.1.3 Measuring Particle Sizes of Ni and TiC Powders by Laser Diffraction Method

An analysis of particle size and size distribution is conducted by laser diffraction which uses the optical behaviour of particles to measure their sizes. The method is based on principles of light diffraction which state that small particles diffract light at a greater angle, compared to large particles which diffract light at smaller angles. The method measures the angle of light scattered by a laser beam passing through a sample of particles dispersed in a liquid medium. Figure 3.1 shows an illustration of laser diffraction in a particle size analyzer *(Laser Diffraction, 2021).* A laser is used to obtain a diffraction pattern from a flow of particles dispersed in a liquid medium, an optical lens focuses the pattern onto a detector where the light pattern data is collected, and particle size data can be generated. The particles are assumed to be spherical in shape, and the refractive indexes of the particles and dispersion liquid are known. In this work, the particle sizes and distributions of all Ni and TiC sampled powders are determined using the Mastersizer 3000E system *(Mastersizer, 2016)* a detailed schematic of the system is shown in Figure 3.2. The system is comprised of the main optical unit, supplementary wet dispersion unit and a measurement cell, labelled as 1, 2, and 3 in Figure 3.2, respectively. The main optical unit is used to transmit red and blue laser light through the particle sample within the measurement cell. The resulting light scattering caused by the particles is detected by a set of light-sensitive sensors and saved as raw data. The Mastersizer software then provides a representation of sample particle size distribution.

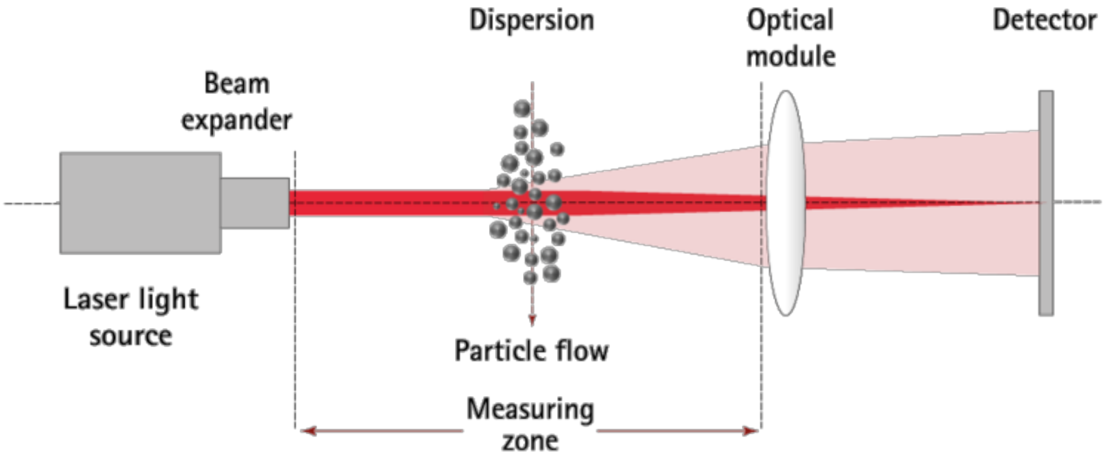

Figure 3.1 Laser Diffraction in a Particle Size Analyzer *(Laser Diffraction, 2021)*

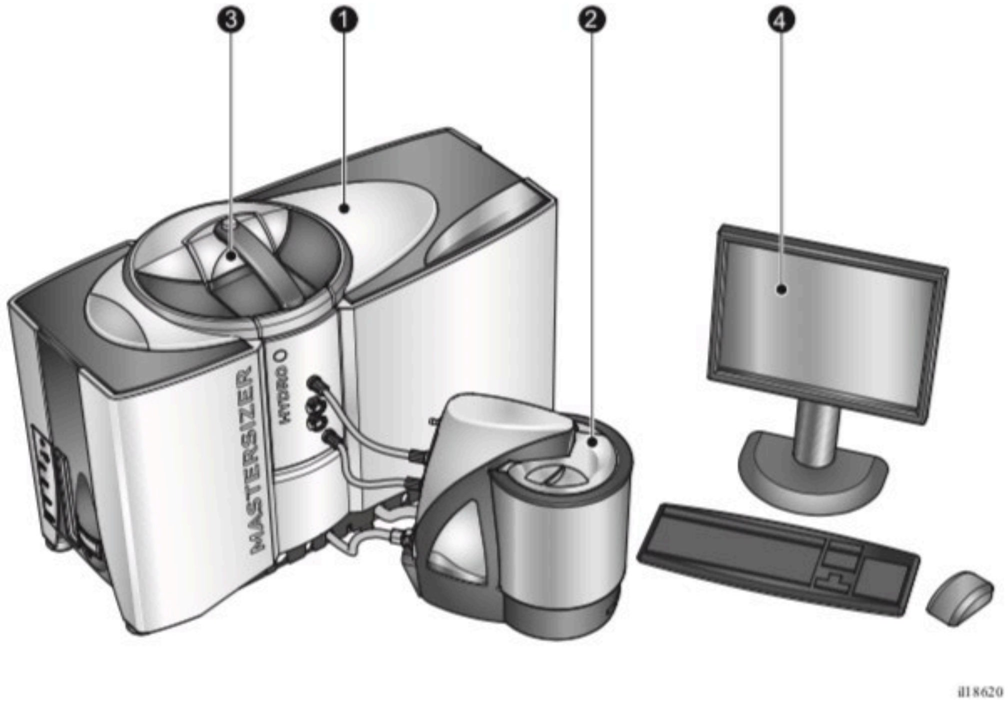

①	Optical unit	③	Wet cell
②	Wet dispersion unit	④	Computer running the Mastersizer application software

Figure 3.2 Main components of the Mastersizer 3000E laser diffraction particle size analyzer

A small powder sample of about 0.005 kg (~5g) is obtained from the bulk powder sample (0.25 kg), described in the previous section, using a metal spatula to transfer the powder onto a small circular sheet of filter paper. The filter paper and sample are placed on a Denver Instrument analytical scale (Model no. PSU25A-14E) to record the weight of the sample. This sample is added to the wet dispersion unit, Hydro LV, with a dispersant, usually deionized water. For the analysis of Ni and TiC powders, Fisherbrand^{TM} Histoprep^{TM} 95% Denatured Ethyl Alcohol (ρ = 804 kg/m^3, 20°C) is used as the liquid dispersant. This is done due to the lower density of ethanol compared with water, which prevents very fine particles (<10 μm) from floating on the surface of the dispersant during analysis, yielding inaccurate particle size measurements. The Hydro LV dispersion unit functions to circulate the liquid sample through the measurement cell and has a volume of 600ml. The complete system is capable of measuring particle sizes ranging from 0.1 to 1000µm *(Mastersizer, 2016).*

3.1.4 Measuring Particle Sizes of WC Powders by Sieve Analysis

Due to the high density and coarse particle sizes of WC powders, wet dispersion laser diffraction is not a suitable method for the particle size analysis of WC powders used in this study. Another common method of measuring particle size, known as sieve analysis, was used. Sieve analysis is a technique whereby a sample of known mass of powder is passed through a series of six mesh sieve screens, beginning with the largest sized mesh screen and gradually becoming smaller in size. The bottom or last section is a metal pan to collect the finest fraction of material. The sieve column is then placed inside of a mechanical shaking machine and shaken for some time to separate the powder sample by size. The mass retained by each sieve is measured and tabulated as the mass fraction of the whole sample. In this work, a RO-TAP mechanical sieving machine was used (Manufacturer: W.S. Tyler). Test sample sizes of approximately $2.5\text{x}10^{-5}$ m^3 (25 cm^3) in volume were used for each analysis. Sample size was based on volume rather than mass, as to not physically overload or overfill the sieve pans. American standard test sieve series sieves were used in sizes ranging from 250µm to 20µm (sieve no. 60 to 635). Stainless steel sieves were used for Ni-alloy powders and bronze sieves were used for the more abrasive carbide powders. The samples were shaken for an average of 20 minutes for each test. The retained mass and sieve size numerical values were recorded and used to plot a graph of particle size as a function of percent finer by mass to determine the median particle size, referred to as d50. The d50 represents the median particle size and represents the diameter of particle size where 50% the population lies below this value.

Similarly, 90% of the population lies below d90, and 10% of the population lies below the d10, both values were also obtained from the above-mentioned plot, listed in Appendix A.

3.1.5 Preparation of Ni-TiC and Ni-WC Binary Mixtures

Binary mixtures comprised of Ni and carbide powders are prepared at four different mixture compositions, ranging from 20 to 80% of carbide component in increments of 20% by volume. The total volume ($\mathrm{V_T}$) of a binary powder mixture is taken as a basis of 20 cm^3. In Equation 3.1, The total volume of a mixture is equal to the sum of volumes of powder 1 ($\mathrm{V_1}$) and powder 2 ($\mathrm{V_1}$). The mixture compositions are varied in terms of volume fraction of the larger component, specifically the carbide powder in this work. The total volume can also be written as the sum of products of volume fraction and volume of each powder (v_1 and v_2), in Eqn. 3.1.

$$\mathrm{V_T = V_1 + V_2} \tag{3.1}$$

$$\mathrm{V_T = v_1V_1 + v_2V_2}$$

The masses of each powder 1 (m_1) and 2 (m_2) needed to prepare a binary mixture of known composition, are calculated by rearranging the basic equation for density as shown in Equation 3.2. Where ρ_1 and ρ_2 are the true densities measured in kg/m^3, of powder 1 and powder 2, respectively.

$$\mathrm{m_1 = V_1\rho_1} \tag{3.2}$$

$$\mathrm{m_2 = V_2\rho_2}$$

Once the required masses of each powder are known, the powders are carefully measured out from the sampled bulk powder using a metal spatula to transfer the desired amount of each powder onto a small circular sheet of filter paper placed on the Denver Instrument analytical scale (Model no. PSU25A-14E). The powders are then loaded into the V-shaped mixer (Manufacturer: CapsulCN International Co.) and mixed for 30 minutes. Figure 3.3 shows the V-shaped dry mixer (Model: 5V) used for powder mixing. The mixer is 0.72m x 0.36m x 0.61m in size, with a barrel diameter of 0.13m, and a volume of 5L. It uses 0.55 kW of powder and operates at a constant rotational speed of 20 rpm. After the powders have been mixed, the mixture is collected from the mixing vessel and stored in an airtight glass vial.

Figure 3.3 V5-Blender Dry Powder Mixer Blending Machine by CapsulCN

Each vial is labelled according to material type, composition, and mean size ratio (δ). An example of a complete set of mixtures is shown in Figure 3.4, where Ni (vial #1) and TiC (vial #6) powders are combined to form mixtures where δ is 0.15. Four binary mixtures of Ni-TiC with compositions of 20vol% TiC (vial #2), 40vol% TiC (vial #3), 60vol% TiC (vial #4), and 80vol% TiC (vial #5) are shown. After all the mixtures for one δ value have been prepared, the mixing vessel is detached and cleaned in an ultrasonic bath (Manufacturer: Fisher Scientific) for 1 hour, rinsed with ethanol and allowed to dry overnight. This practice ensures that cross-contamination when changing between Ni-TiC and Ni-WC materials, as well as between same material types but different powder sizes does not occur. The mixer shown in Figure 3.3 is not only used for preparing binary mixtures, but also for homogenous mixing of the as-received Ni, TiC, and WC powders, prior to experimental testing.

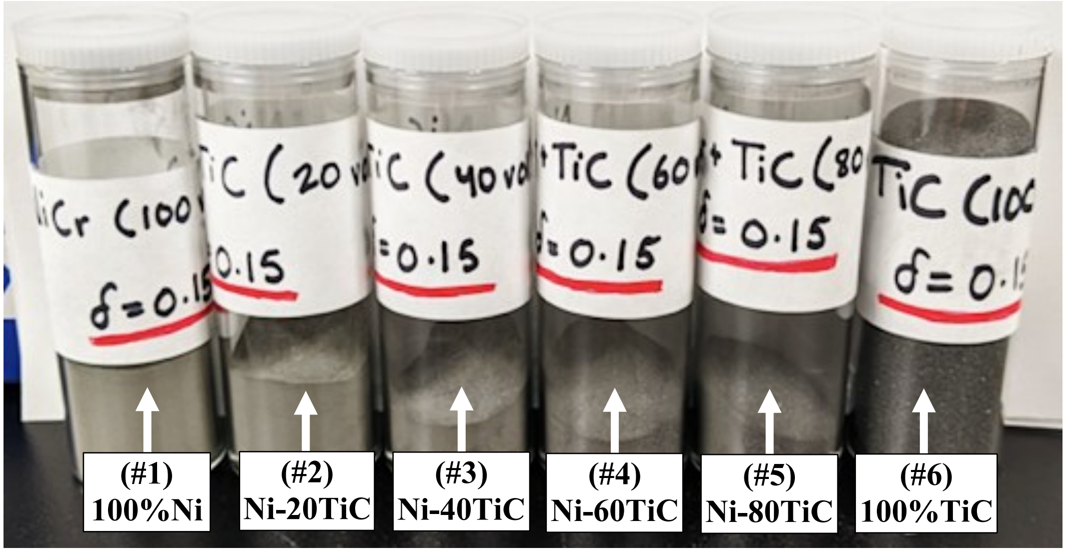

Figure 3.4 Labelled samples of Ni and TiC powders and their mixtures containing varying concentrations of TiC by volume % stored in vials

3.1.6 Measurement of True Density by Pycnometry

In this work, the true densities of Ni powder, TiC powder, WC powder, binary mixtures of all powders, composite filament, and printed solid parts were measured. True density of a material is defined as the density of a solid material, excluding the volume of interparticle voids. The true density was measured by using a pycnometer, a glass flask of pre-calibrated volume determined by measuring the volume of a liquid at a standard temperature (e.g., water at 20°C). The experimental setup for conducting density measurements in this study is shown in Figure 3.5, the assembly consists of a pycnometer bottle with a lateral capillary tube and a thermometer stopper. The bottle has a volume of 50ml ± 0.001 at 20°C and was manufactured by Marienfield Inc. Due to the size constraints of the pycnometer bottle opening, the composite filament was cut into small pieces (~ 1 cm in length) for sampling and the printed parts were sectioned into small segments using the Buehler IsoMet^{TM} 4000 Wear Precision Saw with MetAbrase^{TM} abrasive cut-off wheel for non-ferrous materials (product code: 11-4217-010). The physical form of these samples is shown in Figure 3.6, where the composite filament is in small "needle-like" fragments and the printed samples are clear-cut rectangular-shaped pieces. First, the pycnometer must be calibrated by measuring the volume of the pycnometer at a specific temperature using a liquid of known density. The empty glass pycnometer and thermometer (±0.01°C) are cleaned, dried, and weighed using a Denver Instrument analytical scale (Model no. PSU25A-14E). The liquid used in this study is Fisherbrand^{TM} Histoprep^{TM} 95% Denatured Ethyl Alcohol (ρ = 804 kg/m^3, 20°C) is due to its lower density compared to deionized water (ρ = 1000 kg/m^3, 20°C), in order to prevent fine particles (<10 μm) from floating on the surface and being expelled from the capillary tube. The thermometer is removed, and ethanol is filled to the marked level indicated near the opening of the pycnometer bottle, as shown in Figure 3.5.

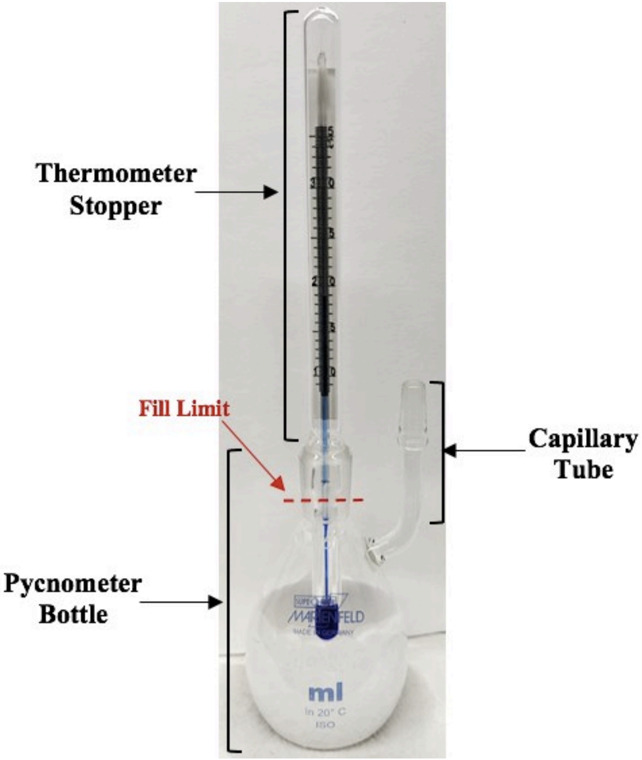

Figure 3.5 Components of pycnometer used for true density measurements

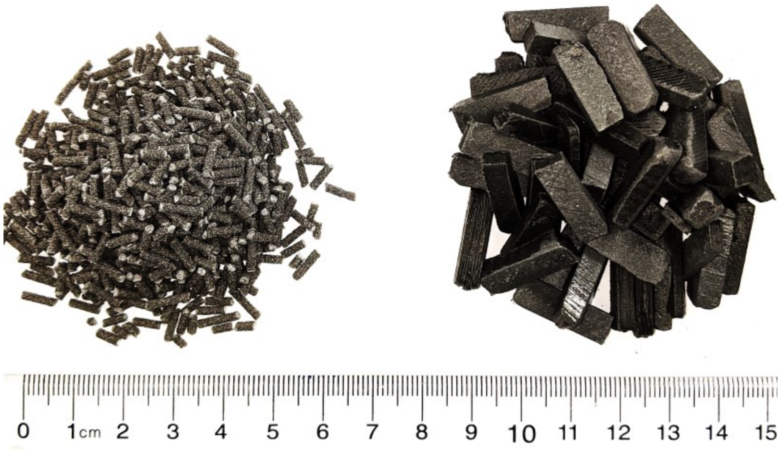

Figure 3.6 Samples of composite filament (left) and printed parts (right) used for pycnometry

The thermometer is inserted, and the excess liquid is dispelled through the capillary tube. The pycnometer is wiped dry using a delicate task wipe and the mass of the ethanol is recorded. All pycnometer experiments are repeated 3 times. The calibrated volume of the pycnometer, $V_{\mathrm{pyc,t(°C)}}$ measured in m^3 at a temperature, T (°C), is calculated by rearranging the fundamental relationship for density as in Equation 3.3:

$$V_{\mathrm{pyc,T(°C)}} = \frac{m_{\mathrm{EA}}}{\rho_{\mathrm{EA,T(°C)}}} \tag{3.3}$$

Where m_{EA} is the mass of 95% ethanol (kg), and $\rho_{\mathrm{EA,T(°C)}}$ is the density (kg/m^3) of 95% ethanol at temperature, T (°C). Once the pycnometer volume has been calibrated for a specific temperature, the volume of a solid sample can be determined. First the empty, clean, and dried pycnometer and thermometer are weighed and tared on the scale. Next, the powder sample is added to the empty pycnometer and the mass of the sample is measured and recorded (m_{S}). It is important to note that in order to achieve a precise reading, the sample should occupy at least a third of the empty pycnometer volume to achieve an accurate result. The remaining pycnometer volume is filled with ethanol and the bottle is gently tapped 10 to 15 times to release any trapped bubbles that may be present between the particles. The pycnometer is rested for 1 minute after tapping to ensure any remaining bubbles escape before the thermometer stopper is carefully placed on. The excess ethanol escaping from the capillary tube is dried before measuring the mass of the sample and ethanol ($m_{\mathrm{S+EA}}$). The sample volume, V_s, and experimental true density, $\rho_{\mathrm{T,exp}}$ can be then calculated using Equations 3.4 and 3.5, respectively.

$$V_S = V_{pyc,T(°C)} - \left(\frac{m_{EA}}{\rho_{EA,tT°C)}}\right) \quad (3.4)$$

$$\rho_{T,exp} = \frac{m_S}{V_S} \quad (3.5)$$

3.1.7 Measurement of Bulk Density using Hall Flowmeter

Bulk density is defined as the mass of a material divided by the total volume that it occupies, which includes the particle volume, interparticle void volume, and the volume of porosity within the particles. In this study, the bulk densities of individual filler powders and their binary mixtures are determined according to Metal Powder Industries Federation (MPIF) standard 04, for measurement of apparent density of free-flowing metal powders using the Hall apparatus *(MPIF Standard 04, 1992)*. The hall flowmeter assembly is shown in Figure 3.7, and consists of a hall flowmeter funnel, a stand to hold the flowmeter funnel, and a cylindrical density cup (25 ± 0.05 cm^3) to collect the sample.

Figure 3.7 Hall Flowmeter Set-up for Bulk Density Measurement

A 30 to 40 cm^3 powder sample is loaded into the hall flowmeter funnel (Manufacturer: Alcan Powers and Pigments) and allowed to flow out of a 2.54 mm size opening located at the bottom of the funnel. The sample is collected in the density cup located beneath the funnel, until it completely fills the cup and begins to overflow. Once completely full, the sample flow from the funnel is stopped and the excess sample in the cup is levelled off from using a straight edge, such as, a ruler or spatula. The mass of the sample collected in the cup is measured and recorded. By measuring the mass of a powder sample occupying a space of known volume within a container, the bulk density can be calculated using Equation 3.6:

$$\rho_{\mathrm{B,exp}} = \frac{\mathrm{m_S}}{\mathrm{V_C}} \tag{3.6}$$

Where $\rho_{\mathrm{B,exp}}$ is the experimental bulk density of the sample measured in $\mathrm{kg/m}^3$, m_S is the mass of the sample collected in the cup (in kg), and V_C is the pre-calibrated volume of the density cup equalling $2.5\mathrm{x}10^{-5}$ m^3 (25 cm^3). The mixture of particles collected in the cup are considered to be in a state of "random-loose" packing, reasonably justified as the sample is not subject to any mechanical or vibrational tapping, causing particle settling and increasing packing density, before weighing. The process is repeated five times for each powder sample and the average numerical value for experimental bulk density is reported.

3.1.8 Calculation of Void Fraction

First, the average bulk and true densities of the individual filler powders are experimentally measured. These powders include all Ni, TiC, and WC powders of every size distribution used in this investigation. These measurements are considered to be the densities of the powders in their pure, unmixed, or "as-received" state. The random loose void fractions of each pure powder (Θ) is calculated using Eqn 2.1. Next, the bulk and true densities of any binary mixture consisting of the pure powders can be predicted using the ROM equation for density (Eqn. 2.3). The mixture densities obtained from the ROM are used in Eqn. 2.1 to predict the values for void fraction of binary mixtures. Since the void fractions are obtained using densities based on the ROM, these values for void fraction are specifically denoted as Θ_{ROM}. The actual or experimental values for void fraction of a binary mixture, denoted as Θ_{exp}, are calculated using the average values of bulk and true density obtained from experimental data collected using the Hall flowmeter and pycnometer, as described previously.

In this study, five combinations of Ni-TiC powders and four combinations of Ni-WC powders are created, varying in mean particle size of each filler forming the binary. The nine binary systems of powders are classified based on a value for δ between 0 and 1, specifying the mean particle sizes of Ni and carbide in the mixture. The compositions of the mixtures are based on vol% carbide in the mixture, therefore, the concentration of carbide is varied in increments of 20vol% (20, 40, 60, 80vol%) for each of the nine-binary system of powders. Therefore, a total of 36 mixtures are prepared for analysis. The average bulk and true densities of these mixtures having compositions ranging between 20-80vol% carbide, are experimentally measured and compared to the values found using the ROM, for which only the densities of the pure filler components are considered.

3.2 Extrusion Strandline

The composite filaments were developed using an extrusion strandline system at InnoTech Alberta located in Alberta, Canada. The experimental set-up for filament extrusion is shown in Figure 3.8

and includes: a filler auger, pellet auger, extruder, cooling water bath, laser measurement device, puller, and spooling device. The diagram in Figure 3.8 groups each type of equipment forming the strandline based on the color of the box. For example, the pellet auger, extruder, and cooling bath (shown in blue) are all part of a single unit of machinery purchased from a manufacturer. It is important to note that the spooling device shown in the above set-up, was designed, and built by Juan Segura at InnoTech Alberta. The specifications and operating mechanisms of the spooling device are not described in this section, as it is proprietary knowledge owned by InnoTech Alberta. The spooling apparatus was developed for complete integration of the filament extrusion process, allowing the filament to be wound onto spools for storage and easily used as incorporated into the FFF assembly. A description of all apparatus used in the extrusion strandline, as seen in Figure 3.8, is presented in the following subsections 3.2.1 through 3.2.3.

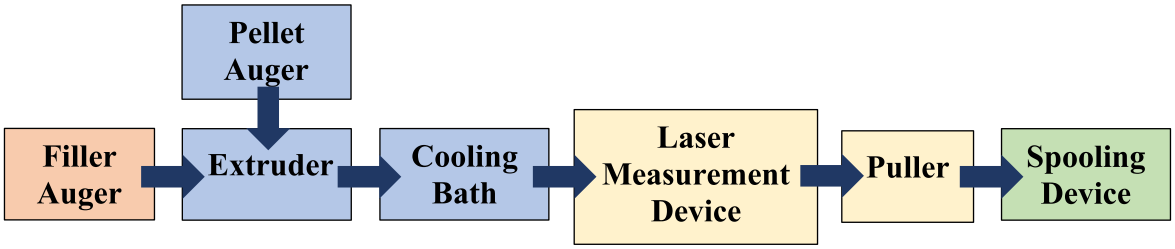

Figure 3.8 Diagram showing extrusion strandline setup

3.2.1 Material Feeding

Filler powder and HDPE pellets are fed separately but simultaneously into the extruder, at pre-calibrated feed rates to control the compositions of the extruded composite filaments. Two horizontal electric augers are used to introduce the raw materials into the hopper of the extruder, as shown in Figure 3.9.

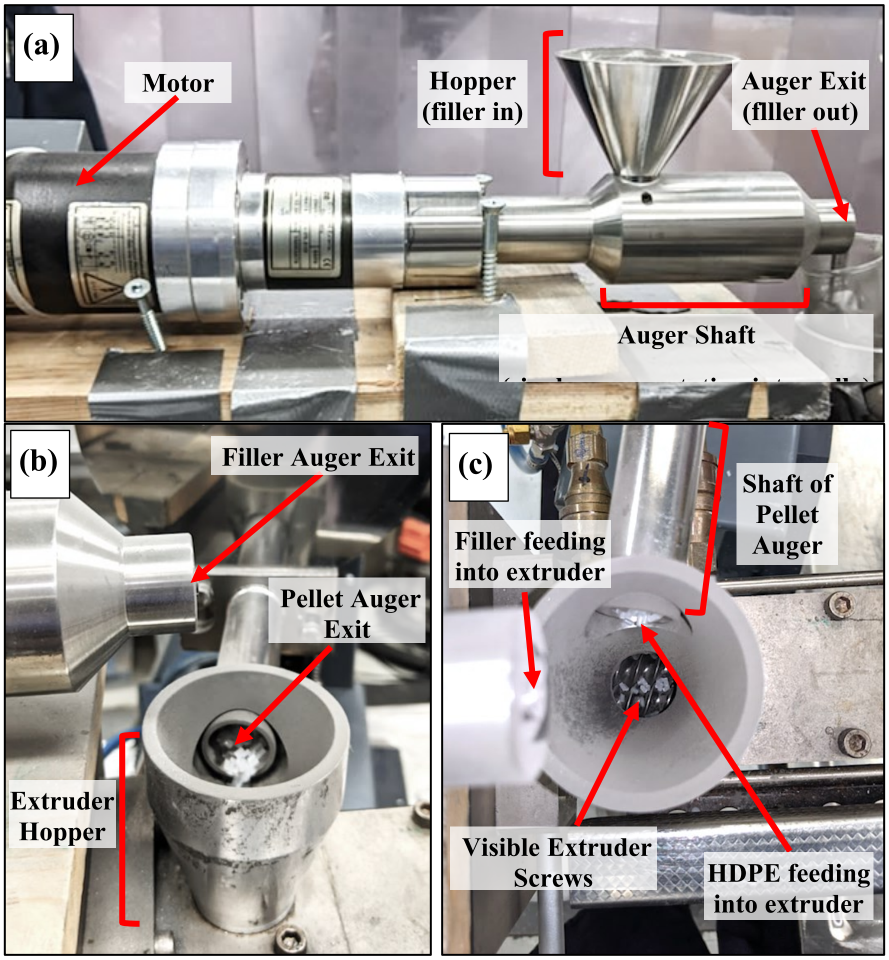

Figure 3.9 Methods of Raw Material Feeding (a) Filler feeding, (b) Positioning of the filler and HDPE feeders relative to the extruder hopper, (c) Top view of extruder hopper showing twin-screws inside

The auger used for pellet feeding is a part of the ThermoScientific™ EuroLab 16 XL twin-screw extruder system which is described in the following sub-section. The auger responsible for feeding filler was developed at InnoTech Alberta and was designed to fit horizontally onto a flat surface near the opening of the extruder hopper, as shown in Figure 3.9 (a). The filler is loaded into the hopper of the auger, travelling along the shaft of the feeder until it flows out of the opening located directly above the extruder hopper, as seen in (b). The vertical distance between the auger opening (where filler flows out) and the top of the extruder hopper is approximately 50mm. Fig 3.9 (b) also shows the relative position of the pellet auger, which feeds HDPE pellets directly into the extruder through a cut-out in the wall of the extruder hopper. The screws of the extruder are clearly visible when observed from a top view of the extruder hopper, as in (c).

3.2.2 Twin-Screw Extruder System

The ThermoScientific™ EuroLab 16 XL twin-screw extruder system used for lab-scale filament extrusion is shown in Figure 3.10 *(ThermoScientific, 2016)*. The labelled figure shows that the full system consists of a touchscreen interface, twin-screw extruder, pellet hopper, and cooling water bath. The extruder barrel is comprised of 6 heated zones, zone 1 is located at the hopper and zone 6 is the nozzle, heated using a 250W die heater. A maximum temperature of 400 °C may be set for each zone and is easily controlled using the touchscreen interface. Two co-rotating screws are both 15.6mm in diameter, enclosed within the extruder barrel which has a 40:1 length to diameter ratio. The twin-screws are capable of reaching rotational speeds upwards of 1000 rpm, using a 2.5 kW motor. The manufacturer reports an output of up to 10 kg/hr for the system, when operating as a continuous process *(ThermoScientific, 2016).* As molten filament exits the nozzle, it is submerged in a cooling bath filled with water and guided by 6 rubber rollers positioned along the length of the cooling bath, two parallel air fans dry off the excess water (located at the end of the bath tank) as the cooled and solidified filament strand exits the bath. Additional technical specifications for the EuroLab extruder system are summarized in Appendix B. The extrusion process is an extremely delicate balance between feeding, cooling, pulling, and spooling of filament. The process begins by first stabilizing the extrusion line by extruding purely HDPE. The extruder is first heated to the set barrel temperatures, once the set temperatures are reached, extrusion is started by engaging the screws for the set speed in rpm. The HDPE feeding is started and pellets flow into the extruder, where the temperature is set for zone 1. A polymer melt is formed as the pellets are heated inside the extruder barrel. Co-rotating screws in the barrel mix the melt and push the material along the barrel length and through the nozzle die located at the end of the barrel. Hot extrudate flows from the end of the nozzle and into the cooling water bath below. Due to the high rotational speeds of the screws, the molten HDPE flowing out of the nozzle does so at a very fast rate.

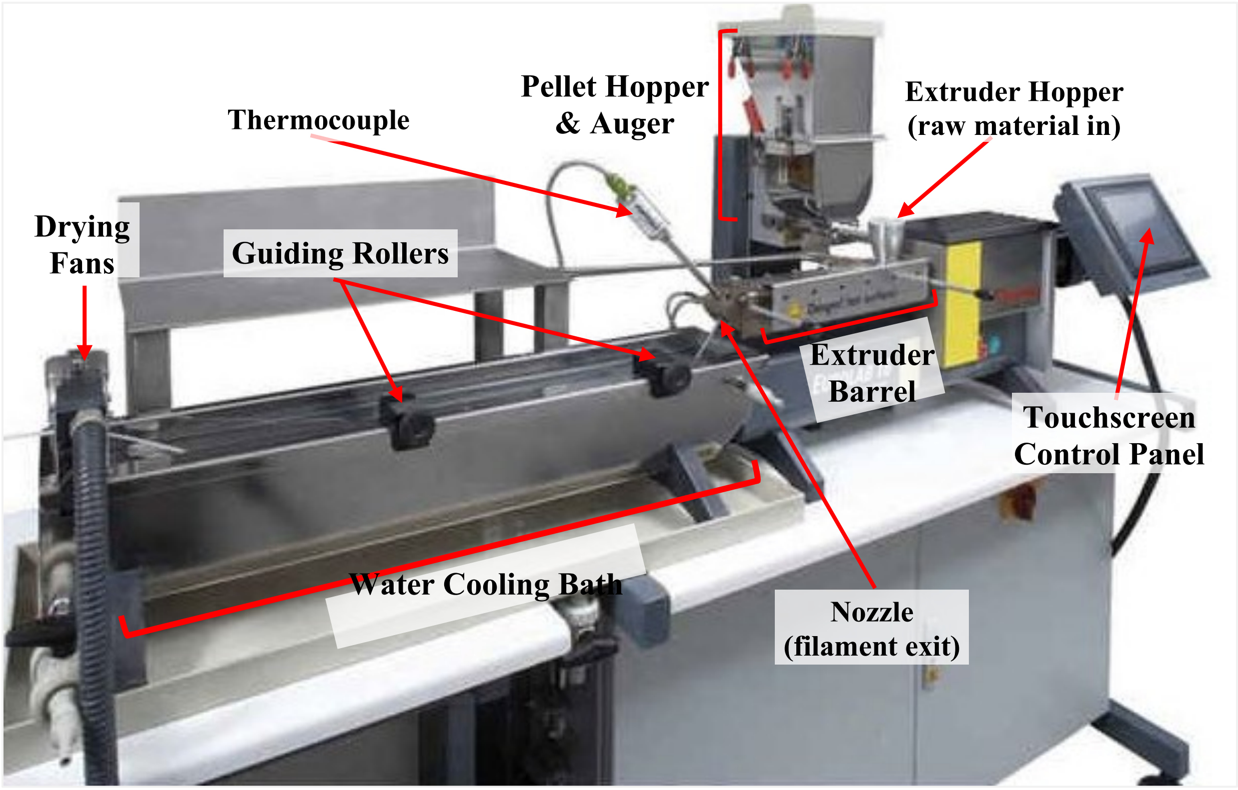

Figure 3.10 Labelled Components of the EuroLab 16 XL Twin-Screw Extruder
(ThermoScientific, 2016)

The pulling speed is adjusted to draw the strand of polymer filament so that it maintains the flow of material being extruded at the speed of extrusion, and cools at the size of desired diameter, indicated by the laser diameter measuring instrument. A continuous strand of filament is initiated by submerging and hand-pulling a portion of hot extrudate across the length of the cooling water bath, between the parallel drying hoses, through the base of the laser diameter measuring sensor, and feeding the solidified end of the strand in between the rolling conveyor belts of the puller the horizontal conveyor belts of the puller. The cooling of the filament is critical to the stability of the extrusion strandline, and therefore extra care must be taken to stabilize the portion of the extruded strand which occupies the length of the cooling bath. The positioning of the filament strand is adjusted as the filament is pulled and hot extrudate flows continuously from the nozzle. The body of the extruded filament is delicately submerged into the cooling tank and secured by passing in between a set of three rollers located along the tank length. This is done to creating tension in the filament and maintain a constant cooling rate during continuous extrusion. The hot extrudate must be submerged into the tank quickly upon exiting the nozzle, in order to preserve the size and shape of filament as molded by the die. A constant rate of cooling ensures that the solidified filament remains uniform in size during the process of continuous extrusion Once the production line is producing a continuous strand of HDPE filament, the speed of pulling may be adjusted to achieve a desired size of filament. An increase in pulling speed results in a decrease in filament diameter, and vice versa. The laser measurement device displays the average size of filament passing through the sensor during extrusion, therefore adjustments to the pulling speed are made accordingly. The production line is stable when all extrusion operations (feeding, cooling, and pulling) are fully automated and producing a 1.75 mm nominal diameter HDPE filament. Filler feeding is then initiated. Once the filler feeding has begun, three changes in the extruded filament strand line were observed. First, is a sudden decrease in filament diameter and filament flowing out of the extrusion nozzle. Second is an increase in extrusion pressure, and third is a change in filament color from translucent white to dark gray. The pulling speed is adjusted to adjust to the change in the rate of extrusion, due to the change in the rheology of the molten material being extruded.

3.2.3 Laser Diameter Measuring Instrument and Pulling System

Filament size is controlled by the speed of pulling during extrusion. The dynamic outer filament diameter is measured using a laser diameter measuring instrument (Model: LST-25/JIIB). The laser measuring device is part of a horizontal pulling system, specifically the high-speed caterpillar haul off unit. Both machines are manufactured by Labtech Engineering Company Ltd. located in Thailand. The technical specifications for both units are listed in Table 3.1 below.

Table 3.1 Specifications of Laser Measurement Device and Puller

Laser Diameter Measuring Device	
Measuring Range (mm)	0.1-25
Accuracy (mm)	± 0.002
Resolution (mm)	0.001
Gauge Dimensions (mm)	320 x 60 x 256
Weight (kg)	5
Power Consumption (W)	15
Laser Scanning Speed (times/sec)	600-1400
Pulling Device	
Belt Length (mm)	610
Belt Width (mm)	82
Passage (mm)	40
Max Pulling Speed (m/min)	100

3.3 3D-Printing (FFF)

Test sample profiles are modelled and drafted using Autodesk TinkerCAD, a three- dimensional computer aided design (CAD) platform. The software produces a stereolithography file format (.STL) of the model for export and download. Cura (4.8.0) software is used to process the STL and “slice” model into horizontal layers while generating toolpaths to efficiently print each layer. The slicing software calculates the number of layers required, the amount of filament needed, and an estimation of the time required to complete the print. The sliced model is then exported as a G-code and opened using Repetier Host (1.2.0), which is the interface between the part to be printed and the FFF machine itself. Using this software, the movements of the FFF machine can be controlled prior to, during, and post-printing. Five samples of each composite filament are printed using the Machina Mk2 X20 FFF 3D-printer. Dimensions of the printed samples are measured using an electronic caliper (Mitutoyu Corp, model no. CD-6”CSX) which is accurate to ± 0.01 mm. A labelled schematic of the Machina 3D-printer is seen in Figure 3.11. The printer has a 250 x 210 x 250 mm build volume and supports a minimum resolution of 20 µm, features include: a hardware vibration dampening shell, a dual supporting Z Axis bed and active and passive heat management systems *(Machina Corp, 2016).* The printer uses a 1.75 mm diameter filament as feedstock, stored on a spool and held in place by a large removable bolt (Fig. 3.11 a) allowing for simple loading and unloading. The filament is fed through a nylon Bowden tube and into the extruder head. A bottom view of the printer (Fig 3.11 b) shows a heated glass print bed, capable of reaching max temperatures of 110°C. The print bed consists of two layers, a top glass layer and bottom aluminum layer. The lower aluminum platform contains heating elements which provide even conduction to the removable glass top layer. The glass provides a smooth surface for deposition and maintains an adjustable temperature required for effective printing of specific materials. The main extruder printhead is seen in Fig 3.11 (c), where filament is fed into the opening located on the top of the extruder and is secured by a lockable lever which applies tension to the filament for controlled feeding into the heated nozzle below. The extruder printhead assembly is comprised of a extruder (DyzeXtruder GT) and a hot-end (DyzEND-X), both components are manufactured by Dyze Design, located in Quebec, Canada. The technical drawings and specifications of both components are provided in Appendix B. The extrusion nozzle can reach temperatures up to 500°C and has a 0.8 mm opening. The printer provides an efficient and reliable method for rapid prototyping and manufacturing with greater dimensional control and surface finish.

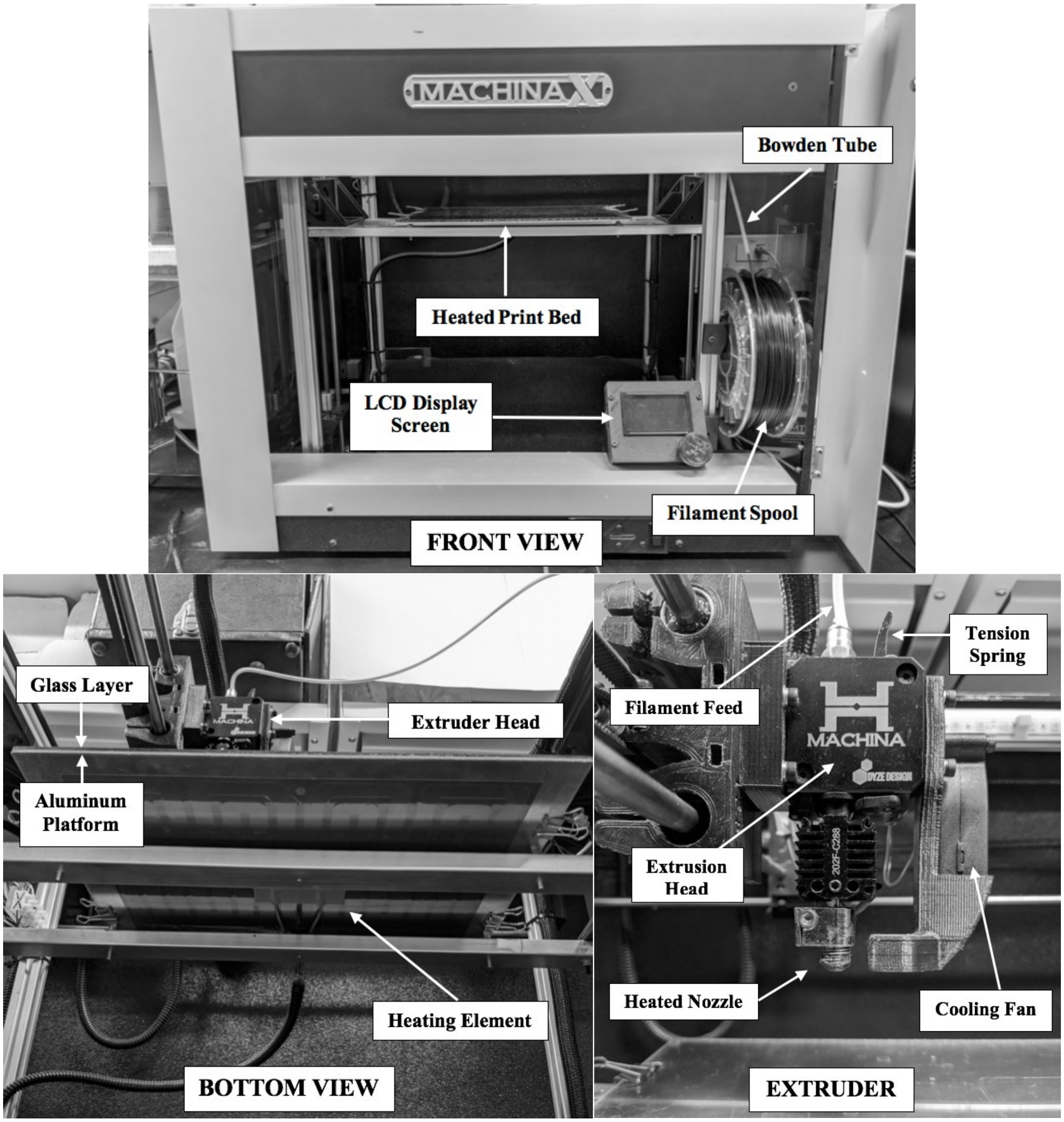

Figure 3.11 Labelled configurations of the Machina Mk2 X20 3D Printer

3.4 Composite Characterization Methods

This section describes the methods used to characterize the extruded composite filaments and the samples printed from these filaments by FFF, referred to as green-body parts.

3.4.1 Filament Diameter

The nominal diameter of 1.75 mm with a tolerance of 0.05 mm is standard sizing for commercially produced polymer filaments. The nominal diameter of all composites filaments is evaluated based on 100 randomized measurements of diameter using an electronic caliper (Mitutoyu Corp, model no. CD-6"CSX) accurate to ± 0.01 mm

3.4.2 Filament Flowability

The final method of characterization explored for the evaluation of composite filaments is the measurement of filament flow rate. When printing, the volumetric polymer flowrate, FR_P (mm^3/s) depends on your layer height (mm), nozzle diameter (mm) and print speed (mm/s), calculated using Equation 3.7. When conducting flowrate measurements by extruding a steady stream of filament into air, we can assume that the diameter of molten filament exiting the nozzle is slightly greater than the diameter of the nozzle itself. We can calculate the flowrate of the filament using the linear feed rate of the filament and the cross-sectional area of the filament using Equation 3.8.

$$FR_P = (\text{nozzle diameter}) \times (\text{layer height}) \times (\text{print speed}) \qquad (3.7)$$

$$FR_{air} = FF \times A_F \qquad A_F = \pi\left(\frac{D}{2}\right)^2 \qquad (3.8)$$

Where, FR_{air} is the polymer volume flow rate in air (mm^3/s), FF is the filament feed rate (mm/s), A_F is the cross-sectional area of filament (mm^2), and D is the average diameter of filament fed into printer (mm). Five measurements of flow rate at temperatures of 190, 200, 210, 220, and 230°C, were recorded for each filament. An average of the 5 test values for flow rate was taken.

4. PARTICLE PACKING

Chapter 4 describes the methodology for optimizing particle packing density and carbide content in binary powder mixtures for use as fillers in sinterable composite filaments. The results of the particle packing experiments performed for pure Ni, TiC, and WC powders, and binary mixtures of Ni-TiC and Ni-WC are presented. Linear rule-of-mixtures (ROM) theory is used to predict the void fractions of powder mixtures based on the conditions for ideal mixing, and therefore, represents ideal particle packing. The experimental values of void fraction found in this work represent non-ideal particle packing. In this study, poured random loose packing is observed, as it most closely demonstrates the conditions of powder introduction during composite extrusion. A comparison between ideal and non-ideal particle packing in binary particle systems is discussed, to validate the ROM theory. Particle packing diagrams are illustrated to show the deviation from ideality. The effects of mixture composition, specifically carbide content, and mean particle size on the random loose packing of particles are also discussed.

The chapter is organized in the following manner: Section 4.1 characterises the properties of the individual powders and their mixtures, Section 4.2 presents the experimental results of ideal and non-ideal particle packing in Ni-TiC and Ni-WC mixtures, and provides a detailed analysis of the results for filler selection, Section 4.3 compares the results of ideal and non-ideal packing and discusses the deviation from ideality based on observations for maximum void depression, lastly, a concise chapter summary is provided in Section 4.4.

4.1 Characterization of Powder Properties

Powder characteristics such as size, morphology, and composition all influence the various stages of the manufacturing process. Above all, the particle packing fraction in a polymer composite is critical for densification and to achieving successful sintering of a composite green part. Therefore, it is necessary to characterize the properties of the individual powders prior to mixing. Three main factors affect the packing of particles in a binary mixture: particle shape, particle size, and mean size ratio. Another factor of importance is the mixture composition or fraction of each component. In this work, the mixture composition is specific to the carbide content in the binary mixture. This section characterizes the properties of all metal and ceramic powders used in this investigation based on type, shape, size, and distribution of particles. A description of the mean size ratios used to prepare binary mixtures is also included.

4.1.1 Powder Type

In this study, metallic nickel-chromium alloy (Ni) powders are mixed with titanium carbide (TiC), and tungsten carbide (WC) ceramic powders to form binary Ni-TiC and Ni-WC filler mixtures. Table 4.1 lists the type of powder, supplier, batch numbers and chemical composition for each powder, as provided by the suppliers *(Titanium Carbide, 2020) (Tungsten Carbide, 2020) (Oerlikon Metco, 2020).* The Ni powder was obtained from Oerlikon Metco located in Switzerland, whereas the two ceramic powders, TiC and WC, were manufactured by Pacific Particulate Materials located in Canada.

Table 4.1. Properties of Metal and Ceramic Powders Used

Powder	Supplier	Grade	Batch no.	Composition (wt%)
Nickel-alloy (Ni)	Oerlikon Metco	43VF-NS	W149660	Ni: 79.15 Cr: 19.43 Si: 0.96 Fe: 0.40 Total C: 0.06
Titanium Carbide (TiC)	Pacific Particulate Materials Ltd.	TiC-1028	13208	Ti: 80.52 Total C: 19.46 Fe: 0.02
Tungsten Carbide (WC)	Pacific Particulate Materials Ltd.	WC-1065	8336 (Batch 1) 8337 (Batch 2)	W: 93.87 Total C: 6.13

The Ni powder used in this study is from the same batch of powder received from the supplier, however the powder was delivered in two different containers. Therefore, the powders from each container are referred to individually as Batch 1 and Batch 2. Ni powder from Batch 1 was combined with TiC to form Ni-TiC mixtures, and Ni powder from Batch 2 was used to prepare Ni-WC.

4.1.2 Particle Shape

The morphologies of the pure filler powders were observed by scanning electron microscopy, representative micrographs are seen in Figure 4.1. The shapes of the Ni particles (Figure 4.1a) can be described as relatively spherical with a high degree of satellites, including some elongated and irregular shaped particles.

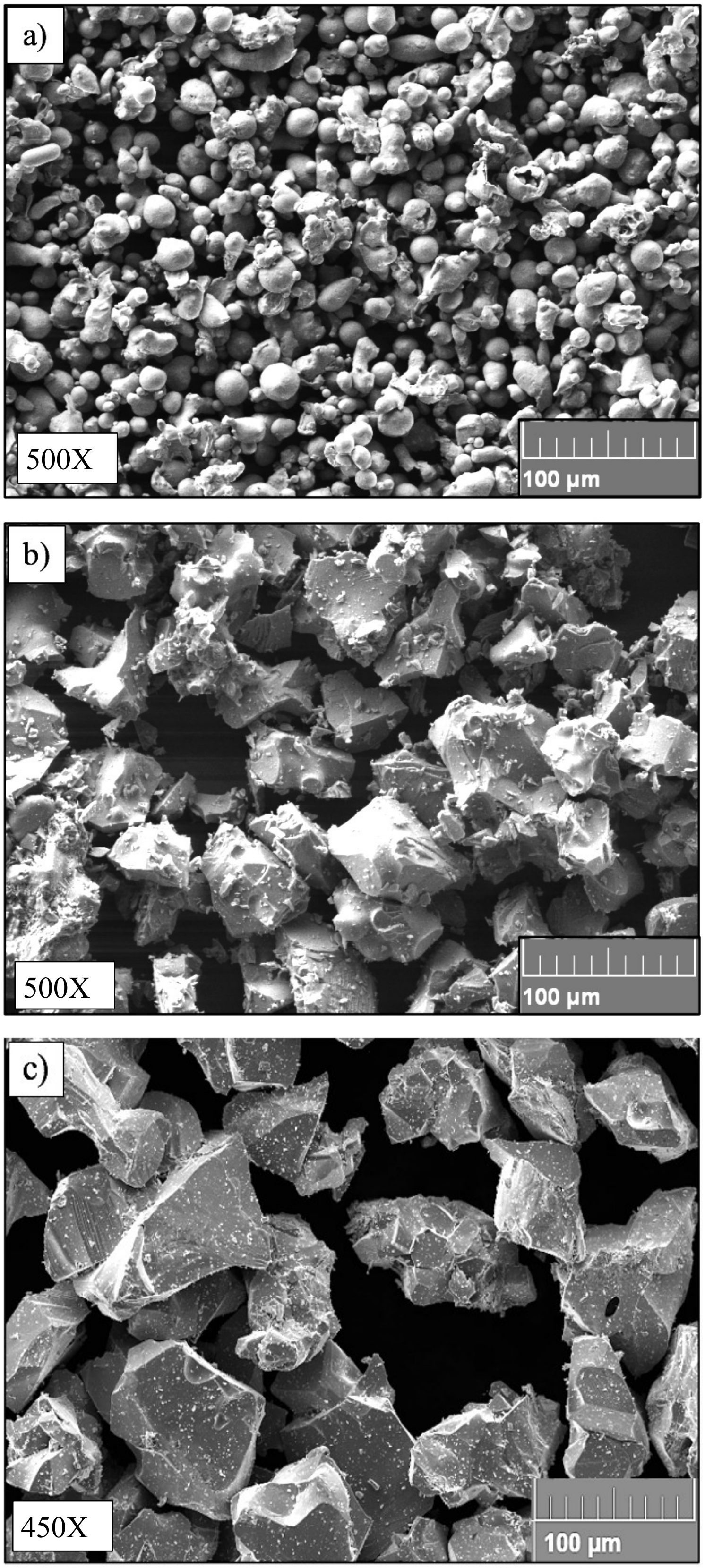

Figure 4.1 Morphology of (a) Ni, (b) TiC, and c) WC powders

The irregular morphology of the inter-dispersed Ni particles can be attributed to the water atomization process by which the powder was produced. Both ceramic particles, TiC (b) and WC (c), appear more angular in shape, with particles having flat and sharp edges. In contrast, small satellites are observed on the surfaces of TiC particles, while the WC particles appear more faceted. Most importantly, is that all three powders shown in Fig 4.1 are non-spherical in shape and therefore, non-ideal in terms of particle shape. An ideal morphology is described as a smooth, frictionless, uniform sphere. It is known that particles having irregular or non-spherical morphologies pack less densely than perfectly spherical particles *(Metzner, 1985) (German & Bose, 1997).* The lower packing ability of particles having non-ideal morphologies, is due to an increase in interparticle friction caused by "interlocking" between non-spherical or angular-shaped particles *(Yunn et al., 2011)*. Interparticle friction can also be attributed to the high hardness of ceramic particles compared to metallic particles *(German, 2013)*. It is the high hardness of carbide particles which provide the wear resistance properties needed in components used in oilsands applications.

4.1.3 Particle Size and Distribution

The mean particle size and particle size distribution (PSD) are critical factors in improving particle packing and sintering of powdered materials *(Tan et al., 2017).* While small particles are desired for sintering densification and component shape retention, large particles are desired for impurity accumulation or specific wear resistance properties *(German, 2013) (German & Bose, 1997).* A fundamental concept in powder metallurgy in relation to particle packing is that packing efficiency may be improved by adding small particles, comparable in size to the voids found in a loosely packed coarse powder. Understanding the particle size distribution of the individual powders and selecting a complementary size range will increase particle packing. In this work, the Ni particles will act as the small particles that will fill the voids in between the larger carbide (TiC or WC) particles. The PSD curves for the Ni and TiC powders used to form Ni-TiC mixtures are presented in Figure 4.2. Similarly, the PSD curves for Ni and WC powders used to create Ni-WC mixtures are plotted in Figure 4.3. These figures plot volume density (%) as a function of particle size in microns (μm) and follow a gaussian log normal distribution. From the PSD graphs, the relevant particle size data including: d10, d50 and d90 are listed in Table 4.2. The d50 represents the median particle size and represents the diameter of particle size where 50% of the population lies below this value. Similarly, 90% of the population lies below d90 value, and 10% of the population lies below the d10 value. The d50 value is commonly referred to as the mean or average particle size of a distribution of particles. In order to determine the most effective mean particle sizes of Ni and TiC particles that fit together to form the densest packing, three different sizes of Ni and TiC powders each are investigated. The Ni particles are less than 45μm in size with mean particle sizes equalling 20μm or less, which is the size range used in MIM *(German & Bose, 1997)* or AM processes such as SLM *(Duffy, 2020)*. Fine particle sizes as such have the tendency to become agglomerated due to interparticle forces, therefore the particles are sieved to try and break up the agglomerations before mixing with carbides in future steps. The TiC particles are coarser in size, with particle sizes less than 200μm. Although, the Ni powders contain particles sizes much smaller than those in the TiC powders, both are organized into the same size categories labelled (in ascending order) as: very fine, fine, and coarse, for consistency of referencing. The mean particle sizes (d50) of Ni powders are 13.5μm (very fine), 15.6μm (fine), and 19.7μm (coarse), as listed in Table 4.2.

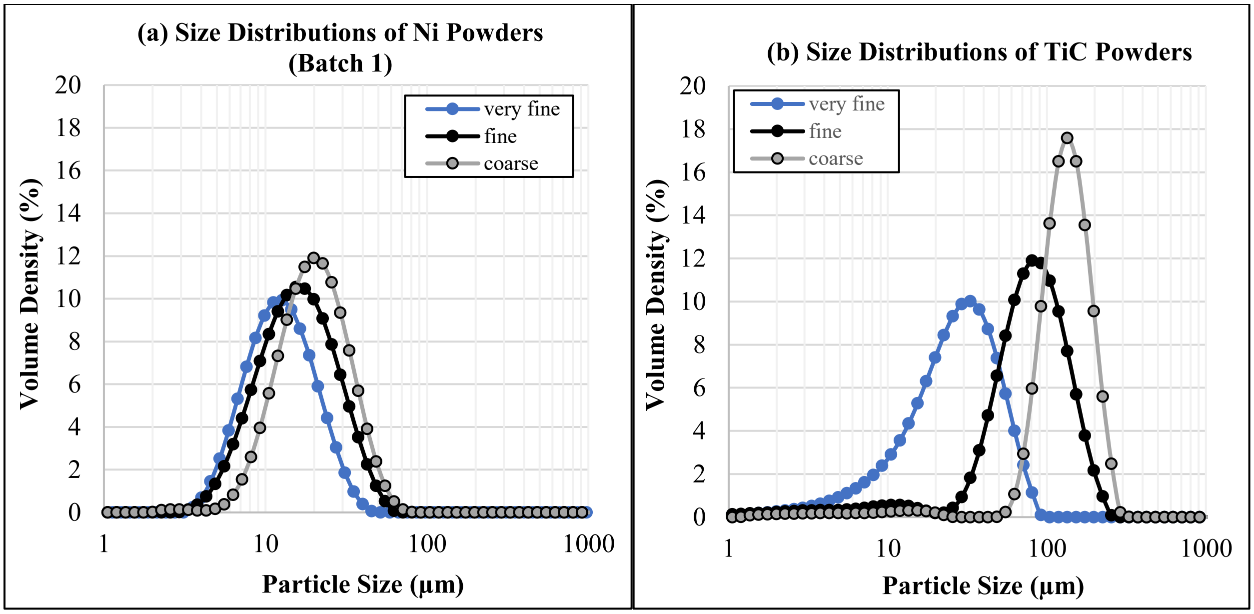

Figure 4.2 Particle size distribution curves for three different sizes of (a) Ni, and (b) TiC powders

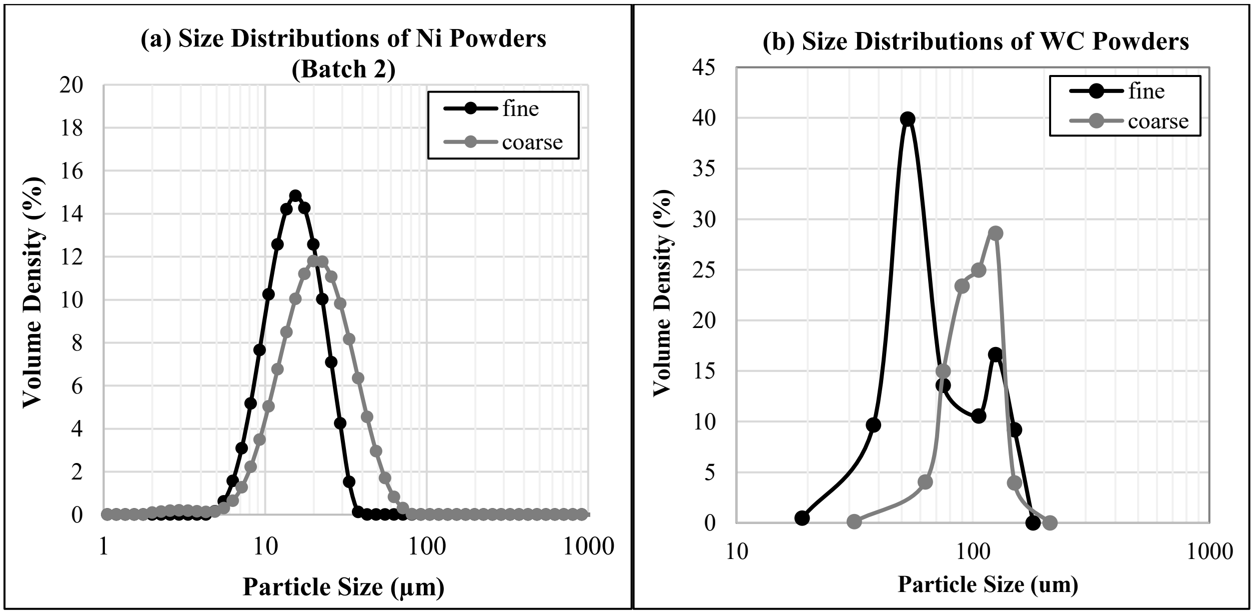

Figure 4.3 Particle size distribution curves for two different sizes of (a) Ni, and (b) WC powders

The coarse Ni powder is as-received, whereas the fine and very fine Ni powders are obtained by sieving the as-received Ni powder using 400-Mesh and 632-Mesh screens to obtain particles sizes below 37μm and 20μm, respectively. In Figure 4.2, PSD curves for the three Ni powders are noted to be similar in width and quite symmetrical. For TiC powders, Table 4.2 shows the d50 values to be 27.0μm (very fine), 79.8μm (fine), and 132.0μm (coarse). The three different distributions of TiC powders are obtained using a similar sieving process, as described for Ni powders. The fine TiC powder is as-received, and the very fine and coarse distributions are obtained through sieving fine TiC using a standard 200-Mesh screen to separate the particles into two different powder distributions. The fraction of powder that passes through the 200-mesh screen is considered to comprise of particles below 75μm in size (very fine TiC). The fraction of powder which is retained in the sieve is assumed to contain particle sizes above 75μm (coarse TiC). The PSD curves obtained through light diffraction particle size analysis of TiC powders (Fig 4.2b) show that the widths of the curves are dissimilar. The curve for coarse TiC, shows a narrower distribution compared to the very fine and fine TiC curves. The fine TiC appears to be most similar in width to the Ni curves in Fig 4.2 (a). Lastly, the very fine TiC curve appears to be negatively skewed, revealing a slight elongation of the left-side tail end, indicating that the powder contains a greater amount of smaller sized particles compared to the fine and coarse TiC. There is evidence to suggests that very fine powders in the range of 0 - 45μm particle size, with a skewed distribution containing a greater content of fine sized particles, have a greater bulk and tapped density, and in turn pack more densely than particles of a traditional gaussian bell-shaped distribution *(Liu et. al, 2011)*. The very fine TiC powder will be used to investigate the particle packing behaviour of a binary mixture (Ni-TiC) having similar mean particle sizes. The mean size of the very fine TiC powder (27.0μm) most closely matches that of the coarse sized Ni powder (19.7μm), used in this study. The PSD curves for Ni and WC powders used to form Ni-WC mixtures are shown in Figure 4.3. The relevant numerical particle size data for these powders is also listed Table 4.2. The coarse

Ni powder from Batch 2 is as-received, and the fine Ni distribution is obtained by sieving the as-received powder for particle sizes below 20 μm using a 632-Mesh screen. Comparing fine and coarse Ni powders from Batch 1 and Batch 2, the fine Ni in Batch 2 has a narrower distribution while both batches have relatively the same d50. It is well established that a wide distribution of particles leads to increased packing efficiency and reduces the void fraction in a bed of particles *(Hoffman & Finkers, 1995).*

Table 4.2. Numerical Particle Size Distribution Data (d10, d50, d90)

Powder	Size Category	d10 (μm)	d50 (μm)	d90 (μm)
Ni (Batch 1)	very fine	6.9	13.5	26.7
	fine	7.6	15.6	31.5
	coarse	10.1	19.7	36.7
Ni (Batch 2)	fine	8.9	15.1	24.4
	coarse	10.6	20.6	38.7
TiC	very fine	9.2	27.0	53.3
	fine	36.6	79.8	146.0
	coarse	82.2	132.0	200.0
WC	fine	53.0	75.0	148.5
	coarse	80.8	111.7	144.7

The PSD for WC powders in Fig 4.3b, are obtained from sieve analysis rather than light diffraction method. Therefore, the numerical d10, d50, and d90 values in Table 4.2 are obtained manually from a cumulative size distribution plot of the sieve data (available in Appendix A), rather than the PSD curves seen in Fig. 4.3 (b). The PSD curves for both WC powders reveals a bi-modal distribution of particles, evident from the two discernable peaks seen in the PSD curves (Fig. 4.3b) for these powders. Table 4.2 shows that the d50 of both fine-sized WC and TiC powders are nearly identical and just below 80μm. One notable difference between these powders is that the fine WC has a slightly narrower distribution, whereby the powder contains fewer fine particles overall, when compared to the fine TiC powder. This can be clearly identified by comparing the d10 values of the two fine-sized carbide powders, with TiC having a d10 of 36.6µm and WC featuring a greater d10 of 53.0µm. A similar comparison can be made for the coarse-sized carbides powders. First, it is clear that the d50 of the coarse-sized powders are relatively similar however the d50 of WC powder is smaller (111.7µm) than that reported for TiC (132.0µm). The other main difference can be seen when comparing the d90 values of the two carbide powders. Table 4.2 shows that coarse TiC has a d90 of 200.0µm, compared to a d90 of 144.7µm recorded for coarse WC. Therefore, the coarse WC particle distribution contains fewer larger particles overall, compared to the coarse TiC powder.

4.1.4 Mean Size Ratio

The mean size ratio of a mixture is defined as the ratio of the mean particle size of small to large particles in a bimodal mixture containing two different sized particles. In this work, small-size particles refer to those found in Ni powders and carbide powders (TiC and WC) represent the large-size particles in a binary mixture. Therefore, the mean size ratio (δ) of the mixture can be expressed using Equation 4.1. Where, $d50_{Ni}$ and $d50_{C}$ are the mean particle sizes (µm) of the Ni and carbide powders used to form the mixture, respectively.

$$\delta = \frac{d50_{Ni}}{d50_{C}} \tag{4.1}$$

As δ approaches 1, the mean sizes of the two powders become comparable in size. On the contrary, as δ approaches 0, the mean sizes of the two powders become more dissimilar. it is important to note that particle packing is dependent on both the mean size ratio and the fraction of each constituent present in the binary mixture (composition).

In one of the earliest works on particle packing of ideal binary mixtures, it was found that for a bimodal mixture comprised of mono-sized small and large spheres, a mean size ratio of 1:7 ($\delta \sim 0.14$), where the large spheres are 7x the size of the small particles yields the maximum packing density of 86% *(McGeary, 1961).* However, in practice it is most difficult or in some cases impossible to obtain metal or ceramic powders comprised of mono-sized particles with perfectly spherical shapes. Eastwood et. al reported that for a binary mixture of glass beads, void contractions occurred with increasing concentrations of the larger component when $\delta < 0.59$ *(Eastwood et al.,1969)*. Maximum void depressions occurred in mixtures having δ in the range of 0.11 - 0.24, for a mixture comprising of 50-70% large spheres. When $\delta > 0.74$, void expansions in the mixture were observed. Additionally, for binary mixtures having $\delta > 0.74$, contraction was observed within the mixture over the entire composition range. At $0.74 < \delta < 0.84$ expansions occurred within the mixture over part of the composition range, with one exception where a mixture having δ equal to 0.80 where bed expansion occurred over the entire composition range *(Eastwood et al.,1969)*. Another work relating the mean size ratio to the specific effect caused by adding small particles to a binary mixture, states that small particles tend to effectively fill voids, rather than expand voids when δ is approximately less than 0.33 *(Haughey & Beveridge, 1969).* Therefore, the effect of mean size ratio on the particle packing behaviour of a binary mixture comprised of a distribution of particles for each constituent, both with non-spherical (non-ideal) morphologies must be experimental determined. Based on the literature, binary mixtures of Ni-TiC and Ni-WC fillers were prepared having δ in the range of 0.10 - 0.27. The mean particle sizes and values of δ for each mixture prepared for particle packing analysis, discussed in the following section, are summarized in Table 4.3. One additional mixture, TiC-0.73 was prepared having a δ exceeding the ideal range, as mentioned above.

Table 4.3. Mean Particle Sizes and Size Ratios used for Mixture Preparation

Binary System	δ	$d50_{Ni}$ (µm)	$d50_{C}$ (µm)
Ni-TiC	0.10	13.5	132.0
	0.15	19.7	132.0
	0.20	15.6	79.8
	0.25	19.7	79.8
	0.73	19.7	27.0
Ni-WC	0.13	15.1	111.7
	0.18	20.6	111.7
	0.20	15.1	75.0
	0.27	20.6	75.0

This mixture was prepared to determine the critical value of δ, above which void expansions are expected to occur in the binary mixtures, as reported in other works *(Eastwood et al.,1969)*.

4.2 Random Loose Particle Packing

In this section, experimental values of nominal bulk and true density are used to calculate the experimental void fractions in pure Ni, TiC, and WC powders. Following this, the linear rule-of-mixtures (ROM) is used to predict the void fractions in binary mixtures formed from the pure powders. The experimental void fractions observed in Ni-TiC and Ni-WC powder mixtures are presented. The data from the experimental results is curve fitted to generate particle packing diagrams for Ni-TiC and Ni-WC binary particle systems. The packing diagrams are used to select filler mixtures for extrusion, based on optimization of particle packing and carbide content.

Finally, the validity of the ROM in predicting void fractions in binary powder mixtures is evaluated by comparison of experimental and ROM values of void fraction.

4.2.1 Void Fractions in Pure Powders

The measured bulk and true densities for all sizes of pure powders used in this study are listed in Table 4.4. The experimental void fractions of each powder are calculated using Eqn 4.1. The densities and void fractions listed in Table 4.4 represent an average value based on experimental work and standard deviations for these measurements are included. The effect of mean particle size (d50) on void fraction in pure powder (Θ_{exp}) is seen in Figure 4.4. A linear trendline has been applied to fit the data, the relevant curve-fitting data is shown in Table 4.5. One exception is made for TiC, where the linear trendline excludes the datapoint pertaining to very fine TiC (27.0, 0.580), this will be explained further.

Table 4.4 Average Particle Sizes, Densities, and Void Fractions of Pure Powders

Powder	d50 (µm)	Average Density (kg/m^3)		Θ_{exp}
		Bulk	True	
Ni (Batch 1)	13.5	4005 ± 24	7892 ± 48	0.493 ± 0.004
	15.6	3892 ± 13		0.507 ± 0.004
	19.7	3635 ± 9		0.539 ± 0.004
Ni (Batch 2)	15.1	3737 ± 19		0.526 ± 0.004
	20.6	3477 ± 23		0.559 ± 0.005
TiC	27.0	1861 ± 12	4434 ± 48	0.580 ± 0.007
	79.8	2043 ± 8		0.539 ± 0.006
	132.0	1858 ± 2		0.581 ± 0.006
WC	75.0	6916 ± 11	14,291± 42	0.516 ± 0.002
	111.7	6918 ± 11	14,710 ± 42	0.530 ± 0.002

First, examining the particle packing of Ni powders, Figure 4.4 shows that as expected, Θ_{exp} increases linearly with d50. The finest Ni powder from Batch 1 (13.5µm), reports the lowest Θ_{exp} of 0.493. As the d50 of Ni powders increase to a max. size of 20.6µm (Batch 2), Θ_{exp} increases to a max. of 0.559. In ideal particle packing, where the particles are mono-sized spheres, a PF between 0.60–0.64 is expected, meaning that Θ is between 0.35- 0.40 *(German, 2005).* Based on these values of Θ for ideal packing, it is clear from the Θ_{exp} values found for Ni powder in this study that less-than-ideal packing is observed. The increase in experimental compared to ideal values for Θ, can be explained by either the non-spherical shape of the particles, or the fine particle sizes of the powders. Fine particles, usually less than 20µm in size, experience interparticle friction due to increased surface area. This causes an increase in Θ as particles struggle to slide past one another and arrange into a dense packed structure. Therefore, it is reasonable to expect greater values for Θ in fine powders, than those predicted based on ideal packing. When observing the packing in TiC powders, Figure 4.4 shows that these particles report the greatest overall Θ_{exp} for all sizes when compared to Ni or WC powders. One unusual data point is the fine-sized (79.8 µm) TiC which reports the lowest Θ_{exp} (0.539), compared to the other TiC powders. Both the very fine (27.0 µm) and coarse (132.0) TiC particles pack exhibit very loose random packing, with both sizes reported a nearly identical Θ_{exp} of about 0.580, despite the large differences in particle sizes. One explanation for the unusually high Θ_{exp} reported for very fine TiC, compared to the fine TiC, may lie in the size distribution of particles. Previously seen in Figure 4.2, this powder has a skewed distribution and contains a greater content of small sized particles compared to the uniform distribution of fine-sized TiC. It is likely that this high content of small sized particles are forcing the larger particles in the distribution apart, causing expansions within the structure. The combined effect of both the highly angular shape of the particles and the small particle sizes having high surface area, highly influence the interparticle friction, causing the large increase in Θ_{exp}. The coarse TiC particles also demonstrate loose packing, compared to the fine TiC powder.

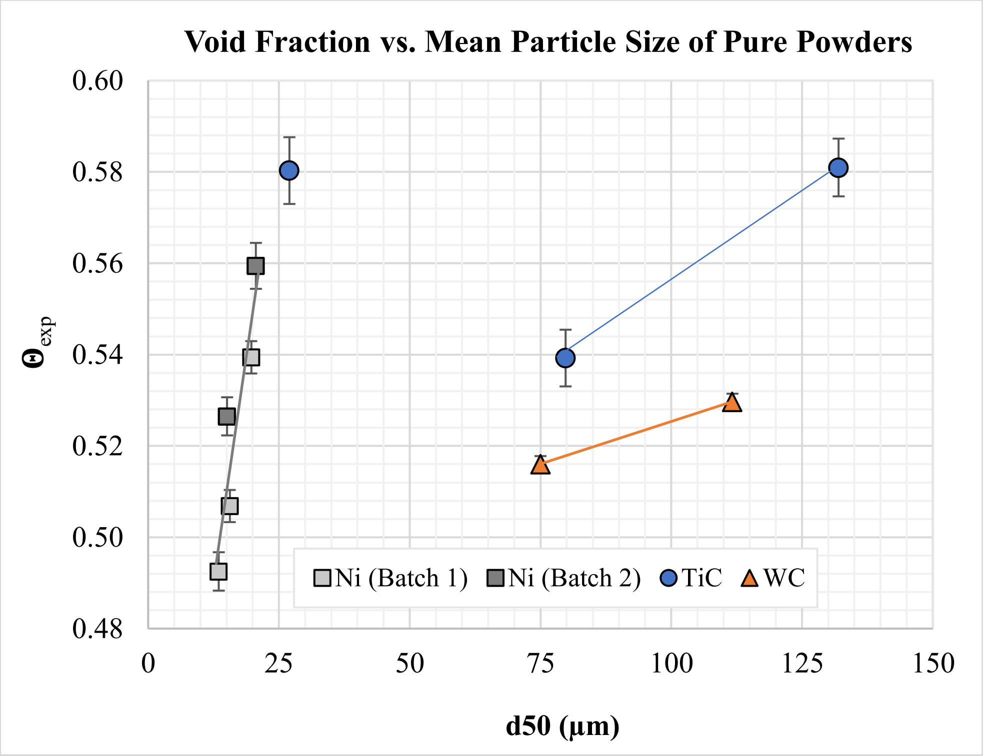

Figure 4.4 The effect of mean particle size on void fraction in pure Ni, TiC, and WC powders

Figure 4.4 shows that an increase in d50 of a distribution of TiC particles from 79.8 to 132.0µm, results in an 0.0.42 increase in Θ_{exp}. As the d50 of the powder increases, the size of the interparticle voids increases as well, a wider distribution of particles having small size particles are useful in filling these voids. An increase in Θ_{exp} for coarse TiC is expected, based on the narrow PSD seen previously (Fig.4.2b), compared to fine TiC. In contrast, Θ_{exp} in WC powders are shown to increase from 0.516 to 0.530 with increasing d50 from 75.0 to 111.7µm. WC and Ni powders in this study report similar Θ_{exp} in a random loose state of packing, despite the overall larger sizes of the WC particles. Furthermore, the results show that WC particles form a much denser packing than TiC particles, when the d50 is between 75 and 132µm. The main reason for the difference in packing behaviors between the two carbide powders, is the bi-modal PSD of WC powders, which has been shown to form denser packed structures. The data in Table 4.5 suggests that the effect of particle size is strongest for Ni powders, based on the large slope value seen in the linear trendline equation for Ni. The slope for Ni is shown to be an order of magnitude greater than the slopes listed for the carbide powders. Comparing the two carbide powders, Table 4.5 shows that the effect of d50 is more influential in TiC than WC, for d50 between 75-132µm.

Table 4.5 Trendline Data for Void Fraction vs. Mean Particle Size Plot

Powder	Linear Trendline Equation	R^2
Ni	y = 7.87E-03x + 3.92E-01	8.46E-01
TiC*	y = 7.99E-04x + 4.75E-01	1.00E+00
WC	y = 3.72E-04x + 4.88E-01	1.00E+00

*for 79.8 < d50 < 132.0

Based on the experimental results for void fraction presented in this section, a comment can be made regarding effect of particle shape on particle packing. Based on the powder morphologies described previously in Section 4.1.2, the Ni particles are shown to be more rounded and spherical in shape, relative to the carbide particles which are mostly angular. Based on ideal packing theory, since the Ni particles are more ideal in shape, it is expected that the particles will pack more densely than both carbide powders. Since the void fractions in Ni and carbide powders of similar d50 was not investigated, a prediction based on the linear trends seen for the experimental results are used to validate this assumption. If the linear trendlines for Ni (Fig 4.4) are forecast forward to predict the packing of Ni particles having the same d50 as very fine TiC (27.0µm), the void fraction in Ni and TiC would be more or less equal. Therefore, the differences in particle shape between Ni and TiC have no effect on the void fractions in particles with a d50 of 27μm. Thus, confirming that the packing behavior of very small sized particles (<45μm) is strongly linear and independent of particle shape or material. The particle packing results from this section, specifically the values of Θ_{exp} found for various pure Ni, TiC, and WC powders are used in the following section to predict the packing of Ni-TiC and Ni-WC binary mixtures formed by ideal mixing of the pure powders. The values of Θ_{exp} for each pure powder are used as initial values for void fraction, from which the void fractions in ideal mixtures of Ni and carbide are calculated.

4.2.2 Ideal Particle Packing in Binary Powder Mixtures

A linear rule-of-mixture (ROM) model is applied to the void fraction in binary mixtures of particles over a range of mixture compositions. The void fractions in Ni-TiC and Ni-WC mixtures calculated using the ROM (Θ_{ROM}), are used as reference points to compare with the experimental void fractions (Θ_{exp}) found by measuring the bulk and true densities of actual prepared Ni-TiC and Ni-WC powder blends. Based on the results presented for pure powder density (Table 4.4) in the previous section, the ROM (Eqn 2.1) is used to calculate Θ_{ROM} in six different mixtures of Ni-TiC defined previously in Table 4.3. Figure 4.5 shows the plot of Θ_{ROM} as a function of composition, specifically volume percent of TiC in the mixture. In Figure 4.5, the void fraction of purely Ni powder (Batch 1) is shown by the data points corresponding to 0 vol% TiC along the x-axis, have overall lower $\boldsymbol{\Theta}_{\text{ROM}}$ than TiC particles shown as the set of data points at 100 vol% TiC on the x-axis. Figure 4.5 shows that there is a linear increase in $\boldsymbol{\Theta}_{\text{ROM}}$, with an increase in vol% TiC for all δ-values. One exception is for δ of 0.25, where TiC content has no effect on the packing in the mixture, clear from the constant value seen for $\boldsymbol{\Theta}_{\text{ROM}}$ even as %TiC increases. This is expected as both sizes of Ni and TiC powders used to form this binary, individually pack to a void fraction of about 0.54 (Table 4.4).

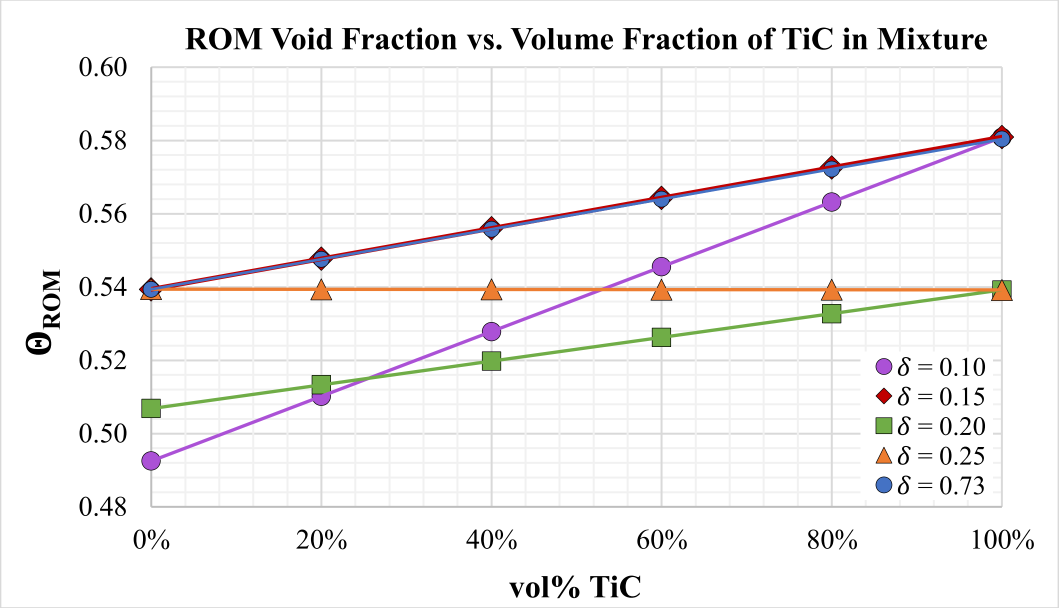

Figure 4.5 Rule-of-mixtures void fraction as a function of vol% TiC in mixture

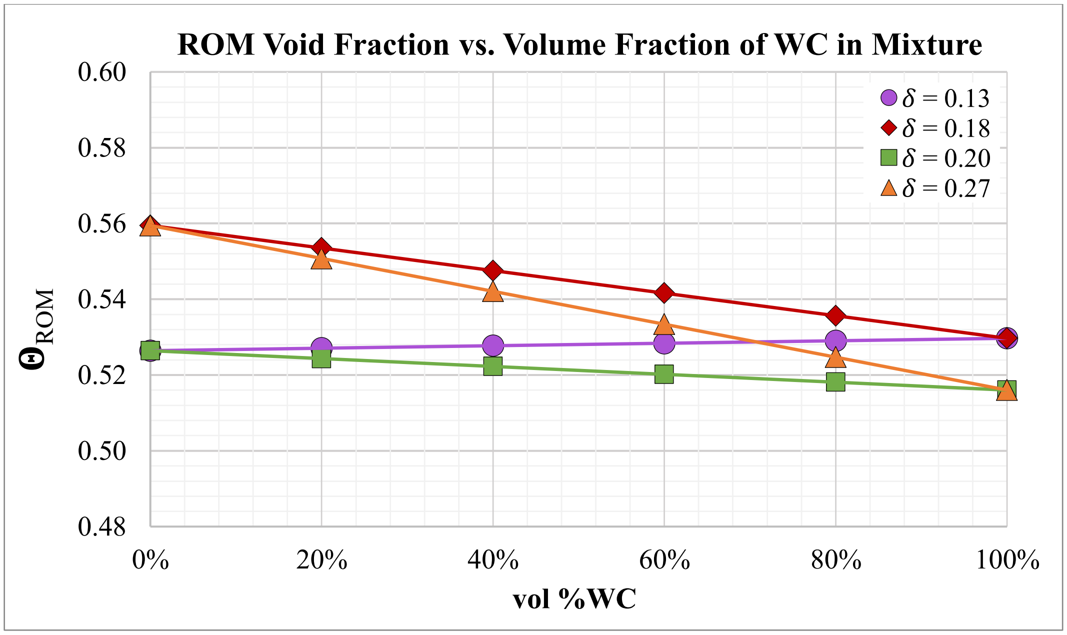

Figure 4.6 Rule-of-mixtures void fraction as a function of vol% WC in mixture

Therefore, using an ideal model to predict particle packing in this mixture, the composition is shown to have no effect on the Θ_{ROM} in the mixture. Similarly, two sizes of Ni powders were mixed with two sizes of WC powders to form four binary combinations of Ni-WC mixtures with δ between 0.13 – 0.27. The Θ_{ROM} versus composition (vol% WC) is plotted in Figure 4.6. The pure WC powders, previously reported values of Θ_{exp} similar to those for pure Ni powders in Batch 2 (Fig.4.4). Based on these results, it is expected that when applying the ROM, values of Θ_{ROM} decrease linearly with increasing WC content, as seen for most curves in Figure 4.6. One exception is for the mixture having the smallest δ (0.13), which shows a constant or unchanging relationship between Θ_{ROM} and composition, similar to the observations made for the Ni-TiC mixture with δ equalling 0.25. The significance of this result is to emphasis the limitations of using an ideal packing model, such as the ROM, to predict the void fractions in binary mixtures. In the case where the void fractions of the two pure powders which form the binary mixture, are near-identical or similar, then the relationship between void fraction and composition is shown to be constant and unchanging.

4.2.3 Experimental Particle Packing in Binary Powder Mixtures

Binary powder blends consisting of Ni-TiC and Ni-WC powders are created by mixing powders together and measuring the average bulk and true densities of each mixtures. The actual or experimental poured random loose void fractions (Θ_{exp}) in each distinct binary powder blend, at 4 different mixture compositions, ranging from 0 to 100 vol% carbide in increments of 20% were experimentally determined. The Θ_{exp} as a function of carbide content (vol%) for each mixture characterized by δ is plotted in Figures 4.7 and 4.8 for Ni-TiC and Ni-WC, respectively. The solid trendlines in these figures represent the linear ROM relationships, as seen in the previous section

(Figs. 4.5 & 4.6), and the dotted lines of same color represent the experimental results. Figure 4.7 shows that for a mixture having a large δ-value, 0.73, where two particles in a binary mixture are comparable in size, void expansions are observed throughout nearly the entire composition range. This is seen for the values of $\mathbf{\Theta}_{\mathrm{exp}}$ (blue-colored dotted series) which show a positive deviation from the corresponding $\mathbf{\Theta}_{\mathrm{ROM}}$ (blue-colored solid line). In this mixture, the largest expansions occur at compositions of 40vol% and 60vol% carbide. At these compositions, the effect of smaller Ni particles forcing apart large TiC particles is the most severe. Another observation is that for this binary mixture, large standard deviations are reported in the measurements of $\mathbf{\Theta}_{\mathrm{exp}}$, this shows that the mixture may not be homogenously mixed. Most importantly, Fig. 4.7 confirms that a binary mixture of Ni-TiC at a δ of 0.73 at any composition, does not yield sufficient particle packing, as $\mathbf{\Theta}_{\mathrm{exp}}$ exceed 0.50. In contrast, when the size of the two particles become more dissimilar, such that δ decreases from 0.73 to 0.25, void contractions occur, shown by the decrease in $\mathbf{\Theta}_{\mathrm{exp}}$ with increasing %TiC for range of compositions between 0 to 60vol% TiC. The binary mixture reaches a minimum value for $\mathbf{\Theta}_{\mathrm{exp}}$ at a composition of 60vol% TiC. At this point, the $\mathbf{\Theta}_{\mathrm{exp}}$ shows the greatest deviation from the linear $\mathbf{\Theta}_{\mathrm{ROM}}$, indicating the conditions of maximum packing in the mixture. An increase in TiC content beyond 60vol% in the binary mixture results in an increase in $\mathbf{\Theta}_{\mathrm{exp}}$, with particles effectively causing expansions in the mixture, until reaching a composition of 100vol% TiC. For mixtures having smaller size ratios, in the range of 0.10 to 0.25, large void contractions occur in all mixtures. In this range of δ, the effect of small particles filling the voids between the larger ones is dominate, creating more densely packed structures. The max. contraction occurs in mixture compositions between 40-60vol% TiC. Comparing the results for δ of 0.20 and 0.25, a decrease in the overall size of Ni (δ =0.20), causes a decrease in both the $\mathbf{\Theta}_{\mathrm{exp}}$ and vol% TiC at the point of max. contraction.

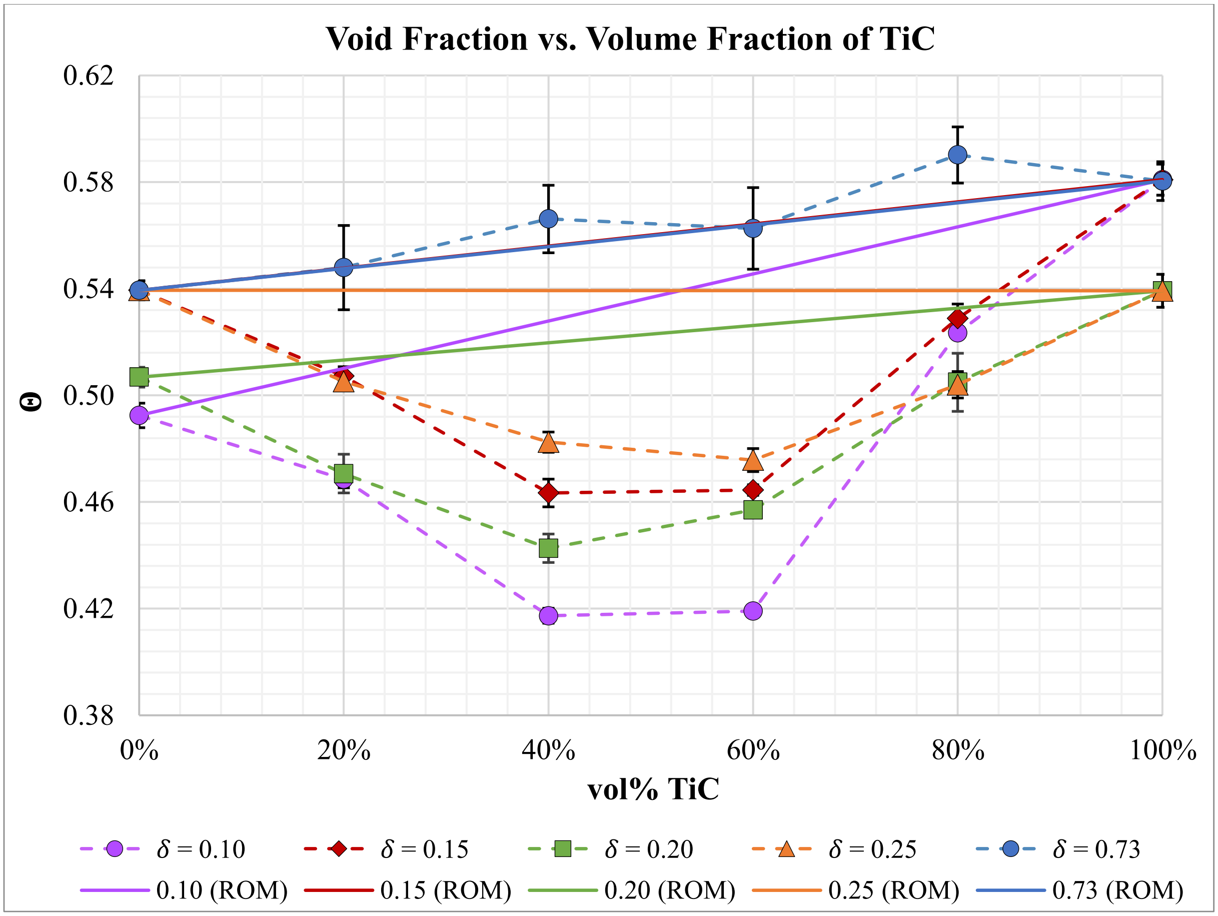

Figure 4.7 Effect of mean size ratio on void fractions in Ni-TiC binary mixtures

Resulting in overall greater particle packing but a decrease in the amount of TiC present in the mixture. Comparing the results for δ of 0.15 and 0.25, its seen that an overall increase in size of the TiC particles in the mixture, resulted in a slight decrease of $\mathbf{\Theta}_{\text{exp}}$ at the point of max. packing, with a decrease in the amount of TiC is noted. This shows that a decrease in size of the small-sized particles is a more effective in increasing the particle packing, than an increase in size of large-sized particles for the same binary mixture. Finally, the combined effect of both a size decrease of small-sized Ni particles, and an increase of large-sized TiC particles is seen for the binary mixture of δ equal to 0.10. At this ratio, the largest void contractions occur, with a minimum possible $\mathbf{\Theta}_{exp}$ of 0.42 reported.

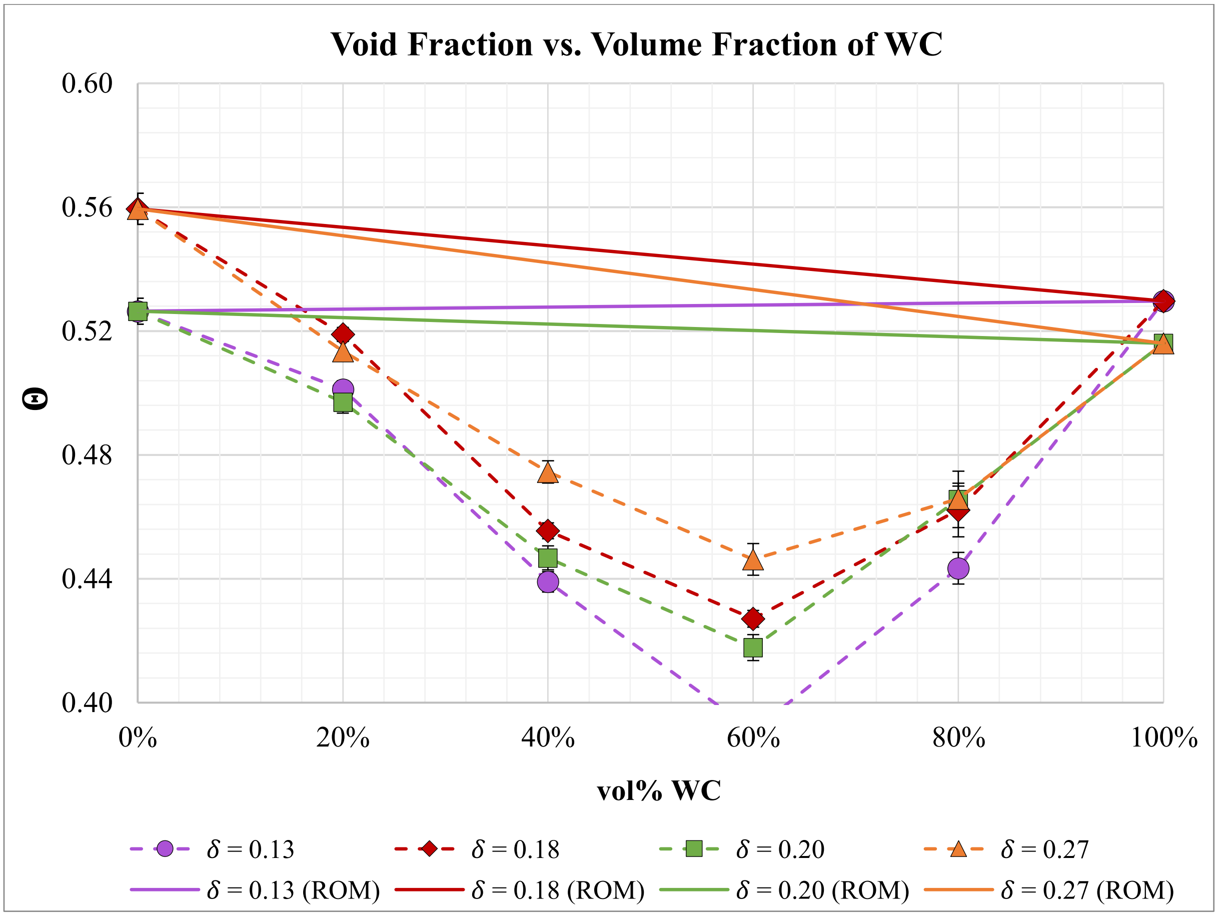

Figure 4.8 Effect of mean size ratio on void fractions in Ni-WC binary mixtures

Similarly, Figure 4.8 shows the results of experimental particle packing observed in Ni-WC binary powder blends where δ ranges from 0.13 to 0.27. It is clearly seen that void contractions occur for all mixtures over the entire range of compositions. Furthermore, the minimum values of $\mathbf{\Theta}_{exp}$ occur at a composition of 60vol% WC, in all of the Ni-WC powder blends seen in Figure 4.8. At this composition, the effect of δ on the minimum $\mathbf{\Theta}_{exp}$ achievable is shown by a decrease in values for

$\mathbf{\Theta}_{exp}$ from 0.45 to 0.39, in the order of δ from 0.25, 0.18, 0.20, and 0.13. As the composition of WC is increased to 80vol%, all blends report nearly identical values for $\mathbf{\Theta}_{exp}$, about 0.46, with the exception of the blend where δ equals 0.13. In this blend a slightly lower $\mathbf{\Theta}_{exp}$ of 0.44 is reported. At the smallest δ, the minimum possible $\mathbf{\Theta}_{exp}$ achievable in a Ni-WC powder blend is 0.39, which occurs at composition of 60vol% WC.

4.3 Mixture Optimization

Based on the experimental results for non-ideal particle packing presented in Section 4.2, optimized powder blends of Ni-TiC and Ni-WC are selected as fillers for extrusion to form sinterable polymer composite filaments for FFF. The criteria for filler selection are such that a suitable powder mixture is one having a:

(1) Maximum particle packing fraction (PF greater than 50vol%)

(2) Minimum void fraction (Θ less than 50vol%)

(3) Maximum carbide content

A maximum packing fraction ensures that densification necessary for future sintering will be possible for this powder mixture. An assumption is made that the void fraction in a dry powder mixture represents the volume that is occupied by polymer during extrusion. Therefore, a low void fraction ensures that the filler mixture is as densely packed with powder as possible, in the random loose state when introduced to polymer melt during extrusion. A maximum carbide content in the filler ensures that the resulting sintered parts have good wear resistance properties. Above all, the PF in a polymer composite is critical for densification and in achieving successful sintering of a green part.

This section describes the curve fitting of experimental void fraction data, from which particle packing diagrams for Ni-TiC and Ni-WC particle systems are constructed to model the ideal and non-ideal particle packing behaviour studied in the thesis work. The particle packing diagrams are used to select optimal filler mixtures for extrusion, described in the following Chapter 5.

4.3.1 Curve Fitting of Experimental Void Fraction Data

In order to select the compositions of binary mixtures for extrusion, the $\boldsymbol{\Theta}_{\mathrm{exp}}$ data presented previously in Figures 4.7 and 4.8 must be curve fitted so that the $\boldsymbol{\Theta}_{\mathrm{exp}}$ in mixtures having compositions other than those measured at 20vol% increments of carbide can be accurately interpolated. One of the critical design criteria for this process, is the maximization of carbide content in the filler mixtures, hence the mixture compositions containing 60vol% and 80vol% carbide are most significant. In order to evaluate the most suitable curve fit for the empirical void fraction data polynomial curve fitting is applied to fit the data. To quantify the quality of the applied curve fitting, the percent difference between the measured average value of void fraction and the value obtained using the curve fitting equation generated by excel for the same composition of mixture, is computed by Equation 4.2. Where Θ_{exp} is an average value for experimental void fraction in a mixture of known composition and Θ_{fit} is the value for Θ obtained using the curve fitting equation at the same composition.

$$\text{Difference } (\%) = \frac{|\Theta_{\mathrm{exp}} - \Theta_{\mathrm{fit}}|}{\Theta_{\mathrm{exp}}} \text{ x } 100\% \qquad (4.2)$$

A difference less than 5% between the experimental value and the curve fitted values of Θ is generally deemed an excellent fit for data when choosing a trendline. Therefore, this criteria for selecting a suitable order of polynomial curve to fit the data is valid and required for fitting all Θ_{exp} data for all mean size ratios of a binary mixture of powders in order to accurately interpolate data using the curve fitting equation. The % difference in all mixtures at compositions of 60vol% and 80vol% carbide with 2nd to 5th order polynomial curve fitting applied, are compared using the bar graphs in Figures 4.9 and 4.10. Figure 4.9 shows that the greatest % difference between the average measured and curve-fitted value of void fractions occurs when applying a 2nd degree polynomial fit for binary mixtures of Ni-WC and Ni-TiC at a composition of 60vol% carbide for nearly all mean size ratios. The exception being Ni-60TiC mixtures with δ of 0.15 and 0.25, for which 3rd degree curve fitting, rather than a 2nd degree fit, shows greater % difference between void fraction values. The % difference, when applying 2nd degree curve fitting, is greatest in binary mixtures having the lowest size ratio of particles, specifically 0.10 for Ni-TiC and 0.13 for Ni-WC. The greatest deviations are noted as 7.6% for a Ni-60WC (δ = 0.13) and 5.6% Ni-60TiC (δ = 0.10). A similar difference of 5.2% is noted for Ni-TiC mixtures having the same mean size ratio, but a higher carbide content of 80vol%, as reported in Figure 4.10. Due to % differences greater than 5% seen in both Ni-WC and Ni-TiC mixtures for at least one δ-value, a 2nd degree polynomial curve is unsuitable to fit this data. When analyzing the effect of applying 3rd degree polynomial curve fitting, Figures 4.9 and 4.10 show that for binary mixtures of Ni-60WC and Ni-80WC, % differences below 5% are reported over the full range of δ-values. The greatest % differences are 4.1% and 3.6% for Ni-60WC and Ni-80WC, respectively, for mixtures with a δ of 0.13. For Ni-80WC mixtures, greater values of % difference are seen for 3rd degree curve fitting compared to 2nd degree curve fitting for all δ-values, with the exception of 0.27.

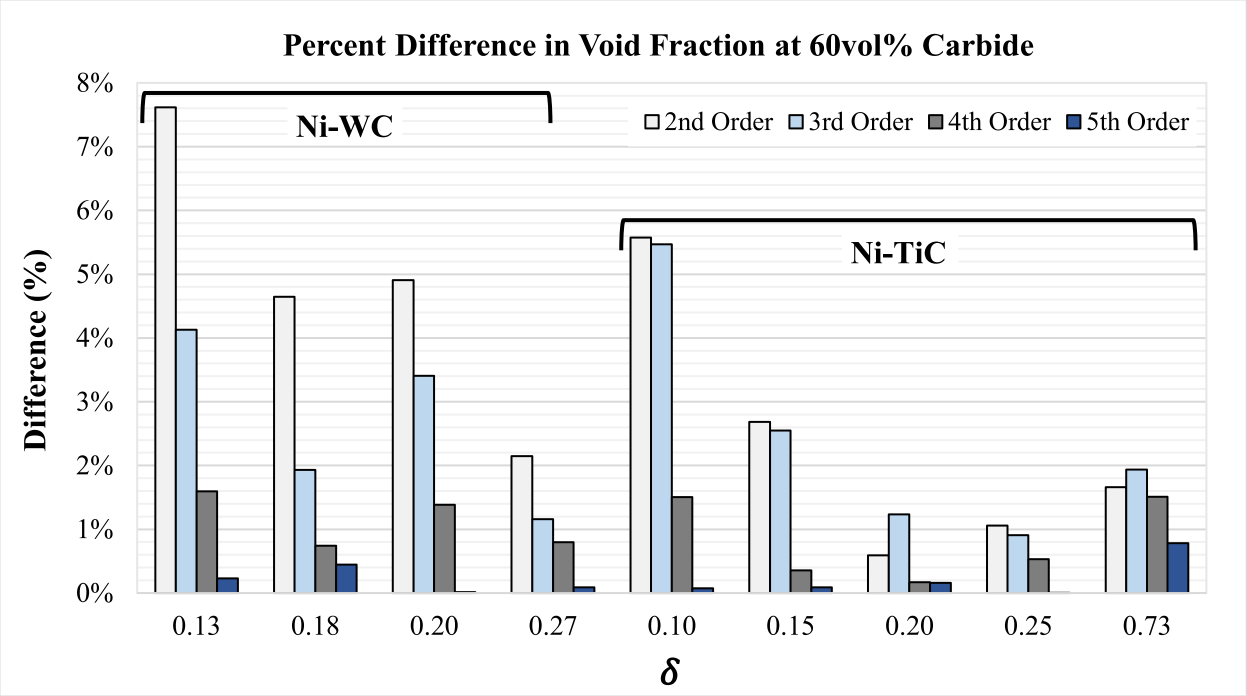

Figure 4.9. Percent difference in void fraction for mixtures containing 60vol% carbide

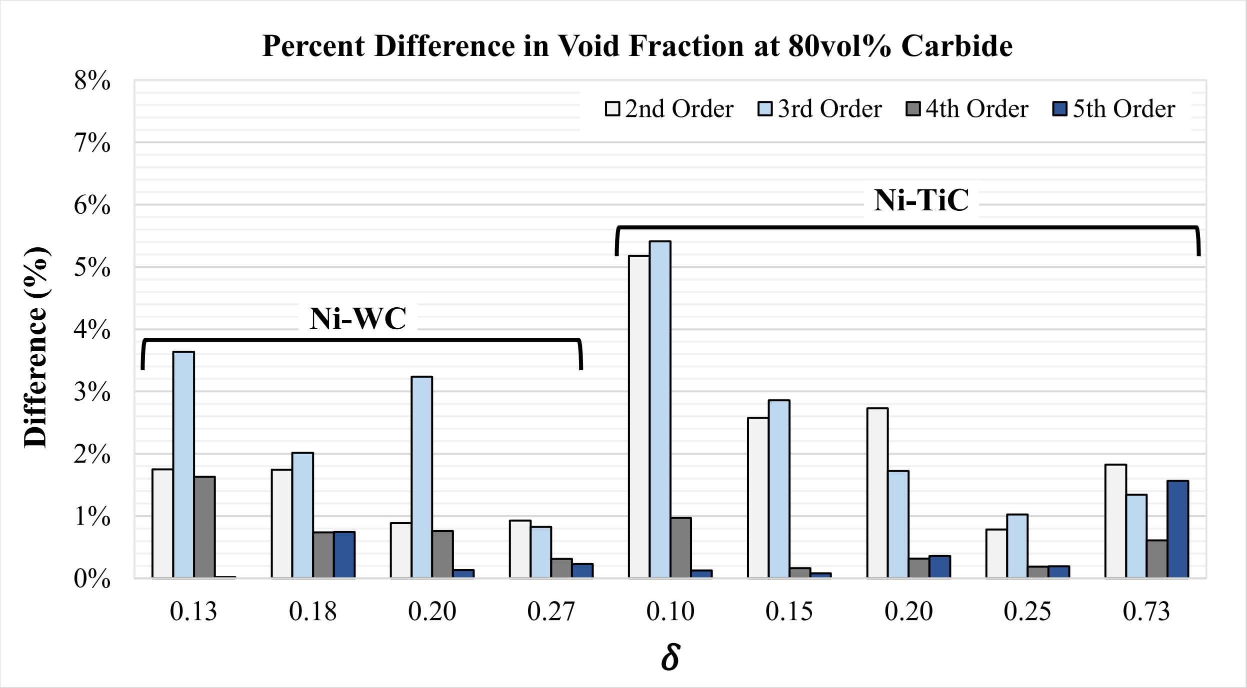

Figure 4.10. Percent difference in void fraction for mixtures containing 80vol% carbide

In contrast, observing the effect of 3rd degree polynomial curve fitting of void fractions as a function of mean size ratio in binary mixtures of Ni-TiC, a % difference below 5% is not seen over the full range of δ-values studied. In fact, mixtures with δ of 0.10, for both Ni-60TiC and Ni-80TiC, reported similar % differences of about 5.4%. Therefore, applying a 3rd degree polynomial fit does not meet the criteria required to be considered a good fit for the entire range of data. Increasing the degree of polynomial further to 4th degree polynomial curve fitting, shows a drastic drop in % differences to a max value of 1.6% for both compositions of Ni-WC mixtures, 1.5% for Ni-60TiC, and 1.0% for Ni-80TiC, at mixtures with the lowest δ-values. Evidence seen in Figures 4.12 and 4.13 shows that applying 4th degree polynomial curve fitting effectively decreases the % difference between the measured and curve fitted values of void fraction to less than 2% for all mixtures studied. A degree of 4 is selected for polynomial curve fitting of the experimental void fraction data obtained from particle packing experiments, which is shown to be an excellent fit for binary mixtures of Ni-WC and Ni-TiC with compositions of 60vol% carbide or greater.

4.3.2 Selection of Filler Mixtures for Extrusion

As discussed previously, the selection of binary powder mixtures suitable as fillers in polymer for successful sintering of the composite material, is based on maximizing carbide content and particle packing (PF). For the purpose of producing a sintered part with specific performance capabilities, such as wear resistance, the composition and microstructure of the powder particles is of main importance. A suitable filler mixture is a balance between particle packing as well as carbide content. The most crucial requirement for selecting a suitable filler mixture is the minimum particle packing density required in order to achieve densification and sintering to form fully dense cermet parts. The selected filler mixture must have, at minimum, a packing density of 50vol% (or max.

of 0.5). Mixtures having packing densities greater than 50 vol% solids loading allow for the green-part to easily retain its shape during polymer decomposition and minimize shrinkage in the final sintered brown part. However, a binary powder mixture in its most densely packed state may occur at a composition for which the microstructural benefits of one component of the mixture are not reflected in the final sintered part. In the interest of wear resistance, the maximization of carbide content in dry powder filler mixtures, typically compositions containing 60vol% carbide or greater are required to sustain the wear resistant properties of the hard carbide particles in the final brown part *(German & Bose, 2007)*. The optimization of carbide content is subject to the above-mentioned particle packing constraint required to satisfy the conditions for sintering. In order to clearly demonstrate the ideal and non-ideal particle packing behaviours of Ni-TiC and Ni-WC mixtures as well as and provide a clear method for filler mixture selection, particle packing diagrams are shown in Figures 4.11 and 4.12, for Ni-TiC and Ni-WC particle systems, respectively. The packing diagrams plot $\boldsymbol{\Theta}$ as a function of composition, where the linear relationships represent the values of $\boldsymbol{\Theta}_{ROM}$ showing ideal packing and the polynomial trendlines represent the experimental results from this study, based on the values found for $\boldsymbol{\Theta}_{exp}$. The experimental data is shown using dotted trendlines, and ROM data is identified by the solid trendlines in the packing diagrams. The trendline equations for each data set, including the residual values generated by excel are provided in Table 4.6 for all powder mixtures. In Figs. 4.11 and 4.12, the highlighted blue region represents the range of compositions for each mixture which satisfy the primary condition for selection, pertaining to the maximum allowable void fraction value of 0.5. In this region, a minimum particle packing of 50% or greater is observed within powder mixtures in a poured random loose state. The yellow region labelled as “Optimizing Carbide Content” indicates the range of compositions for which optimization of carbide content from 60vol% and upwards to a maximum value, while still meeting the requirements to satisfy the primary constraints stated for void fraction, is possible. Figure 4.11 showing the packing behaviour of Ni-TiC mixtures, the blue overlaid area illustrates that an acceptable range of void fraction within Ni-TiC mixtures that is necessary for sintering, occurs for mixture compositions having up to 80vol% TiC. Depending on the size ratios of the two powders, as well as the void fractions of the independent Ni powder (indicated at 0 vol% TiC), the range of mixture compositions where particle packing density is 50vol% or greater varies.

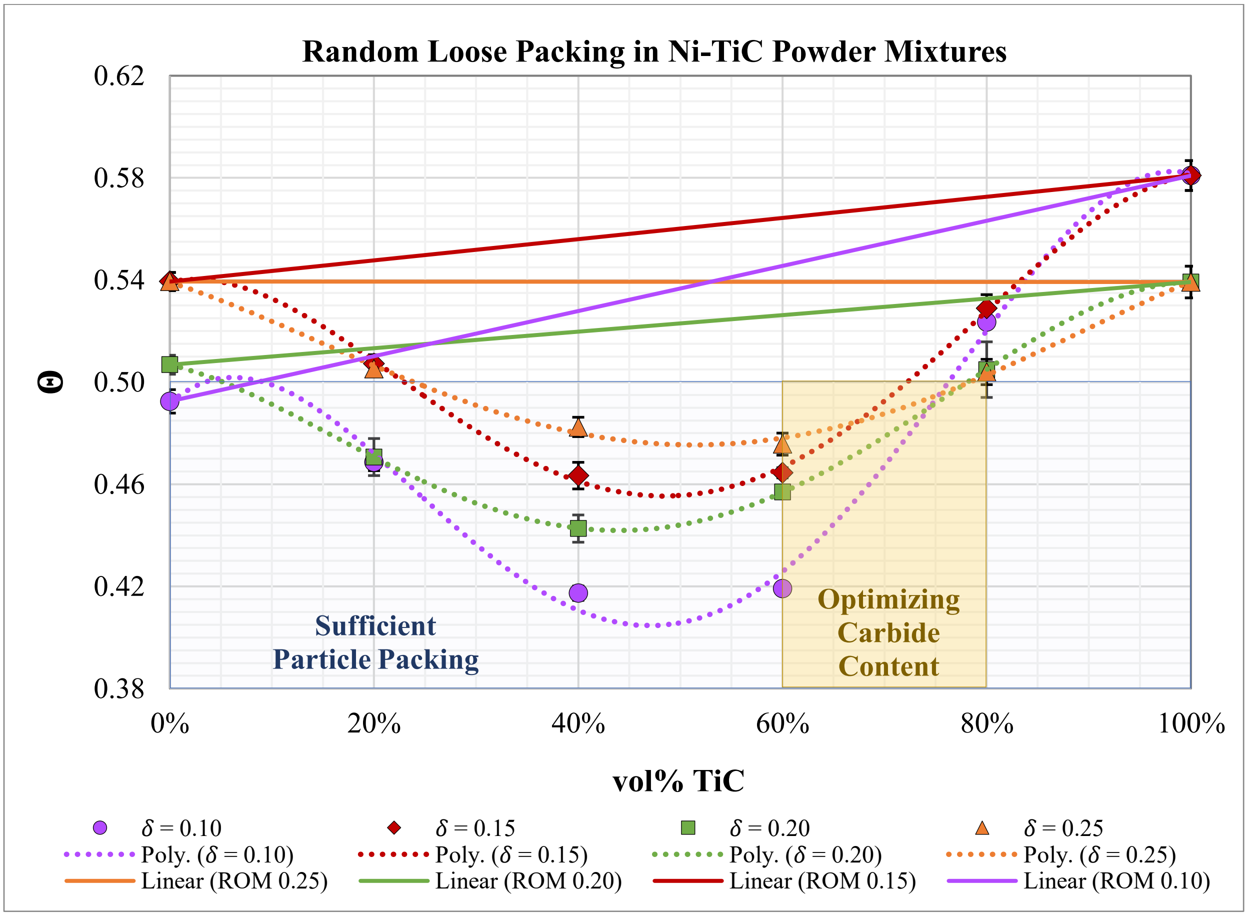

Figure 4.11 Particle Packing Diagram for Ni-TiC Binary Mixtures

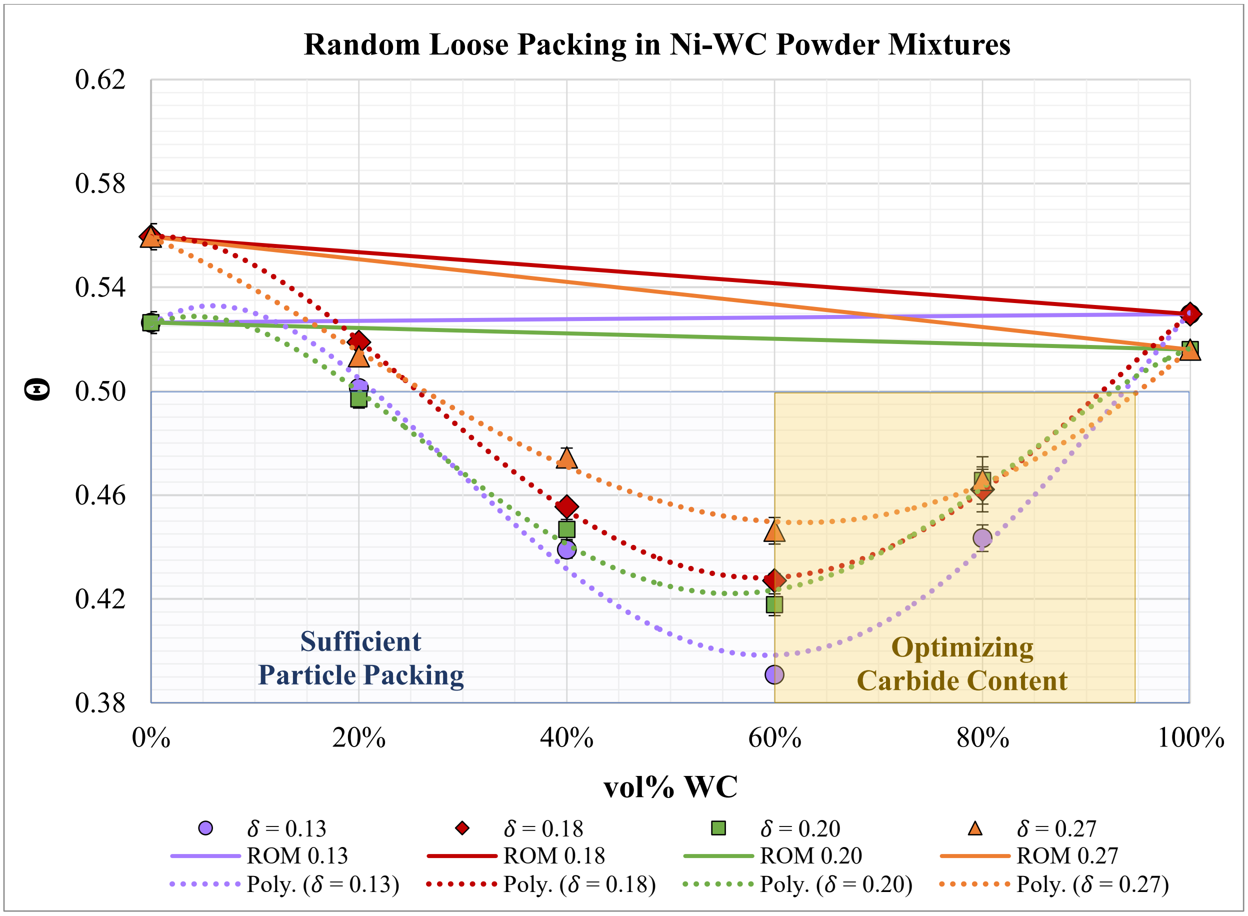

Figure 4.12 Particle Packing Diagram for Ni-WC Binary Mixtures

When considering mixture compositions where there is a desire to maximize carbide content, Fig 4.11 shows that the optimal range of compositions for selecting mixtures based on the desire to maximize carbide content for this binary system of powders, is between 60vol% up to a maximum of about 80vol% carbide. Beyond this point, any additional increase in TiC content in the mixture, yields a mixture where particle packing density is below 50 vol% and the first condition for filler selection is not met. Similarly, for Ni-WC mixtures it has been found that sufficient particle packing occurs in mixtures containing between 20 and 95 vol% WC, with the opportunity to optimize carbide content from 60vol% up to a maximum value of about 95 vol% WC, clearly indicated in Figure 4.12. In order to narrow down the selection process, two main points in the above packing plots are of interest. The first point of importance is referred to as the point of "maximum particle packing", seen in the packing plots as the minimum void fraction achievable for all binary mixtures, previously seen in Figure 2.2. The second point of interest is the point of maximum carbide content, this occurs at the point where the mixture of powders is comprised of the greatest content of carbide possible while maintaining a maximum value of 0.5 for void fraction. Using the 4th order polynomial curve fitting equations listed in Table 4.6 below, the void fractions and compositions at these points of interest can be interpolated.

Table 4.6 Curve Fitting Equations for Random Loose Packing of MMC Particle Mixtures

Mixture	δ	Trendline Equation (4th order Polynomial Fit)	R^2
Ni-TiC	0.10	$y = -3.00E{+}00x^4 + 6.05E{+}00x^3 - 3.31E{+}00x^2 + 3.45E{-}01x + 4.92E{-}01$	0.99
	0.15	$y = -1.72E{+}00x^4 + 3.51E{+}00x^3 - 1.83E{+}00x^2 + 8.45E{-}02x + 5.39E{-}01$	1.00
	0.20	$y = -1.06E{+}00x^4 + 1.96E{+}00x^3 - 7.75E{-}01x^2 - 9.63E{-}02x + 5.07E{-}01$	1.00
	0.25	$y = -4.25E{-}01x^4 + 8.91E{-}01x^3 - 3.37E{-}01x^2 - 1.28E{-}01x + 5.39E{-}01$	1.00
Ni-WC	0.13	$y = -1.54E{+}00x^4 + 3.78E{+}00x^3 - 2.50E{+}00x^2 + 2.57E{-}01x + 5.26E{-}01$	0.99
	0.18	$y = -1.16E{+}00x^4 + 2.74E{+}00x^3 - 1.63E{+}00x^2 + 2.76E{-}02x + 5.59E{-}01$	1.00
	0.20	$y = -1.52E{+}00x^4 + 3.36E{+}00x^3 - 2.00E{+}00x^2 + 1.48E{-}01x + 5.26E{-}01$	0.99
	0.27	$y = -2.72E{-}01x^4 + 8.10E{-}01x^3 - 4.13E{-}01x^2 - 1.67E{-}01x + 5.59E{-}01$	1.00

The void fraction and composition corresponding to the points of maximum particle packing ($\boldsymbol{\Theta}_{min}$, X_{min}) and maximum carbide content ($\boldsymbol{\Theta}_{max}$, X_{max}) obtained from the particle packing plots for each mixture of Ni-TiC (Fig 4.11) and Ni-WC (Fig. 4.12) powders are presented in Table 4.7. When observing the maximum particle packing achievable in Ni-WC mixtures, the evidence shows these mixtures reach between 55-60vol% solids loading when in their most densely packed state. In this state of maximum particle packing, the mixtures comprising of nearly 56–62% WC by volume.

For Ni-TiC mixtures, the maximum observed particle packing is between 52-59vol% for mixtures containing approximately 44-51 vol% TiC. According to the data, powder mixtures of Ni-WC and Ni-TiC both reach maximum packing density within a similar range of solids loading, noted to be between 52-60vol%. However, when particles in both powder systems reach their most densely packed state, Ni-WC mixtures are shown as containing roughly 10vol% more carbide than Ni-TiC mixtures. In order to take advantage of the wear resistance properties of hard carbide particles, the data in Table 4.7 lists the constraints in terms of mixture composition, for maximizing carbide content while meeting the set condition for maximum void fraction (Θ_{max}). The value of Θ_{max} is set to 0.50 for all mixtures, which can be expressed in equivalent terms as setting a minimum of 50vol% solids loading for all mixtures. The data in Table 4.7 reveals, Ni-WC particle mixtures can reach a maximum void fraction of 0.50 for mixtures containing upwards of nearly 90-95% of WC particles by volume. For Ni-TiC particle mixtures, the data shows that a maximum carbide content of 72-79vol% TiC particles is achievable in Ni-TiC particle mixtures based on the packing behaviour observed for binary mixtures.

Table 4.7. Critical Values of Particle Packing in Binary Mixtures of MMC Powders

Mixture	δ	**Maximizing Particle Packing**		**Maximizing Carbide Content**	
		Θ_{min}	X_{min} **(vol%)**	Θ_{max}	X_{max} **(vol%)**
Ni-WC	0.13	0.40	59.5	0.50	94.9
	0.18	0.43	58.2	0.50	90.0
	0.20	0.42	55.9	0.50	93.2
	0.27	0.45	62.5	0.50	94.8
Ni-TiC	0.10	0.40	47.1	0.50	76.5
	0.15	0.46	48.4	0.50	72.3
	0.20	0.44	44.1	0.50	78.7
	0.25	0.48	51.3	0.50	78.2

As discussed previously, one of the main goals of this work is to utilize the efficiency of traditional polymer 3D-printing by producing polymer filaments containing "functional fillers". For the benefit of enhancing part performance, coupled with the need for cost effective and simplistic methods of producing wear-resistant parts, there is a strong basis for optimization of carbide content in fillers. Therefore, all eight Ni-WC and Ni-TiC mixtures listed in Table 4.7, with compositions listed for maximizing carbide content (X_{max}) are selected to proceed with extrusion. An exception was made regarding the very high content of WC in compositions noted as X_{max} for Ni-WC mixtures in Table 4.7. Typically, WC-containing hard-metal fillers used in IM feedstocks, are composed of a maximum carbide content of about 92-94wt% WC or roughly 90vol% WC *(Chuankrerkkul, Messer & Davies, 2007) (Baojun, Xuanhui & Ying, 2002)*. Fully dense parts manufactured with this material composition are extremely difficult to produce and process. There is an additional concern regarding the processability of Ni-WC due to the high carbide content and density of Ni-WC powder mixtures causing wear-out of the extrusion equipment when operating at high speeds. Therefore, to manage the risks associated with processing mixtures with a high content of carbide-containing powders the WC content in Ni-WC mixtures is not to exceed 90vol%. All Ni-WC mixtures (δ = 0.14 to 0.27) to be used as fillers were adjusted to have a composition of Ni-90WC by volume for X_{max}, the void fractions of the mixtures at this composition were recalculated using the best fit equations in Table 4.6. A summary of the ten filler mixtures optimized for extrusion are listed in Table 4.8 for convenience. The compositions mean size ratios, experimental void fractions ($\boldsymbol{\Theta}_{exp}$), and the optimizing factor are included in the table. Additionally, for the purpose of comparison, two Ni-TiC mixtures in a state of maximum particle packing were selected for extrusion at compositions listed as X_{min} in Table 4.7. These two densely packed Ni-TiC mixtures are listed in Table 4.8 as Filler no. 5 and 6. The mixtures were selected randomly based on availability of materials.

Table 4.8. Mixture Data for Fillers Selected for Extrusion

Mixture no.	Composition (vol%)	δ	Θ_{exp}	PF	Optimizing Factor
F1	Ni+90WC	0.13	0.48	0.52	carbide content
F2	Ni+90WC	0.18	0.50	0.50	
F3	Ni+90WC	0.20	0.49	0.51	
F4	Ni+90WC	0.27	0.49	0.51	
F5	Ni+47TiC	0.10	0.40	0.60	particle packing
F6	Ni+51TiC	0.25	0.48	0.52	
F7	Ni+76TiC	0.10	0.50	0.50	carbide content
F8	Ni+72TiC	0.15	0.50	0.50	
F9	Ni+79TiC	0.20	0.50	0.50	
F10	Ni+78TiC	0.25	0.50	0.50	

4.4 Discussion of Maximum Void Depression and Deviation from Ideal Packing

The final characteristic of importance with respect to particle packing is the degree of maximum volumetric void depression, denoted as $\Delta\Theta_{max}$, occurring in binary particle mixtures. As discussed previously in Chapter 2, $\Delta\Theta_{max}$ is the difference between the ROM and experimental values for void fraction at the point of maximum packing in a binary mixture of particles. The $\Delta\Theta_{max}$ describes the deviation of the experimental results which represent non-ideal particle packing from the ideal results predicted using the ROM. Figure 4.13 shows that when δ is plotted against a log base 10 scale and the data from this work is fitted using a logarithmic trendline, a clear correlation between $\Delta\Theta_{max}$ and δ is seen. The blue circle-shaped markers in the figure correspond to the data collected for Ni-TiC mixtures, and Ni-WC mixture data is marked using orange triangles. Figure

4.13 shows the relationship between $\Delta\Theta_{max}$ and δ for all mixtures studied in this work (solid trendline), and includes the relationship found by Epstein & Young (dashed trendline) when investigating binary mixtures of glass spheres *(Epstein & Young, 1962)*. The correlations for maximum void depression and size ratio published by Epstein & Young, and from the results of this study are listed Table 4.9. The data from this work provides strong evidence to support that increasing δ beyond a value of 0.1, results in a decrease in the maximum void depression that can be achieved for that binary mixture, evident from the negative slope of the trendline. It is simply shown that particles of dissimilar size show a greater degree of void depression than those having similar sizes. As the two particles become more similar in size (i.e $\delta \rightarrow 1$) the degree of void depression achieved will decrease ($\Delta\Theta_{max} \rightarrow 0$) until a critical value of δ is reached. Void expansions begin to form in the binary mixture, when δ exceeds this critical value. The expansion effect is mainly due to the lack of small-sized particles needed for particle packing to fill the voids formed in interparticle regions of the binary particle structure. An example of this behavior has been previously seen in Figure 4.7 for a mixture of Ni-TiC where δ is 0.73. In this case, the value of $\Delta\Theta_{max}$ for Ni-TiC ($\delta = 0.73$) is negative to account for the void expansion effect. This effect is aptly noted in this mixture by the Ni-TiC datapoint shown in Fig.4.13, where $\Delta\Theta_{max}$ equals close to -0.02. Comparing between Ni-TiC and Ni-WC mixtures overall, Ni-TiC mixtures consistently show lower values of $\Delta\Theta_{max}$ than those reported for Ni-WC mixtures. This is a clear indication that mixtures of Ni-WC powders packed more efficiently than mixtures of Ni-TiC, despite sharing similar values for δ. Generally, the particle size and density do not affect the void fraction of particles, with the exception of very small or light particles *(Hoffman & Finkers. 1995).* Based on this, a valid comparison can be made between the results found in this work and those observed by Epstein and Young. Independent of dissimilarities that exist in size, shape, and densities of the investigated particles, the relationship observed by Epstein and Young is comparable to the findings in this investigation.

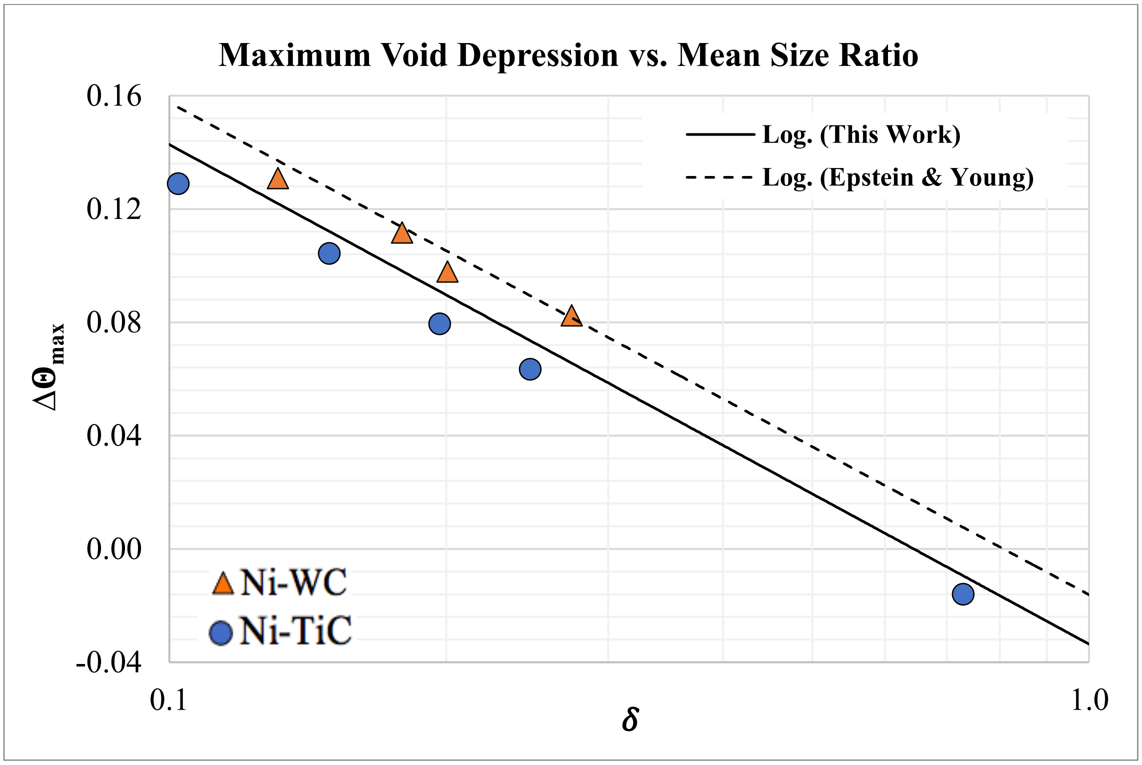

Figure 4.13 Effect of size ratio on maximum void depression in binary particle packings

In addition to the near-identical values of slope, listed in Table 4.9, the high residual value (0.93) reported for the correlation found in this work shows excellent fit of the data. As both TiC and WC particles used in this study are similar in overall size and shape, the superior packing demonstrated by Ni-WC mixtures, is likely a result of the bimodal size distribution of the WC particles used. Bimodal powder distributions have been shown to improve particle packing in several studies *(Bai et al, 2017) (Yu & Standish, 1993) (Averardi et al., 2020)*. Epstein and Young note that the coefficient for δ seen in the logarithmic expressions for $\Delta\boldsymbol{\Theta}_{max}$, as reported in Table 4.9, suggest the limiting conditions for particle packing where void depressions will occur.

Table 4.9 Relationships for Maximum Void Depression as a Function of Mean Size Ratio

Author	Relationship	R^2	Critical Condition
Epstein & Young	$\Delta\boldsymbol{\Theta}_{max} = -0.174\log_{10}(0.807\delta)$	0.992	void depression: $\delta < 0.807$
Bhardwaj et al. (This Work)	$\Delta\boldsymbol{\Theta}_{max} = -0.176\log_{10}(0.645\delta)$	0.931	void depression: $\delta < 0.645$

The authors conclude that for random dense packings of glass microspheres, the critical value for δ is about 0.81. When δ was below this value, void contractions were observed in the binary packings. Above this value, void contractions could not be relied on to occur and instead void expansions were noted *(Epstein & Young, 1962*). The correlation reported for the binary mixtures studied in the current thesis work, reveals the critical value of δ as being approximately 0.65. This finding can be confirmed based on the results seen in Section 4.2.3, for a Ni-TiC mixture where δ equals 0.73 and exceeds the newly discovered value for critical δ. Clear void expansions are reported for this mixture, with composition showing no effect on improving particle packing conditions, verifying the results of this study.

4.5 Chapter Summary

This chapter examines the particle packing behavior of non-ideal binary mixtures of Ni-TiC and Ni-WC powders, by measuring the void fractions in nine different powder blends of these mixtures. The main factors that influence particle packing are particle size and mixture composition. The effect of particle size is investigated based on the ratio of mean size ratio (δ). Binary mixtures are prepared with δ ranging from 0.10 to 0.27, at varying fractions of carbide in the mixture. The experimental results show that the linear ROM is not valid for binary mixtures comprised of particles having non-ideal characteristics, including non-spherical morphologies and continuous distributions of particle size. The packing behaviour of a binary mixture cannot be predicted based solely on the packing of the individual components of the mixture. The experimental results of this chapter are used to generate particle packing diagrams for Ni-TiC and Ni-WC mixtures, which show that a maximum packing of 52-60vol% is achievable in mixtures containing 40-60vol% carbide. Ten binary mixtures are selected as filler for filament extrusion. Fillers are optimized for wear resistance performance by maximizing carbide content in the mixture, while meeting the critical criteria of 50vol% particle packing required for sintering. Lastly, the maximum void depression ($\Delta\boldsymbol{\Theta}_{\mathrm{max}}$) shows a strong correlation to δ, and the critical value of δ is 0.65. Above this value, particle packing does not occur.

5. FILAMENT MANUFACTURING, GREEN-PART PRODUCTION, AND COMPOSITE CHARACTERIZATION

Chapter 5 builds on the fundamental findings related to particle packing in dry powder mixtures of Ni-TiC and Ni-WC filler, as presented in previous Chapter 4. Ten filler mixtures were selected based on optimizations relating to particle packing and material performance criteria. The void fractions in the dry fillers were determined and represent the maximum volume fraction of polymer that can be injected into the filler during filament extrusion. Section 5.1 details the entire process of filament extrusion. A characterization of filament properties, including density, filler content, size, and flowability are presented in Section 5.2. The following Section 5.3 describes the FFF process for fabricating green-body parts using each filament. The final section of Chapter 5 compares the filler void fractions in dry fillers to the polymer contents in the extruded filaments and printed green parts.

5.1 Filament Extrusion

The manufacturing process used for filament-making in this study is dual-screw extrusion. The extrusion process is effectively used for both homogenous mixing of the filler and polymer and forming the rod-like profile characteristic of a filament. Since the filaments are to be used as feed material for FFF, the design criteria for producing filaments depends mainly on the requirements of the FFF machine. Ideally, the produced filaments should meet the criteria listed in Table 5.1. The most common size of filaments used in traditional polymer FFF are 1.75mm in nominal diameter, with some filaments available 2.85mm or 3 mm sizes. From a manufacturing perspective it is easier to produce filaments of larger diameter compared to smaller diameters, mainly due to the combined effect of high friction and pressure forces required to push semi-molten viscous material through a small nozzle opening. However, print resolution is significantly compromised when using larger diameter filaments. In some cases, the printing of certain geometric features becomes nearly impossible. The FFF printer used in this work is designed for 1.75 mm filaments and therefore, the key requirement for filament-making is to produce filaments of this nominal size.

Table 5.1 Basic Requirements of Filament as FFF Feedstock

Criteria	Value
Average diameter	1.75 mm
Diameter tolerance	0.05 - 0.1 mm
Max extrusion temperature	400ºC
Max printing temperature	500ºC

Due to the nature of the manufacturing process, FFF filaments have an acceptable diameter tolerance between values of ± 0.05 – 0.1 mm. The diameter tolerance plays a very important role during the printing process, if the tolerance in diameter is too high, the flow of material during printing will be highly inconsistent resulting in various printing defects. If the diameter is too large, it may not fit into the nozzle opening, clog, or otherwise jam the extruder gear causing the filament to become shredded by the gear and unable to pass through. If filament is too thin, it may lack sufficient pressure required for the extruder gear to grip and steadily feed the filament into the nozzle. The filament must have a circular cross section, consistent with the shape of the extrusion nozzle opening. The filament must be strong enough to retain its shape during feeding into the liquefier section of the extruder head without buckling, but flexible enough to be coiled onto a spool. Overall, the filament must be homogenous in terms of size and shape, but also in terms of the distribution of fillers within the filament to ensure that the properties of the material are uniform across the entire length of filament, and ultimately the resultant printed and sintered part. It is most desirable that the filament be free of defects, contaminations or inconsistencies which may cause future issues. Most polymers used for FFF have a working temperature of about 180 - 280 ºC *(Riecker et al., 2016),* which is the temperature requirement for filament making based on the maximum operational temperatures of the extruder and printer apparatus listed in Table 5.1. The produced filaments must meet all design requirements in order to function as an acceptable feedstock material for the following FFF step of the manufacturing process.

5.1.1 High-Density Polyethylene (HDPE) Binder

A high-density polyethylene (HDPE) polymer was used as the binder component for the development of all composite filaments in this work. The polymer was in the form of a spooled filament commercially available for 3D-printing and was obtained from an online retailer (HDPE, 2020) located in Ontario, Canada. The HDPE was natural and colorless, with an average measured true density of 938 ± 3 kg/m^3. HDPE has a melting temperature between 128-135 ºC *(Mahajan, 2001)*, and an extrusion temperature of 175 ºC *(Hamod, 2014).* The HDPE filament was pelletized prior to use in extrusion.

5.1.2 Assumptions

The process of filament extrusion is used to compound the polymer and fillers together to form a composite filament suitable for FFF. The filler is a pre-blended powder mixture prepared according to the specifications listed in Table 4.8. During filler feeding, the powder mixture is loaded into the hopper of the auger, which features a single rotating screw. The screw rotates and pushes the filler forward and out of the auger opening, into the extruder below. During both, filler feeding when the powder is subject to the rotational forces of the screw and the vertical distance the filler particles must fall before reaching the opening of the extruder below, the mixture of particles in the filler irrevocably become rearranged. Due to the nature of the filler particles, specifically the large differences in size and density *(Liu, 2018),* it is very likely that some degree of particle segregation occurs within the dry filler prior to extrusion. Therefore, the composition of the pre-mixed filler entering the auger feeder, may not be consistent with the composition of filler that is introduced into the extruder. It was not possible to study the effect of varying filler introduction methods on properties of binary filler powder mixtures mainly due to the time and resource constraints of this work.

As discussed previously, the true density of a powder material is a measurement of the solid particle density only. Therefore, true density of a binary mixture at any given composition of the two components is a linear function, compared to the bulk density, which is not linear with composition. To confirm the linearity of true density with respect to mixture composition, Figure 5.1 shows the nominal true density measured for all mixtures of Ni-TiC and Ni-WC powders plotted against nominal % carbide in the mixture. The nominal composition is shown in 20% increments of increasing carbide by volume. The triangular markers in the figure represent the nominal values measured for Ni-WC mixtures, and circular markers show Ni-TiC values.

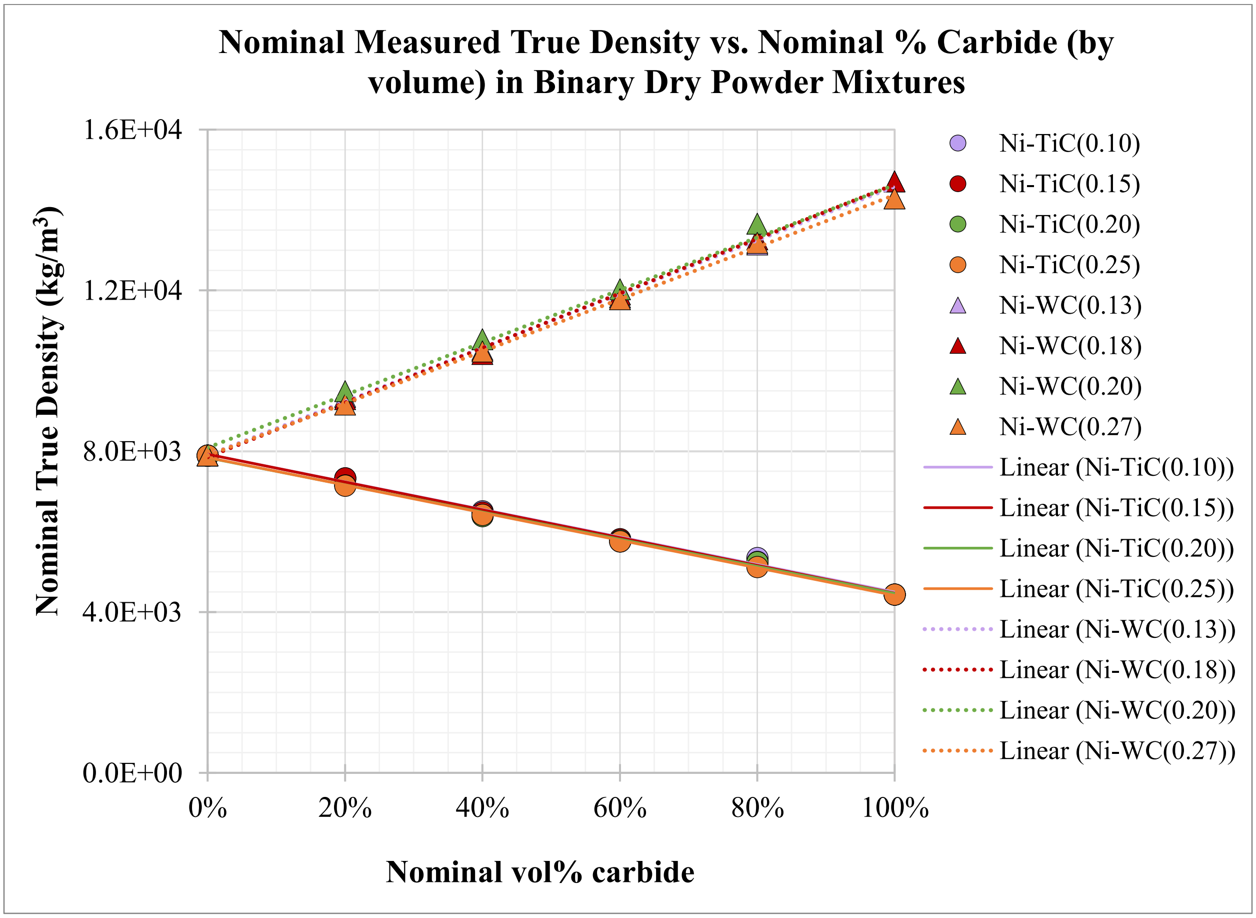

Figure 5.1 The linear relationship between true density and mixture composition

Each data point represents a nominal value, based on 3 measurements taken for density. The standard deviations for these measurements are applied in the form of error bars, however, they cannot be seen in Figure 5.1, as the error values are smaller in size than the markers used to represent the data itself. Linear trendlines are applied to each individual data set to show the linear correlation between nominal true density and mixture composition. Solid trendlines are used to show Ni-TiC correlations and dashed trendlines are applied to Ni-WC data. The near-identical and overlapping trendlines seen in Figure 5.1, show that true density is indeed a linear function of composition in all binary mixtures of MMC powders. Therefore, the true densities of a filler at the desired compositions formulated for extrusion can be confidently interpolated from Figure 5.1. The true density of a filler mixture is assumed to remain constant throughout the feeding and extrusion process. The full data set, including the standard deviations for each data point, and equations of best fit for the linear relationships seen in Figure 5.1 are in Appendix A.

5.1.3 Determining Filler Feed Rates for Extrusion

The desired filler contents of the filaments to be extruded are known and based on the values for packing fraction (PF) found for all fillers, previously in Chapter 4. The mass fraction of fillers (w_f) present in a composite material comprised of filler and polymer can be expressed using Equation 5.1. Here, the mass of filler (in kg) or filler feed rate (in kg/s) is represented by m_f. Similarly, m_p is used to denote the mass or feed rate of the polymer material in the composite. In manufacturing, however, it may be more appropriate to use a volume basis for calculations, therefore, the volume fraction of fillers (v_f) in a composite material is expressed by Equation 5.2. The true densities of the polymer (ρ_p) and filler (ρ_f) are measured in kg/m^3.

$$\mathrm{w_f} = \frac{\mathrm{m_f}}{\mathrm{m_p} + \mathrm{m_f}} \tag{5.1}$$

$$\mathrm{v_f} = \frac{\left(\frac{\mathrm{m_f}}{\rho_\mathrm{f}}\right)}{\left(\frac{\mathrm{m_p}}{\rho_\mathrm{p}}\right)+\left(\frac{\mathrm{m_f}}{\rho_\mathrm{f}}\right)} \tag{5.2}$$

Under perfect conditions of extrusion, the volume occupied by voids in dry loosely packed filler mixtures is occupied by polymer during melt extrusion. The result is the formation of a perfectly solid void-free composite material. Therefore, the filler feed rate ($\mathrm{m_f}$) required for extrusion of each filament is calculated by substituting the value of PF for $\mathrm{v_f}$ in Eqn. 5.2 and using the interpolated value of nominal filler true density (ρ_f) from Figure 5.1. The nominal true density of HDPE is known and measured to be 940 kg/m^3.

5.1.4 Calibration of Material Feed Rates

Material feed rate calibration was performed to find suitable parameters of feeding which resulted in material outputs most consistent with the required values for filler feed rate calculated in the previous section. The average material feed rates (kg/s) of HDPE and all fillers were determined, at varying screw speeds of each auger used for raw material feeding during extrusion. It is important to note, that HDPE was fed using the hopper attachment included as part of the EuroLab extruder system. Two difference sizes of feeders, referred to simply as “large feeder” and “small feeder”, were used to supply the filler powders. The larger feeder was intended to be used exclusively for filler feeding during extrusion of all filaments, however, due to an unrelated motor malfunction occurring during the strict time-period scheduled for extrusion, a smaller feeder was substituted for the remainder of the extrusions. Due to the difference in feeder size, filler feed rates were calibrated at lower speeds for the larger feeder and higher speeds for the smaller feeder. Generally, it is expected that for any given material, an increase in the speed of the feeding results in an increase in material output. The calibration curves for HDPE pellets and Ni-WC fillers are seen in Figures 5.2 and 5.3, respectively. Figure 5.4 shows the calibration of Ni-TiC filler feed rates using both small and large-sized feeders. The average feed rates are measured in kilograms per second of material entering the extruder. Linear trendlines are applied to the calibration curves and curve-fitting parameters are listed in Table 5.2. First, examining the calibration curve for HDPE in Fig 5.2, it appears that a linear relationship with a residual value of 1.0 (Table 5.2) exists for the rotational screw speed of the hopper feeder and the rate of HDPE pellet feeding. This is further evidence that the feeding of HDPE is very stable during extrusion. Next, assessing the feed rates of Ni-WC fillers in Figure 5.3, a similar linear behaviour is observed for the feeding of Ni-WC filler with respect to auger speed, as noted previously for HDPE.

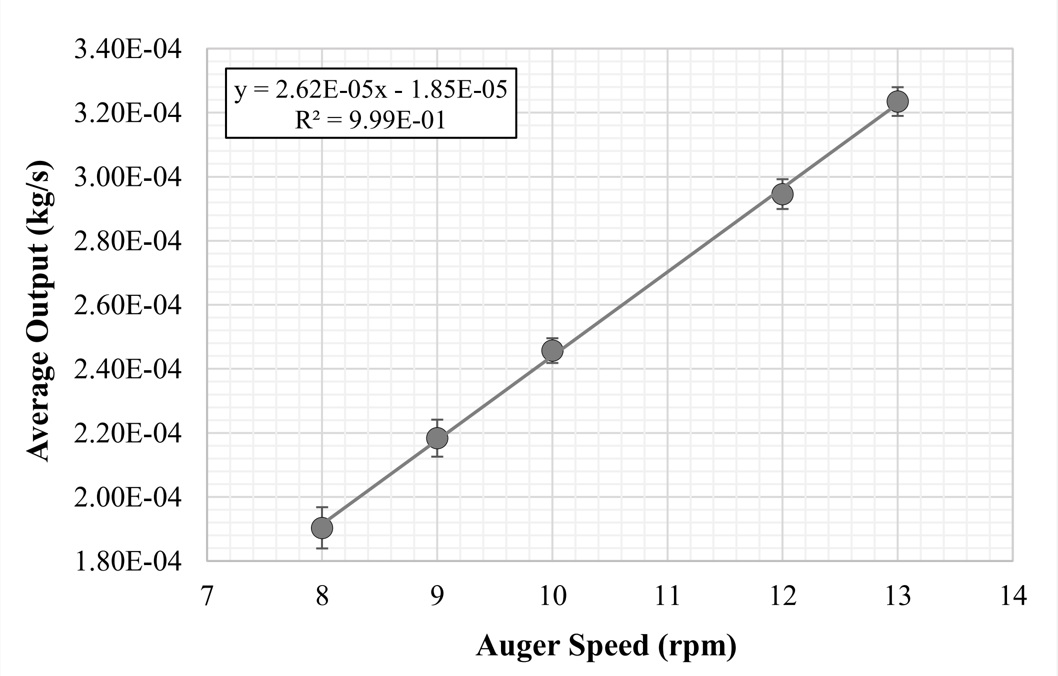

Figure 5.2 HDPE Feed Rate Calibration Curve

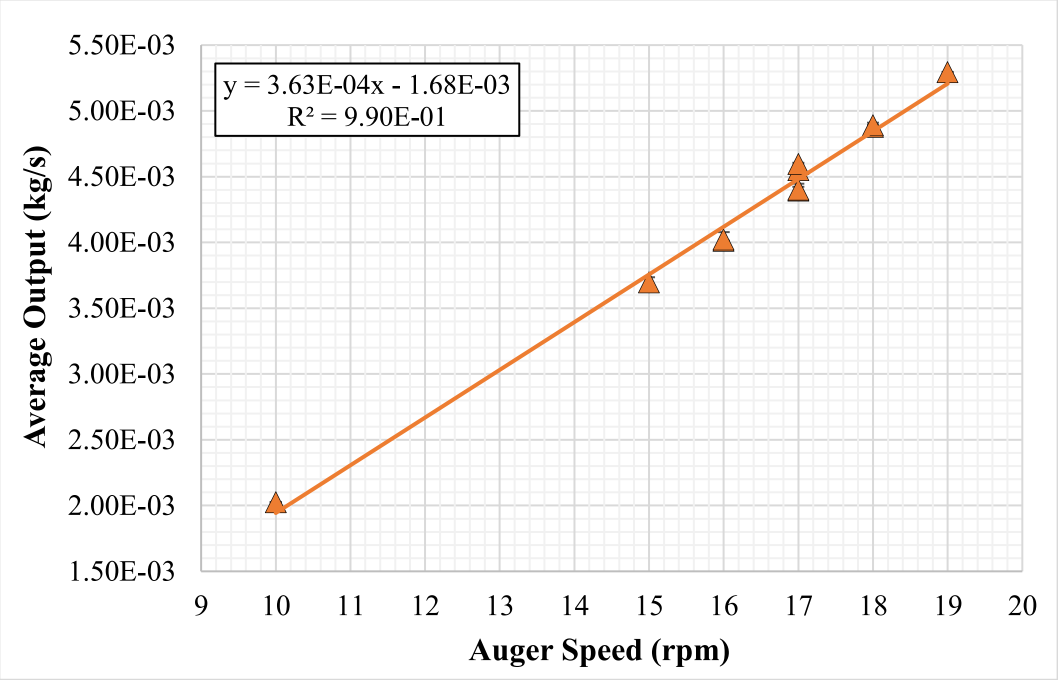

Figure 5.3 Feed Rate Calibration Curve for Ni-WC Fillers

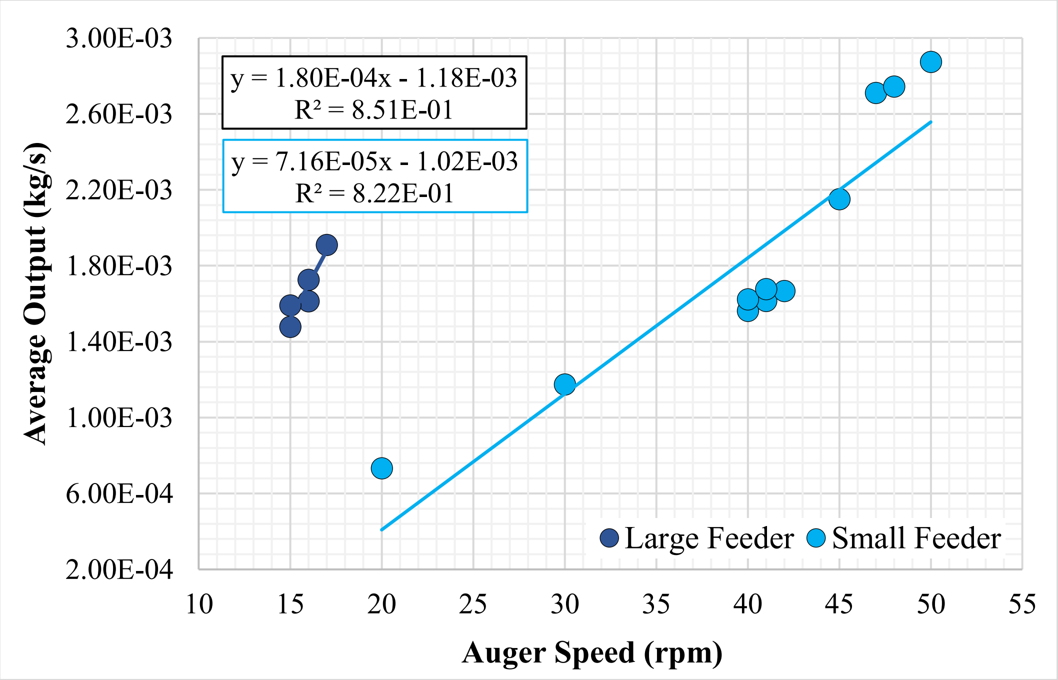

Figure 5.4 Feed Rate Calibration Curves of Ni-TiC Fillers Based on Feeder Size

However, unlike HDPE, the Ni-WC filler output ranges between about 2.0E-3 kg/s at a low auger speed of 10 rpm, to upwards of nearly 5.3E-3 kg/s when the screw speed of the larger auger is increased to a max. value of 19 rpm. The significant increase in feed rate is due to the high density of the WC powders present in this filler. The feed rates of Ni-TiC fillers calibrated using the same large-sized auger feeder (Fig 5.4 dark-blue series) are reported between 1.5E-3 and 1.9E-3 kg/s at auger speeds around 15 to 17 rpm. Whereas feed rates between 3.7E-3 and 4.5E-3 kg/s are reported for Ni-WC fillers within the same range of speeds. Comparing the residual values obtained from linear curve fitting of these two filler systems (Table 5.2), the Ni-WC fillers are revealed to have greater consistency during feeding than Ni-TiC fillers.

Table 5.2 Curve Fitting Parameters for Material Feed Rate Calibration

Material	Feeding System	Trendline (Linear Fit)	R^2
HDPE	Extruder Hopper	y = 2.62E-05x - 1.85E-05	1.0
Ni-WC	Large Auger Feeder	y = 3.63E-04x - 1.68E-03	0.99
Ni-TiC	Large Auger Feeder	y = 1.80E-04x - 1.18E-03	0.85
Ni-TiC	Small Auger Feeder	y = 7.16E-05x - 1.02E-03	0.82

The relationship between feed rate and screw speed for Ni-WC fillers is shown to follow a linear function ($R^2 = 0.99$), compared to Ni-TiC fillers ($R^2 = 0.85$). One explanation for the difference in feed rate consistency is the difference in densities of the two types of fillers. The compositions of all four Ni-WC fillers are constant. All mixtures contain 90vol% WC, therefore, the true densities are more or less the same. Thus, resulting in the near-perfect linear relationship between feed rate and screw speed. In comparison, the four Ni-TiC fillers vary in both composition and density, leading to a possible variation in flowability of the mixture. Another comparison is the calibrated feed rates of Ni-TiC fillers reported for small and large feeders. Figure 5.4 shows that the reported feed rates for a range of high screw speeds between 20-50 rpm are distinctively those generated by the smaller auger feeder. The calibration curve corresponding to the calibration curve for Ni-TiC obtained using the small feeder (Figure 5.4 light-blue series) does show an increase in feed rate with increasing auger speed. When a linear trendline is applied, the lowest overall value for the residual ($R^2 = 0.82$) is reported for the feed rate calibrated values obtained using the small feeder. However, when comparing to results obtained for Ni-TiC using the large feeder, a small difference of 0.03 in residual values is insignificant and negligible. Both sizes of auger feeders are sufficient for use during extrusion. The calibrated feed rate in g/min will subsequently be denoted as $f_{f,cal}$ in this work. In order to minimize the number of independent variables associated with filament extrusion and maintain controlled conditions for experimental testing, HDPE was fed at an average constant rate of 2.95E-04 kg/s using a speed of 12 rpm, for all filament extrusions.

Lastly, the calibrated filler feed rates used for extrusion were selected based on the closest match to the required feed rates calculated in the previous section. The feeder screw speed corresponding to the selected calibrated value of feed rate was a critical process parameter for extrusion. The feeding calibrations were critical in achieving the desired filament compositions, as the screw speed of the material feeders could only be adjusted along a scale of integer values. A summary of the filler true densities, calculated required filler feed rates, and calibrated filler feed rates values are listed in Table 5.3 below. The interpolated values of nominal filler true density and PF are used to calculate the required filler feed rates. Due to the above-mentioned limitations of the material feeding equipment, the actual feed rates used during extrusion were the calibrated values shown. The calibrated feeds in Table 5.3 represent the nominal measured rates of filler feeding, which are shown to differ from the calculated values. To evaluate the effect of adjusting the filler feed rates, from required to calibrated, on overall filler content in the composite, Eqn 5.2 is used to calculate the volume fraction of filler (v_f) in the composite extruded using the calibrated filler feed rate. Comparing the values for filler fraction of the desired composite, it is evident that in most cases, the difference in filler content between PF and v_f is minimal (~1 vol%), the largest difference calculated as 2vol% for F9. Therefore, the effect is negligible, and the calibrated values are acceptable for extrusion.

Table 5.3 Selected Filler Densities, Calculated and Calibrated Feed Rates for Extrusion

Filler no.	Nominal Filler Density, ρ_f (kg/m^3)	Filler Feed Rate (kg/s)		Volume Fraction of Filler	
		Required (calculated)	Calibrated (nominal)	PF_{dry} (required)	v_f (calibrated)
F1	13914	4.78E-03	4.55E-03	0.52	0.51
F2	13960	4.38E-03	4.40E-03	0.50	0.50
F3	13971	4.54E-03	4.60E-03	0.51	0.51
F4	13724	4.55E-03	4.40E-03	0.51	0.51
F5	6314	2.92E-03	2.71E-03	0.59	0.58
F6	6094	2.11E-03	2.15E-03	0.52	0.53
F7	5320	1.67E-03	1.68E-03	0.50	0.50
F8	5438	1.71E-03	1.60E-03	0.50	0.48
F9	5171	1.62E-03	1.62E-03	0.50	0.50
F10	5167	1.62E-03	1.61E-03	0.50	0.50

5.1.5 Parameters of Extrusion

A pilot-scale twin-screw extruder, located at InnoTech Alberta, Canada, was used to manufacture composite filaments (up to 300m in length) for FFF. Filaments were extruded using extrusion barrel temperatures of 170°C (hopper) to 180°C (zone 1) to 185°C (zones 2-4) to 180°C (die zone) through a 3 mm diameter nozzle. The rotational co-rotating screw speed of the extruder was 220 rpm for all filaments, with the exception of two filaments containing Ni-WC fillers. The extrusion speed was 210 rpm for filament containing Ni+90WC filler having δ equal to 0.18, and 230 rpm for Ni+90WC where δ is 0.13. The screw speed of the feeder used for extruding Ni-WC filaments, was kept constant at 17 rpm, although average filler feed rate varied based on slight difference in filler densities. Two different sized feeders were used for Ni-TiC filament extrusions, therefore feeder speed and average feed rates largely varied. A full table of the process parameters used for extrusion of each composite are listed in Appendix C.

5.2 Filament Characterization

The extruded composite filaments, composed of HDPE and various metal-ceramic filler powders, were characterized according to density, fraction of fillers, diameter, and flowability during printing.

5.2.1 Density

The density of a composite material can be predicted using the rule-of-mixtures, given by Equation 5.3. This density is considered as the theoretical density of a composite material (ρ_c), based on the assumptions that the material is free of voids, contaminants, and the distribution of constituents is perfectly homogenous.

$$\rho_c = v_f \rho_f + (1 - v_f)\rho_p \tag{5.3}$$

In this work, the theoretical density of a composite filament is equal to the density obtained by using the values of PF for volume fraction of filler (v_f) as shown in Eqn 5.3. The theoretical values are then compared with average values of measured filament density (ρ_m), obtained using a pycnometer. A visual comparison between the dry filler, theoretical composite, and measured filament densities is illustrated in Figure 5.5. The dark, grey-colored bars positioned left in each group of results, are the densities of the individual filler component in each filament. In all cases, the filler densities are much greater than the composite densities. This is expected due to the portion of composite composed of HDPE, which has a very low density relative to any metal or ceramic material. This is most apparent in the filler densities seen for F1-F4, due to the high density of WC in the filler mixture. It is important to reiterate that all Ni-WC mixtures were prepared based on identical compositions of 90vol% WC, resulting in near-identical values for filler density seen in Fig 5.5 for F1-F4.

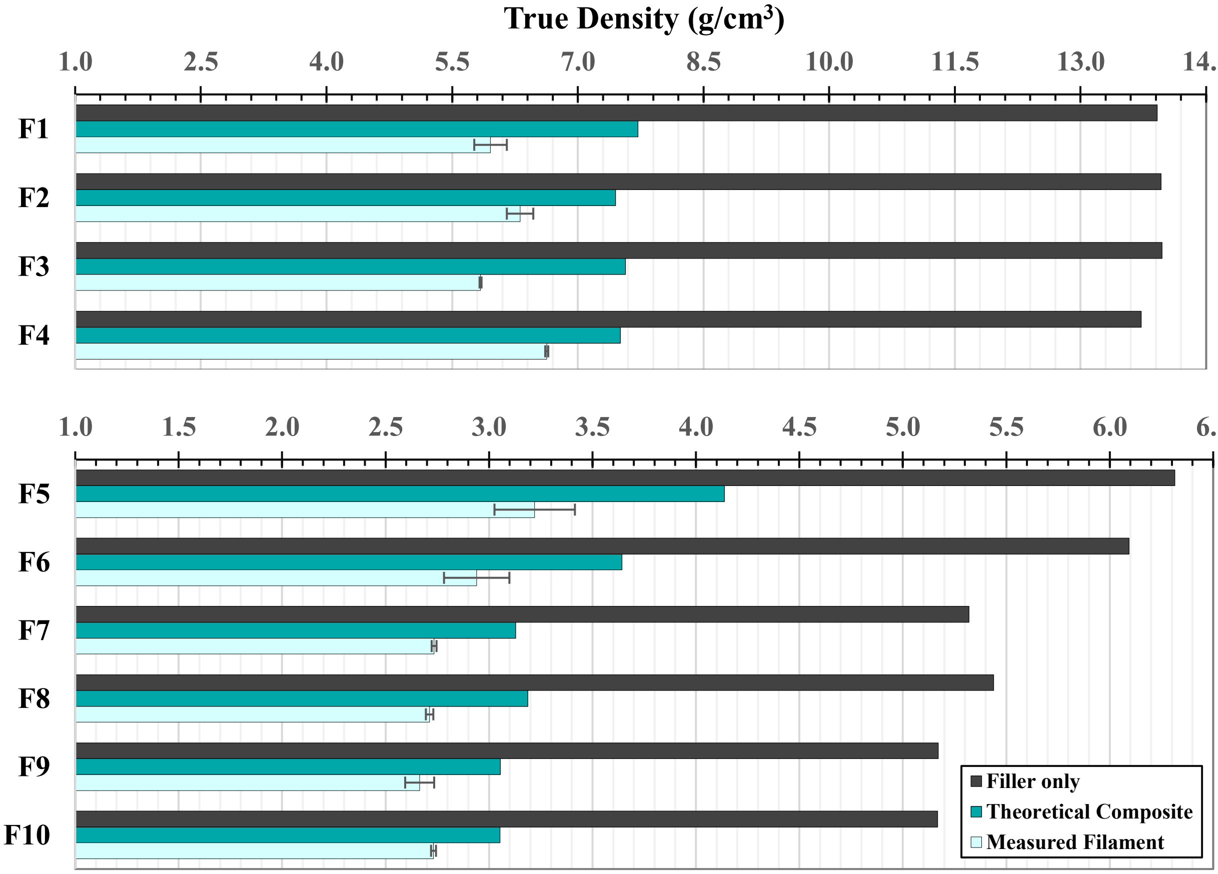

Figure 5.5 Densities of Fillers and Composite Filaments

Comparing the theoretical and measured composite densities in Figure 5.5, the measured values of density, shown as the light blue bars (positioned right), are much lower than the theoretical densities, dark teal bars (positioned center) obtained by applying the rule-of-mixtures (Eqn 5.3). The observed differences in theoretical and measured composite densities indicate a clear presence of voids existing within the extruded filaments, causing a decrease in the measured values of composite density. In addition to the possibility of void formation during extrusion, the lower values reported for measured density relative to theoretical density may simply be due to a lack of filler present in the filament. An SEM image of a cross section of F10 filament is shown in Figure 5.6, the internal surface of the filament is seen at a magnification of 502X and 1000X. The filler particles are clearly seen as the light-colored bodies embedded within a darker-colored polymer matrix. The figure reveals the presence of small micro-voids existing in regions surrounding individual filler particles (a), as well as interparticle areas between two in-contact particles (b). However, due to the soft nature of the polymer matrix, it is difficult to ascertain whether these micro-voids were formed during the process of extrusion or as a result of sectioning during sample preparation for SEM imaging, causing the particles to become dislodged from the matrix during sample preparation. In the occasion that the micro-voids seen in Figure 5.6 were formed during extrusion, it is most likely due to the inability of the molten HDPE to properly "wet" the surface of the filler particles and maintain adhesion at the interface. The lack of binder-polymer adhesion is a contributing factor for particle fall-out during processing as well as handling. The use of surfactants, such as, stearic acid, palm stearin, paraffin wax, and carnauba wax have been reported to improve wettability of metal and ceramic particles and decrease the overall viscosity of MIM feedstocks *(Matula, 2008) (Petiraksakul, 2000) (Edirisinghe, 1991).* No additives or processing aids were used in filaments developed in this work.

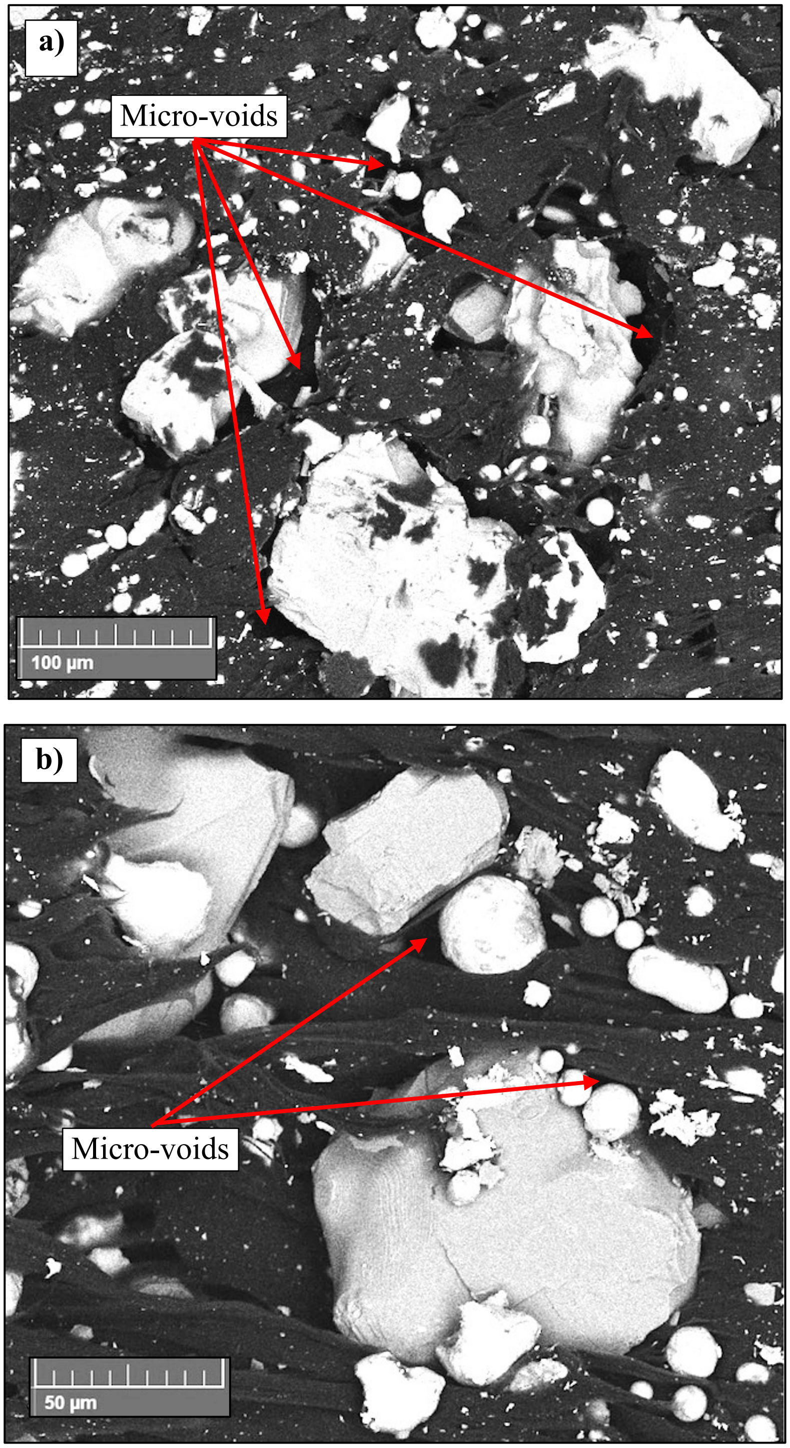

Figure 5.6 SEM Micrograph showing cross section of F10 filament at: a) 502X, and b)1000X

One reason is to establish a baseline of knowledge for the packing of filler mixtures in neat HDPE. Another reason is that, for each organic component added to the filament, special considerations must be taken to burn off each individual component during future debinding and sintering processes, adding another level of complexity to achieving a final fully dense sintered part. Aside from the fraction of volume occupied by filler particles in the filament, the remaining volume fraction consists of polymer and possibly small micro-voids. Based on the values for composite density seen in Figure 5.5, the fraction of volume which accounts for these micro-voids or additional polymer content from a lack of filler content in the filament, is found by calculating the percent difference between the measured and theoretical values of filament density in Equation 5.4 *(Bansal, 2017).*

$$\mathrm{v_E}(\%) = \frac{\rho_c - \rho_m}{\rho_c} \qquad (5.4)$$

For consistency, the volume fraction described above is written as a percentage and symbolized by $\mathrm{v_E}$. The subscript E is used to denote “excess polymer and voids”. The theoretical composite and measured filament densities of each filament are listed in Table 5.4, the measured values represent average values with standard deviations shown. The values corresponding to $\mathrm{v_E}$ are also in Table 5.4. The data listed in the table reveals that a difference upwards of 23vol% is noted for filament density. The greatest differences (23%) are reported in F1, F3, and F5.

Table 5.4 Calculated Void Fraction Data for Extruded Filaments

Filament	True Density (kg/m^3)		v_E (%)
	Theoretical (ρ_c)	Measured Filament (ρ_m)	
F1	7718	5958 ± 194	23
F2	7450	6310 ±158	15
F3	7567	5839 ±12	23
F4	7507	6629 ±18	12
F5	4138	3221 ±70	22
F6	3642	2940 ±12	19
F7	3129	2734 ±25	13
F8	3188	2713 ±26	15
F9	3054	2665 ±13	13
F10	3053	2732 ±11	11

5.2.2 Fraction of Filler

It is reasonable to consider that voids occupy a volume, but do not add mass to a composite. Therefore, it can be generalized that the sum of volume fractions corresponding to each component in a composite filament, including the filler, polymer, and voids, equals unity. The individual volume fractions of each component are, denoted using the subscripts f, p, and v, to represent the filler, polymer, and voids, as expressed in Equation 5.5.

$$v_f + v_p + v_v = 1 \tag{5.5}$$

Based on the analysis presented for composite density in the preceding section, v_E is used to factor in the volume fraction of additional polymer or voids in the composite filament based on differences between theoretical and measured filament density. Since the presence of micro-voids cannot fully be confirmed, an assumption is made for the composition of the extruded filaments that they are comprised of polymer and filler only. Thus, the v_E is accounted for in the term used to represent the total fraction of polymer, v_p, present in the filament. Based on this assumption, the rule-of-mixtures (Eqn 5.3) is applied to determine the fraction of fillers and HDPE in filaments. The results are illustrated by the stacked bar graph in Figure 5.7, where composition is shown as volume fraction.

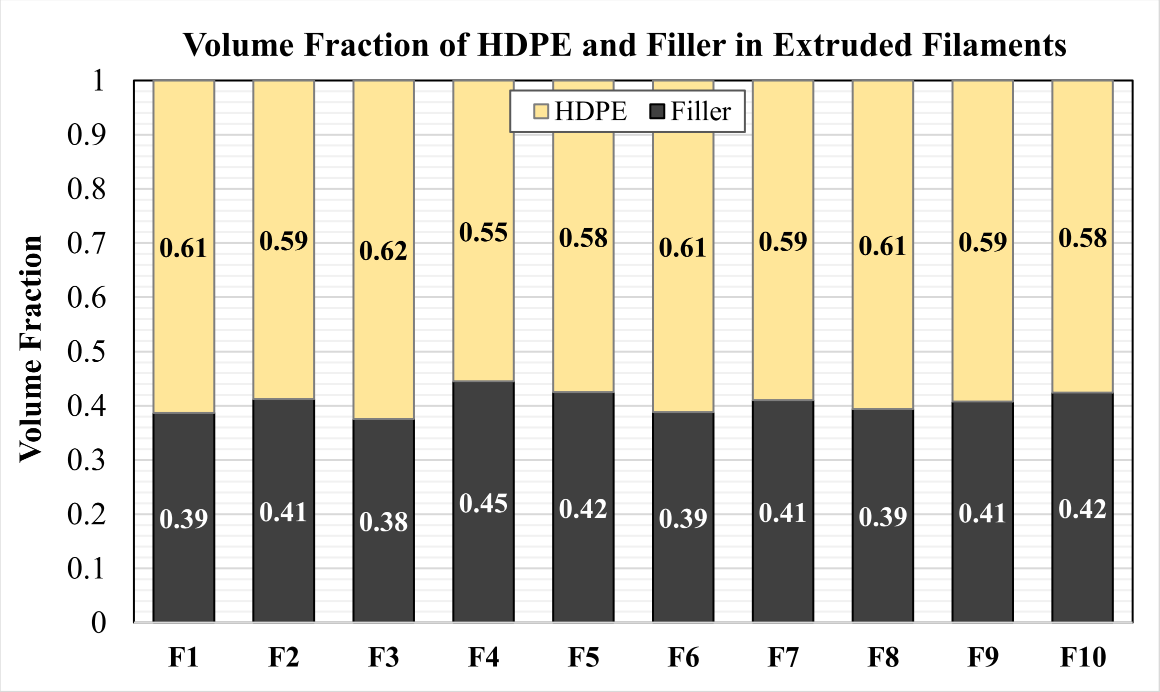

Figure 5.7 Fractional Compositions of Extruded Filaments

Figure 5.7 shows that the maximum filler fraction is 0.45 for F4. The maximum filler content of 0.42 is seen for Ni-TiC filaments, F5 and F10. In contrast, F1 and F3 are shown to contain the lowest fraction of filler, about 0.39. A similar value is noted for Ni-TiC filaments, F6 and F8. The most useful observation shown by Figure 5.7 is the limit of filler loading achievable using the filament-making methods demonstrated in this work, which is about 45vol%. An average filler content of about 41vol% is noted in both Ni-WC (F1-F4) and Ni-TiC filaments (F5-F10).

5.2.3 Diameter

Filament size and consistency in size are both crucial for smooth, uniform printing. Large deviations in filament diameter can cause extruder jams and contribute to irregular gaps in-between individual printed lines, resulting in parts having undesired characteristics such as poor surface finish, under or over-extruded infill *(Cardona et al., 2016)*. The filament diameter is mainly a function of the extruder screw speed and pulling speed during filament extrusion. In this study, the screw speed during extrusion was kept constant at 200 rpm for all filament production, with the exception of F1 and F2, where speeds of 230 rpm and 210 rpm were used, respectively. An average pulling speed of 65 m/s was typically used to pull composite filaments to the desired dimensional size. Figure 5.8 shows average diameters and standard deviations of each extruded filament. A horizontal dashed line marks the criteria set for desired nominal filament diameter (1.75 mm) in Fig 5.8, the light-shaded green area represents the range of acceptable filament sizes based on a max. deviation of 0.1 mm for filament diameter. The variation in diameter is shown using vertical error bars, marking the range of diameters for each extruded filament. The red-shaded region shows the range of diameters “too-large” in size to pass through the FFF extruder head, diameters “too-thin” in size are shown by the yellow-shaded region. In this case, small-sized filament fails to provide the pressure required between the filament and feeding gears, necessary to grip the filament for feeding into the heated nozzle. Figure 5.8 shows that overall, filaments containing Ni-WC fillers (F1-F4) on average were extruded with thinner filament sizes between (1.69-1.72 mm) compared to most Ni-TiC filaments (F5, F8, F9, F10) having diameters of about 1.74-1.77 mm.

Observing the sizes of F1 and F2, where extruder screw speed varied slightly from the speed used for producing all other filaments, there appears to be no impact on average size between the two. A difference in diameter variation, however, is noted. F1 shows remarkably high deviations of ± 0.2 mm in diameter using a relatively high screw speed (230 rpm), the reported size deviation is unacceptable for FFF.

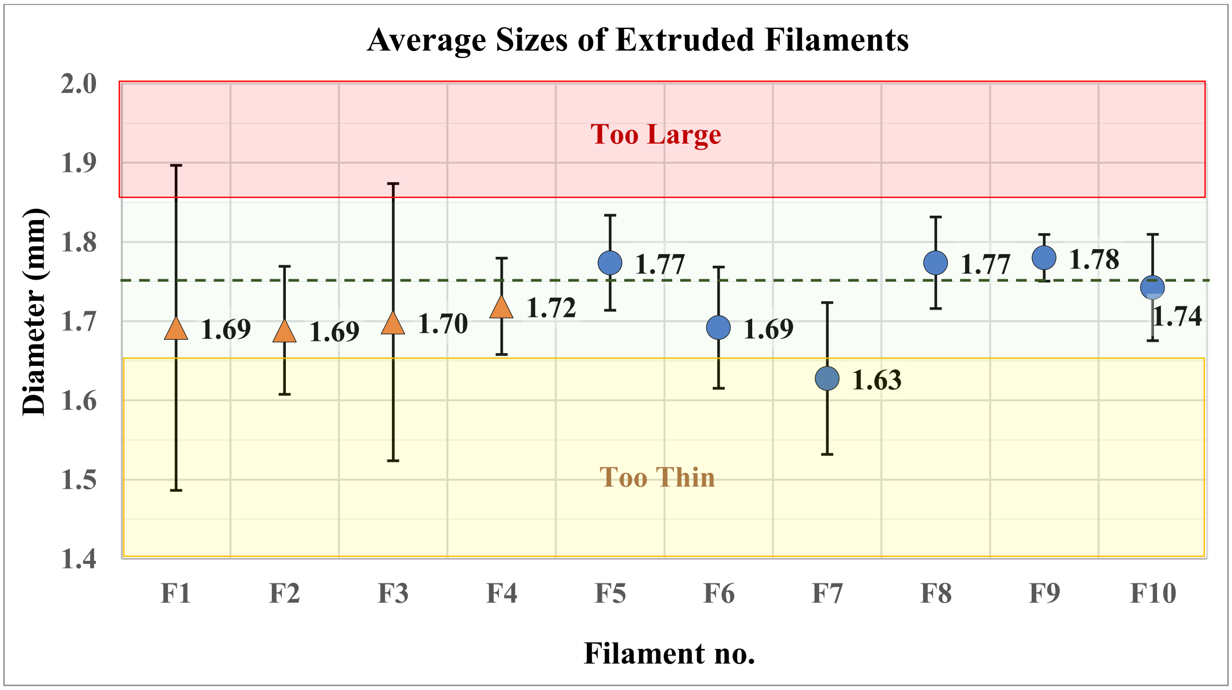

Figure 5.8 Average filament diameters of particle-filled HDPE filaments

F2, however, is within an acceptable level of variation (± 0.08 mm) as seen in commercial filaments. When comparing with other Ni-WC filaments, such as F3, the significant size variation reported in F1 is closely matched by F3 (± 0.18 mm). Based on near-identical properties of both filaments (i.e filler density, filler content, and carbide content), it seems that the high tolerance is a result of inter-particle friction during extrusion. F4 has an average diameter (1.72 mm) most consistent with 1.75 mm, it is the only filament containing Ni-WC filler, which safely occupies the shaded-green region in Fig 5.8, indicating that this filament meets the size requirements for printable filament. Examination of Ni-TiC containing filament diameters reveals that the smallest variation in filament size was 0.03 mm for F9. Four out of six Ni-TiC filaments meet the size requirements for printing. F5, F8, F9 were slightly larger in average diameter (1.77-1.78) than the target 1.75mm, F10 (1.74 mm) most closely measures the desired size, followed by F6 & F7 reporting the lowest diameters of 1.69 and 1.63 mm. The thin diameter sizes for F6 and F7, coupled with high size deviations show both filaments may have difficulties printing. Considering this, it is important to state that all filaments were in fact successfully 3D-printed to obtain 3D green-body composite parts of each filament. For filaments having high deviation in average size, segments of the filaments compatible in size for FFF, were sectioned and these smaller length portions were used for printing. During printing trials that the smallest and largest printable filament diameters compatible with the Machina 3D-Printer used in this study were 1.60 mm and 1.89 mm, respectively.

5.2.4 Flowability

The flowability of the extruded filaments was assessed based on material output from a 0.8mm nozzle, using a feed speed of 25mm/s, at varying nozzle temperatures between 190°C and 230°C. Filament flow is a function of the filament diameter and nozzle temperature during printing. The relative filament flow is a ratio of the nominal flow rates of filled-HDPE filament flowing out of the nozzle to the nominal flow rate measured for unfilled or neat HDPE material flowing from the nozzle at a given nozzle temperature. Figure 5.9 is a plot of the relative filament flow as a function of nozzle temperatures which show the flowability of each filament. The flow of unfilled HDPE between 190°C and 230°C is found to stay fairly constant, at a rate between 7.4 - 7.6 mm^3/s. Figure

5.9 shows that for the range of temperatures shown, the flow of all filaments increases with increasing temperature. For most filaments the increase in flow is approximately linear, although linear trendlines are not applied to the data, demonstrating that the flow of HDPE is the main factor in influencing overall composite flow.

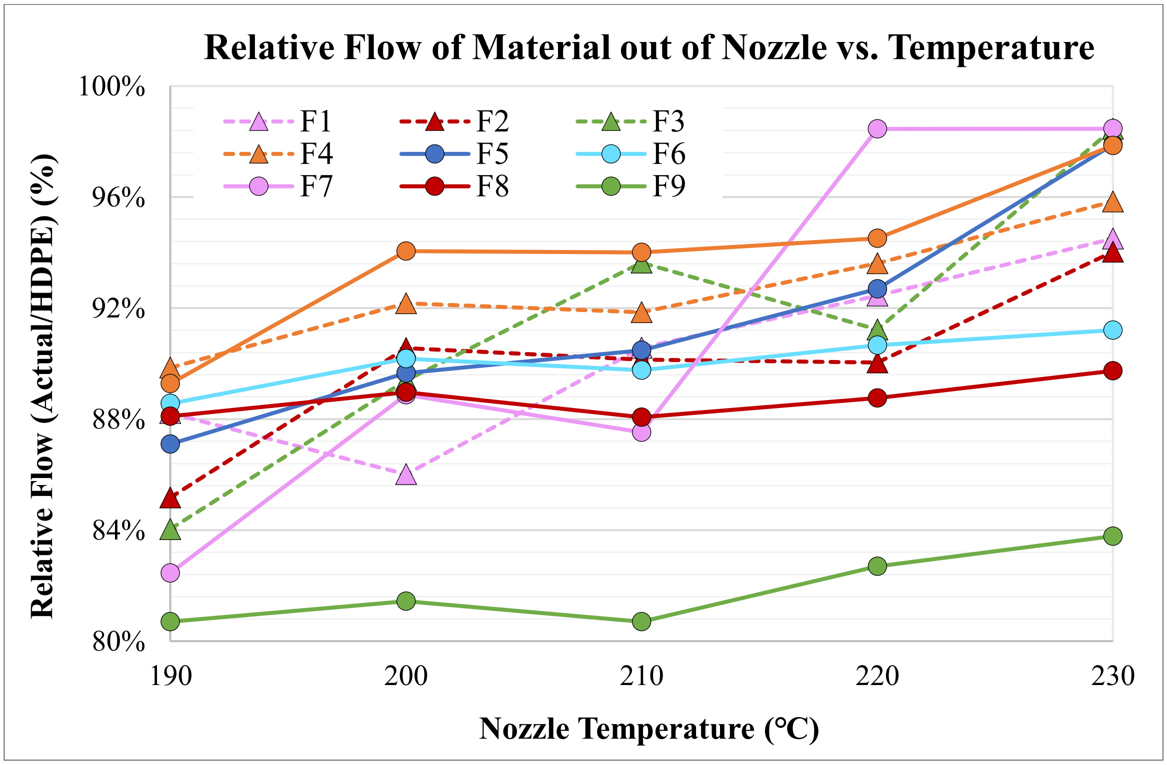

Figure 5.9 Relative flow of molten material extruded from nozzle as a function of nozzle temperature during 3D-printing

5.3 3D-Printing of Composite Filaments by FFF

The FFF process is crucial in obtaining high quality final sintered parts. The structure of the printed green-parts relies heavily on the bonding between deposited layers of material. Insufficient bonding leads to structural defects, such as gaps formed within the part during printing, which cannot be removed during the sintering process. The structure and homogeneity of the printed part is essential in achieving a quality sintered part capable of meeting the requirements of desired mechanical performance. Therefore, it is important to establish a set of optimal printing parameters for new materials, such as the composites developed in this work. The main printing process parameters include nozzle and bed temperatures, print speed, raster angle, layer height, infill density, and shell count. The layer thickness is the height of a single printed line. Another term for describing layer thickness is layer height. The raster angle is described as the angle formed between the nozzle path during printing relative to the x-axis, or simply, the direction of printing. The raster width is the width of a single printed line, theoretically the width is equivalent to the nozzle size. The shell is the wall printed along the outside perimeter of the print. Generally, the outside shell of the print is deposited first, then the infill is printed line-by-line, bonding the shell and infill. Air gaps or "layer gaps" are formed in regions between the shell and infill, or between adjacent printed lines. Any type of defect or porosity present in a part printed with 100% infill density (solid), results in a decrease in printed part density and introduces processing difficulties for future sintering practices.

Certain printing parameters can be adjusted to minimize or eliminate layer gaps, such as, increasing infill overlap % to fill the gaps occurring between the shell and infill. Likewise, a slight decrease in the distance between infill lines creates an overlapping in order to increase the adhesion between adjacent lines of deposited material. Printed overlap minimizes void formation, at the expense of surface quality of the part due to over-extrusion. The full FFF process, including the creation of a sample CAD profile, slicing and gcode generation, and final printing is shown in the schematic seen in Figure 5.10. To keep the printing process reasonable simple and user-friendly, several key printing parameters were kept constant throughout sample printing. These parameters include: 0.3 mm layer height, -45 º/45º raster angle, 100% infill density, 30% infill overlap, and 0.6 mm infill line distance. Based on these specifications, the slicing software (Ultimaker Cura 4.8.0) reveals the sample is comprised of 16 layers. Additionally, Cura generated toolpaths for the FFF printer in the form of a gcode, the raster angle orientation can be clearly seen in Fig 5.10 (2), where material deposition occurs at 45º to the x-axis, alternating with each layer. Typically, layer height values range between 0.1 and 0.4 mm *(Rahim et al., 2019)*. In this work, the main requirement for layer height is that it should be larger than the largest particle diameter, which is around 0.2mm.

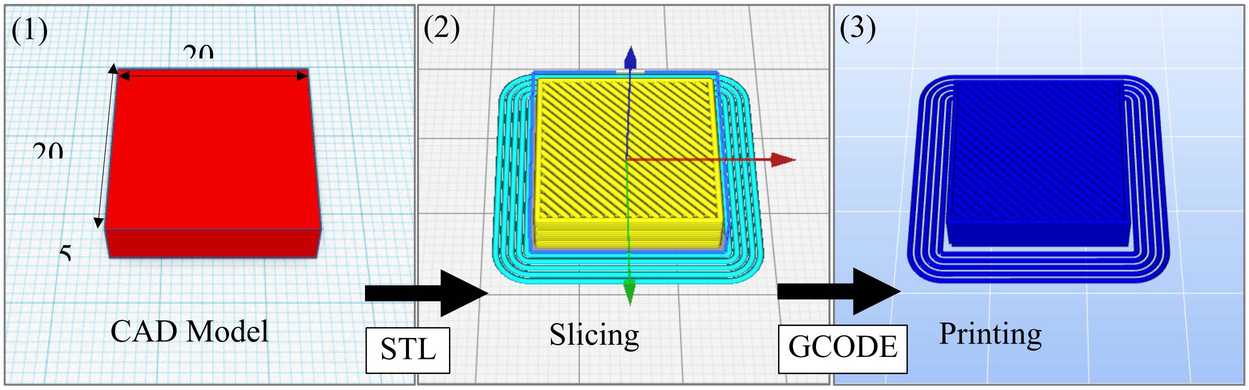

Figure 5.10 Step-by-step Sample Printing Process: (1) generation of a CAD model, (2) model slicing by Cura, and (3) part printing by Repetier

It is known that HDPE is a difficult material to print, due to its tendency for shrinkage during crystallization upon cooling *(Chong et al., 2017) (Schirmeister et al., 2019)*, therefore samples were printed using a decreased value of 0.6mm for infill line distance to offset any potential shrinkage during printing of the HDPE composite filaments. Additionally, both filament retraction and cooling fan were also off during printing to minimize the effect of thermal shrinkage during cooling. A square sheet (114 x 114 mm) of Buildtak 3D-printing surface was applied to the glass print bed to aid in adhesion during printing of the initial layer. The buildtak sheets provided sufficient adhesion of the printed material throughout the duration of the sample printing process, and final printed samples were easily peeled off when complete. After sample removal, the buildtak surface remained undamaged, therefore, the sheets were reused multiple times. All samples were printed with a 4.0 mm wide brim (Fig 5.10 c), to increase the surface area of the initial deposited layer and increase the adhesion to the build plate. A wear-resistant stainless steel 0.8 mm nozzle was used to protect against possible abrasion damage caused by passing of hard carbide particles in the molten filament during printing. Suitable printing parameters were selected based on a trial-and-error approach. Five samples of each filament are printed for repeatability. The complete g-code used for sample printing is available in Appendix D.

5.3.1 Optimal Printing Parameters

Filament flowability varied amongst the ten filaments mainly due to differences in density and diameter. As a result, the nozzle temperature (°C), print speed (mm/s), and material flow (%) parameters required optimization to effectively deposit the initial few layers of material. These parameters are adjusted manually using Repetier Host software during printing of layers 1-4. The remaining 12 layers are printed according to parameters specified for printing layer 4 of the sample. After the first 4 layers are deposited, all filaments are printed using a speed of 25mm/s and 125% flow, except for F1 and F3 which are printed at a slightly lower speed of 20 mm/s. Also, F3 requires a flow of 150% for printing beyond layer 3. The optimized printing parameters for all filaments are listed in Table 5.5, where the material flow and print speed gradually increase from layer 1 to 4. The initial layer is printed at a low speed (10 mm/s) to ensure that molten material flowing from the nozzle firmly attaches to the bed surface. Generally, it was more difficult to print the Ni-WC filaments (F1-F4), due to the brittle nature of the filaments. As the highest deviations in filament diameter were recorded in F1 and F3, these filaments were printed using lower initial layer print speeds (7 to 9 mm/s), with F3 requiring a 150% flow to successfully deposit material during printing of layer 4 and beyond.

Table 5.5 Table of Optimum Printing Parameters

Filament	Nozzle Temp. (°C)	Speed (mm/s)				Material Flow (%)			
		L1	L2	L3	L4	L1	L2	L3	L4
F1	220	7	20	20	20	81	100	120	125
F2		10	25	25	25	81	100	125	125
F3		9	20	20	20	81	100	125	150
F4		10	25	25	25	72	90	100	125
F5	190	10	25	25	25	72	90	110	125
F6	190							110	
F7	220							100	
F8	220							110	
F9	210							110	
F10	220							100	

All Ni-WC filaments were printed using a nozzle temperature of 220°C. The filaments containing Ni-TiC fillers (F5-F10) were easier to print, and mostly were printed using constant values for flow and print speed, with small variations required for flow % in layer 3 (Table 5.5). The optimal nozzle temperature, however, was lower for printing filaments F5 and F6, where a lower content of carbide particles is present in the filament. Since the carbide particles are larger in size compared to Ni, higher print temperatures are needed to increase polymer mobility in the composite filament and generate the necessary inertia required to move the solid particles and increase flowability.

5.3.2 Dimensional Accuracy and Printed Part Quality

Visual inspection and dimensional accuracy of FFF printed parts determine the part quality. A sample printed using F10 filament is shown in Figure 5.11. A top view of the sample reveals the surface roughness of the printed part, including the individual printed lines of material which are clearly visible in Fig 5.11 (left).

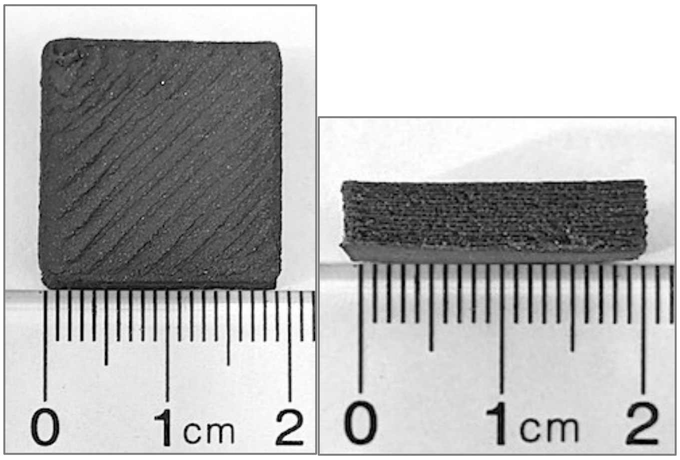

Figure 5.11 Top View (left) and Side view (right) of Final Printed Sample

The absence of any visible porosity between adjacent printed lines, is noted. The individual layers that form the 3D build part are discernable in the side view profile of the printed sample, appearing neatly stacked without any severe overhangs present. However, one difference between the CAD profile and final printed part is the rounded corners of the fabricated part. To assess the dimensional accuracy, the nominal dimensions (length, width, and height) of the printed parts were measured and compared to the dimensions defined in the CAD design. The percent error in dimensions of the printed samples is described using Equation 5.6, where ϕ_O is the CAD dimension and ϕ_{AP} is the nominal value for the printed dimension. The difference in length, width, and height of all printed parts is shown in Figure 5.12. It was found that, on average printed samples had at most, a 2% difference in length (x) and width (y) compared to the dimensions outlined in the CAD.

$$\text{Dimensional Error (\%)} = \frac{|\phi_O - \phi_{AP}|}{\phi_O} \tag{5.6}$$

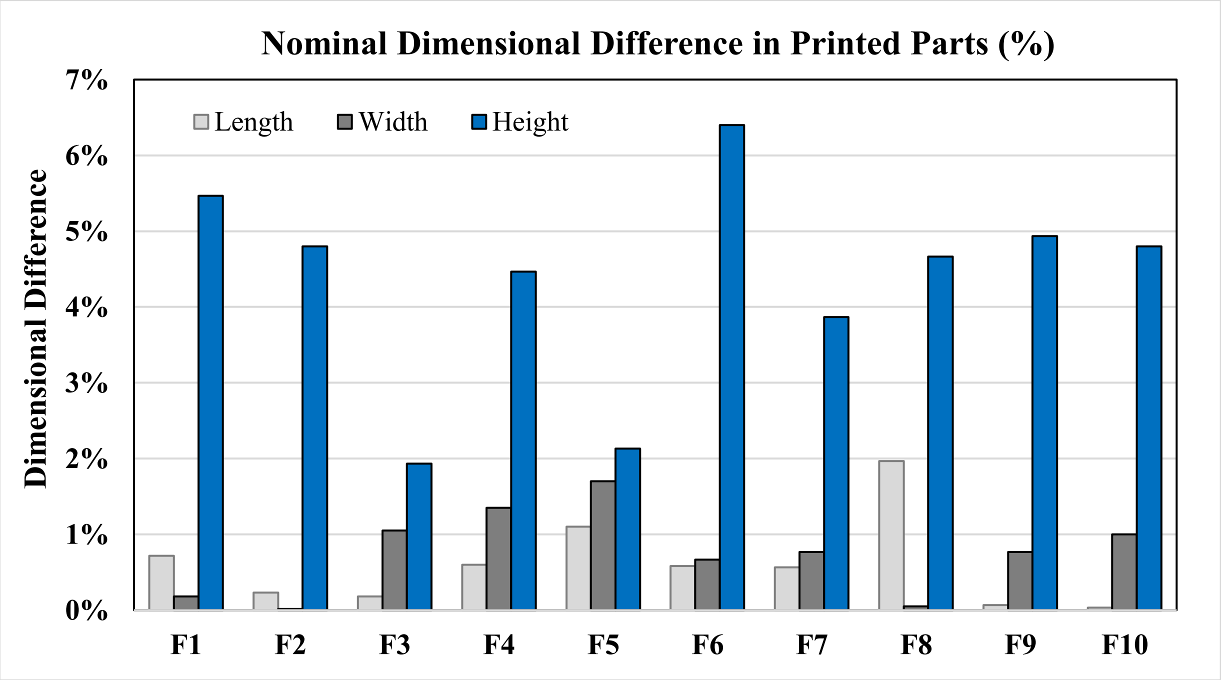

Figure 5.12 Nominal difference between CAD design and printed sample geometry

A maximum difference of 6% was observed in height (z). In other words, the percent error in dimensions of printed parts is negligible in terms of length and width, whereas the height (or thickness) of the part was always below the desired value of 5 mm. Comparing to a maximum value of 2% reported for dimensional tolerances of MIM parts (Table 1.1), the FFF printed tolerances reported for length and width in this work meet this criterion. A full data table of sample dimensional data, including mean and standard deviation values for length, width, and height, of all printed materials can be found in Appendix E.

5.3.3 Green Density of Printed Parts

To evaluate the consistency of the full FFFC process, it is essential that a comparison between the properties of the fillers, filaments, and final printed parts is done. First, a comparison between the properties of the filament and printed parts can be made based on the average densities of the composite materials. It is expected that the nominal true density of the filament is equal to that of the printed part, as both are comprised of the same material. However, the printed density may be influenced by the presence of air gaps forming between deposited layers of printed material. A comparison between nominal values of filament density and printed part density is seen in the parity plots in Figure 5.13. The diagonal line of reference drawn in the plots represent the values where filament and printed nominal densities are equal ($y = x$). A positive deviation from the reference line indicates a greater printed density, whereas a negative deviation suggests a greater filament density. It is clear that the printed part densities are very similar to the filament densities, shown by the clusters of data points for Ni-WC (F1-F4) and Ni-TiC (F1-F10) in close proximity to the reference line. All filaments reported average printed densities having standard deviations within values reported for average filament density. A full table of measured filament and printed densities is available in Appendix E. Based on the values recorded for average printed density, the volume fraction of polymer in the printed parts can be found using ROM Eqn 5.3.

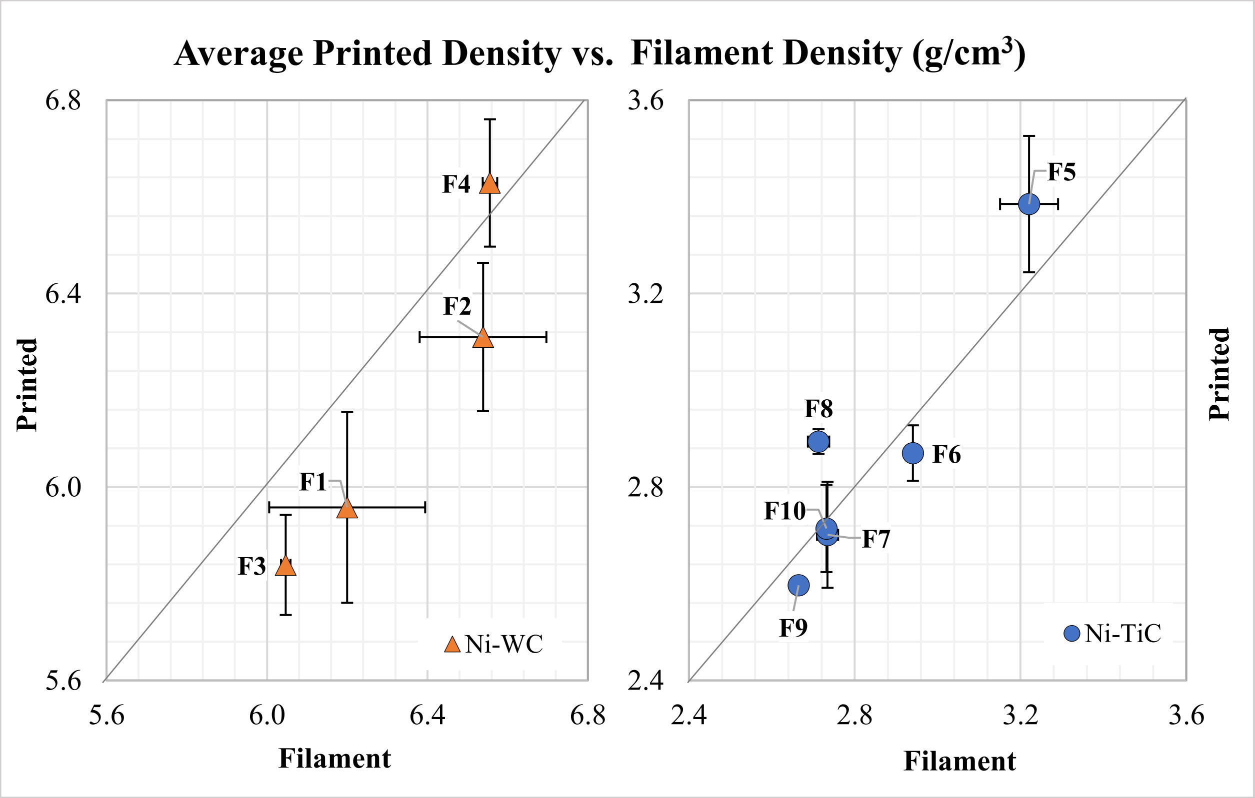

Figure 5.13 Average Printed Part Density versus Extruded Filament Density

5.4 Discussion of Results

To compare the overall results of this study, the differences between the experimental values of void fraction in dry fillers, polymer fraction in extruded filaments, and polymer fraction in printed parts, must be compared to the ideal ROM void fractions in the dry filler mixtures. The ideal ROM void fractions represent the maximum fraction of polymer that can be mixed into the filler to form the composite filaments and printed parts. The fraction of polymer in both composites is presented in this chapter based on the average measured values for density.

Beginning with the dry fillers, the deviation from the ideal ROM observed for dry powder filler mixtures ($\Delta\Theta_{dry}$) is based on the difference between the values of experimental void fraction (Θ_{dry}) and ROM void fraction (Θ_{ROM}), shown in Equation 5.7.

$$\Delta\Theta_{dry} = \Theta_{exp} - \Theta_{ROM} \tag{5.7}$$

Similarly, the difference between the ROM void fraction at a composition equal to the filament composition, and the actual fraction of polymer in the filament prepared according to the same composition ($\Delta\Theta_{polymer}$), shows the deviation of the experimental results obtained in Chapter 5, from the ideal ROM, expressed in Equation 5.8. The same difference can be noted between the ROM void fraction and the polymer content in the printed parts and calculated using Equation 5.9. The significance of these comparisons shows how the ideal particle packing predicted for a dry filler mixture, representing the maximum possible fraction of volume available for polymer injection, compares to the actual results found by combining polymer with dry filler to occupy the volume of voids. The equations to show the non-ideal particle packing in composites, is based on the difference in polymer content in the filament and printed parts as expressed using Equations 5.8 and 5.9, respectively.

$$\Delta\Theta_{polymer} = \Theta_{filament} - \Theta_{ROM} \tag{5.8}$$

$$\Delta\Theta_{polymer} = \Theta_{printed} - \Theta_{ROM} \tag{5.9}$$

Figure 5.14 shows the deviation from ideality of dry packings of binary powder mixtures based on the values calculated for $\Delta\mathbf{\Theta}_{dry}$ (grey data markers) and the values of $\Delta\mathbf{\Theta}_{polymer}$ for filaments (orange markers) are plotted as a function of mean size ratio (δ), along a log-scale axis. The data points differentiate Ni-WC and Ni-TiC mixtures using triangle and circle marker shapes, respectively. It has been discussed in the previous chapter, that the maximum void depression ($\Delta\mathbf{\Theta}_{max}$) observed in dry binary packings is a strong function of the mean size ratio (δ).

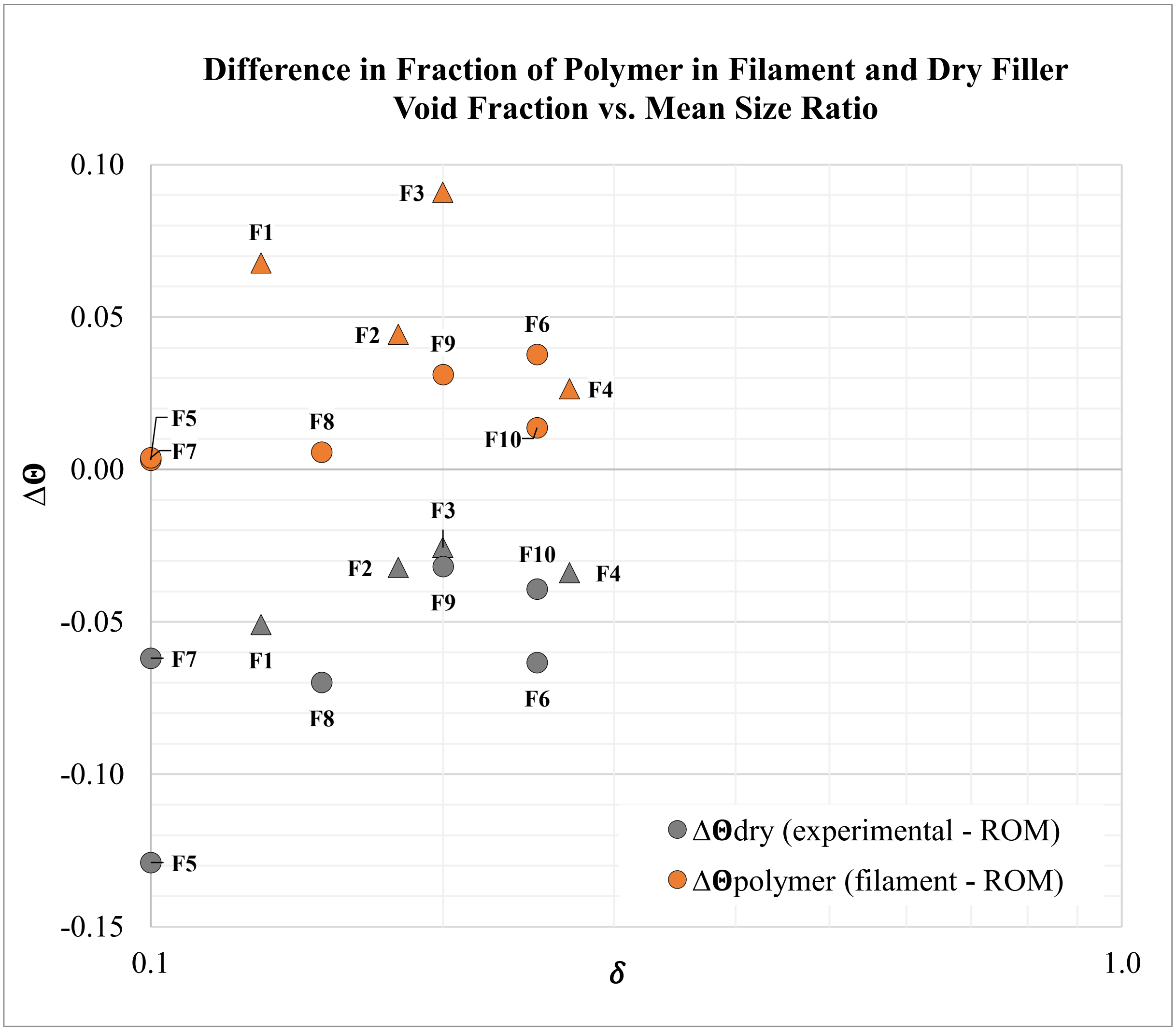

Figure 5.14 Differences in Dry Filler Void Fraction and Polymer Content in Filament

The greater the difference in mean particle sizes of the two constituents forming the binary mixture, the greater the potential for void depression. Figure 5.14 shows that in the case of dry filler, a negative deviation from ideality (ROM) is observed for all mixtures F1-F10. This negative deviation is a result of increased packing observed in the experimental data, versus the ROM approximation. Generally, the data shows that increasing size ratio ($\delta \rightarrow 1$) causes a decrease in the magnitude of deviation from the ROM, for both Ni-WC and Ni-TiC dry fillers. As for the case after polymer is mixed into the dry filler, Fig 5.14 shows that for Ni-WC filaments (F1-F4), the greater the packing in the dry filler (or larger the deviation from the ROM), the greater the polymer content in the filaments post-extrusion. One exception is for F3, which reports the highest $\Delta\boldsymbol{\Theta}_{\text{polymer}}$ (+0.91), despite having the lowest $\Delta\boldsymbol{\Theta}_{\text{dry}}$. For Ni-TiC filaments (F5-F10), a similar trend observed in dry filler mixtures, of decreasing size ratio (δ) with increasing $\Delta\boldsymbol{\Theta}_{\text{polymer}}$, is seen. F5 and F7, which show high deviations from ROM in a dry state, report the lowest deviations in respective filaments. Similarly, Figure 5.15 shows the differences in volume fractions of polymer in the printed parts compared to the ROM. The data for printed $\Delta\boldsymbol{\Theta}_{\text{polymer}}$ shows that for Ni-WC parts, there is little to no change between filaments and printed parts behaviour. For printed Ni-TiC parts, an overall increase in $\Delta\boldsymbol{\Theta}_{\text{polymer}}$ is reported compared to the corresponding values previously seen for filaments, except for F5 which remains relatively unchanged. Again, a high degree of particle packing in dry metal-ceramic powder mixtures, yields high polymer contents in extruded composite filaments. The average difference between the values of $\Delta\boldsymbol{\Theta}_{\text{polymer}}$ and $\Delta\boldsymbol{\Theta}_{\text{dry}}$ for filaments is 0.09 ± 0.03 and is 0.10 ± 0.03 for printed parts. The near-identical values provide evidence to show that, overall, the difference in particle packing between filament and printed parts is negligible. The differences seen between the ideal ROM void fractions and the polymer contents in the composites manufactured in this work, show that the ideal fraction of volume calculated using the ROM cannot be used to accurately predict the polymer contents of composites containing metal-ceramic fillers. During manufacturing, the packing structures of the dry filler powders become rearranged and the volume fractions of the fillers in a dry random-loose state, are not representative of the volume occupied by polymer in the composite.

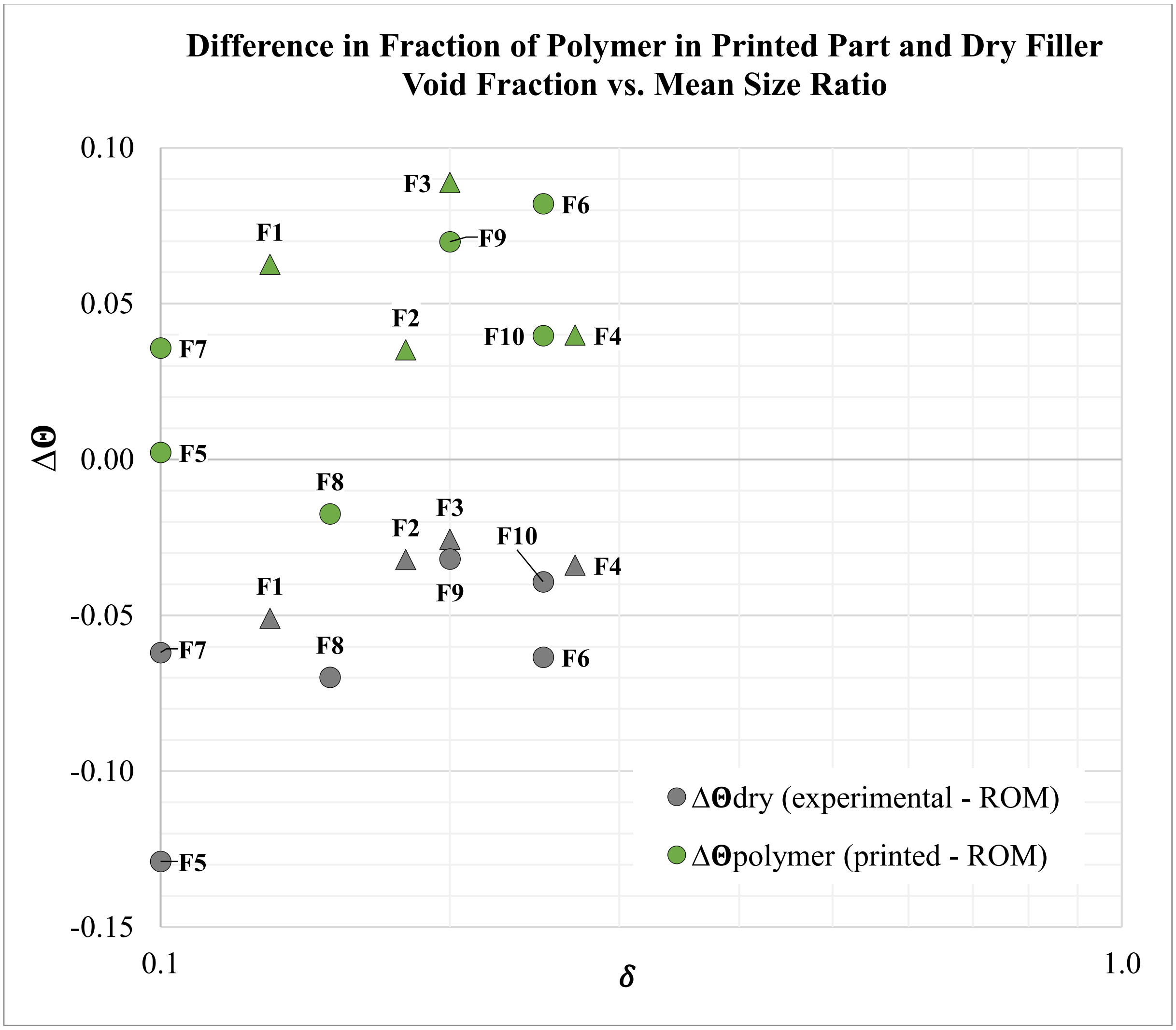

Figure 5.15 Differences in Dry Filler Void Fraction and Polymer Content in Printed Parts

6. CONCLUSION AND FUTURE WORK

This thesis presents a framework for the development of Ni-TiC and Ni-WC green-parts using the FFFC process and a characterization of the resultant composite materials. The non-ideal particle packing of binary powder mixtures is investigated to determine the maximum content of filler that can be mixed with polymer to form sinterable composite filaments for FFF. Based on this analysis, composite filaments are prepared and printed. A comparison between the particle packing in dry fillers is compared to the packing in the composite materials. The results of this thesis work provide base knowledge for designing sinterable composite filaments for FFF, to provide an economical AM method for producing wear-resistant metal-ceramic parts.

6.1 Conclusion

The optimization of particle filler systems for mixing with polymer binder to form sinterable composite feedstock, is based on the random-loose particle packing of binary mixtures. The results of this work conclude:

- Particle packing of Ni-TiC and Ni-WC binary powder mixtures is non-ideal and deviates negatively from the linear rule-of-mixtures packing theory.
- Particle packing diagrams for Ni-TiC and Ni-WC particles illustrate the packing behavior of these mixtures and allow for optimization based on maximization of carbide content and particle packing fraction.
- Mean size ratio (δ) has been found to have a strong effect on the maximum void depression ($\Delta\mathbf{\Theta}_{max}$) in powder mixtures. The relationship is found to be: $\Delta\mathbf{\Theta}_{max} = -0.176\log_{10}(0.645\delta)$

- Composite filaments and printed parts contain lower filler contents and higher polymer contents, compared to the experimental void fractions in dry binary mixtures.

6.2 Future Work

In the future, the results of this thesis work may be expanded on further by development of sintering cycles to complete the final step of the proposed FFFC process and achieve fully dense metal-ceramic parts. Building on the composite characterization provided for filaments and printed green parts in this work, the properties of the sintered body can be explored and compared to the properties of similar parts developed via MIM. Further research on metal-ceramic 3D printing could provide advantages in cost effectiveness and efficiency in the manufacturing industry.

References

(Alsop, 2020) Alsop, Thomas. (2020) Most used 3D printing technologies in 2020, Available online: https://www.statista.com/statistics/560304/worldwide-survey-3d-printing-top-technologies/, Accessed: November 2020

(Amin et al., 2014) Amin SY, Muhamad N, Jamaludin KR, Fayyaz A and Yunn HS. 2014 Jan 1 Characterization of the feedstock properties of metal injection-molded WC-Co with palm stearin binder system Sains Malaysiana 43 123-8

(Antonov et al., 2017) Antonov, M., Yung, D.L., Goljandin, D., Mikli, V., Hussainova, I., Effect of erodent particle impact energy on wear of cemented carbides, 2017

(ASTM B215-15, 2015) ASTM Standard B215-15, *Sampling Metal Powders,* American Society for Testing and Materials International, 2015.

(Averardi et al., 2020) Averardi, A., Cola, C., Zeltmann, S. E., & Gupta, N. (2020). Effect of particle size distribution on the packing of powder beds: A critical discussion relevant to additive manufacturing. *Materials Today Communications*, *24*, 100964. https://doi.org/10.1016/j.mtcomm.2020.100964

(Ayeni, 2018) Ayeni, O.1., Sintering and characterization of 3D printed Bronze Metal Filament, Masters Thesis, Purdue University, 2018.

(Bansal, 2017) Bansal, G. (2017) Determination and Reduction of Casting Cavity Befalling in CFF Filled Epoxy Based Hybrid Biocomposites. SF J Mat Res Let 1:2.

(Baojun et. at., 2002) Baojun, Z., Xuanhui, Q., & Ying, T. (2002). Powder injection molding of WC–8%Co tungsten cemented carbide. *International Journal of Refractory Metals and Hard Materials*, *20*(5–6), 389–394. https://doi.org/10.1016/S0263-4368(02)00015-X

(Beddoes and Bibby, 1999) Beddoes, J., Bibby, M. J. (1999). *Principles of metal manufacturing processes.* London: Arnol

(Bigg, 1987) Bigg, D. M. (1987). Mechanical properties of particulate filled polymers. *Polymer Composites*, *8*(2), 115–122. https://doi.org/10.1002/pc.750080208

(Brown et al., 1950) Brown, C. G., et al., Unit Operations, *Wiley*, 1950
(Canadian Oil Sands, 2013) Canadian Oil Sands. (2013, 12 09). Canadian Oil Sand. Retrieved 12 10, 2014, from Canadian Oil Sands Website: http://www.cdnoilsands.com/Media-

(Burkhardt et al., 2016) Burkhardt, C., Freigassner, P., Weber, O., Imgrund, P., Hampel, S: (2016) *FFF of 316L Green Parts for the MIM Process,* European Congress and Exhibition on Powder Metallurgy. European PM Conference Proceedings; Shrewsbury.

(Campbell et al., 2011) Campbell, T., Williams, C., Ivanova, O., and Garrett, B., (2011) Could 3D Printing Change the World? Technologies, Potential, and Implications of Additive Manufacturing.

(Cardona et al., 2016) Cardona, C., Curdes, A. H., & Isaacs, A. J. (2016). Effects of Filament Diameter Tolerances in Fused Filament Fabrication. *IU Journal of Undergraduate Research*, *2*(1), 44–47. https://doi.org/10.14434/iujur.v2i1.20917

(Chong et al., 2017) Chong, S., Pan, G.-T., Khalid, M., Yang, T. C.-K., Hung, S.-T., & Huang, C.-M. (2017). Physical Characterization and Pre-assessment of Recycled High-Density Polyethylene as 3D Printing Material. *Journal of Polymers and the Environment*, *25*(2), 136–145. https://doi.org/10.1007/s10924-016-0793-4

(Chuankrerkkul, Messer & Davies, 2007) Chuankrerkkul, N., Messer, P. F., & Davies, H. A. (2007). Powder Injection Moulding of Cemented Carbides: Feedstock Preparation and Injection Moulding. 5.

(Colorfabb, 2019) Available online: https://colorfabb.com/filaments/specials-filaments, Accessed: May, 2019

(Crump, 1989) Crump, Scott. S. (1989) Apparatus and method for creating three-dimensional objects. *U.S. Patent No. 5,121,329,* Minnetonka, MN: U.S Patent and Trademark Office

(Dave, 1995) Dave, V. R. (1995). Electron Beam (EB) Assisted Materils Fabrication. Massachusetts Institute of Technology.

(Deckard, 1986) Deckard, Carl. R. (1986) Method and apparatus for producing parts by selective sintering. *U.S. Patent No. 4,863,538,* Austin, TX: U.S Patent and Trademark Office

(Dias et al., 2004) Dias, R. P., Teixeira, J. A., Mota, M. G., & Yelshin, A. I. (2004). Particulate Binary Mixtures: Dependence of Packing Porosity on Particle Size Ratio. Industrial & Engineering Chemistry Research, 43(24), 7912–7919. https://doi.org/10.1021/ie040048b

(Duffy, 2020) Duffy, J. (2020, April 08). Characterizing metal powders for Additive Manufacturing. Retrieved December 13, 2020, from https://www.materials-talks.com/blog/2018/11/28/analytical-tools-for-characterizing-metal-powders-for-additive-manufacturing/

(Duncan, 2016) Duncan, S., Evaluation of Rock Particle Media Shape Contribution to Abrasive Wear, Thesis, 2016

(Eastwood et al.,1969) Eastwood, J., Matzen, E. J. P., Young, M. J., Epstein, N., Random loose porosity of packed beds, *British Chemical Engineering*. 14(11), 1542-1545, 1969

(Edirisinghe, 1991) Edirisinghe, M. J. (1991). The effect of processing additives on the properties of a ceramic-polymer formulation. *Ceramics International*, *17*(2), 89–96. https://doi.org/10.1016/0272-8842(91)90037-Z

(Epstein & Young, 1962) Epstein, N., Young, M., Random Loose Packing of Binary Mixtures of Spheres. *Nature* 196, 885–886 (1962). https://doi.org/10.1038/196885a0

(Filaments, 2019) Available online: https://filaments.ca/collections/1-75mm-3d-filaments/metal, Accessed: February 2019

(Formfutura, 2019) Available online: https://www.formfutura.com/shop/category/composite-materials-metalfiltm-174, Accessed: May 2019

(Geissbauer et al, 2017) Geissbauer, R., Wunderlin, R., Lehr, J. (2017) The future of spare parts is 3D: A look at the challenges and opportunities of 3D printing

(German, 2005) German, R. M (2005). Powder Metallurgy and Particulate Materials Processing: The Processes, Materials, Products, Properties and Applications. Princeton, NJ: Metal Powder Industries Federation, ISBN: 9780976205715, pp. 130

(German & Bose, 1997) German, R. M., & Bose, A. (1997). *Injection molding of metals and ceramics*. Princeton, NJ: Metal Powder Industries Federation.

(German, 2013) German, R. (2013). Progress in Titanium Metal Powder Injection Molding. *Materials*, *6*(8), 3641–3662. https://doi.org/10.3390/ma6083641

(Hamod, 2014) Hamod, H. (2014) Sustainability of recycled HDPE for 3D printing filament (Unpublished master's thesis) Arcada University of Applied Science

(Haughey & Beveridge, 1969) Haughey, D.P. and Beveridge, G.S.G. (1969), Structural properties of packed beds — A review. Can. J. Chem. Eng., 47: 130-140.

(HDPE, 2020) HDPE Filament - Natural - 1.75mm. Retrieved June 8, 2020, from https://filaments.ca/products/hdpe-filament-natural-1-75mm

(Hoffman & Finkers. 1995) A.C. Hoffmann, H.J. Finkers, A relation for the void fraction of randomly packed particle beds, Powder Technology, Volume 82, Issue 2, 1995, Pages 197-203, ISSN 0032-5910, https://doi.org/10.1016/0032-5910(94)02910-G.

(Hull, 1984) Hull, Charles, V. (1984) Apparatus for production of three-dimensional objects by stereolithography. *U.S. Patent No. 4,575,330,* Arcadia, CA: U.S Patent and Trademark Office

(Ifam, 2010) Ifam, F. (2010) The MIM process, Bremen, Germany

(Kitzmantel et al., 2018) Kitzmantel, M., Lengauer, W., Duretek I., Schwarz V., Kukla C., Lieberwirth, C., Morrison, V., Wilfinger, T., Neubauer, E., (2018). *Potential of Extrusion Based 3D-printed Hardmetal and Cermet Parts*. 9.

(Kukla et al., 2016) Kukla, C., Duretek, I., Schuschnigg, S., Gonzalez-Gutierrez, J., Holzer, C: (2016) *Properties for PIM Feedstocks Used in FFF,* Proc. WorldPM

(Laser Diffraction, 2021) *Particle Measurement Laser Diffraction*, Sympatec GmbH. Retrieved August 1, 2021, from https://www.sympatec.com/en/particle-measurement/sensors/laser-diffraction/

(Lengauer et al., 2019). Walter Lengauer, Ivica Duretek, Markus Fürst, Viktoria Schwarz, Joamin Gonzalez-Gutierrez, Stephan Schuschnigg, Christian Kukla, Michael Kitzmantel, Erich Neubauer, Clemens Lieberwirth, Vincent Morrison, *Fabrication and properties of extrusion-based 3D-printed hardmetal and cermet components*,International Journal of Refractory Metals and Hard Materials, Vol 82, 2019, Pages 141-149,

(Lieberwirth et al., 2017) Clemens Lieberwirth, Arne Harder, & Hermann Seitz. (2017). Extrusion Based Additive Manufacturing of Metal Parts. *Journal of Mechanics Engineering and Automation*, *7*(2). https://doi.org/10.17265/2159-5275/2017.02.004

(Liu et al, 2011) B. Liu, R. Wildman, C. Tuck, I. Ashcroft, R. Hague, Investigation the Effect of Particle Size Distribution on Processing Parameters Optimisation in Selective Laser Melting Process, Sff. (2011) 227–238. doi:10.1017/CBO9781107415324.004.

(Liu, 2018) Liu, G. (2018) Understanding and minimizing powder segregation. *Powder and Bulk Engineering*, Retrieved from powderbulk.com

(Machina Corp, 2016) Machina Corp, "Machina Mk2 X20 3D Printer by MACHINA Corp 3D Printers and Services | MACHINA Corp 3D Printers and Services", MACHINA Corp 3D Printers and Services, 2016. [Online]. Available: https://store.machinacorp.ca/collections/machina- corp-desktop-3d-printers. [Accessed: 25-Feb-2018]

(Mahajan, 2001) Mahajan, S. (2001) Polyethylene: high-density. In Encyclopedia of Materials: Science and Technology. Elsevier, pp. 7172-7181

(Matula, 2008) Matula, G. (2008). Influence of binder composition on structure and properties of carbide alloyed composite manufactured with the PIM method. *Journal of Achievements in Materials and Manufacturing Engineering*, *30*(2), 4.

(Matula et al, 2008) Matula, G., Dobrzański, L. A., Várez, A., & Levenfeld, B. (2008). Development of a feedstock formulation based on PP for MIM of carbides reinforced M2. *Journal of Achievements in Materials and Manufacturing Engineering*, *27*(2), 4.

(Mastersizer, 2020) Mastersizer 3000 User Manual, 1st ed Malvern Instruments Ltd., Worcestershire, United Kingdom, Nov.2015, pp. 15-24, Accessed on: February 22, 2020. [Online]. Available: https://www.malvernpanalytical.com/en/support/product-support/mastersizer-range/mastersizer-3000

(McGeary, 1961) McGeary, R. K. (1961). Mechanical Packing of Spherical Particles. Journal of the American Ceramic Society, 44(10), 513–522. https://doi.org/10.1111/j.1151-2916.1961.tb13716.x

(McKee and Wu, 1997) McKee, B., & Wu, J. (1997, July). An Overview of Wear Resistant Alloys for the Mining Industry. CIM Bulletin, 71-74.

(Metzner, 1985) Metzner, A. B. (1985). Rheology of Suspensions in Polymeric Liquids. Journal of Rheology, 29(6), 739–775. https://doi.org/10.1122/1.549808

(Mohan et al, 2017) N. Mohan, P. Senthil, S. Vinodh & N. Jayanth (2017) A review on composite materials and process parameters optimization for the fused deposition modelling process, Virtual and Physical Prototyping, 12:1, 47-59

(Montero et al, 2019) Montero, Joaquin & Atzberger, Alexander & Bleckmann, M & Holtmannspoetter, Jens & Paetzold, Kristin. (2019). Enhancing the Additive Manufacturing process for spare parts by applying Agile Hardware Development principles.

(MPIF Standard 04, 1992) MPIF Standard 04, *Standard Test Methods for Metal Powders and Powder Metallurgy Products,* Metal Powder Industries Federation, New Jersey, USA.

(MPIF, 2020) Metal Powder Industries Federation (MPIF)*, Metal Injection Molding Process*, Available online:https://www.mpif.org/IntrotoPM/Processes/MetalInjectionMolding.aspx Accessed: June 2020

(Oerlikon Metco, 2016) Oerlikon Metco, Material Product Datasheet: Cast Tungsten carbide/Nickel chromium boron silicon powders for plasma transfer arc (PTA), 2016

(Oerlikon Metco, 2020) Material Certification for METCO 43VF-NS Powder, Oerlikon Metco, 2020

(Onagoruwa et. al., 2001) Onagoruwa, S., Bose, S., & Bandyopadhyay, A. (2001). Fused Deposition of Ceramics (FDC) and Composites. 9.

(Petiraksakul, 2000) Petiraksakul, P., (2000). *Effect of Stearate/ stearic acid coating on filled high density polyethylene properties*, Doctoral Thesis, Institute of Polymer Technology and Materials Engineering, Loughborough University, UK. https://hdl.handle.net/2134/11166

(Powder Metallurgy Review, 2020) *The basic Powder Metallurgy process for structural press and sintered components,* Powder Metallurgy Review, Accessed: Jan 2020, Available online:

https://www.pm-review.com/introduction-to-powder-metallurgy/the-powder-metallurgy-process/

(Protopasta, 2019) Avaliable online: https://www.proto-pasta.com/collections/metal-composite-htpla, Accessed: February, 2019

(Qu et al., 2005) Qu, X., Gao, J., Qin, M., & Lei, C. (2005). Application of a wax-based binder in PIM of WC–TiC–Co cemented carbides. *International Journal of Refractory Metals and Hard Materials*, *23*(4–6), 273–277. https://doi.org/10.1016/j.ijrmhm.2005.04.006

(Rahim et al., 2019) Rahim, T. N. A. T., Abdullah, A. M., & Md Akil, H. (2019). Recent Developments in Fused Deposition Modeling-Based 3D Printing of Polymers and Their Composites. *Polymer Reviews*, *59*(4), 589–624. https://doi.org/10.1080/15583724.2019.1597883

(Riecker et al., 2016) Riecker,S., Clouse, J., Studnitzky, T., Andersen, O., Kieback, B., Fused Deposition Modeling-Opportunities for cheap metal AM. In Proceedings of the World PM2016 Congress & Exhibition, Hamburg, Germany, 9–13 October 2016

(Rodea, 2012) Rodea, J.A., Advanced Ceramic Structural Engineering, Thesis, 2012

(Rothon, 2003) Rothon, R., *Particulate-filled polymer composites*. Shrewsbury, UK: Rapra Technology, 2003.

(Schirmeister et al., 2019) Schirmeister, C. G., Hees, T., Licht, E. H., & Mülhaupt, R. (2019). 3D printing of high density polyethylene by fused filament fabrication. *Additive Manufacturing*, *28*, 152–159. https://doi.org/10.1016/j.addma.2019.05.003

(Spool3D, 2019) Avaliable online: https://spool3d.ca/filament/metalfill/, Accessed: February 2019

(Tan et al., 2017) Tan, J. H., Wong, W. L. E., & Dalgarno, K. W. (2017). An overview of powder granulometry on feedstock and part performance in the selective laser melting process. *Additive Manufacturing*, *18*, 228–255. https://doi.org/10.1016/j.addma.2017.10.011

(Tarrago et al., 2015) Tarrago, J.M., Ferrari, C., Reig, B., Coureaux, D., Schneider, L., Llaines, L., (2015) Mechanics and Mechanisms of Fatigue in a WC-Ni Hardmetal and a Comparative Study with respect to WC-Co Hardmetals

(ThermoScientific, 2016) "Comprehensive Compounding and Extrusion Solutions for Materials Science", ThermoScientific, 2016. [Online] Available at: https://assets.thermofisher.com /TFS-Assets/MSD/brochures/BR6233097-twin-screw-extrusion-brochure.pdf. [Accessed: 27-Mar-2018]

(Torralba et al., 2013) Torralba, J. M., Hidalgo, J., & Morales, A. J. (2013). Powder injection moulding: Processing of small parts of complex shape. *International Journal of Microstructure and Materials Properties*, *8*(1/2), 87. https://doi.org/10.1504/IJMMP.2013.052648

(Titanium Carbide, 2020) *Certificate of Analysis for Titanium Carbide (TiC-1028),* Pacific Particulate Materials Ltd

(Tungsten Carbide, 2020) *Certificate of Analysis for Tungsten Carbide (WC-8336/8337)*, Pacific Particulate Materials Ltd, 2020

(Virtual Foundry, 2019) Avaliable online: https://shop.thevirtualfoundry.com/, Accessed: May, 2019

(Yarmuch et. al, 2009) Yarmuch, M., Patchett, B., Ivey, D., & Anderson, M. (2009). Effect of Welding Parameters and Gas Composition on PTAW Behaviour. Trends in Welding Research, Proceedings of the 8th International Conference (pp. 705-714). Pine Mountian, Georgia: ASM International.

(Yu & Standish, 1993) Yu, A. B., & Standish, N. (1993). A study of the packing of particles with a mixture size distribution. Powder Technology, 76(2), 113–124. https://doi.org/10.1016/S0032-5910(05)80018-X

(Yunn et al., 2011) Yunn, H. S., Muhamad, N., Sulong, A. B., Fayyaz, A., & Li, H. P. (2011). Critical Solid Loading and Rheological Study of WC-10%Co. Applied Mechanics and Materials, 52–54, 97–102. https://doi.org/10.4028/www.scientific.net/AMM.52-54.97

APPENDICES

APPENDIX A - POWDER PROPERTIES

This section includes the experimental data and plotted figures based on results from dry particle characterization.

A.1 Data for Particle Size Sieve Analysis of WC Powders

A.2 Nominal Bulk and True Densities of Binary Powder Mixtures

A.1 Data from Particle Size Sieve Analysis of WC Powders

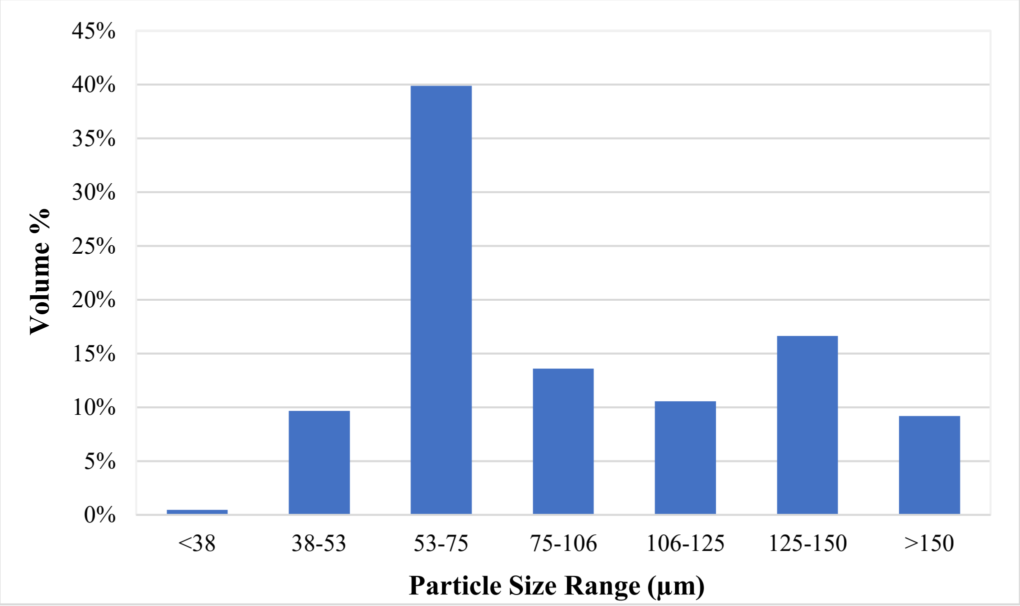

Figure A-1 Particle Size Distribution from Sieve Analysis of Fine WC Powder (Batch no.8336)

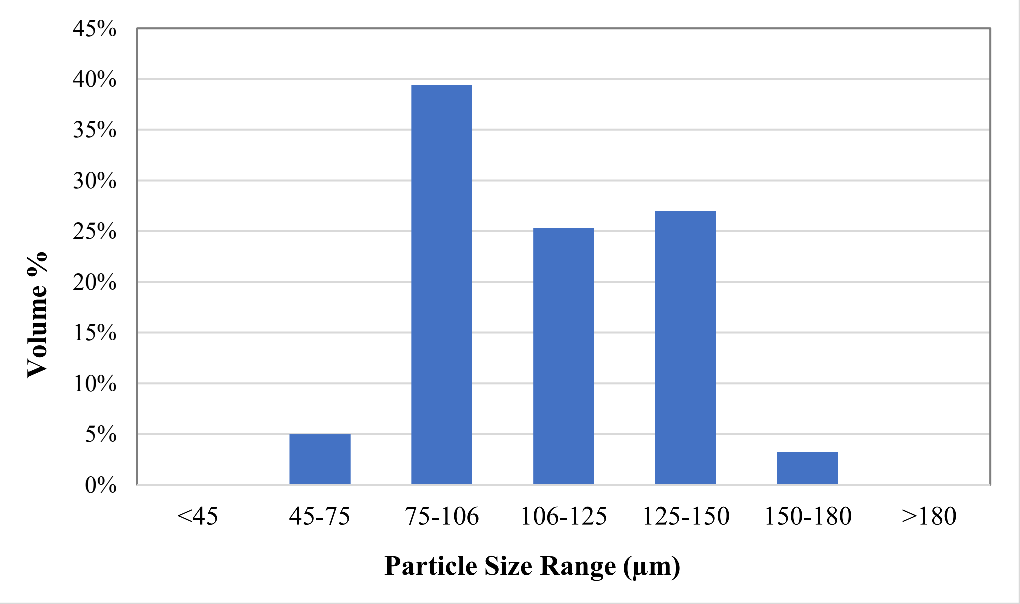

Figure A-2 Particle Size Distribution from Sieve Analysis of Coarse WC Powder (Batch no.8337)

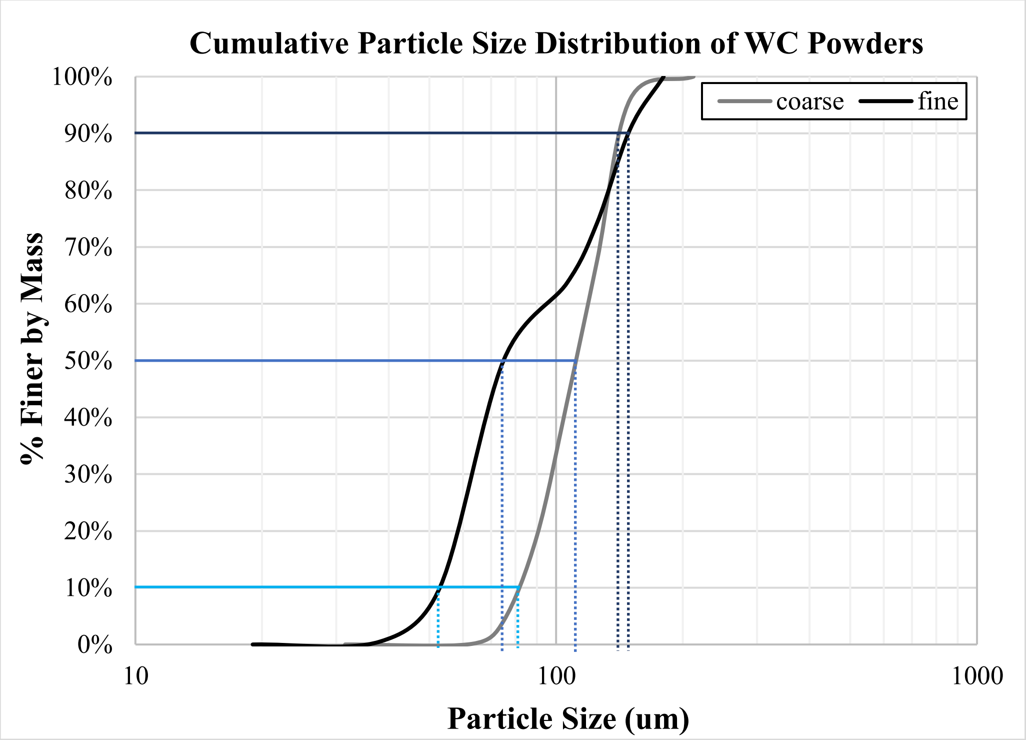

Figure A-3 Cumulative Particle Size Distribution of Fine and Coarse WC powders used to determine d10, d50, and d90

A.2 Nominal Bulk and True Densities of Binary Powder Mixtures

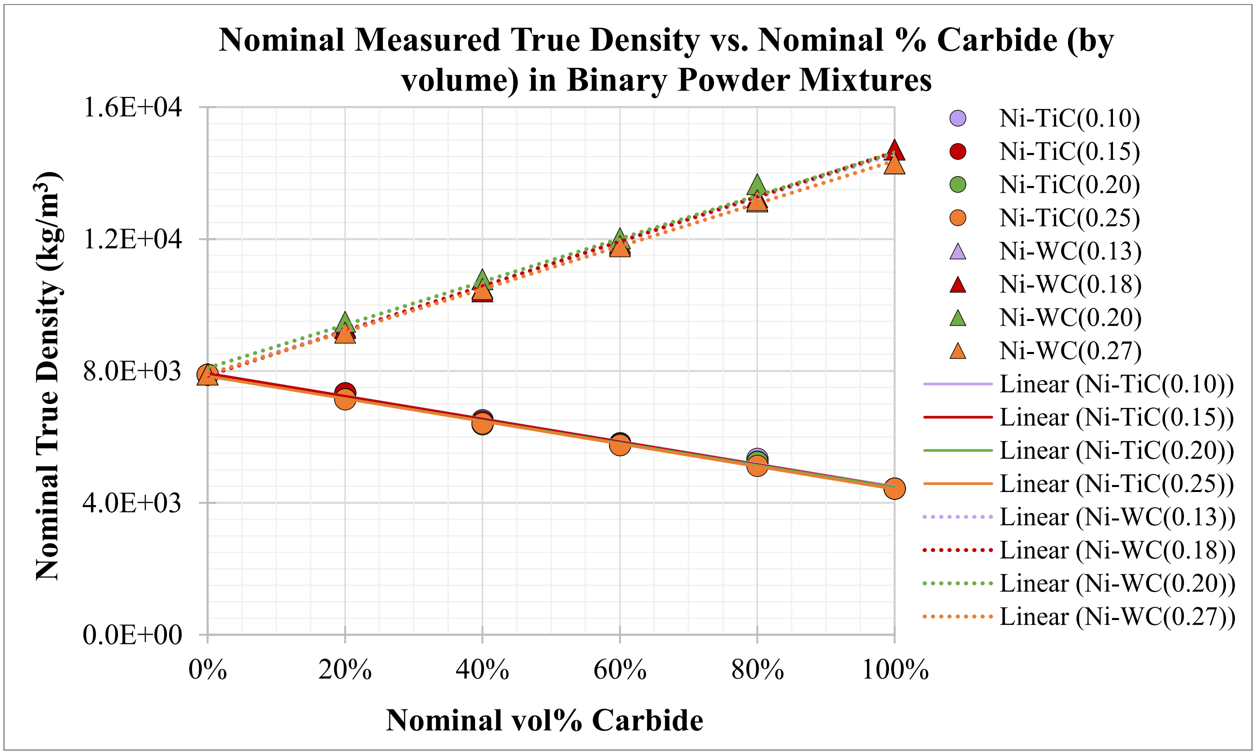

Figure A-4 Nominal True Densities of Binary Powder Mixtures

Table A-1 Trendline Data from Nominal True Densities of Binary Powder Mixtures Plot

Binary Mixture	δ	Trendline Equation (Linear Fit)	R^2
Ni-TiC	0.10	y = -3.43E+00x + 7.93E+00	9.93E-01
	0.15	y = -3.45E+00x + 7.93E+00	9.97E-01
	0.20	y = -3.38E+00x + 7.84E+00	9.97E-01
	0.25	y = -3.43E+00x + 7.84E+00	9.99E-01
Ni-WC	0.13	y = 6.68E+00x + 7.90E+00	9.98E-01
	0.18	y = 6.79E+00x + 7.85E+00	9.99E-01
	0.20	y = 6.54E+00x + 8.09E+00	9.91E-01
	0.27	y = 6.48E+00x + 7.89E+00	9.99E-01

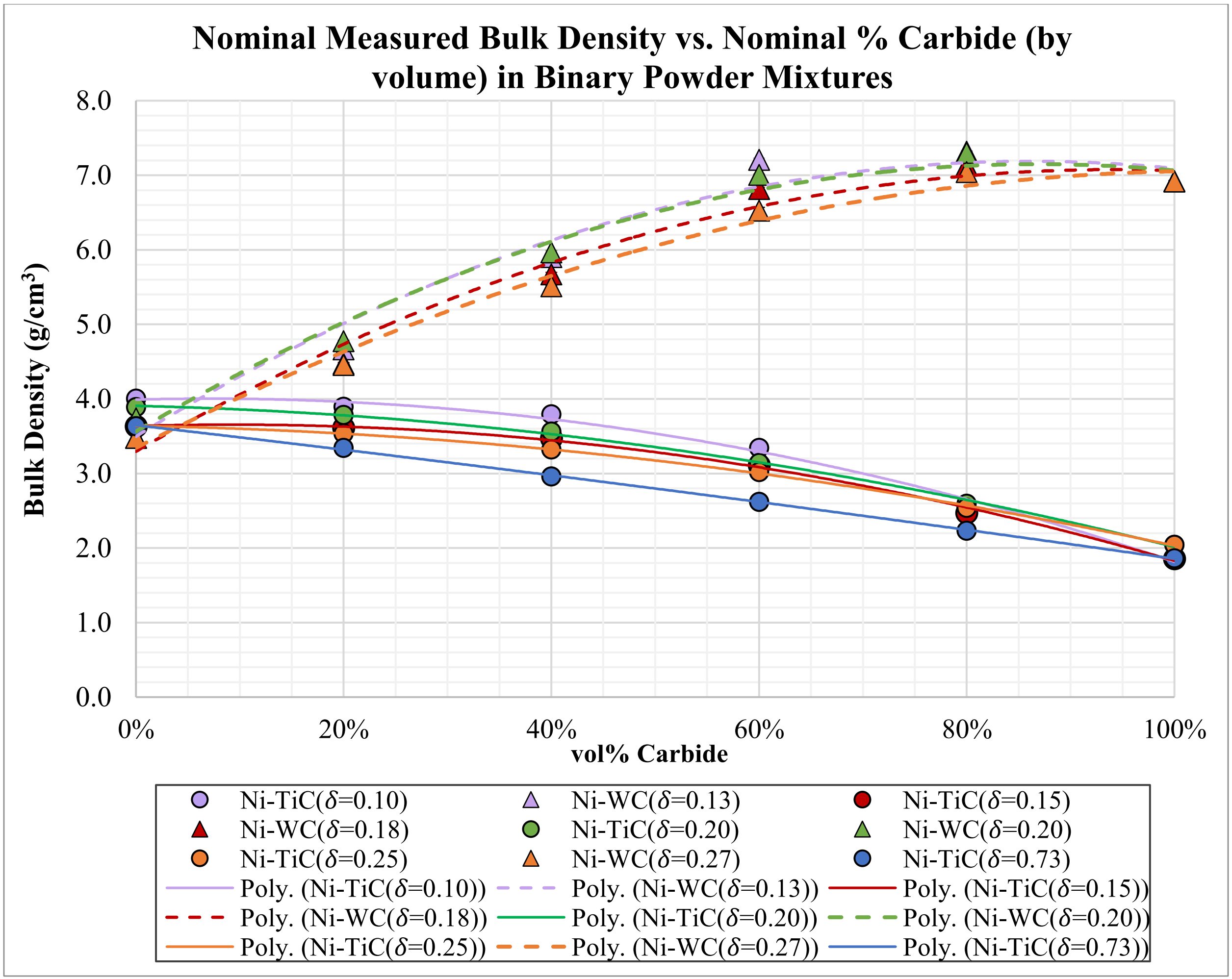

Figure A.5 Nominal Bulk Densities of Binary Powder Mixtures

Table A-2 Trendline Data from Nominal Bulk Densities of Binary Powder Mixtures Plot

Binary Mixture	δ	Trendline Equation (2nd Order Polynomial Fit)	R^2
Ni-TiC	0.10	$y = -2.53E+00x^2 + 3.56E-01x + 3.99E+00$	9.93E-01
	0.15	$y = -2.21E+00x^2 + 4.06E-01x + 3.64E+00$	9.97E-01
	0.20	$y = -1.57E+00x^2 - 3.21E-01x + 3.91E+00$	9.98E-01
	0.25	$y = -1.36E+00x^2 - 2.48E-01x + 3.64E+00$	9.99E-01
	0.73	$y = -1.90E-01x^2 - 1.60E+00x + 3.65E+00$	9.99E-01
Ni-WC	0.13	$y = -4.97E+00x^2 + 8.56E+00x + 3.50E+00$	9.62E-01
	0.18	$y = -4.28E+00x^2 + 8.04E+00x + 3.30E+00$	9.80E-01
	0.20	$y = -4.76E+00x^2 + 8.27E+00x + 3.56E+00$	9.80E-01
	0.27	$y = -3.42E+00x^2 + 7.13E+00x + 3.34E+00$	9.87E-01

APPENDIX B - TECHNICAL SPECIFICATIONS FOR EXPERIMENTAL APPARATUS

This section includes the experimental data obtained from pycnometry and technical specifications of the extruder and FFF printer.

B.1 Density vs. Temperature for 95%Ethanol Aqueous Solution

B.2 EuroLab 16 XL Twin-Screw Extruder

B.3 FFF Printhead Assembly

B.1 Density vs. Temperature for 95%Ethanol Aqueous Solution

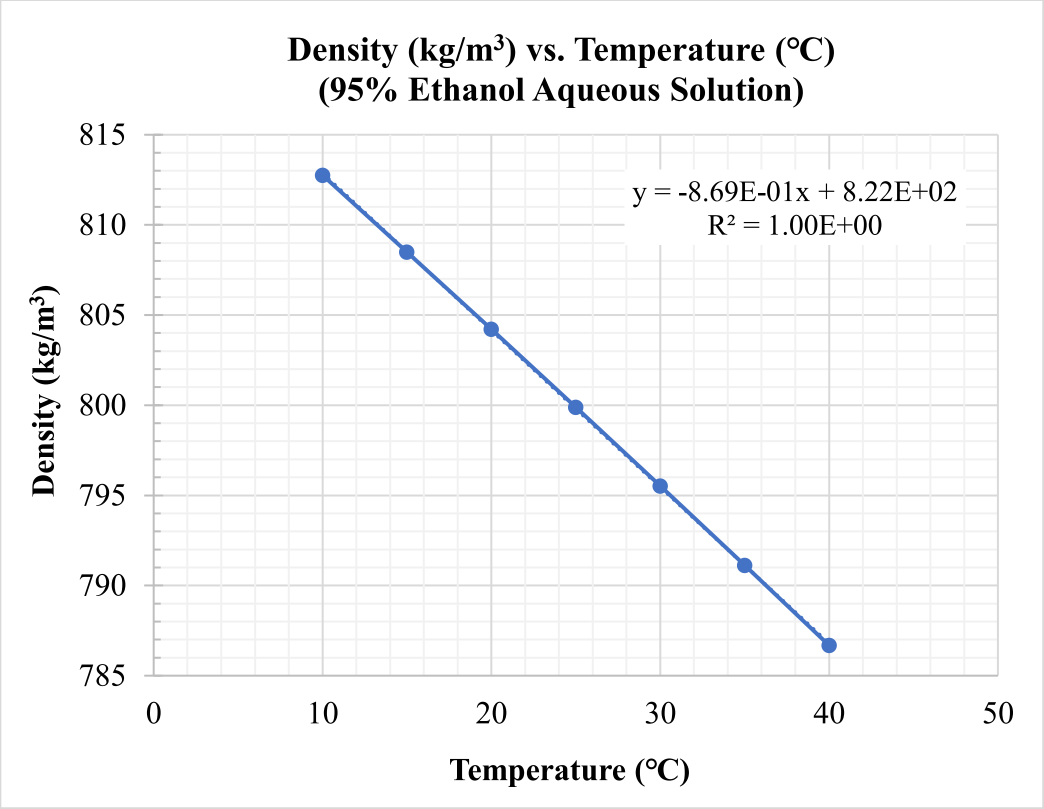

Figure B-1 Density of 95%Ethanol Aqueous Solution as a function of Temperature

B.2 EuroLab 16 XL Twin-Screw Extruder

Table B-1 Technical Specifications for Extruder

Item	Specification
Barrel Bore Diameter	16 mm
Barrel Length L/D	40:1
Center Line Spacing	12.5 mm
Center to Radius Ratio	1.56
Channel Depth	3.3 mm
Die Heater Rating	250W
Max. Screw Speed	1000 rpm
Max. Temperature	400°C
Motor Power	2.5 kW
Screw Diameter	15.6 mm
Direction of Screw Rotation	co-rotating
Torque per Shaft	12 Nm
Typical Output	up to 10 kg/h
Extruder Cooling Water 20°C	5 L/min.

B.3 FFF Printhead Assembly

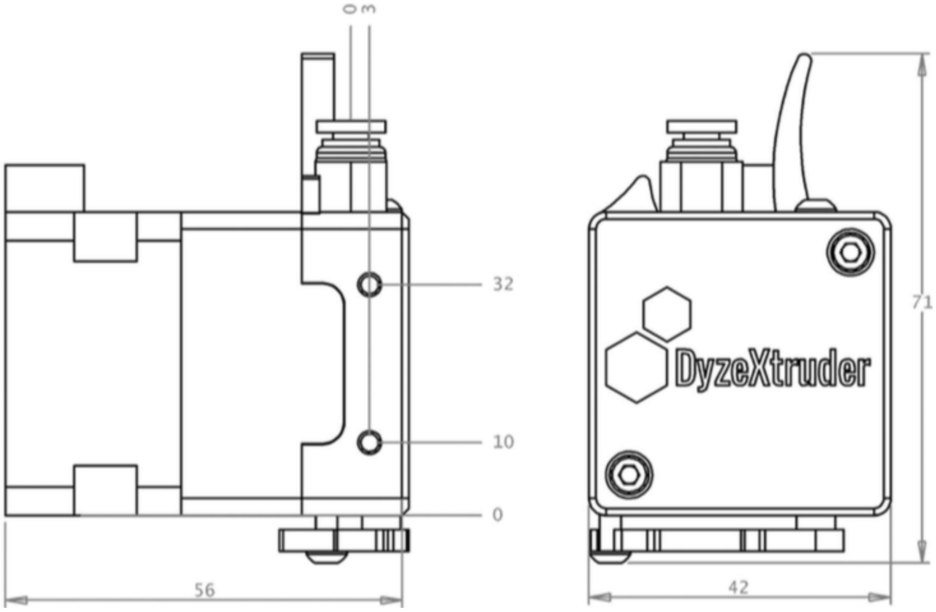

Figure B-2 Technical Drawing of DyzeXtruder GT Extruder

Table B-2 Specifications for DyzeXtruder GT Extruder

Parameter	Value	Units
Weight	275	g
Filament diameter	1.75	mm
Operating current	1	A
Operating temperature (air cooled)	0 to +60	°C
Operating temperature (liquid cooled)	0 to +120	°C
Top fitting tube OD	4.00	mm
Gear ratio	5.65 : 1	
Groove mount head thickness	2 - 5	mm
Mounting screw thread	M3	
Mounting screw min thread depth	5	mm
Resolution (Full step)	0.0042	mm^3

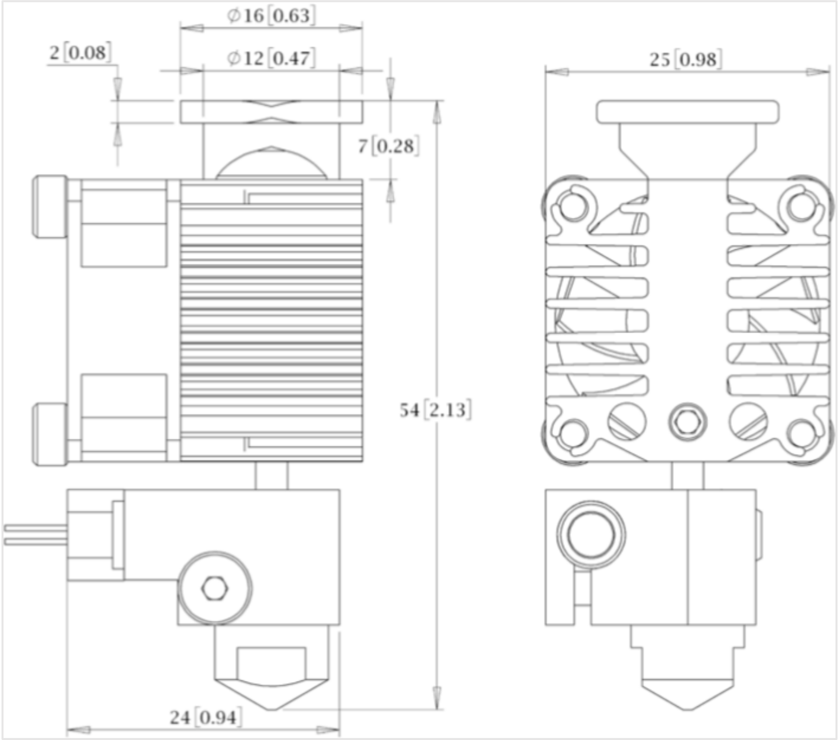

Figure B-3 Technical Drawing of DyZEND-X Hotend

Table B-3 Specifications for DyZEND-X Hotend

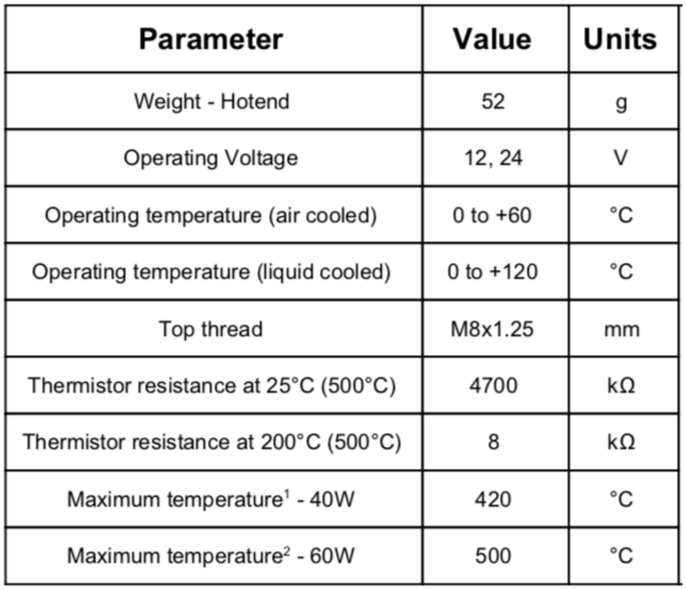

Parameter	Value	Units
Weight - Hotend	52	g
Operating Voltage	12, 24	V
Operating temperature (air cooled)	0 to +60	°C
Operating temperature (liquid cooled)	0 to +120	°C
Top thread	M8x1.25	mm
Thermistor resistance at 25°C (500°C)	4700	kΩ
Thermistor resistance at 200°C (500°C)	8	kΩ
Maximum temperature[1] - 40W	420	°C
Maximum temperature[2] - 60W	500	°C

APPENDIX C - PARAMETERS OF EXTRUSION

This section includes the parameters used for filament extrusion.

C.1 Parameters of Filler Powder Feeding

C.2 Conditions and Parameters of Filament Extrusion

C.1 Parameters of Filler Powder Feeding

Table C-1 Filler Feed Rates used in Filament Extrusion

Filament no.	Filler		
	Feeder Size	**Feeder Screw Speed (rpm)**	**Average Feed Rate (g/min)**
1	large	17	272.99 (± 1.01)
2			263.71 (± 3.07)
3			275.74 (± 0.59)
4			264.12 (± 1.26)
5	small	47	162.67 (± 0.26)
6	small	45	129.14 (± 0.47)
7	small	41	100.62 (± 1.04)
8	large	15	95.96 (± 0.70)
9	small	41	96.93 (± 0.26)
10	large	16	96.84 (± 1.25)

C.2 Conditions and Parameters of Filament Extrusion

Table C-2 Process Parameters and Conditions of Extrusion

Filament no.	Extruder Screw Speed (rpm)	Pulling Speed (m/s)	Extrusion Torque (%)	Extrusion Conditions
1	230	65	104	Plug
2	210	65	100-104	Plug
3	220	65	98-100	Borderline
4	220	65	90-100	Stable
5	220	65	104	Plug
6	220	65	96-103	Plug/BL
7	220	65	100-104	Plug
8	220	65	90-100	Stable
9	220	65	98-100	Borderline
10	220	65	104	Plug

APPENDIX D - PARAMETERS OF 3D-PRINTING (FFF)

This section includes the data collected from filament flow rate analysis and lists all relevant parameters used for sample printing.

D.1 Filament Flow Rate vs. Nozzle Temperature

D.2 Cura Slicing Parameters

D.3 Gcode for Sample Printing

D.1 Filament Flow Rate vs. Nozzle Temperature

Table D-1 Experimental Average Flow Rates of Extruded Filaments

Filament	Average Flow Rate				
	190 °C	200 °C	210 °C	220 °C	230 °C
HDPE	6.91 ± 0.06	6.91 ± 0.03	7.02 ± 0.03	6.96 ± 0.05	6.99 ± 0.05
F1	6.10 ± 0.23	5.94 ± 0.15	6.36 ± 0.24	6.44 ± 0.23	6.60 ± 0.17
F2	5.89 ± 0.21	6.25 ± 0.09	6.33 ± 0.16	6.27 ± 0.08	6.57 ± 0.15
F3	5.81 ± 0.15	6.17 ± 0.18	6.57 ± 0.15	6.35 ± 0.16	6.88 ± 0.23
F4	6.21 ± 0.16	6.37 ± 0.21	6.45 ± 0.19	6.52 ± 0.22	6.69 ± 0.22
F5	6.02 ± 0.10	6.19 ± 0.09	6.35 ± 0.13	6.45 ± 0.09	6.84 ± 0.09
F6	6.12 ± 0.11	6.23 ± 0.11	6.30 ± 0.05	6.31 ± 0.07	6.37 ± 0.12
F7	5.70 ± 0.12	6.14 ± 0.15	6.14 ± 0.13	6.85 ± 0.19	6.88 ± 0.15
F8	6.09 ± 0.05	6.14 ± 0.07	6.18 ± 0.06	6.18 ± 0.04	6.27 ± 0.07
F9	5.58 ± 0.07	5.62 ± 0.09	5.66 ± 0.04	5.76 ± 0.09	5.85 ± 0.10
F10	6.17 ± 0.13	6.50 ± 0.11	6.60 ± 0.08	6.58 ± 0.04	6.84 ± 0.13

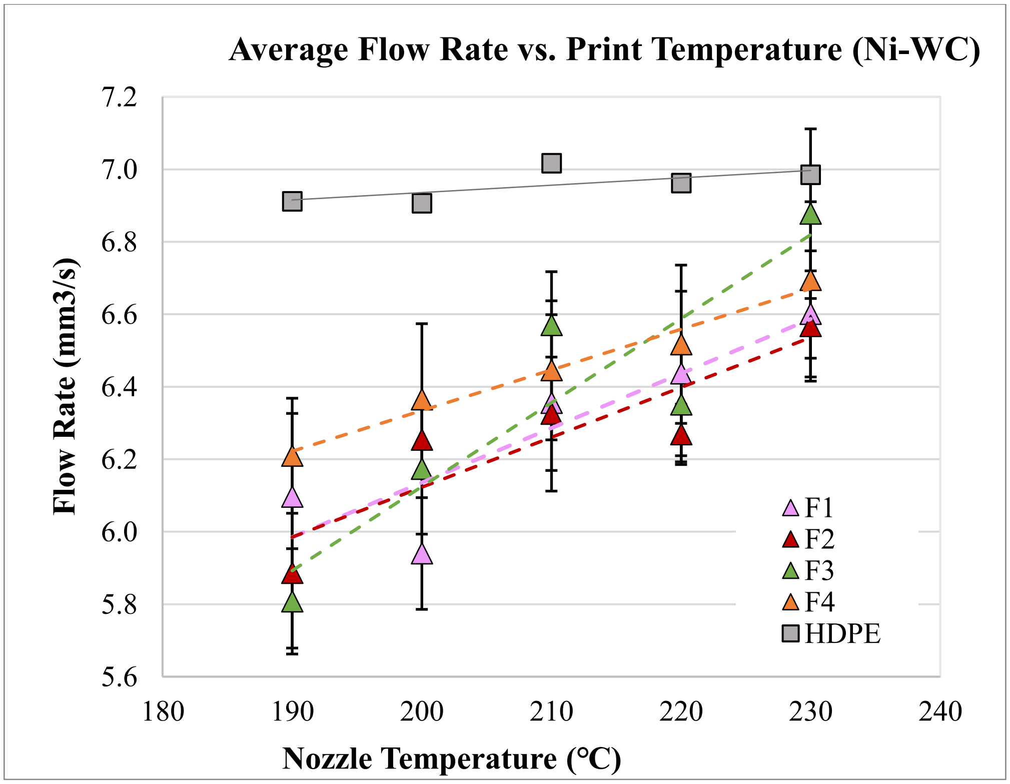

Figure D-1 Average Filament Flow Rate vs, Print Temperature (F1-F4)

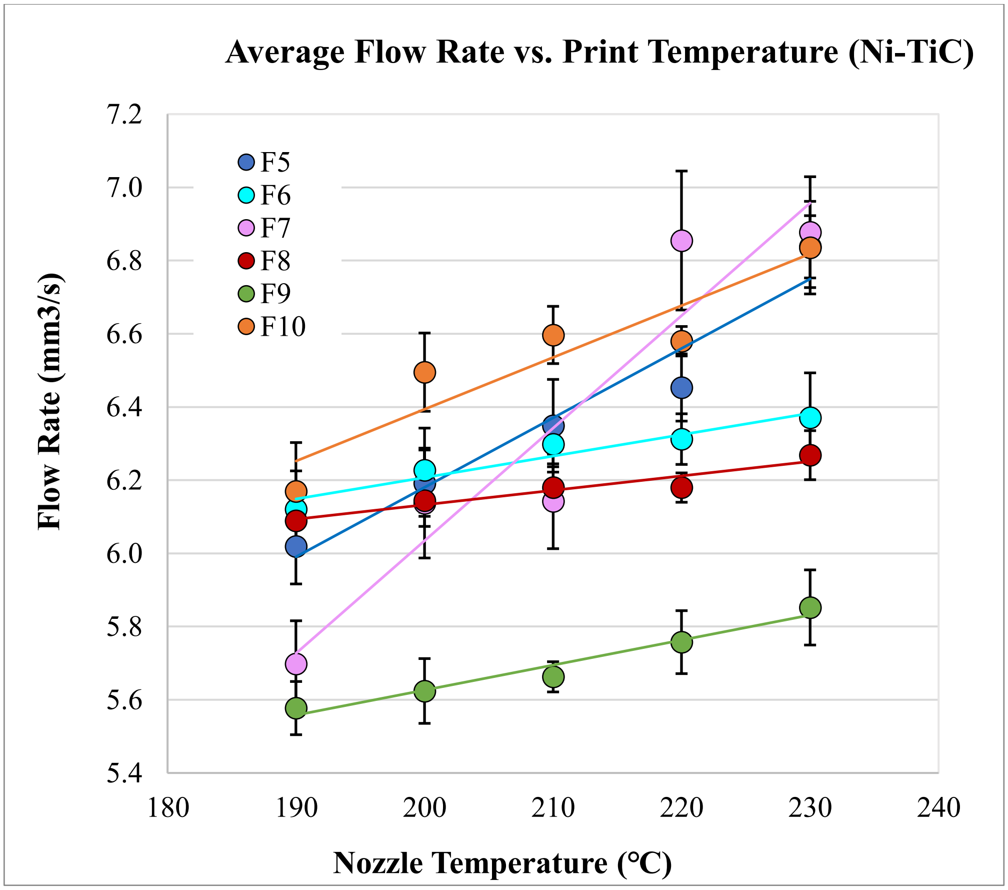

Figure D-2 Average Filament Flow Rate vs, Print Temperature (F5-F10)

Table D-2 Trendline Data for Flow Rate vs. Temperature Plots

Filament	Trendline Equation (Linear Fit)	Residual
HDPE	y = 2.03E-03x + 6.53E+00	0.45
F1	y = 1.50E-02x + 3.13E+00	0.80
F2	y = 1.38E-02x + 3.37E+00	0.79
F3	y = 2.32E-02x + 1.49E+00	0.82
F4	y = 1.12E-02x + 4.09E+00	0.97
F5	y = 1.90E-02x + 2.38E+00	0.95
F6	y = 5.85E-03x + 5.04E+00	0.93
F7	y = 3.08E-02x - 1.17E-01	0.91
F8	y = 3.94E-03x + 5.34E+00	0.91
F9	y = 6.83E-03x + 4.26E+00	0.96
F10	y = 1.42E-02x + 3.56E+00	0.87

D.2 Cura Slicing Parameters

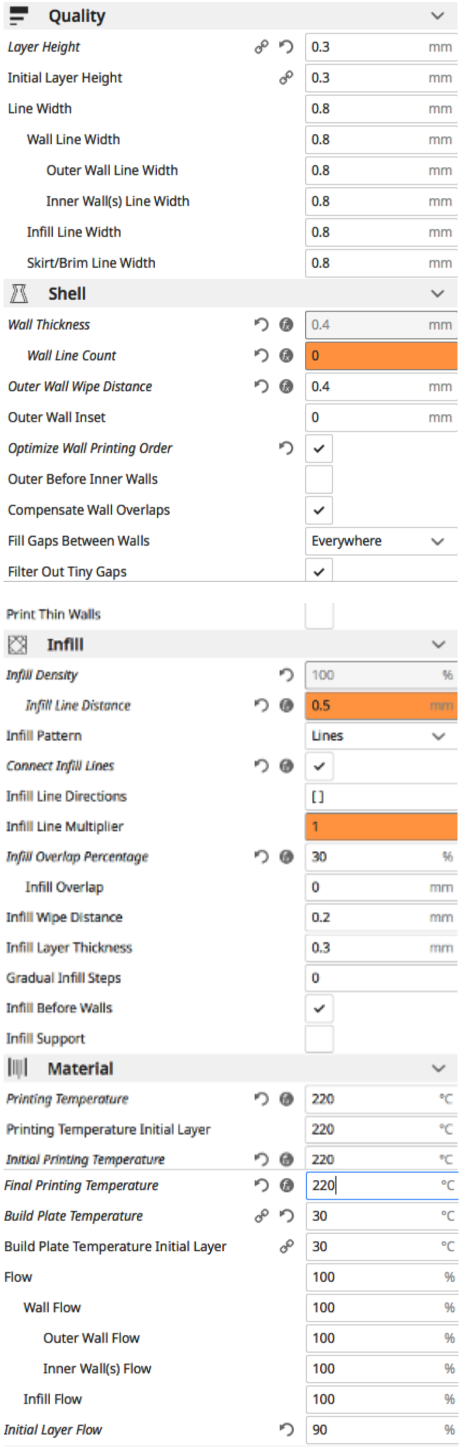

Quality

Layer Height	0.3	mm
Initial Layer Height	0.3	mm
Line Width	0.8	mm
Wall Line Width	0.8	mm
Outer Wall Line Width	0.8	mm
Inner Wall(s) Line Width	0.8	mm
Infill Line Width	0.8	mm
Skirt/Brim Line Width	0.8	mm

Shell

Wall Thickness	0.4	mm
Wall Line Count	0	
Outer Wall Wipe Distance	0.4	mm
Outer Wall Inset	0	mm
Optimize Wall Printing Order	✓	
Outer Before Inner Walls	☐	
Compensate Wall Overlaps	✓	
Fill Gaps Between Walls	Everywhere	
Filter Out Tiny Gaps	✓	
Print Thin Walls	☐	

Infill

Infill Density	100	%
Infill Line Distance	0.5	mm
Infill Pattern	Lines	
Connect Infill Lines	✓	
Infill Line Directions	[]	
Infill Line Multiplier	1	
Infill Overlap Percentage	30	%
Infill Overlap	0	mm
Infill Wipe Distance	0.2	mm
Infill Layer Thickness	0.3	mm
Gradual Infill Steps	0	
Infill Before Walls	✓	
Infill Support	☐	

Material

Printing Temperature	220	°C
Printing Temperature Initial Layer	220	°C
Initial Printing Temperature	220	°C
Final Printing Temperature	220	°C
Build Plate Temperature	30	°C
Build Plate Temperature Initial Layer	30	°C
Flow	100	%
Wall Flow	100	%
Outer Wall Flow	100	%
Inner Wall(s) Flow	100	%
Infill Flow	100	%
Initial Layer Flow	90	%

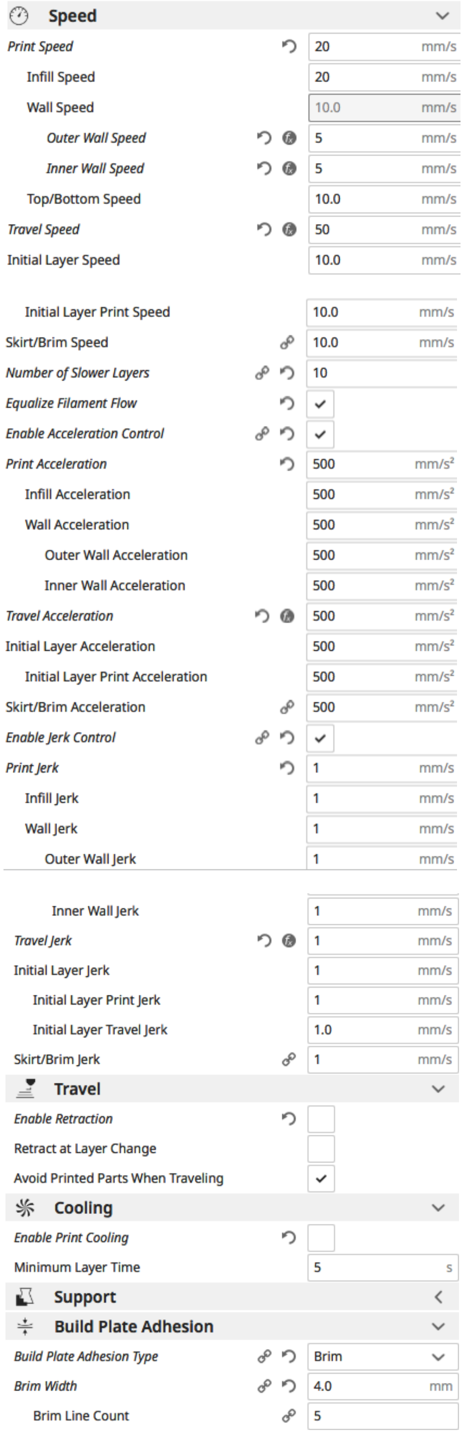

Speed

Print Speed	20	mm/s
Infill Speed	20	mm/s
Wall Speed	10.0	mm/s
Outer Wall Speed	5	mm/s
Inner Wall Speed	5	mm/s
Top/Bottom Speed	10.0	mm/s
Travel Speed	50	mm/s
Initial Layer Speed	10.0	mm/s
Initial Layer Print Speed	10.0	mm/s
Skirt/Brim Speed	10.0	mm/s
Number of Slower Layers	10	
Equalize Filament Flow	✓	
Enable Acceleration Control	✓	
Print Acceleration	500	mm/s²
Infill Acceleration	500	mm/s²
Wall Acceleration	500	mm/s²
Outer Wall Acceleration	500	mm/s²
Inner Wall Acceleration	500	mm/s²
Travel Acceleration	500	mm/s²
Initial Layer Acceleration	500	mm/s²
Initial Layer Print Acceleration	500	mm/s²
Skirt/Brim Acceleration	500	mm/s²
Enable Jerk Control	✓	
Print Jerk	1	mm/s
Infill Jerk	1	mm/s
Wall Jerk	1	mm/s
Outer Wall Jerk	1	mm/s
Inner Wall Jerk	1	mm/s
Travel Jerk	1	mm/s
Initial Layer Jerk	1	mm/s
Initial Layer Print Jerk	1	mm/s
Initial Layer Travel Jerk	1.0	mm/s
Skirt/Brim Jerk	1	mm/s

Travel

Enable Retraction	☐	
Retract at Layer Change	☐	
Avoid Printed Parts When Traveling	✓	

Cooling

Enable Print Cooling	☐	
Minimum Layer Time	5	s

Support

Build Plate Adhesion

Build Plate Adhesion Type	Brim	
Brim Width	4.0	mm
Brim Line Count	5	

D.3 Gcode for Sample Printing

```
;FLAVOR:Repetier
;TIME:836
;MINX:121.4
;MINY:81.4
;MINZ:0.3
;MAXX:148.6
;MAXY:108.6
;MAXZ:4.8
;Generated with Cura_SteamEngine 4.8.0
M190 S30
M104 S220
M109 S220
M82 ;absolute extrusion mode
G28 ;Home
G1 Z15.0 F6000 ;Move the platform down 15mm
;Prime the extruder
G92 E0
G1 F200 E3
G92 E0
G92 E0
G92 E0
;LAYER_COUNT:16
;LAYER:0
M107
M202 X5000 Y5000
M207 X1
G0 F1500 X122.022 Y82.978 Z0.3
M201 X500 Y500
;TYPE:SKIRT
G1 F600 X122.355 Y82.558 E0.04813
G1 X122.747 Y82.192 E0.09629
G1 X123.189 Y81.889 E0.14442
G1 X123.672 Y81.654 E0.19265
G1 X124.183 Y81.494 E0.24074
G1 X124.713 Y81.411 E0.28892
G1 X125 Y81.4 E0.31471
G1 X145 Y81.4 E2.11076
G1 X145.535 Y81.44 E2.15893
G1 X146.058 Y81.559 E2.2071
G1 X146.557 Y81.754 E2.25521
G1 X147.022 Y82.022 E2.30341
G1 X147.442 Y82.355 E2.35154
G1 X147.808 Y82.747 E2.3997
G1 X148.111 Y83.189 E2.44783
G1 X148.346 Y83.672 E2.49606
G1 X148.506 Y84.183 E2.54415
G1 X148.589 Y84.713 E2.59232
G1 X148.6 Y85 E2.61812
G1 X148.6 Y105 E4.41416
G1 X148.56 Y105.535 E4.46234
G1 X148.441 Y106.058 E4.51051
G1 X148.246 Y106.557 E4.55862
G1 X147.978 Y107.022 E4.60682
G1 X147.645 Y107.442 E4.65495
G1 X147.253 Y107.808 E4.70311
G1 X146.811 Y108.111 E4.75124
G1 X146.328 Y108.346 E4.79947
G1 X145.817 Y108.506 E4.84756
G1 X145.287 Y108.589 E4.89573
G1 X145 Y108.6 E4.92153
G1 X125 Y108.6 E6.71757
G1 X124.465 Y108.56 E6.76575
G1 X123.942 Y108.441 E6.81392
G1 X123.443 Y108.246 E6.86203
G1 X122.978 Y107.978 E6.91023
G1 X122.558 Y107.645 E6.95836
G1 X122.192 Y107.253 E7.00652
G1 X121.889 Y106.811 E7.05465
G1 X121.654 Y106.328 E7.10288
G1 X121.494 Y105.817 E7.15097
G1 X121.411 Y105.287 E7.19914
G1 X121.4 Y105 E7.22494
G1 X121.4 Y85 E9.02098
G1 X121.44 Y84.465 E9.06916
G1 X121.559 Y83.942 E9.11733
G1 X121.754 Y83.443 E9.16544
G1 X122.022 Y82.978 E9.21364
G0 F1500 X122.816 Y83.247
G1 F600 X123.142 Y82.905 E9.25607
G1 X123.521 Y82.622 E9.29854
G1 X123.943 Y82.407 E9.34107
G1 X124.394 Y82.266 E9.38351
G1 X125 Y82.2 E9.43825
G1 X145 Y82.2 E11.2343
G1 X145.471 Y82.24 E11.27675
G1 X145.929 Y82.359 E11.31924
G1 X146.36 Y82.553 E11.36169
G1 X146.753 Y82.816 E11.40415
G1 X147.095 Y83.142 E11.44658
```

```
G1 X147.378 Y83.521 E11.48906
G1 X147.593 Y83.943 E11.53159
G1 X147.734 Y84.394 E11.57403
G1 X147.8 Y85 E11.62877
G1 X147.8 Y105 E13.42482
G1 X147.76 Y105.471 E13.46726
G1 X147.641 Y105.929 E13.50976
G1 X147.447 Y106.36 E13.5522
G1 X147.184 Y106.753 E13.59467
G1 X146.858 Y107.095 E13.6371
G1 X146.479 Y107.378 E13.67958
G1 X146.057 Y107.593 E13.72211
G1 X145.606 Y107.734 E13.76454
G1 X145 Y107.8 E13.81928
G1 X125 Y107.8 E15.61533
G1 X124.529 Y107.76 E15.65778
G1 X124.071 Y107.641 E15.70028
G1 X123.64 Y107.447 E15.74272
G1 X123.247 Y107.184 E15.78519
G1 X122.905 Y106.858 E15.82762
G1 X122.622 Y106.479 E15.87009
G1 X122.407 Y106.057 E15.91263
G1 X122.266 Y105.606 E15.95506
G1 X122.2 Y105 E16.0098
G1 X122.2 Y85 E17.80585
G1 X122.24 Y84.529 E17.8483
G1 X122.359 Y84.071 E17.89079
G1 X122.553 Y83.64 E17.93324
G1 X122.816 Y83.247 E17.9757
G0 F1500 X123.35 Y83.87
G1 F600 X123.607 Y83.565 E18.01152
G1 X123.92 Y83.317 E18.04738
G1 X124.276 Y83.136 E18.08325
G1 X124.661 Y83.029 E18.11913
G1 X125 Y83 E18.14969
G1 X145 Y83 E19.94573
G1 X145.398 Y83.04 E19.98165
G1 X145.779 Y83.158 E20.01747
G1 X146.13 Y83.35 E20.0534
G1 X146.435 Y83.607 E20.08922
G1 X146.683 Y83.92 E20.12508
G1 X146.864 Y84.276 E20.16094
G1 X146.971 Y84.661 E20.19683
G1 X147 Y85 E20.22738
G1 X147 Y105 E22.02343
G1 X146.96 Y105.398 E22.05935
G1 X146.842 Y105.779 E22.09517
G1 X146.65 Y106.13 E22.1311
G1 X146.393 Y106.435 E22.16691
G1 X146.08 Y106.683 E22.20278
G1 X145.724 Y106.864 E22.23864
G1 X145.339 Y106.971 E22.27452
G1 X145 Y107 E22.30508
G1 X125 Y107 E24.10113
G1 X124.602 Y106.96 E24.13705
G1 X124.221 Y106.842 E24.17287
G1 X123.87 Y106.65 E24.20879
G1 X123.565 Y106.393 E24.24461
G1 X123.317 Y106.08 E24.28047
G1 X123.136 Y105.724 E24.31634
G1 X123.029 Y105.339 E24.35222
G1 X123 Y105 E24.38278
G1 X123 Y85 E26.17882
G1 X123.04 Y84.602 E26.21474
G1 X123.158 Y84.221 E26.25056
G1 X123.35 Y83.87 E26.28649
G0 F1500 X123.957 Y84.407
G1 F600 X124.143 Y84.16 E26.31426
G1 X124.386 Y83.969 E26.34201
G1 X124.67 Y83.846 E26.36981
G1 X125 Y83.8 E26.39973
G1 X145 Y83.8 E28.19577
G1 X145.307 Y83.84 E28.22358
G1 X145.593 Y83.957 E28.25133
G1 X145.84 Y84.143 E28.27909
G1 X146.031 Y84.386 E28.30685
G1 X146.154 Y84.67 E28.33464
G1 X146.2 Y85 E28.36456
G1 X146.2 Y105 E30.16061
G1 X146.16 Y105.307 E30.18841
G1 X146.043 Y105.593 E30.21616
G1 X145.857 Y105.84 E30.24393
G1 X145.614 Y106.031 E30.27169
G1 X145.33 Y106.154 E30.29948
G1 X145 Y106.2 E30.3294
G1 X125 Y106.2 E32.12545
G1 X124.693 Y106.16 E32.15325
```

```
G1 X124.407 Y106.043 E32.181
G1 X124.16 Y105.857 E32.20877
G1 X123.969 Y105.614 E32.23652
G1 X123.846 Y105.33 E32.26432
G1 X123.8 Y105 E32.29424
G1 X123.8 Y85 E34.09028
G1 X123.84 Y84.693 E34.11809
G1 X123.957 Y84.407 E34.14584
G0 F1500 X124.64 Y84.827
G1 F600 X124.75 Y84.688 E34.16175
G1 X125 Y84.6 E34.18556
G1 X145 Y84.6 E35.9816
G1 X145.173 Y84.64 E35.99755
G1 X145.312 Y84.75 E36.01347
G1 X145.4 Y85 E36.03727
G1 X145.4 Y105 E37.83332
G1 X145.361 Y105.173 E37.84924
G1 X145.25 Y105.312 E37.86521
G1 X145 Y105.4 E37.88902
G1 X125 Y105.4 E39.68506
G1 X124.827 Y105.361 E39.70099
G1 X124.688 Y105.25 E39.71696
G1 X124.6 Y105 E39.74076
G1 X124.6 Y85 E41.53681
G1 X124.64 Y84.827 E41.55276
;MESH:20x20x5_square.stl
G0 F1500 X125.79 Y85.79
;TYPE:SKIN
G1 F600 X144.21 Y85.79 E43.20692
G1 X144.21 Y104.21 E44.86108
G1 X125.79 Y104.21 E46.51524
G1 X125.79 Y85.79 E48.1694
G0 F1500 X143.849 Y87.281
G1 F600 X142.718 Y86.149 E48.3131
G0 F1500 X141.586 Y86.149
G1 F600 X143.849 Y88.412 E48.6005
G0 F1500 X143.849 Y89.543
G1 F600 X140.455 Y86.149 E49.03153
G0 F1500 X139.324 Y86.149
G1 F600 X143.849 Y90.675 E49.60627
G0 F1500 X143.849 Y91.806
G1 F600 X138.192 Y86.149 E50.32471
G0 F1500 X137.061 Y86.149
G1 F600 X143.849 Y92.937 E51.18678
G0 F1500 X143.849 Y94.069
G1 F600 X135.929 Y86.149 E52.19262
G0 F1500 X134.798 Y86.149
G1 F600 X143.849 Y95.2 E53.34209
G0 F1500 X143.849 Y96.331
G1 F600 X133.667 Y86.149 E54.6352
G0 F1500 X132.535 Y86.149
G1 F600 X143.849 Y97.463 E56.07208
G0 F1500 X143.849 Y98.594
G1 F600 X131.404 Y86.149 E57.65259
G0 F1500 X130.273 Y86.149
G1 F600 X143.849 Y99.726 E59.3768
G0 F1500 X143.849 Y100.857
G1 F600 X129.141 Y86.149 E61.24471
G0 F1500 X128.01 Y86.149
G1 F600 X143.849 Y101.988 E63.25626
G0 F1500 X143.849 Y103.12
G1 F600 X126.878 Y86.149 E65.41158
G0 F1500 X126.149 Y86.551
G1 F600 X143.447 Y103.849 E67.60842
G0 F1500 X142.316 Y103.849
G1 F600 X126.149 Y87.682 E69.66162
G0 F1500 X126.149 Y88.814
G1 F600 X141.185 Y103.849 E71.57113
G0 F1500 X140.053 Y103.849
G1 F600 X126.149 Y89.945 E73.33693
G0 F1500 X126.149 Y91.076
G1 F600 X138.922 Y103.849 E74.9591
G0 F1500 X137.791 Y103.849
G1 F600 X126.149 Y92.208 E76.43756
G0 F1500 X126.149 Y93.339
G1 F600 X136.659 Y103.849 E77.77233
G0 F1500 X135.528 Y103.849
G1 F600 X126.149 Y94.47 E78.96346
G0 F1500 X126.149 Y95.602
G1 F600 X134.396 Y103.849 E80.01083
G0 F1500 X133.265 Y103.849
```

```
G1 F600 X126.149 Y96.733 E80.91456
G0 F1500 X126.149 Y97.864
G1 F600 X132.134 Y103.849 E81.67465
G0 F1500 X131.002 Y103.849
G1 F600 X126.149 Y98.996 E82.29098
G0 F1500 X126.149 Y100.127
G1 F600 X129.871 Y103.849 E82.76367
G0 F1500 X128.74 Y103.849
G1 F600 X126.149 Y101.259 E83.09267
G0 F1500 X126.149 Y102.39
G1 F600 X127.608 Y103.849 E83.27796
G0 F1500 X126.477 Y103.849
G1 F600 X126.149 Y103.521 E83.31962
;MESH:NONMESH
G0 X126.149 Y103.521 Z0.6
G0 F1500 X125.79 Y85.79
;TIME_ELAPSED:103.249249
;LAYER:1
;TYPE:SKIN
;MESH:20x20x5_square.stl
G1 F600 X144.21 Y85.79 E85.15757
G1 X144.21 Y104.21 E86.99553
G1 X125.79 Y104.21 E88.83348
G1 X125.79 Y85.79 E90.67144
G0 F1800 X126.149 Y86.548
G1 F600 X126.548 Y86.149 E90.72774
G0 F1800 X127.679 Y86.149
G1 F600 X126.149 Y87.679 E90.94364
G0 F1800 X126.149 Y88.811
G1 F600 X128.81 Y86.149 E91.31921
G0 F1800 X129.942 Y86.149
G1 F600 X126.149 Y89.942 E91.85444
G0 F1800 X126.149 Y91.073
G1 F600 X131.073 Y86.149 E92.54927
G0 F1800 X132.204 Y86.149
G1 F600 X126.149 Y92.205 E93.40376
G0 F1800 X126.149 Y93.336
G1 F600 X133.336 Y86.149 E94.41793
G0 F1800 X134.467 Y86.149
G1 F600 X126.149 Y94.468 E95.59176
G0 F1800 X126.149 Y95.599
G1 F600 X135.599 Y86.149 E96.92526
G0 F1800 X136.73 Y86.149
G1 F600 X126.149 Y96.73 E98.41835
G0 F1800 X126.149 Y97.862
G1 F600 X137.861 Y86.149 E100.07111
G0 F1800 X138.993 Y86.149
G1 F600 X126.149 Y98.993 E101.88354
G0 F1800 X126.149 Y100.124
G1 F600 X140.124 Y86.149 E103.85556
G0 F1800 X141.255 Y86.149
G1 F600 X126.149 Y101.256 E105.98725
G0 F1800 X126.149 Y102.387
G1 F600 X142.387 Y86.149 E108.27861
G0 F1800 X143.518 Y86.149
G1 F600 X126.149 Y103.519 E110.72963
G0 F1800 X126.949 Y103.849
G1 F600 X143.849 Y86.95 E113.11433
G0 F1800 X143.849 Y88.081
G1 F600 X128.081 Y103.849 E115.33937
G0 F1800 X129.212 Y103.849
G1 F600 X143.849 Y89.212 E117.40481
G0 F1800 X143.849 Y90.344
G1 F600 X130.343 Y103.849 E119.31058
G0 F1800 X131.475 Y103.849
G1 F600 X143.849 Y91.475 E121.05668
G0 F1800 X143.849 Y92.606
G1 F600 X132.606 Y103.849 E122.64319
G0 F1800 X133.737 Y103.849
G1 F600 X143.849 Y93.738 E124.07003
G0 F1800 X143.849 Y94.869
G1 F600 X134.869 Y103.849 E125.33721
G0 F1800 X136 Y103.849
G1 F600 X143.849 Y96.001 E126.44472
G0 F1800 X143.849 Y97.132
G1 F600 X137.132 Y103.849 E127.39256
G0 F1800 X138.263 Y103.849
```

```
G1 F600 X143.849 Y98.263 E128.1808
G0 F1800 X143.849 Y99.395
G1 F600 X139.394 Y103.849 E128.80938
G0 F1800 X140.526 Y103.849
G1 F600 X143.849 Y100.526 E129.27829
G0 F1800 X143.849 Y101.657
G1 F600 X141.657 Y103.849 E129.58761
G0 F1800 X142.788 Y103.849
G1 F600 X143.849 Y102.789 E129.73726
;MESH:NONMESH
G0 X143.849 Y102.789 Z0.9
G0 F1800 X125.79 Y85.79
;TIME_ELAPSED:152.636105
;LAYER:2
;TYPE:SKIN
;MESH:20x20x5_square.stl
G1 F600 X144.21 Y85.79 E131.57521
G1 X144.21 Y104.21 E133.41317
G1 X125.79 Y104.21 E135.25112
G1 X125.79 Y85.79 E137.08908
G0 F2100 X143.849 Y87.281
G1 F600 X142.718 Y86.149 E137.24874
G0 F2100 X141.586 Y86.149
G1 F600 X143.849 Y88.412 E137.56808
G0 F2100 X143.849 Y89.543
G1 F600 X140.455 Y86.149 E138.04701
G0 F2100 X139.324 Y86.149
G1 F600 X143.849 Y90.675 E138.6856
G0 F2100 X143.849 Y91.806
G1 F600 X138.192 Y86.149 E139.48387
G0 F2100 X137.061 Y86.149
G1 F600 X143.849 Y92.937 E140.44173
G0 F2100 X143.849 Y94.069
G1 F600 X135.929 Y86.149 E141.55933
G0 F2100 X134.798 Y86.149
G1 F600 X143.849 Y95.2 E142.83652
G0 F2100 X143.849 Y96.331
G1 F600 X133.667 Y86.149 E144.27331
G0 F2100 X132.535 Y86.149
G1 F600 X143.849 Y97.463 E145.86984
G0 F2100 X143.849 Y98.594
G1 F600 X131.404 Y86.149 E147.62596
G0 F2100 X130.273 Y86.149
G1 F600 X143.849 Y99.726 E149.54175
G0 F2100 X143.849 Y100.857
G1 F600 X129.141 Y86.149 E151.61721
G0 F2100 X128.01 Y86.149
G1 F600 X143.849 Y101.988 E153.85226
G0 F2100 X143.849 Y103.12
G1 F600 X126.878 Y86.149 E156.24706
G0 F2100 X126.149 Y86.551
G1 F600 X143.447 Y103.849 E158.68799
G0 F2100 X142.316 Y103.849
G1 F600 X126.149 Y87.682 E160.96933
G0 F2100 X126.149 Y88.814
G1 F600 X141.185 Y103.849 E163.091
G0 F2100 X140.053 Y103.849
G1 F600 X126.149 Y89.945 E165.053
G0 F2100 X126.149 Y91.076
G1 F600 X138.922 Y103.849 E166.85541
G0 F2100 X137.791 Y103.849
G1 F600 X126.149 Y92.208 E168.49815
G0 F2100 X126.149 Y93.339
G1 F600 X136.659 Y103.849 E169.98123
G0 F2100 X135.528 Y103.849
G1 F600 X126.149 Y94.47 E171.30471
G0 F2100 X126.149 Y95.602
G1 F600 X134.396 Y103.849 E172.46845
G0 F2100 X133.265 Y103.849
G1 F600 X126.149 Y96.733 E173.47259
G0 F2100 X126.149 Y97.864
G1 F600 X132.134 Y103.849 E174.31714
G0 F2100 X131.002 Y103.849
G1 F600 X126.149 Y98.996 E175.00195
G0 F2100 X126.149 Y100.127
G1 F600 X129.871 Y103.849 E175.52717
G0 F2100 X128.74 Y103.849
```

```
G1 F600 X126.149 Y101.259 E175.89271
G0 F2100 X126.149 Y102.39
G1 F600 X127.608 Y103.849 E176.09859
G0 F2100 X126.477 Y103.849
G1 F600 X126.149 Y103.521 E176.14488
;MESH:NONMESH
G0 X126.149 Y103.521 Z1.2
G0 F2100 X125.79 Y85.79
;TIME_ELAPSED:202.056908
;LAYER:3
;TYPE:SKIN
;MESH:20x20x5_square.stl
G1 F600 X144.21 Y85.79 E177.98283
G1 X144.21 Y104.21 E179.82079
G1 X125.79 Y104.21 E181.65874
G1 X125.79 Y85.79 E183.4967
G0 F2400 X126.149 Y86.548
G1 F600 X126.548 Y86.149 E183.553
G0 F2400 X127.679 Y86.149
G1 F600 X126.149 Y87.679 E183.7689
G0 F2400 X126.149 Y88.811
G1 F600 X128.81 Y86.149 E184.14447
G0 F2400 X129.942 Y86.149
G1 F600 X126.149 Y89.942 E184.6797
G0 F2400 X126.149 Y91.073
G1 F600 X131.073 Y86.149 E185.37453
G0 F2400 X132.204 Y86.149
G1 F600 X126.149 Y92.205 E186.22903
G0 F2400 X126.149 Y93.336
G1 F600 X133.336 Y86.149 E187.24319
G0 F2400 X134.467 Y86.149
G1 F600 X126.149 Y94.468 E188.41702
G0 F2400 X126.149 Y95.599
G1 F600 X135.599 Y86.149 E189.75052
G0 F2400 X136.73 Y86.149
G1 F600 X126.149 Y96.73 E191.24361
G0 F2400 X126.149 Y97.862
G1 F600 X137.861 Y86.149 E192.89637
G0 F2400 X138.993 Y86.149
G1 F600 X126.149 Y98.993 E194.7088
G0 F2400 X126.149 Y100.124
G1 F600 X140.124 Y86.149 E196.68082
G0 F2400 X141.255 Y86.149
G1 F600 X126.149 Y101.256 E198.81251
G0 F2400 X126.149 Y102.387
G1 F600 X142.387 Y86.149 E201.10387
G0 F2400 X143.518 Y86.149
G1 F600 X126.149 Y103.519 E203.55489
G0 F2400 X126.949 Y103.849
G1 F600 X143.849 Y86.95 E205.9396
G0 F2400 X143.849 Y88.081
G1 F600 X128.081 Y103.849 E208.16463
G0 F2400 X129.212 Y103.849
G1 F600 X143.849 Y89.212 E210.23007
G0 F2400 X143.849 Y90.344
G1 F600 X130.343 Y103.849 E212.13584
G0 F2400 X131.475 Y103.849
G1 F600 X143.849 Y91.475 E213.88195
G0 F2400 X143.849 Y92.606
G1 F600 X132.606 Y103.849 E215.46845
G0 F2400 X133.737 Y103.849
G1 F600 X143.849 Y93.738 E216.8953
G0 F2400 X143.849 Y94.869
G1 F600 X134.869 Y103.849 E218.16247
G0 F2400 X136 Y103.849
G1 F600 X143.849 Y96.001 E219.26998
G0 F2400 X143.849 Y97.132
G1 F600 X137.132 Y103.849 E220.21782
G0 F2400 X138.263 Y103.849
G1 F600 X143.849 Y98.263 E221.00607
G0 F2400 X143.849 Y99.395
G1 F600 X139.394 Y103.849 E221.63464
G0 F2400 X140.526 Y103.849
G1 F600 X143.849 Y100.526 E222.10356
G0 F2400 X143.849 Y101.657
G1 F600 X141.657 Y103.849 E222.41287
G0 F2400 X142.788 Y103.849
```

```
G1 F600 X143.849 Y102.789 E222.56252
;MESH:NONMESH
G0 X143.849 Y102.789 Z1.5
G0 F2400 X125.79 Y85.79
;TIME_ELAPSED:251.019501
;LAYER:4
;TYPE:SKIN
;MESH:20x20x5_square.stl
G1 F600 X144.21 Y85.79 E224.40047
G1 X144.21 Y104.21 E226.23843
G1 X125.79 Y104.21 E228.07638
G1 X125.79 Y85.79 E229.91434
G0 F2700 X143.849 Y87.281
G1 F600 X142.718 Y86.149 E230.07401
G0 F2700 X141.586 Y86.149
G1 F600 X143.849 Y88.412 E230.39334
G0 F2700 X143.849 Y89.543
G1 F600 X140.455 Y86.149 E230.87227
G0 F2700 X139.324 Y86.149
G1 F600 X143.849 Y90.675 E231.51087
G0 F2700 X143.849 Y91.806
G1 F600 X138.192 Y86.149 E232.30913
G0 F2700 X137.061 Y86.149
G1 F600 X143.849 Y92.937 E233.26699
G0 F2700 X143.849 Y94.069
G1 F600 X135.929 Y86.149 E234.38459
G0 F2700 X134.798 Y86.149
G1 F600 X143.849 Y95.2 E235.66178
G0 F2700 X143.849 Y96.331
G1 F600 X133.667 Y86.149 E237.09857
G0 F2700 X132.535 Y86.149
G1 F600 X143.849 Y97.463 E238.6951
G0 F2700 X143.849 Y98.594
G1 F600 X131.404 Y86.149 E240.45122
G0 F2700 X130.273 Y86.149
G1 F600 X143.849 Y99.726 E242.36701
G0 F2700 X143.849 Y100.857
G1 F600 X129.141 Y86.149 E244.44247
G0 F2700 X128.01 Y86.149
G1 F600 X143.849 Y101.988 E246.67753
G0 F2700 X143.849 Y103.12
G1 F600 X126.878 Y86.149 E249.07232
G0 F2700 X126.149 Y86.551
G1 F600 X143.447 Y103.849 E251.51325
G0 F2700 X142.316 Y103.849
G1 F600 X126.149 Y87.682 E253.79459
G0 F2700 X126.149 Y88.814
G1 F600 X141.185 Y103.849 E255.91626
G0 F2700 X140.053 Y103.849
G1 F600 X126.149 Y89.945 E257.87827
G0 F2700 X126.149 Y91.076
G1 F600 X138.922 Y103.849 E259.68067
G0 F2700 X137.791 Y103.849
G1 F600 X126.149 Y92.208 E261.32342
G0 F2700 X126.149 Y93.339
G1 F600 X136.659 Y103.849 E262.80649
G0 F2700 X135.528 Y103.849
G1 F600 X126.149 Y94.47 E264.12997
G0 F2700 X126.149 Y95.602
G1 F600 X134.396 Y103.849 E265.29371
G0 F2700 X133.265 Y103.849
G1 F600 X126.149 Y96.733 E266.29785
G0 F2700 X126.149 Y97.864
G1 F600 X132.134 Y103.849 E267.1424
G0 F2700 X131.002 Y103.849
G1 F600 X126.149 Y98.996 E267.82721
G0 F2700 X126.149 Y100.127
G1 F600 X129.871 Y103.849 E268.35243
G0 F2700 X128.74 Y103.849
G1 F600 X126.149 Y101.259 E268.71797
G0 F2700 X126.149 Y102.39
G1 F600 X127.608 Y103.849 E268.92386
G0 F2700 X126.477 Y103.849
G1 F600 X126.149 Y103.521 E268.97014
;MESH:NONMESH
G0 X126.149 Y103.521 Z1.8
G0 F2700 X125.79 Y85.79
;TIME_ELAPSED:300.067602
;LAYER:5
```

```
;TYPE:SKIN
;MESH:20x20x5_square.stl
G1 F600 X144.21 Y85.79 E270.80809
G1 X144.21 Y104.21 E272.64605
G1 X125.79 Y104.21 E274.484
G1 X125.79 Y85.79 E276.32196
G0 F3000 X126.149 Y86.548
G1 F600 X126.548 Y86.149 E276.37826
G0 F3000 X127.679 Y86.149
G1 F600 X126.149 Y87.679 E276.59416
G0 F3000 X126.149 Y88.811
G1 F600 X128.81 Y86.149 E276.96973
G0 F3000 X129.942 Y86.149
G1 F600 X126.149 Y89.942 E277.50496
G0 F3000 X126.149 Y91.073
G1 F600 X131.073 Y86.149 E278.19979
G0 F3000 X132.204 Y86.149
G1 F600 X126.149 Y92.205 E279.05429
G0 F3000 X126.149 Y93.336
G1 F600 X133.336 Y86.149 E280.06845
G0 F3000 X134.467 Y86.149
G1 F600 X126.149 Y94.468 E281.24228
G0 F3000 X126.149 Y95.599
G1 F600 X135.599 Y86.149 E282.57578
G0 F3000 X136.73 Y86.149
G1 F600 X126.149 Y96.73 E284.06887
G0 F3000 X126.149 Y97.862
G1 F600 X137.861 Y86.149 E285.72163
G0 F3000 X138.993 Y86.149
G1 F600 X126.149 Y98.993 E287.53406
G0 F3000 X126.149 Y100.124
G1 F600 X140.124 Y86.149 E289.50608
G0 F3000 X141.255 Y86.149
G1 F600 X126.149 Y101.256 E291.63777
G0 F3000 X126.149 Y102.387
G1 F600 X142.387 Y86.149 E293.92913
G0 F3000 X143.518 Y86.149
G1 F600 X126.149 Y103.519 E296.38015
G0 F3000 X126.949 Y103.849
G1 F600 X143.849 Y86.95 E298.76486
G0 F3000 X143.849 Y88.081
G1 F600 X128.081 Y103.849 E300.98989
G0 F3000 X129.212 Y103.849
G1 F600 X143.849 Y89.212 E303.05533
G0 F3000 X143.849 Y90.344
G1 F600 X130.343 Y103.849 E304.9611
G0 F3000 X131.475 Y103.849
G1 F600 X143.849 Y91.475 E306.70721
G0 F3000 X143.849 Y92.606
G1 F600 X132.606 Y103.849 E308.29372
G0 F3000 X133.737 Y103.849
G1 F600 X143.849 Y93.738 E309.72056
G0 F3000 X143.849 Y94.869
G1 F600 X134.869 Y103.849 E310.98773
G0 F3000 X136 Y103.849
G1 F600 X143.849 Y96.001 E312.09524
G0 F3000 X143.849 Y97.132
G1 F600 X137.132 Y103.849 E313.04308
G0 F3000 X138.263 Y103.849
G1 F600 X143.849 Y98.263 E313.83133
G0 F3000 X143.849 Y99.395
G1 F600 X139.394 Y103.849 E314.45991
G0 F3000 X140.526 Y103.849
G1 F600 X143.849 Y100.526 E314.92882
G0 F3000 X143.849 Y101.657
G1 F600 X141.657 Y103.849 E315.23813
G0 F3000 X142.788 Y103.849
G1 F600 X143.849 Y102.789 E315.38778
;MESH:NONMESH
G0 X143.849 Y102.789 Z2.1
G0 F3000 X125.79 Y85.79
;TIME_ELAPSED:348.801208
;LAYER:6
;TYPE:SKIN
;MESH:20x20x5_square.stl
G1 F600 X144.21 Y85.79 E317.22574
G1 X144.21 Y104.21 E319.06369
G1 X125.79 Y104.21 E320.90165
G1 X125.79 Y85.79 E322.7396
G0 F3000 X143.849 Y87.281
```

```
G1 F600 X142.718 Y86.149 E322.89927
G0 F3000 X141.586 Y86.149
G1 F600 X143.849 Y88.412 E323.2186
G0 F3000 X143.849 Y89.543
G1 F600 X140.455 Y86.149 E323.69753
G0 F3000 X139.324 Y86.149
G1 F600 X143.849 Y90.675 E324.33613
G0 F3000 X143.849 Y91.806
G1 F600 X138.192 Y86.149 E325.13439
G0 F3000 X137.061 Y86.149
G1 F600 X143.849 Y92.937 E326.09225
G0 F3000 X143.849 Y94.069
G1 F600 X135.929 Y86.149 E327.20985
G0 F3000 X134.798 Y86.149
G1 F600 X143.849 Y95.2 E328.48704
G0 F3000 X143.849 Y96.331
G1 F600 X133.667 Y86.149 E329.92383
G0 F3000 X132.535 Y86.149
G1 F600 X143.849 Y97.463 E331.52036
G0 F3000 X143.849 Y98.594
G1 F600 X131.404 Y86.149 E333.27648
G0 F3000 X130.273 Y86.149
G1 F600 X143.849 Y99.726 E335.19228
G0 F3000 X143.849 Y100.857
G1 F600 X129.141 Y86.149 E337.26773
G0 F3000 X128.01 Y86.149
G1 F600 X143.849 Y101.988 E339.50279
G0 F3000 X143.849 Y103.12
G1 F600 X126.878 Y86.149 E341.89758
G0 F3000 X126.149 Y86.551
G1 F600 X143.447 Y103.849 E344.33851
G0 F3000 X142.316 Y103.849
G1 F600 X126.149 Y87.682 E346.61985
G0 F3000 X126.149 Y88.814
G1 F600 X141.185 Y103.849 E348.74152
G0 F3000 X140.053 Y103.849
G1 F600 X126.149 Y89.945 E350.70353
G0 F3000 X126.149 Y91.076
G1 F600 X138.922 Y103.849 E352.50594
G0 F3000 X137.791 Y103.849
G1 F600 X126.149 Y92.208 E354.14868
G0 F3000 X126.149 Y93.339
G1 F600 X136.659 Y103.849 E355.63175
G0 F3000 X135.528 Y103.849
G1 F600 X126.149 Y94.47 E356.95523
G0 F3000 X126.149 Y95.602
G1 F600 X134.396 Y103.849 E358.11897
G0 F3000 X133.265 Y103.849
G1 F600 X126.149 Y96.733 E359.12312
G0 F3000 X126.149 Y97.864
G1 F600 X132.134 Y103.849 E359.96766
G0 F3000 X131.002 Y103.849
G1 F600 X126.149 Y98.996 E360.65247
G0 F3000 X126.149 Y100.127
G1 F600 X129.871 Y103.849 E361.17769
G0 F3000 X128.74 Y103.849
G1 F600 X126.149 Y101.259 E361.54324
G0 F3000 X126.149 Y102.39
G1 F600 X127.608 Y103.849 E361.74912
G0 F3000 X126.477 Y103.849
G1 F600 X126.149 Y103.521 E361.7954
;MESH:NONMESH
G0 X126.149 Y103.521 Z2.4
G0 F3000 X125.79 Y85.79
;TIME_ELAPSED:397.728452
;LAYER:7
;TYPE:SKIN
;MESH:20x20x5_square.stl
G1 F600 X144.21 Y85.79 E363.63336
G1 X144.21 Y104.21 E365.47131
G1 X125.79 Y104.21 E367.30927
G1 X125.79 Y85.79 E369.14722
G0 F3000 X126.149 Y86.548
G1 F600 X126.548 Y86.149 E369.20352
G0 F3000 X127.679 Y86.149
G1 F600 X126.149 Y87.679 E369.41942
G0 F3000 X126.149 Y88.811
```

```
G1 F600 X128.81 Y86.149 E369.79499
G0 F3000 X129.942 Y86.149
G1 F600 X126.149 Y89.942 E370.33022
G0 F3000 X126.149 Y91.073
G1 F600 X131.073 Y86.149 E371.02505
G0 F3000 X132.204 Y86.149
G1 F600 X126.149 Y92.205 E371.87955
G0 F3000 X126.149 Y93.336
G1 F600 X133.336 Y86.149 E372.89371
G0 F3000 X134.467 Y86.149
G1 F600 X126.149 Y94.468 E374.06754
G0 F3000 X126.149 Y95.599
G1 F600 X135.599 Y86.149 E375.40104
G0 F3000 X136.73 Y86.149
G1 F600 X126.149 Y96.73 E376.89413
G0 F3000 X126.149 Y97.862
G1 F600 X137.861 Y86.149 E378.54689
G0 F3000 X138.993 Y86.149
G1 F600 X126.149 Y98.993 E380.35932
G0 F3000 X126.149 Y100.124
G1 F600 X140.124 Y86.149 E382.33135
G0 F3000 X141.255 Y86.149
G1 F600 X126.149 Y101.256 E384.46304
G0 F3000 X126.149 Y102.387
G1 F600 X142.387 Y86.149 E386.75439
G0 F3000 X143.518 Y86.149
G1 F600 X126.149 Y103.519 E389.20542
G0 F3000 X126.949 Y103.849
G1 F600 X143.849 Y86.95 E391.59012
G0 F3000 X143.849 Y88.081
G1 F600 X128.081 Y103.849 E393.81515
G0 F3000 X129.212 Y103.849
G1 F600 X143.849 Y89.212 E395.88059
G0 F3000 X143.849 Y90.344
G1 F600 X130.343 Y103.849 E397.78636
G0 F3000 X131.475 Y103.849
G1 F600 X143.849 Y91.475 E399.53247
G0 F3000 X143.849 Y92.606
G1 F600 X132.606 Y103.849 E401.11898
G0 F3000 X133.737 Y103.849
G1 F600 X143.849 Y93.738 E402.54582
G0 F3000 X143.849 Y94.869
G1 F600 X134.869 Y103.849 E403.813
G0 F3000 X136 Y103.849
G1 F600 X143.849 Y96.001 E404.9205
G0 F3000 X143.849 Y97.132
G1 F600 X137.132 Y103.849 E405.86834
G0 F3000 X138.263 Y103.849
G1 F600 X143.849 Y98.263 E406.65659
G0 F3000 X143.849 Y99.395
G1 F600 X139.394 Y103.849 E407.28517
G0 F3000 X140.526 Y103.849
G1 F600 X143.849 Y100.526 E407.75408
G0 F3000 X143.849 Y101.657
G1 F600 X141.657 Y103.849 E408.06339
G0 F3000 X142.788 Y103.849
G1 F600 X143.849 Y102.789 E408.21304
;MESH:NONMESH
G0 X143.849 Y102.789 Z2.7
G0 F3000 X125.79 Y85.79
;TIME_ELAPSED:446.462058
;LAYER:8
;TYPE:SKIN
;MESH:20x20x5_square.stl
G1 F600 X144.21 Y85.79 E410.051
G1 X144.21 Y104.21 E411.88895
G1 X125.79 Y104.21 E413.72691
G1 X125.79 Y85.79 E415.56486
G0 F3000 X143.849 Y87.281
G1 F600 X142.718 Y86.149 E415.72453
G0 F3000 X141.586 Y86.149
G1 F600 X143.849 Y88.412 E416.04386
G0 F3000 X143.849 Y89.543
G1 F600 X140.455 Y86.149 E416.52279
G0 F3000 X139.324 Y86.149
G1 F600 X143.849 Y90.675 E417.16139
G0 F3000 X143.849 Y91.806
```

```
G1 F600 X138.192 Y86.149 E417.95965
G0 F3000 X137.061 Y86.149
G1 F600 X143.849 Y92.937 E418.91751
G0 F3000 X143.849 Y94.069
G1 F600 X135.929 Y86.149 E420.03511
G0 F3000 X134.798 Y86.149
G1 F600 X143.849 Y95.2 E421.31231
G0 F3000 X143.849 Y96.331
G1 F600 X133.667 Y86.149 E422.7491
G0 F3000 X132.535 Y86.149
G1 F600 X143.849 Y97.463 E424.34562
G0 F3000 X143.849 Y98.594
G1 F600 X131.404 Y86.149 E426.10175
G0 F3000 X130.273 Y86.149
G1 F600 X143.849 Y99.726 E428.01754
G0 F3000 X143.849 Y100.857
G1 F600 X129.141 Y86.149 E430.093
G0 F3000 X128.01 Y86.149
G1 F600 X143.849 Y101.988 E432.32805
G0 F3000 X143.849 Y103.12
G1 F600 X126.878 Y86.149 E434.72284
G0 F3000 X126.149 Y86.551
G1 F600 X143.447 Y103.849 E437.16378
G0 F3000 X142.316 Y103.849
G1 F600 X126.149 Y87.682 E439.44511
G0 F3000 X126.149 Y88.814
G1 F600 X141.185 Y103.849 E441.56679
G0 F3000 X140.053 Y103.849
G1 F600 X126.149 Y89.945 E443.52879
G0 F3000 X126.149 Y91.076
G1 F600 X138.922 Y103.849 E445.3312
G0 F3000 X137.791 Y103.849
G1 F600 X126.149 Y92.208 E446.97394
G0 F3000 X126.149 Y93.339
G1 F600 X136.659 Y103.849 E448.45701
G0 F3000 X135.528 Y103.849
G1 F600 X126.149 Y94.47 E449.78049
G0 F3000 X126.149 Y95.602
G1 F600 X134.396 Y103.849 E450.94423
G0 F3000 X133.265 Y103.849
G1 F600 X126.149 Y96.733 E451.94838
G0 F3000 X126.149 Y97.864
G1 F600 X132.134 Y103.849 E452.79293
G0 F3000 X131.002 Y103.849
G1 F600 X126.149 Y98.996 E453.47774
G0 F3000 X126.149 Y100.127
G1 F600 X129.871 Y103.849 E454.00295
G0 F3000 X128.74 Y103.849
G1 F600 X126.149 Y101.259 E454.3685
G0 F3000 X126.149 Y102.39
G1 F600 X127.608 Y103.849 E454.57438
G0 F3000 X126.477 Y103.849
G1 F600 X126.149 Y103.521 E454.62066
;MESH:NONMESH
G0 X126.149 Y103.521 Z3
G0 F3000 X125.79 Y85.79
;TIME_ELAPSED:495.389302
;LAYER:9
;TYPE:SKIN
;MESH:20x20x5_square.stl
G1 F600 X144.21 Y85.79 E456.45862
G1 X144.21 Y104.21 E458.29657
G1 X125.79 Y104.21 E460.13453
G1 X125.79 Y85.79 E461.97248
G0 F3000 X126.149 Y86.548
G1 F600 X126.548 Y86.149 E462.02879
G0 F3000 X127.679 Y86.149
G1 F600 X126.149 Y87.679 E462.24469
G0 F3000 X126.149 Y88.811
G1 F600 X128.81 Y86.149 E462.62025
G0 F3000 X129.942 Y86.149
G1 F600 X126.149 Y89.942 E463.15549
G0 F3000 X126.149 Y91.073
G1 F600 X131.073 Y86.149 E463.85032
G0 F3000 X132.204 Y86.149
G1 F600 X126.149 Y92.205 E464.70481
G0 F3000 X126.149 Y93.336
```

```
G1 F600 X133.336 Y86.149 E465.71898
G0 F3000 X134.467 Y86.149
G1 F600 X126.149 Y94.468 E466.89281
G0 F3000 X126.149 Y95.599
G1 F600 X135.599 Y86.149 E468.2263
G0 F3000 X136.73 Y86.149
G1 F600 X126.149 Y96.73 E469.7194
G0 F3000 X126.149 Y97.862
G1 F600 X137.861 Y86.149 E471.37216
G0 F3000 X138.993 Y86.149
G1 F600 X126.149 Y98.993 E473.18458
G0 F3000 X126.149 Y100.124
G1 F600 X140.124 Y86.149 E475.15661
G0 F3000 X141.255 Y86.149
G1 F600 X126.149 Y101.256 E477.2883
G0 F3000 X126.149 Y102.387
G1 F600 X142.387 Y86.149 E479.57965
G0 F3000 X143.518 Y86.149
G1 F600 X126.149 Y103.519 E482.03068
G0 F3000 X126.949 Y103.849
G1 F600 X143.849 Y86.95 E484.41538
G0 F3000 X143.849 Y88.081
G1 F600 X128.081 Y103.849 E486.64042
G0 F3000 X129.212 Y103.849
G1 F600 X143.849 Y89.212 E488.70585
G0 F3000 X143.849 Y90.344
G1 F600 X130.343 Y103.849 E490.61163
G0 F3000 X131.475 Y103.849
G1 F600 X143.849 Y91.475 E492.35773
G0 F3000 X143.849 Y92.606
G1 F600 X132.606 Y103.849 E493.94424
G0 F3000 X133.737 Y103.849
G1 F600 X143.849 Y93.738 E495.37108
G0 F3000 X143.849 Y94.869
G1 F600 X134.869 Y103.849 E496.63826
G0 F3000 X136 Y103.849
G1 F600 X143.849 Y96.001 E497.74577
G0 F3000 X143.849 Y97.132
G1 F600 X137.132 Y103.849 E498.69361
G0 F3000 X138.263 Y103.849
G1 F600 X143.849 Y98.263 E499.48185
G0 F3000 X143.849 Y99.395
G1 F600 X139.394 Y103.849 E500.11043
G0 F3000 X140.526 Y103.849
G1 F600 X143.849 Y100.526 E500.57934
G0 F3000 X143.849 Y101.657
G1 F600 X141.657 Y103.849 E500.88866
G0 F3000 X142.788 Y103.849
G1 F600 X143.849 Y102.789 E501.0383
;MESH:NONMESH
G0 X143.849 Y102.789 Z3.3
G0 F3000 X125.79 Y85.79
;TIME_ELAPSED:544.122908
;LAYER:10
;TYPE:SKIN
;MESH:20x20x5_square.stl
G1 F600 X144.21 Y85.79 E502.87626
G1 X144.21 Y104.21 E504.71421
G1 X125.79 Y104.21 E506.55217
G1 X125.79 Y85.79 E508.39012
G0 F3000 X143.849 Y87.281
G1 F600 X142.718 Y86.149 E508.54979
G0 F3000 X141.586 Y86.149
G1 F600 X143.849 Y88.412 E508.86912
G0 F3000 X143.849 Y89.543
G1 F600 X140.455 Y86.149 E509.34805
G0 F3000 X139.324 Y86.149
G1 F600 X143.849 Y90.675 E509.98665
G0 F3000 X143.849 Y91.806
G1 F600 X138.192 Y86.149 E510.78492
G0 F3000 X137.061 Y86.149
G1 F600 X143.849 Y92.937 E511.74278
G0 F3000 X143.849 Y94.069
G1 F600 X135.929 Y86.149 E512.86037
G0 F3000 X134.798 Y86.149
G1 F600 X143.849 Y95.2 E514.13757
G0 F3000 X143.849 Y96.331
G1 F600 X133.667 Y86.149 E515.57436
```

```
G0 F3000 X132.535 Y86.149
G1 F600 X143.849 Y97.463 E517.17088
G0 F3000 X143.849 Y98.594
G1 F600 X131.404 Y86.149 E518.92701
G0 F3000 X130.273 Y86.149
G1 F600 X143.849 Y99.726 E520.8428
G0 F3000 X143.849 Y100.857
G1 F600 X129.141 Y86.149 E522.91826
G0 F3000 X128.01 Y86.149
G1 F600 X143.849 Y101.988 E525.15331
G0 F3000 X143.849 Y103.12
G1 F600 X126.878 Y86.149 E527.5481
G0 F3000 X126.149 Y86.551
G1 F600 X143.447 Y103.849 E529.98904
G0 F3000 X142.316 Y103.849
G1 F600 X126.149 Y87.682 E532.27038
G0 F3000 X126.149 Y88.814
G1 F600 X141.185 Y103.849 E534.39205
G0 F3000 X140.053 Y103.849
G1 F600 X126.149 Y89.945 E536.35405
G0 F3000 X126.149 Y91.076
G1 F600 X138.922 Y103.849 E538.15646
G0 F3000 X137.791 Y103.849
G1 F600 X126.149 Y92.208 E539.7992
G0 F3000 X126.149 Y93.339
G1 F600 X136.659 Y103.849 E541.28228
G0 F3000 X135.528 Y103.849
G1 F600 X126.149 Y94.47 E542.60575
G0 F3000 X126.149 Y95.602
G1 F600 X134.396 Y103.849 E543.76949
G0 F3000 X133.265 Y103.849
G1 F600 X126.149 Y96.733 E544.77364
G0 F3000 X126.149 Y97.864
G1 F600 X132.134 Y103.849 E545.61819
G0 F3000 X131.002 Y103.849
G1 F600 X126.149 Y98.996 E546.303
G0 F3000 X126.149 Y100.127
G1 F600 X129.871 Y103.849 E546.82821
G0 F3000 X128.74 Y103.849
G1 F600 X126.149 Y101.259 E547.19376
G0 F3000 X126.149 Y102.39
G1 F600 X127.608 Y103.849 E547.39964
G0 F3000 X126.477 Y103.849
G1 F600 X126.149 Y103.521 E547.44593
;MESH:NONMESH
G0 X126.149 Y103.521 Z3.6
G0 F3000 X125.79 Y85.79
;TIME_ELAPSED:593.050152
;LAYER:11
;TYPE:SKIN
;MESH:20x20x5_square.stl
G1 F600 X144.21 Y85.79 E549.28388
G1 X144.21 Y104.21 E551.12184
G1 X125.79 Y104.21 E552.95979
G1 X125.79 Y85.79 E554.79775
G0 F3000 X126.149 Y86.548
G1 F600 X126.548 Y86.149 E554.85405
G0 F3000 X127.679 Y86.149
G1 F600 X126.149 Y87.679 E555.06995
G0 F3000 X126.149 Y88.811
G1 F600 X128.81 Y86.149 E555.44551
G0 F3000 X129.942 Y86.149
G1 F600 X126.149 Y89.942 E555.98075
G0 F3000 X126.149 Y91.073
G1 F600 X131.073 Y86.149 E556.67558
G0 F3000 X132.204 Y86.149
G1 F600 X126.149 Y92.205 E557.53007
G0 F3000 X126.149 Y93.336
G1 F600 X133.336 Y86.149 E558.54424
G0 F3000 X134.467 Y86.149
G1 F600 X126.149 Y94.468 E559.71807
G0 F3000 X126.149 Y95.599
G1 F600 X135.599 Y86.149 E561.05156
G0 F3000 X136.73 Y86.149
G1 F600 X126.149 Y96.73 E562.54466
G0 F3000 X126.149 Y97.862
G1 F600 X137.861 Y86.149 E564.19742
G0 F3000 X138.993 Y86.149
```

```
G1 F600 X126.149 Y98.993 E566.00985
G0 F3000 X126.149 Y100.124
G1 F600 X140.124 Y86.149 E567.98187
G0 F3000 X141.255 Y86.149
G1 F600 X126.149 Y101.256 E570.11356
G0 F3000 X126.149 Y102.387
G1 F600 X142.387 Y86.149 E572.40492
G0 F3000 X143.518 Y86.149
G1 F600 X126.149 Y103.519 E574.85594
G0 F3000 X126.949 Y103.849
G1 F600 X143.849 Y86.95 E577.24064
G0 F3000 X143.849 Y88.081
G1 F600 X128.081 Y103.849 E579.46568
G0 F3000 X129.212 Y103.849
G1 F600 X143.849 Y89.212 E581.53112
G0 F3000 X143.849 Y90.344
G1 F600 X130.343 Y103.849 E583.43689
G0 F3000 X131.475 Y103.849
G1 F600 X143.849 Y91.475 E585.18299
G0 F3000 X143.849 Y92.606
G1 F600 X132.606 Y103.849 E586.7695
G0 F3000 X133.737 Y103.849
G1 F600 X143.849 Y93.738 E588.19634
G0 F3000 X143.849 Y94.869
G1 F600 X134.869 Y103.849 E589.46352
G0 F3000 X136 Y103.849
G1 F600 X143.849 Y96.001 E590.57103
G0 F3000 X143.849 Y97.132
G1 F600 X137.132 Y103.849 E591.51887
G0 F3000 X138.263 Y103.849
G1 F600 X143.849 Y98.263 E592.30711
G0 F3000 X143.849 Y99.395
G1 F600 X139.394 Y103.849 E592.93569
G0 F3000 X140.526 Y103.849
G1 F600 X143.849 Y100.526 E593.4046
G0 F3000 X143.849 Y101.657
G1 F600 X141.657 Y103.849 E593.71392
G0 F3000 X142.788 Y103.849
G1 F600 X143.849 Y102.789 E593.86357
;MESH:NONMESH
G0 X143.849 Y102.789 Z3.9
G0 F3000 X125.79 Y85.79
;TIME_ELAPSED:641.783758
;LAYER:12
;TYPE:SKIN
;MESH:20x20x5_square.stl
G1 F600 X144.21 Y85.79 E595.70152
G1 X144.21 Y104.21 E597.53948
G1 X125.79 Y104.21 E599.37743
G1 X125.79 Y85.79 E601.21539
G0 F3000 X143.849 Y87.281
G1 F600 X142.718 Y86.149 E601.37505
G0 F3000 X141.586 Y86.149
G1 F600 X143.849 Y88.412 E601.69439
G0 F3000 X143.849 Y89.543
G1 F600 X140.455 Y86.149 E602.17332
G0 F3000 X139.324 Y86.149
G1 F600 X143.849 Y90.675 E602.81191
G0 F3000 X143.849 Y91.806
G1 F600 X138.192 Y86.149 E603.61018
G0 F3000 X137.061 Y86.149
G1 F600 X143.849 Y92.937 E604.56804
G0 F3000 X143.849 Y94.069
G1 F600 X135.929 Y86.149 E605.68563
G0 F3000 X134.798 Y86.149
G1 F600 X143.849 Y95.2 E606.96283
G0 F3000 X143.849 Y96.331
G1 F600 X133.667 Y86.149 E608.39962
G0 F3000 X132.535 Y86.149
G1 F600 X143.849 Y97.463 E609.99615
G0 F3000 X143.849 Y98.594
G1 F600 X131.404 Y86.149 E611.75227
G0 F3000 X130.273 Y86.149
G1 F600 X143.849 Y99.726 E613.66806
G0 F3000 X143.849 Y100.857
G1 F600 X129.141 Y86.149 E615.74352
G0 F3000 X128.01 Y86.149
G1 F600 X143.849 Y101.988 E617.97857
```

```
G0 F3000 X143.849 Y103.12
G1 F600 X126.878 Y86.149 E620.37336
G0 F3000 X126.149 Y86.551
G1 F600 X143.447 Y103.849 E622.8143
G0 F3000 X142.316 Y103.849
G1 F600 X126.149 Y87.682 E625.09564
G0 F3000 X126.149 Y88.814
G1 F600 X141.185 Y103.849 E627.21731
G0 F3000 X140.053 Y103.849
G1 F600 X126.149 Y89.945 E629.17931
G0 F3000 X126.149 Y91.076
G1 F600 X138.922 Y103.849 E630.98172
G0 F3000 X137.791 Y103.849
G1 F600 X126.149 Y92.208 E632.62446
G0 F3000 X126.149 Y93.339
G1 F600 X136.659 Y103.849 E634.10754
G0 F3000 X135.528 Y103.849
G1 F600 X126.149 Y94.47 E635.43102
G0 F3000 X126.149 Y95.602
G1 F600 X134.396 Y103.849 E636.59476
G0 F3000 X133.265 Y103.849
G1 F600 X126.149 Y96.733 E637.5989
G0 F3000 X126.149 Y97.864
G1 F600 X132.134 Y103.849 E638.44345
G0 F3000 X131.002 Y103.849
G1 F600 X126.149 Y98.996 E639.12826
G0 F3000 X126.149 Y100.127
G1 F600 X129.871 Y103.849 E639.65347
G0 F3000 X128.74 Y103.849
G1 F600 X126.149 Y101.259 E640.01902
G0 F3000 X126.149 Y102.39
G1 F600 X127.608 Y103.849 E640.2249
G0 F3000 X126.477 Y103.849
G1 F600 X126.149 Y103.521 E640.27119
;MESH:NONMESH
G0 X126.149 Y103.521 Z4.2
G0 F3000 X125.79 Y85.79
;TIME_ELAPSED:690.711001
;LAYER:13
;TYPE:SKIN
;MESH:20x20x5_square.stl
G1 F600 X144.21 Y85.79 E642.10914
G1 X144.21 Y104.21 E643.9471
G1 X125.79 Y104.21 E645.78505
G1 X125.79 Y85.79 E647.62301
G0 F3000 X126.149 Y86.548
G1 F600 X126.548 Y86.149 E647.67931
G0 F3000 X127.679 Y86.149
G1 F600 X126.149 Y87.679 E647.89521
G0 F3000 X126.149 Y88.811
G1 F600 X128.81 Y86.149 E648.27078
G0 F3000 X129.942 Y86.149
G1 F600 X126.149 Y89.942 E648.80601
G0 F3000 X126.149 Y91.073
G1 F600 X131.073 Y86.149 E649.50084
G0 F3000 X132.204 Y86.149
G1 F600 X126.149 Y92.205 E650.35534
G0 F3000 X126.149 Y93.336
G1 F600 X133.336 Y86.149 E651.3695
G0 F3000 X134.467 Y86.149
G1 F600 X126.149 Y94.468 E652.54333
G0 F3000 X126.149 Y95.599
G1 F600 X135.599 Y86.149 E653.87683
G0 F3000 X136.73 Y86.149
G1 F600 X126.149 Y96.73 E655.36992
G0 F3000 X126.149 Y97.862
G1 F600 X137.861 Y86.149 E657.02268
G0 F3000 X138.993 Y86.149
G1 F600 X126.149 Y98.993 E658.83511
G0 F3000 X126.149 Y100.124
G1 F600 X140.124 Y86.149 E660.80713
G0 F3000 X141.255 Y86.149
G1 F600 X126.149 Y101.256 E662.93882
G0 F3000 X126.149 Y102.387
G1 F600 X142.387 Y86.149 E665.23018
G0 F3000 X143.518 Y86.149
G1 F600 X126.149 Y103.519 E667.6812
```

```
G0 F3000 X126.949 Y103.849
G1 F600 X143.849 Y86.95 E670.0659
G0 F3000 X143.849 Y88.081
G1 F600 X128.081 Y103.849 E672.29094
G0 F3000 X129.212 Y103.849
G1 F600 X143.849 Y89.212 E674.35638
G0 F3000 X143.849 Y90.344
G1 F600 X130.343 Y103.849 E676.26215
G0 F3000 X131.475 Y103.849
G1 F600 X143.849 Y91.475 E678.00826
G0 F3000 X143.849 Y92.606
G1 F600 X132.606 Y103.849 E679.59476
G0 F3000 X133.737 Y103.849
G1 F600 X143.849 Y93.738 E681.02161
G0 F3000 X143.849 Y94.869
G1 F600 X134.869 Y103.849 E682.28878
G0 F3000 X136 Y103.849
G1 F600 X143.849 Y96.001 E683.39629
G0 F3000 X143.849 Y97.132
G1 F600 X137.132 Y103.849 E684.34413
G0 F3000 X138.263 Y103.849
G1 F600 X143.849 Y98.263 E685.13237
G0 F3000 X143.849 Y99.395
G1 F600 X139.394 Y103.849 E685.76095
G0 F3000 X140.526 Y103.849
G1 F600 X143.849 Y100.526 E686.22986
G0 F3000 X143.849 Y101.657
G1 F600 X141.657 Y103.849 E686.53918
G0 F3000 X142.788 Y103.849
G1 F600 X143.849 Y102.789 E686.68883
;MESH:NONMESH
G0 X143.849 Y102.789 Z4.5
G0 F3000 X125.79 Y85.79
;TIME_ELAPSED:739.444607
;LAYER:14
;TYPE:SKIN
;MESH:20x20x5_square.stl
G1 F600 X144.21 Y85.79 E688.52678
G1 X144.21 Y104.21 E690.36474
G1 X125.79 Y104.21 E692.20269
G1 X125.79 Y85.79 E694.04065
G0 F3000 X143.849 Y87.281
G1 F600 X142.718 Y86.149 E694.20031
G0 F3000 X141.586 Y86.149
G1 F600 X143.849 Y88.412 E694.51965
G0 F3000 X143.849 Y89.543
G1 F600 X140.455 Y86.149 E694.99858
G0 F3000 X139.324 Y86.149
G1 F600 X143.849 Y90.675 E695.63718
G0 F3000 X143.849 Y91.806
G1 F600 X138.192 Y86.149 E696.43544
G0 F3000 X137.061 Y86.149
G1 F600 X143.849 Y92.937 E697.3933
G0 F3000 X143.849 Y94.069
G1 F600 X135.929 Y86.149 E698.5109
G0 F3000 X134.798 Y86.149
G1 F600 X143.849 Y95.2 E699.78809
G0 F3000 X143.849 Y96.331
G1 F600 X133.667 Y86.149 E701.22488
G0 F3000 X132.535 Y86.149
G1 F600 X143.849 Y97.463 E702.82141
G0 F3000 X143.849 Y98.594
G1 F600 X131.404 Y86.149 E704.57753
G0 F3000 X130.273 Y86.149
G1 F600 X143.849 Y99.726 E706.49332
G0 F3000 X143.849 Y100.857
G1 F600 X129.141 Y86.149 E708.56878
G0 F3000 X128.01 Y86.149
G1 F600 X143.849 Y101.988 E710.80383
G0 F3000 X143.849 Y103.12
G1 F600 X126.878 Y86.149 E713.19863
G0 F3000 X126.149 Y86.551
G1 F600 X143.447 Y103.849 E715.63956
G0 F3000 X142.316 Y103.849
G1 F600 X126.149 Y87.682 E717.9209
G0 F3000 X126.149 Y88.814
G1 F600 X141.185 Y103.849 E720.04257
```

```
G0 F3000 X140.053 Y103.849
G1 F600 X126.149 Y89.945 E722.00458
G0 F3000 X126.149 Y91.076
G1 F600 X138.922 Y103.849 E723.80698
G0 F3000 X137.791 Y103.849
G1 F600 X126.149 Y92.208 E725.44972
G0 F3000 X126.149 Y93.339
G1 F600 X136.659 Y103.849 E726.9328
G0 F3000 X135.528 Y103.849
G1 F600 X126.149 Y94.47 E728.25628
G0 F3000 X126.149 Y95.602
G1 F600 X134.396 Y103.849 E729.42002
G0 F3000 X133.265 Y103.849
G1 F600 X126.149 Y96.733 E730.42416
G0 F3000 X126.149 Y97.864
G1 F600 X132.134 Y103.849 E731.26871
G0 F3000 X131.002 Y103.849
G1 F600 X126.149 Y98.996 E731.95352
G0 F3000 X126.149 Y100.127
G1 F600 X129.871 Y103.849 E732.47874
G0 F3000 X128.74 Y103.849
G1 F600 X126.149 Y101.259 E732.84428
G0 F3000 X126.149 Y102.39
G1 F600 X127.608 Y103.849 E733.05016
G0 F3000 X126.477 Y103.849
G1 F600 X126.149 Y103.521 E733.09645
;MESH:NONMESH
G0 X126.149 Y103.521 Z4.8
G0 F3000 X125.79 Y85.79
;TIME_ELAPSED:788.371851
;LAYER:15
;TYPE:SKIN
;MESH:20x20x5_square.stl
G1 F600 X144.21 Y85.79 E734.9344
G1 X144.21 Y104.21 E736.77236
G1 X125.79 Y104.21 E738.61031
G1 X125.79 Y85.79 E740.44827
G0 F3000 X126.149 Y86.548
G1 F600 X126.548 Y86.149 E740.50457
G0 F3000 X127.679 Y86.149
G1 F600 X126.149 Y87.679 E740.72047
G0 F3000 X126.149 Y88.811
G1 F600 X128.81 Y86.149 E741.09604
G0 F3000 X129.942 Y86.149
G1 F600 X126.149 Y89.942 E741.63127
G0 F3000 X126.149 Y91.073
G1 F600 X131.073 Y86.149 E742.3261
G0 F3000 X132.204 Y86.149
G1 F600 X126.149 Y92.205 E743.1806
G0 F3000 X126.149 Y93.336
G1 F600 X133.336 Y86.149 E744.19476
G0 F3000 X134.467 Y86.149
G1 F600 X126.149 Y94.468 E745.36859
G0 F3000 X126.149 Y95.599
G1 F600 X135.599 Y86.149 E746.70209
G0 F3000 X136.73 Y86.149
G1 F600 X126.149 Y96.73 E748.19518
G0 F3000 X126.149 Y97.862
G1 F600 X137.861 Y86.149 E749.84794
G0 F3000 X138.993 Y86.149
G1 F600 X126.149 Y98.993 E751.66037
G0 F3000 X126.149 Y100.124
G1 F600 X140.124 Y86.149 E753.63239
G0 F3000 X141.255 Y86.149
G1 F600 X126.149 Y101.256 E755.76408
G0 F3000 X126.149 Y102.387
G1 F600 X142.387 Y86.149 E758.05544
G0 F3000 X143.518 Y86.149
G1 F600 X126.149 Y103.519 E760.50646
G0 F3000 X126.949 Y103.849
G1 F600 X143.849 Y86.95 E762.89117
G0 F3000 X143.849 Y88.081
G1 F600 X128.081 Y103.849 E765.1162
G0 F3000 X129.212 Y103.849
G1 F600 X143.849 Y89.212 E767.18164
G0 F3000 X143.849 Y90.344
G1 F600 X130.343 Y103.849 E769.08741
```

```
G0 F3000 X131.475 Y103.849
G1 F600 X143.849 Y91.475 E770.83352
G0 F3000 X143.849 Y92.606
G1 F600 X132.606 Y103.849 E772.42003
G0 F3000 X133.737 Y103.849
G1 F600 X143.849 Y93.738 E773.84687
G0 F3000 X143.849 Y94.869
G1 F600 X134.869 Y103.849 E775.11404
G0 F3000 X136 Y103.849
G1 F600 X143.849 Y96.001 E776.22155
G0 F3000 X143.849 Y97.132
G1 F600 X137.132 Y103.849 E777.16939
G0 F3000 X138.263 Y103.849
G1 F600 X143.849 Y98.263 E777.95764
G0 F3000 X143.849 Y99.395
G1 F600 X139.394 Y103.849 E778.58621
G0 F3000 X140.526 Y103.849
G1 F600 X143.849 Y100.526 E779.05513
G0 F3000 X143.849 Y101.657
G1 F600 X141.657 Y103.849 E779.36444
G0 F3000 X142.788 Y103.849
G1 F600 X143.849 Y102.789 E779.51409
;TIME_ELAPSED:836.503729
M140 S0
M201 X4000 Y4000
M202 X4000 Y4000
M207 X20
M104 S0
M140 S0
;Retract the filament
G92 E1
G1 E-1 F300
G28 X0 Y0
M84
M82 ;absolute extrusion mode
M104 S0
;End of Gcode
```

APPENDIX E - EXTRA EXPERIMENTAL DATA

This section includes additional experimental data based on results of composite filament and printed part characterization.

E.1 Composite Density Data

E.2 Printed Part Quality and Geometric Tolerance

E.1 Composite Density Data

Table E-1 Theoretical and Measured Composite Densities

Filament	True Density (g/cm^3)		
	Theoretical Composite (ROM)	Average Filament	Average Printed
F1	7.72	5.96 (± 0.19)	6.20 (± 0.20)
F2	7.45	6.31 (± 0.16)	6.54 (± 0.15)
F3	7.57	5.84 (± 0.01)	6.05 (± 0.10)
F4	7.51	6.63 (± 0.02)	6.56 (± 0.13)
F5	4.14	3.22 (± 0.07)	3.39 (± 0.14)
F6	3.64	2.94 (± 0.01)	2.87 (± 0.06)
F7	3.13	2.73 (± 0.03)	2.70 (± 0.11)
F8	3.19	2.71 (± 0.03)	2.89 (± 0.03)
F9	3.05	2.66 (± 0.01)	2.60 (± 0.02)
F10	3.05	2.73 (± 0.01)	2.71 (± 0.09)

Table E-2 Comparison of Experimental data and Ideal ROM data (filament vs. dry)

Filament	δ	Θ_{dry} (ROM)	%Polymer (Filament)	$\Delta\Theta_{polymer}$ (Filament)	Θ_{dry} (exp)	$\Delta\Theta_{dry}$	**Difference** ($\Delta\Theta_{polymer} - \Delta\Theta_{dry}$)
F1	0.13	0.529	0.597	0.068	0.478	-0.051	0.119
F2	0.18	0.532	0.576	0.044	0.500	-0.032	0.076
F3	0.2	0.517	0.608	0.091	0.491	-0.026	0.117
F4	0.27	0.520	0.546	0.026	0.486	-0.034	0.060
F5	0.1	0.534	0.537	0.003	0.405	-0.129	0.132
F6	0.25	0.539	0.577	0.038	0.476	-0.063	0.101
F7	0.1	0.559	0.563	0.004	0.497	-0.062	0.066
F8	0.15	0.569	0.575	0.006	0.499	-0.070	0.076
F9	0.2	0.533	0.564	0.031	0.501	-0.032	0.063
F10	0.25	0.539	0.553	0.014	0.500	-0.039	0.053
						average	0.086
						STD	0.028

Table E-3 Comparison of Experimental data and Ideal ROM data (printed vs. dry)

Filament	δ	Θ_{dry} (ROM)	%Polymer (Printed)	$\Delta\Theta_{polymer}$ (Printed)	Difference ($\Delta\Theta_{polymer}$ - $\Delta\Theta_{dry}$)
F1	0.13	0.529	0.592	0.063	0.114
F2	0.18	0.532	0.567	0.035	0.067
F3	0.2	0.517	0.605	0.089	0.114
F4	0.27	0.520	0.560	0.040	0.074
F5	0.1	0.534	0.536	0.002	0.131
F6	0.25	0.539	0.621	0.082	0.145
F7	0.1	0.559	0.595	0.036	0.098
F8	0.15	0.569	0.551	-0.017	0.052
F9	0.2	0.533	0.602	0.070	0.102
F10	0.25	0.539	0.579	0.040	0.079
				Average	0.098
				STD	0.030

E.2 Printed Part Quality and Geometric Tolerance

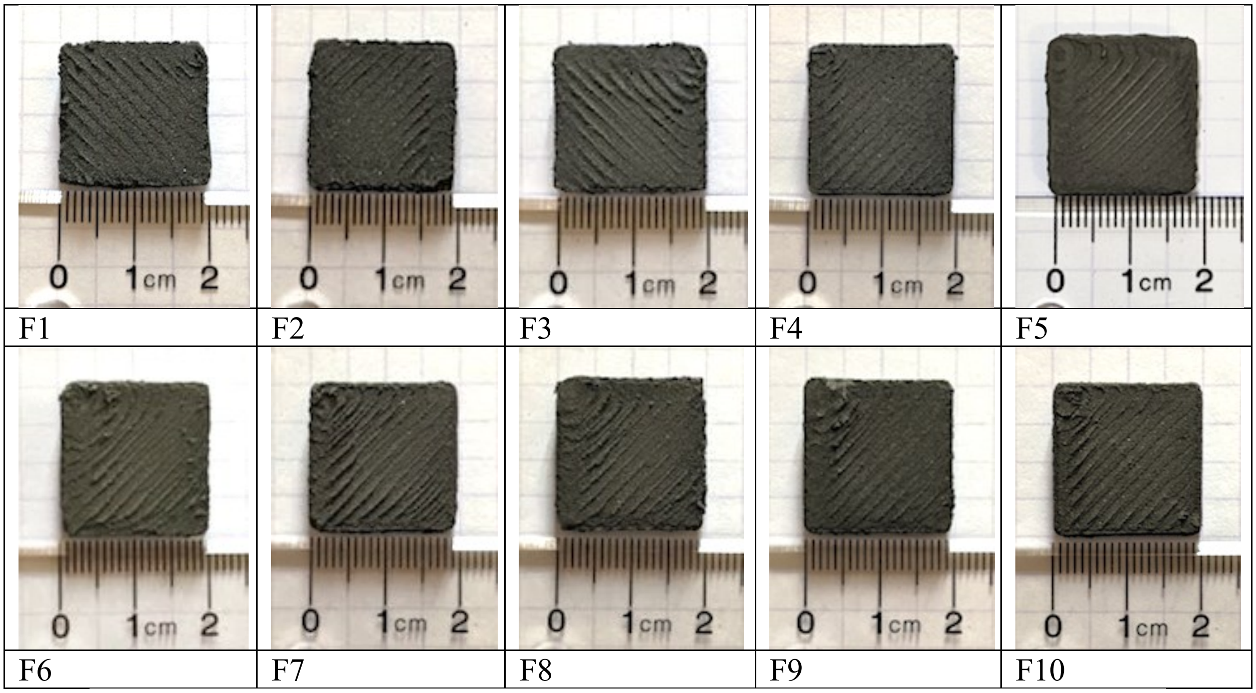
F1 F2 F3 F4 F5

F6 F7 F8 F9 F10

Figure E-1 Visual Comparison of Printed Samples from Each Filament F1-F10

Table E-4 Average Measured Dimensions of Printed Samples

Filament	Length (mm)	Width (mm)	Height (mm)
F1	19.9 ± 0.5	20.0 ± 0.2	4.7 ± 0.1
F2	20.0 ±0.3	20.0 ± 0.3	4.8 ± 0.0
F3	20.0 ± 0.1	19.8 ± 0.1	4.9 ± 0.1
F4	19.9 ± 0.1	19.7 ± 0.2	4.8 ± 0.1
F5	20.2 ± 0.1	19.7 ± 0.3	4.9 ± 0.0
F6	20.1 ± 0.0	19.9 ± 0.0	4.7 ± 0.1
F7	19.9 ± 0.2	19.8 ± 0.2	4.8 ± 0.1
F8	20.4 ± 0.1	20.0 ± 0.1	4.8 ± 0.1
F9	20.0 ± 0.1	19.8 ± 0.1	4.8 ± 0.1
F10	20.0 ± 0.1	19.8 ± 0.1	4.8 ± 0.0

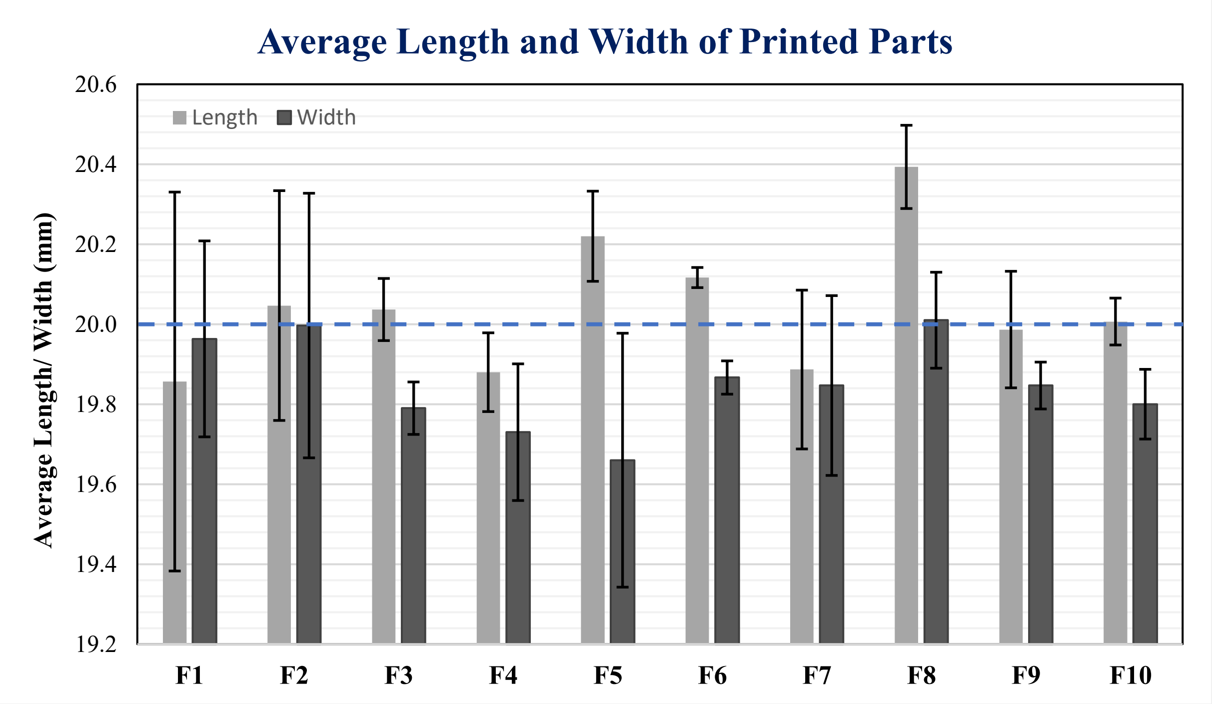

Figure E-2 Average length and width of printed part

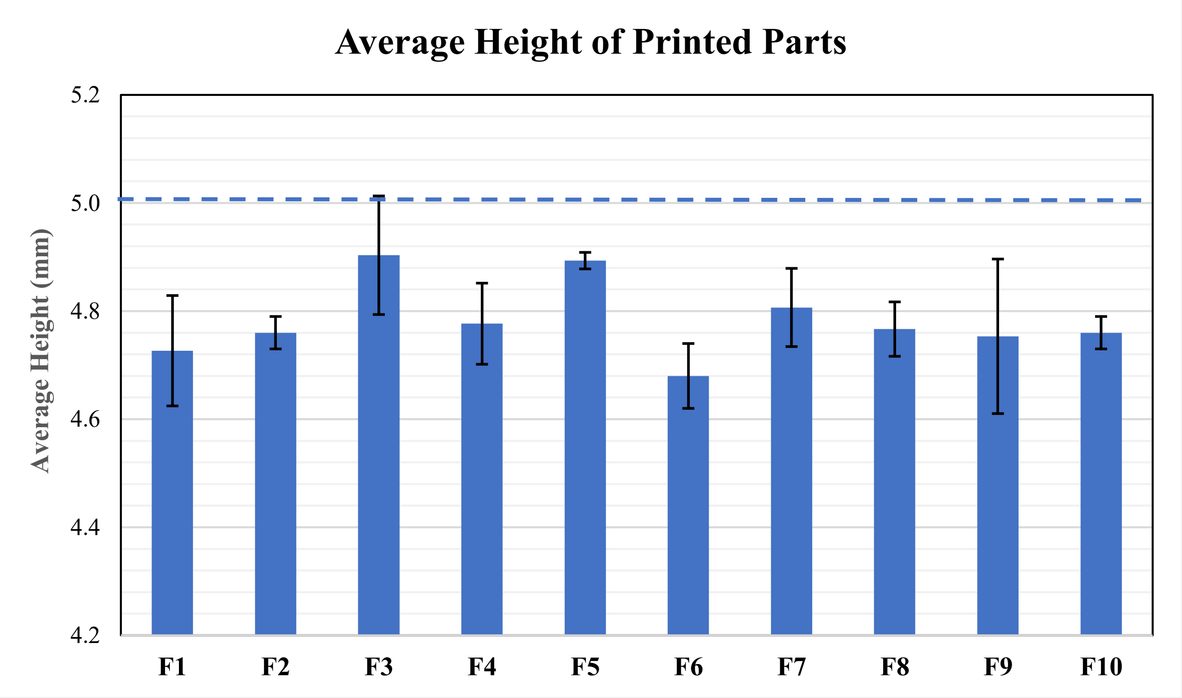

Figure E-3 Average height of printed part